Topological phases, light response and kagome lattice

Julian Legendre

INSTITUT POLYTECHNIQUE DE PARIS

NNT : 2022IPPAX074

Thèse de doctorat

Topological phases, light response and kagome lattice

Thèse de doctorat de l'Institut Polytechnique de Paris
préparée à l'École polytechnique

École doctorale n°626
École doctorale de l'Institut Polytechnique de Paris (ED IP Paris)
Spécialité de doctorat : Physique de la matière condensée

Thèse présentée et soutenue à Palaiseau, le 15 septembre 2022, par

JULIAN LEGENDRE

Composition du Jury :

Walter Hofstetter Professeur, Goethe Universität Frankfurt (Institut für Theoretische Physik)	Président
Grégoire Misguich Chercheur en physique théorique et ingénieur CEA (Institut de Physique Théorique)	Rapporteur
Guillaume Roux Maître de Conférences, Université Paris-Saclay (Laboratoire de Physique Théorique et Modèles Statistiques)	Rapporteur
Pierre Pujol Professeur, Université Paul Sabatier Toulouse (Laboratoire de Physique Théorique)	Examinateur
Ulrich Schneider Profeseur, University of Cambridge (Cavendish Laboratory)	Examinateur
Karyn Le Hur Directrice de Recherche au CNRS et Professeure PCC, Ecole Polytechnique (Centre de Physique Théorique)	Directrice de thèse

Abstract

We theoretically study topological lattice models relevant to current experimental solid-state and artificial systems. We develop an explicit analytical computation of the Chern number in the systems we study and we compare it with other computation methods of this topological invariant. We propose a protocol, based on the local response to a light input, to probe the topological properties of a Haldane boson model in a photonic system. On the kagome lattice, we investigate (i) a magnetic and topological phase transition for a two-channel model, in relation with recently discovered quantum materials, and (ii) a time-reversal topological model with flux, Rashba spin-orbit coupling and Hubbard interactions, relevant for realization in cold-atom gases.

Acknowledgements

I acknowledge the french ANR (Agence Nationale de la Recherche) for support through ANR BOCA. I also acknowledge the Deutsche Forschungsgemeinschaft (DFG, German Research Foundation) under Project No. 277974659 via Research Unit FOR 2414, through which we collaborated with Walter Hofstetter's group (Goethe Universität Frankfurt) and exchanged with the other research groups involved in this Research Unit FOR 2414.

There are many persons with whom I interacted during my PhD time and without whom these last three years would not have been a great time for me.

First I am grateful to Karyn who guided me during this three years and from whom I learned a lot. She is a dedicated and a conscientious advisor and it was a great pleasure to be one of her students.

The members of the Jury, who kindly accepted to spend time for evaluating my PhD, have all my gratitude. Moreover, Guillaume Roux and Laura Messio were both members of my mid-term PhD assessment and were also my professors during my master's studies. Their teaching and advices were very precious to me. More generally I also want to thank all the dedicated teachers I had during my masters' and bachelor's studies; they had a non-negligible impact on my interest in science.

I shared very rewarding discussions with Walter Hofstetter, Irakli titvinidze, Maarten Grothus and Bernhard Irsigler. It has been a pleasure to work with them. I have also shared very interesting discussions with Jérome Estève and Julien Gabelli.

I spent very good moments with the (previous and current) members of Karyn's team,

Ariane, Fan, Philipp, Ephraim, Joel, Frederick and Sariah and I had nice discussions with other members of the CPHT, Benjamin, Jan and Erik.

Jean René Chazottes, Florence Auger, Fadila Debbou and Malika Lang helped me with, often time, with administrative tasks and Danh Pham Kim, Yannick Fitamant, Jean-Luc Bellon and Vazoumana Fofana were always ready to help with informatics issues, and I am grateful to all of them.

Finally, I thank everybody who has contributed to my private social life during these last three years, for every shared moment.

Contents

Introduction

Topology is concerned with continuous deformations between mathematical objects. Topology in condensed matter physics, deals with continuous deformations between Hamiltonians describing quantum systems. It is namely applicable to systems with a gap in the energy spectrum and for which all the states below the gap are occupied. Consider two (insulating) lattice translation-invariant quantum systems, each of which is described by a Hamiltonian. If there exists continuous deformations between both Hamiltonians describing both systems, without any gap closure, then both systems share the same topological properties. The classification of topological phases relies on topological invariants; the dimension and the symmetries of the system determine the associated topological invariant [1]. In this manuscript, we are concerned with two-dimensional systems, which break or do not break time-reversal symmetry, respectively associated to the so-called (first) Chern number and to the $\mathbb{Z}_2$ topological invariant [2–5].

The study of the topological phases of matter has quite a recent history compared to most other phases of matter, *e.g.* magnetically ordered phases, Bose-Einstein condensates or superconductors. One of the first reasons is that the former are less usual and less experimentally accessible than most other phases of matter. Another reason is that the Ginzburg-Landau theory, a theory describing most of the phases of matter, generally fails to describe the topological phases. This is because the latter (most often) are described by a non-local order parameter and may appear without spontaneously broken symmetry while Ginzburg-Landau theory is built on local order parameters and describes ordered phases

characterized by a spontaneously broken symmetry.

In 1980, von Klitzing *et al.* [6] characterized a new phase of matter. They measured the Hall conductance in a two-dimensional electron gas with strong perpendicular magnetic field. Varying the amplitude of the latter, they observed that the Hall conductance evolves by plateaus, each plateau corresponding to a phase with a quantized value of the Hall conductance. Such phases are topological phases called quantum Hall phases. In a quantum Hall phase, the bulk of the sample is insulating while states which are localized at the edges of the sample are associated with chiral non-dissipative currents at the Fermi energy. The quantized Hall conductance [7] can be interpreted as a topological invariant called the Chern number. A phase with non-zero Chern number is called a Chern insulating phase. A usual formulation of the Chern number is the integral of a curvature (called the Berry curvature) over the momentum space [8, 9]. The Berry curvature is the rotational of the so-called Berry connection which depends on the eigenstates of the system. The latter are defined up to a U(1) gauge. This forms a U(1) fiber bundle; the bundle being the Brillouin zone and the fiber being the U(1) gauge of the eigenvectors. The topology of this U(1) bundle is not trivial if the eigenstates can not be trivially connected over the bundle [10].

In mathematics, a two-dimensional closed surface can be characterized by the integral of a curvature (the Gaussian curvature in this case) over the surface. This integral gives a topological invariant which is an integer (Gauss-Bonnet theorem) and which is called the genus of the surface. It is analogue to the Chern number. Two surfaces with the same genus can be continuously transformed into each other (without cutting and pasting) while this is not the case for two surfaces with distinct genus. This is analogue to the impossibility of continuously transforming two distinct Chern insulating phases into each other. The Berry curvature and the Berry connection [9], are quantities which are comparable respectively to the magnetic field and to the magnetic vector potential. The geometrical phase accumulated by a particle during an adiabatic evolution of a quantum system is called the Berry phase;

it is analogue to the Peierls phase (phase accumulated by a particle moving in a magnetic vector potential). The Berry phase concept is essential for the understanding of topology in condensed matter. In particular, degeneracies associated to linear dispersion relation (Dirac points) in a two-level system are sources of Berry curvatures, and are analogues to magnetic Dirac monopoles. The latter are quantized, so as the Chern number which counts the number of monopoles of Berry flux inside the Brillouin zone.

In the quantum Hall effect, an external magnetic field is at the origin of non-trivial Berry curvature which gives a non zero Chern number. In 1988, Haldane introduced a honeycomb lattice model characterized by non-zero Chern number with a vanishing total flux in the unit cell (no Landau levels) [5]. Such a phase is called a quantum anomalous Hall (QAH) phase. The Haldane model has had a huge impact in topology in condensed matter, and it led, a bit more than fifteen years later, to the birth of a topological band theory [11–14]. This theory describes time-reversal invariant topological insulators which are characterized by counter-propagating edges states protected by time-reversal symmetry. The associated topological phase is called a quantum spin Hall (QSH) phase and spin-orbit interaction is crucial for this phase to appear.

These topological phases have been built and investigated in solid states systems and also in artificial systems [15–18]. The Berry phase was first measured using an optical fiber [19]. Artificial systems, which are highly controllable, enable to simulate and study solid state systems. This is particularly relevant for the study of topological phases since gauge fields can be created in artificial systems. Moreover, the latter enable to implement Hubbard interactions and control their strength, which is very helpful for studying correlated systems. Hubbard interactions can have an important effect on the properties of a topological system, as it is the case in several quantum materials which have attracted a lot of attention recently [20–29].

In this manuscript, we investigate topological models on the honeycomb and the kagome

lattice. Nearest-neighbor tight-binding models associated to these lattice show Dirac Fermions which are the origin of topological properties observed when these tight-binding models are changed to topological ones. In artificial systems, the experimental implementation and the measurement of the topological properties can be challenging. We propose a simple protocol, based on the response to a local light input, to probe the topological properties of a Haldane boson system. In kagome models, the computation of the Chern number can be tedious. We develop an explicit analytical computation of this topological invariant for the kagome models we study. We investigate the interplay between topological phases (QAH and quantum spin Hall phases) and magnetic phases by (i) considering the coupling between a topological model and a spin model through a ferromagnetic Hund's coupling term and (ii) studying a time-reversal topological model with flux, Rashba spin-orbit coupling and Hubbard interactions.

In Chapter 1, we introduce the formalism and we review the important discoveries and concepts in topology in condensed matter which we use in this manuscript. The Berry phase is one of the most important concept in this field and its connection with the integer quantum Hall effect, the Chern number and the properties of Chern insulators is explained. We also review the topological band theory describing time-reversal invariant topological systems and the associated topological $\mathbb{Z}_2$ invariant.

In Chapter 2, we consider a circuit quantum electrodynamics (cQED) system which is described by an effective Haldane boson model. We develop an explicit analytical computation of the Chern number for this model [5]. In one-dimensional cQED system, it has been shown that the topological properties are measurable from the reflection of microwave light [30]. Using the insight gained from the computation of the Chern number, we propose a protocol to probe the topological properties through the response to a local light input. This is potentially applicable in other boson systems for which a capacitive coupling to a probe is realizable.

In Chapter 3, we consider two simple topological models on the kagome lattice, one is a Chern insulator, the other is a quantum spin Hall insulator. These topological models have attracted much attention [31–42]. The computation of the (spin) Chern numbers has been performed using diverse methods, however, performing an explicit analytical computation of this invariant from a study of the U(1) gauge of the eigenstates (of the Hamiltonian describing the system) is not an easy task and does not appear in the literature before our publication. Motivated by this, we develop such a computation. We also consider two spin copies of this kagome system and we compute the associated $\mathbb{Z}_2$ invariant. These computations are extended, in Chapter 5, to a bit more involved model. We also investigate the topological properties of small noisy kagome systems, thanks to numerical computations of local observables.

In Chapter 4, we introduce and study a magnetic and topological model on the kagome lattice [193], in relation with recently discovered quantum materials [25–28, 38, 43]. A spin model is coupled to a topological non-interacting model on this lattice, through a ferromagnetic Hund's coupling term. We study the ground state of the spin model and the associated spin-wave excitations. Depending on the parameters of the spin model, we observe two different magnetic phases and we study their impact on the topological properties. We discuss the effects of external parameters, such as the temperature and the pressure, on the magnetic and topological properties of the model. We observe a transition from a ferromagnetic out-of plane long range order to an in-plane magnetic order (with antiferromagnetic correlations) coupled to a topological phase transition. Depending on the amplitude of the Hund's coupling term, the topological phase transition is either a QAH phase to QSH phase transition or a QAH phase to metallic phase transition.

In Chapter 5, we investigate a new time-reversal invariant topological model with flux, Rashba spin-orbit coupling and Hubbard interactions on the kagome lattice [188, 246]. This model is possibly realizable in cold atom gases which are interesting platforms for the im-

plementation of artificial gauge fields and the study of the Hubbard interactions. First we compute the $\mathbb{Z}_2$ phase diagram at vanishing Rashba spin-orbit coupling and vanishing Hubbard interactions, for different on-site potentials configurations, extending the analytical method we developed in Chapter 3. We explicitly show the connection between the bulk gap closure, the choice of the U(1) gauge on the eigenvectors and the discontinuity of the topological invariant. Then we extend the computation of the topological invariant for non-vanishing Rashba spin-orbit. Finally, we study the effects of Hubbard interactions at 2/3 filling and vanishing Rashba spin-orbit coupling for a particular configuration of the on-site potentials. By means of perturbation theory and mean field method [44], we investigate the Mott transition and the magnetic order in the ground state.

Related to the work presented in this manuscript, here is a list of published articles we wrote during the preparation of this thesis (the name of the author of this manuscript is abbreviated "J.L."):

- *Magnetic topological kagome systems*

  J. L. and K. Le Hur

  Phys. Rev. Research **2, 022043(R) (2020)**

- *Spin-orbit coupling in the kagome lattice with flux and time-reversal symmetry*

  Irakli Titvinidze, J. L., Maarten Grothus, Bernhard Irsigler, Karyn Le Hur and Walter Hofstetter

  Phys. Rev. B **103, 195105 (2021)**

- *Hubbard model on the kagome lattice with time-reversal invariant flux and spin-orbit coupling*

  Irakli Titvinidze, J. L. and Karyn Le Hur and Walter Hofstetter

  Phys. Rev. B **105, 235102 (2022)**

An article related to the work presented in Chapter 2, whose authors are J.L. and Karyn

Le Hur, is currently in preparation.

Chapter 1

Background

In this chapter, we give a general introduction about the systems we study in this manuscript: two-dimensional Chern insulators and topological insulators. This chapter is important to introduce and remind definitions and properties on which we rely in the following chapters.

We start by considering a cyclic adiabatic evolution of a quantum system (Sec. 1.1) and we study the geometrical phase, called the Berry phase [9], acquired by the eigenstates during such an evolution. This proves essential for the understanding of topology in condensed matter. The quantum Hall effect [6] has been the starting point of intense research activity in this domain. The topological invariant characterizing the integer quantum Hall effect can be formulated in terms of an integration of the Berry phase over the Brillouin zone parameter space [8]. In Sec. 1.1.3 and Sec. 1.1.4, we review the experimental discovery of the integer quantum Hall effect and its first theoretical understanding [6, 7, 45].

Then we introduce the formalism we use to describe translation-invariant systems (Sec. 1.2), we remind Bloch's theorem [46] and the definition of the Wannier functions [47] that we use in the following. As examples of translation-invariant Hamiltonians, we introduce tight-binding models on both lattices we consider in this manuscript, the honeycomb lattice and the kagome lattice.

The connection between the Berry phase concept and the integer quantum Hall effect (reviewed in Sec. 1.1) is explained via the computation of the Hall conductivity using the Kubo

formula [8] in Sec. 1.3. This leads to the introduction of a topological invariant, the (first) Chern number, which characterizes the topological properties of quantum Hall systems. We also explain that the chiral edge states discussed in Sec. 1.1.4 are a fundamental consequence of a non-vanishing Chern number which is a bulk invariant. In this section, we eventually show the connection between non-vanishing Chern number and the charge polarization which is an observable characterizing topological systems. The concepts introduced in this section are widely used throughout this manuscript.

In Sec. 1.4, we review the $\mathbb{Z}_2$ topological band theory used to describe topological spin systems which are time-reversal invariant. In particular, we focus on the Kane and Mele model [11] and on a formulation of the $\mathbb{Z}_2$ invariant proposed by Fu and Kane [48]. The concepts introduced in this section are relevant for Chapters 4 and 5 where we study (time-reversal invariant) spin-orbit coupled systems.

1.1 Important paradigms in topology in condensed matter and position of this thesis

Here we want to introduce major paradigms concerning the study of topological systems in condensed matter. Gauge fields coming from geometrical phases are at the origin of the topological properties. One of the most important concept in topology is the Berry phase concept [9], directly related to geometrical phases. Even though the theoretical description of quantum geometrical phase was known long before Berry's work, geometrical phase was thought to have no physical effect. Berry's important breakthrough was to realize that, on the contrary, this geometrical phase may have very important physical effects. This is reminiscent of the debate about the reality of the magnetic vector potential and the Aharonov-Bohm breakthrough [49].

The magnetic vector potential has striking topological consequences on condensed matter systems. For instance, in two-dimensional electron gas with perpendicular magnetic field, it

leads to the (integer) quantum Hall effect, which first experimental characterization [6, 45] marked a historic step in condensed-matter physics and have namely led to the development of theoretical and experimental studies of topological systems [50]. The first theoretical understanding of this topological effect, is due to Laughlin who used a quantum pump argument [7]. Thouless *et al.* [8], in 1982, explained the behavior of the quantum Hall conductance relying on the Kubo formula. We introduce their result and point out the link with the Berry phase concept in another section (Sec. 1.3.1).

1.1.1 Aharonov-Bohm effect

Here we first remind the effect of a magnetic vector potential on a (electrically charged) particle. This is very important for the following because the Berry gauge field, an emergent quantity which proves essential for the understanding of topological systems, is a gauge potential, therefore being analogous to a magnetic vector potential.

A particle with electric charge q moving along some path C in a magnetic vector potential $\mathbf{A}$ acquires a phase γ such that

$$\gamma = \frac{q}{\hbar} \int_C d\mathbf{l} \cdot \mathbf{A}. \tag{1.1}$$

This was already known from the beginning of quantum mechanics in 1926 [51]. γ is also called a Peierls phase when used in tight-binding models. However, the magnetic vector potential (in a region where there is neither magnetic field nor electric field) was believed to have no physical significance [51] for at least more than thirty years after 1926. In 1959, Aharonov and Bohm [49] first suggested that measurable effects should be expected for a particle with electric charge q moving along some path C in a magnetic vector potential $\mathbf{A}$ with vanishing local magnetic and electric field. They proposed a double-slit experiment with confined perpendicular magnetic field to test this prediction (interferences should be measured due to the γ phase appearing in Eq. (1.1)), prediction which was later confirmed (see *e.g.* [52]).

1.1.2 Adiabatic Hamiltonian evolution and Berry phase

The Aharonov-Bohm effect (see Sec. 1.1.1) may be interpreted using Berry phase's concept [9]. Berry studied the adiabatic evolution of a Hamiltonian system and showed that during this evolution, a phase factor is acquired by the eigenstates, besides the usual "dynamical" phase factor $\exp\left(\frac{-i}{\hbar}\int_0^t dt' E_n(\mathbf{R}(t'))\right)$. Berry's work is particularly important for the understanding of the topological phases. Here we introduce it, we underline the connection with the Aharonov-Bohm effect, we perform calculations which give an important insight on the topological systems we study in this manuscript and we try to insist on the fact that the Berry phase concept is related to topological (measurable) properties.

Berry phase We consider a quantum system which depends on a vector of parameters that we denote $\mathbf{R} = (X, Y, Z, ...)$. We are interested by the time-evolution (from $t = 0$ to $t = T$) of the system along an arbitrary closed path $\mathcal{C}$ in parameter space, *i.e.* $\mathbf{R}(0) = \mathbf{R}(T)$. We write the associated Hamiltonian $H(\mathbf{R})$, and

$$H(\mathbf{R})\,|n(\mathbf{R})\rangle = E_n(\mathbf{R})\,|n(\mathbf{R})\rangle\,, \tag{1.2}$$

where $E_n(\mathbf{R})$ and $|n(\mathbf{R})\rangle$, are respectively the eigenenergies and the eigenvectors, the later being uniquely and continuously defined along $\mathcal{C}$. We choose a gauge on the phase factor such that it is a smooth function of t. Note however that it may be multiply defined (this is in fact necessary for a topologically non trivial system). The time-evolution of the system is described by the Schrödinger equation

$$i\hbar\partial_t\,|\psi(t)\rangle = H(\mathbf{R}(t))\,|\psi(t)\rangle\,, \tag{1.3}$$

with $|\psi(t)\rangle$ the state of the system at time t. We consider that the parameters $\mathbf{R}(t)$ (and therefore the Hamiltonian) are varying slowly enough in time so that if $|\psi(0)\rangle = |n(\mathbf{R}(0))\rangle$, then, the state at arbitrary time t is, up to a phase factor (to be determined), $|n(\mathbf{R}(t))\rangle$. This result is known as the adiabatic theorem (for more details see Ref. [53]). Then, let us

denote $|\psi(t)\rangle = \mathrm{e}^{i\theta(t)} |n(\mathbf{R}(t))\rangle$. Reporting this in Eq. (1.3) and using Eq. (1.2) gives

$$-\hbar \left(\partial_t \theta(t)\right) |n(\mathbf{R}(t))\rangle + i\hbar \partial_t |n(\mathbf{R}(t))\rangle = E_n(\mathbf{R}(t)) |n(\mathbf{R}(t))\rangle , \tag{1.4}$$

therefore

$$\theta(t) = -\frac{1}{\hbar} \int_0^T dt' E_n(\mathbf{R}(t')) + i \int_0^T dt' \langle n(\mathbf{R}(t'))| \partial_{t'} |n(\mathbf{R}(t'))\rangle . \tag{1.5}$$

The first term in the right-hand side of the last equation is called the dynamical phase factor and was known to appear in the expression of $|\psi(t)\rangle$ long before Berry's work [9] in 1984. The second term, called the Berry phase, however, was believed not to play any physical role before Berry showed its importance. It is interesting to underline the analogy with the magnetic vector potential which, before Aharonov and Bohm paper in 1959 [49], was believed to have no physical significance (see Sec. 1.1.1). The analogy goes further as we detail in the following.

Berry vector potential and gauge choice Let us denote the Berry phase γ_n and notice that the time-dependency in the integral is not required:

$$\gamma_n = i \int_0^T dt' \langle n(\mathbf{R}(t'))| \partial_{t'} |n(\mathbf{R}(t'))\rangle = i \oint_{\mathcal{C}} d\mathbf{R} \cdot \langle n(\mathbf{R})| \nabla |n(\mathbf{R})\rangle , \tag{1.6}$$

with ∇ the gradient in $\mathbf{R}$-space. Let us denote $\mathbf{A}_n = i \langle n(\mathbf{R})| \nabla |n(\mathbf{R})\rangle$ such that

$$\gamma_n = \oint_{\mathcal{C}} d\mathbf{R} \cdot \mathbf{A}_n. \tag{1.7}$$

$\mathbf{A}_n$ is called the Berry vector potential (or the Berry connection) in analogy with the magnetic vector potential and the accumulated phase appearing in Eq. (1.1). The gauge choice on $|n(\mathbf{R})\rangle$ along $\mathcal{C}$ fix the gauge of $\mathbf{A}_n$. Under a transformation $|n(\mathbf{R})\rangle \to \mathrm{e}^{i\mu(\mathbf{R})} |n(\mathbf{R})\rangle$, with $\mu(\mathbf{R})$ a unique and smooth function of $\mathbf{R}$ along $\mathcal{C}$, the Berry vector potential changes according to

$$\mathbf{A}_n \to \mathbf{A}_n + \nabla \mu. \tag{1.8}$$

Note however that because we chose $|n(\mathbf{R})\rangle$ to be unique along $\mathcal{C}$, the contribution $\oint_{\mathcal{C}} d\mathbf{R}\cdot\nabla\mu$ is necessarily $2\pi z$, with z an integer. Therefore, generally speaking, γ_n is defined up to $2\pi z$ which is not a measurable quantity. Nevertheless, we notice that if γ_n is not equal to 2π times an integer, it is necessarily non-vanishing, independently of the gauge choice on $|n(\mathbf{R})\rangle$.

In anticipation of the application of the Berry phase concept to two-dimensional translation invariant systems, it is interesting to consider a path $\mathcal{C}$ around the boundary of the first Brillouin zone. Because the Brillouin zone is a torus, $\mathcal{C}$ is the addition of four paths $\mathcal{C}_1$, $\mathcal{C}_2$, $\mathcal{C}_3$ and $\mathcal{C}_4$, with $\mathcal{C}_3$ and $\mathcal{C}_4$ being respectively the paths $\mathcal{C}_1$ and $\mathcal{C}_2$ traveled in the opposite direction. We conclude that if the Berry phase is non-vanishing, it necessarily means that $\mathbf{A}_n$ can not be uniquely defined along $\mathcal{C}$ and that a smooth gauge transformation $|n(\mathbf{R})\rangle \to \mathrm{e}^{i\mu(\mathbf{R})}\,|n(\mathbf{R})\rangle$ (over all the Brillouin zone) has vanishing contribution $\oint_{\mathcal{C}} d\mathbf{R}\cdot\nabla\mu$. In this case, the Berry phase around the boundary of the first Brillouin zone is a gauge invariant (see Sec. 1.3.2).

Aharonov-Bohm effect Let us show how this approach is related to the Aharonov-Bohm effect previously introduced. Consider electrons (and denote the associated wave-function ψ) traveling around a closed path $\mathcal{C}$ which surround a solenoid. Assume that the perpendicular magnetic field created by the solenoid is non-vanishing only in a region inside $\mathcal{C}$. We denote the magnetic vector potential $\mathbf{A}$. We have

$$\frac{1}{2m}\left(-i\hbar\nabla + e\mathbf{A}\right)^2\psi = E\psi, \tag{1.9}$$

from which we deduce that ψ is proportional to $\exp\left(i\mathbf{k}\cdot\mathbf{r} - i\frac{e}{\hbar}\int_{\mathbf{r}_0}^{\mathbf{r}} d\mathbf{r}'\cdot\mathbf{A}(\mathbf{r}')\right)$. Then the Berry connection is

$$i\,\langle\psi|\,\nabla\,|\psi\rangle = -\mathbf{k} + \frac{e}{\hbar}\mathbf{A}(\mathbf{r}), \tag{1.10}$$

and the Berry phase is

$$\gamma_n = \frac{e}{\hbar}\oint_{\mathcal{C}} d\mathbf{R}\cdot\mathbf{A}(\mathbf{r}), \tag{1.11}$$

which is exactly the phase an electron acquires when completing a closed path around the solenoid.

Berry curvature Let us denote $\mathcal{S}$ an oriented surface whose boundary is $\mathcal{C}$ and $d\mathbf{S}$ the oriented surface element. If all the components of $\mathbf{A}_n$ are smooth functions of $\mathbf{R}$ on the surface $\mathcal{S}$, then using Stokes' theorem from Eq. (1.7) gives

$$\gamma_n = \int_{\mathcal{S}} d\mathbf{S} \cdot (\nabla \times \mathbf{A}_n)\,. \tag{1.12}$$

$(\nabla \times \mathbf{A}_n)$ is called the Berry curvature and is analogous to the magnetic field. Glancing back to Eq. (1.8), it is clear that the Berry curvature is gauge invariant, so is Eq. (1.12).

If $\mathbf{A}_n$ can not be chosen smoothly over all the surface $\mathcal{S}$, then we may cover $\mathcal{S}$ with N smaller non-overlapping regions $\{\mathcal{S}_1, ..., \mathcal{S}_N\}$ which respective boundaries are travelled by the paths $\{\mathcal{C}_1, ..., \mathcal{C}_N\}$ and these paths sum up to $\mathcal{C}$. $\mathbf{A}_n$ is chosen smoothly in $\mathcal{S}_1$ and along each of the paths $\{\mathcal{C}_1, ..., \mathcal{C}_N\}$. Therefore we have

$$\gamma_n = \int_{\mathcal{C}_1} d\mathbf{R}_1 \cdot \mathbf{A}_n + \cdots + \int_{\mathcal{C}_N} d\mathbf{R}_N \cdot \mathbf{A}_n, \tag{1.13}$$

The regions $\{\mathcal{S}_2, ..., \mathcal{S}_N\}$ contain one point where $\mathbf{A}_n$ can not be chosen smoothly, therefore in these regions we define the respective smooth gauge choices $\{\mathbf{A}_{n,1}, ..., \mathbf{A}_{n,N}\}$. Then we have, using Eq. (1.8),

$$\gamma_n = \int_{\mathcal{C}_1} d\mathbf{R}_1 \cdot \mathbf{A}_{n,1} + \cdots + \int_{\mathcal{C}_N} d\mathbf{R}_N \cdot \mathbf{A}_{n,N} + 2\pi z, \tag{1.14}$$

with z an integer. This gives

$$\gamma_n = \int_{\mathcal{S}_1} d\mathbf{S}_1 \cdot (\nabla \times \mathbf{A}_{n,1}) + \cdots + \int_{\mathcal{S}_N} d\mathbf{S}_N \cdot (\nabla \times \mathbf{A}_{n,N}) + 2\pi z. \tag{1.15}$$

The $2\pi z$ factor is usually not specified because it is not a measurable quantity. Moreover, because the Berry curvatures appearing in the last equation are gauge independent, the Berry phase is written

$$\gamma_n = \int_{\mathcal{S}} d\mathbf{S} \cdot (\nabla \times \mathbf{A}_n)\,. \tag{1.16}$$

We shall remember that several gauge choices may be needed over the surface $\mathcal{S}$ to use this last formula.

Computation of the Berry curvature without fixing the gauge Although the Berry curvature is gauge independent, the computation of γ_n using Eq. (1.16) requires to correctly define $\mathbf{A}_n$ over $\mathcal{S}$. Let us now write the Berry phase in a way such that the gauge(s) of $|n(\mathbf{R})\rangle$ over $\mathcal{S}$ has not to be specified. This is important, for instance, if we want to evaluate γ_n numerically or because defining $\mathbf{A}_n$ over $\mathcal{S}$ and computing γ_n (analytically) from Eq. (1.16) can be tricky. Moreover, this is very helpful to understand why systems with degeneracies in their energy levels may have non-trivial topological properties.

From Eq. (1.16), we write

$$\gamma_n = -\mathrm{Im} \int_{\mathcal{S}} d\mathbf{S} \cdot \left(\langle \nabla n(\mathbf{R})| \times |\nabla n(\mathbf{R})\rangle \right), \tag{1.17}$$

where $|\nabla n(\mathbf{R})\rangle$ is the vector (in $\mathbf{R}$-space) defined by

$$\left(\partial_X |n(\mathbf{R})\rangle, \partial_Y |n(\mathbf{R})\rangle, \partial_Z |n(\mathbf{R})\rangle, \dots \right), \tag{1.18}$$

and similarly $\langle \nabla n(\mathbf{R})|$ is defined by

$$\left(\partial_X \langle n(\mathbf{R})|, \partial_Y \langle n(\mathbf{R})|, \partial_Z \langle n(\mathbf{R})|, \dots \right). \tag{1.19}$$

We use the identity $1 = \sum_m |m(\mathbf{R})\rangle \langle m(\mathbf{R})|$ and the fact (from the normalization relation of the eigenvectors) that $\langle \nabla n(\mathbf{R})|n(\mathbf{R})\rangle$ is imaginary to obtain

$$\gamma_n = -\mathrm{Im} \int_{\mathcal{S}} d\mathbf{S} \cdot \left(\sum_{m \neq n} \langle \nabla n(\mathbf{R})|m(\mathbf{R})\rangle \times \langle m(\mathbf{R})|\nabla n(\mathbf{R})\rangle \right). \tag{1.20}$$

$|m(\mathbf{R})\rangle$ being orthogonal to $|n(\mathbf{R})\rangle$ we notice that

$$\langle m(\mathbf{R})| \nabla H(\mathbf{R}) |n(\mathbf{R})\rangle = E_n(\mathbf{R}) \langle m(\mathbf{R})|\nabla n(\mathbf{R})\rangle, \tag{1.21a}$$

$$\langle m(\mathbf{R})| \nabla H(\mathbf{R}) |n(\mathbf{R})\rangle = \langle m(\mathbf{R})| (\nabla H(\mathbf{R})) |n(\mathbf{R})\rangle + E_m(\mathbf{R}) \langle m(\mathbf{R})|\nabla n(\mathbf{R})\rangle. \tag{1.21b}$$

Combining both last equations enable to write

$$\gamma_n = -\int_{\mathcal{S}} d\mathbf{S}\cdot\mathbf{V}_n, \tag{1.22a}$$

$$\mathbf{V}_n = \mathrm{Im}\sum_{m\neq n}\frac{\langle n(\mathbf{R})|\left(\nabla H(\mathbf{R})\right)|m(\mathbf{R})\rangle\times\langle m(\mathbf{R})|\left(\nabla H(\mathbf{R})\right)|n(\mathbf{R})\rangle}{\left(E_n(\mathbf{R})-E_m(\mathbf{R})\right)^2}. \tag{1.22b}$$

The last formula now involve only the $\mathbf{R}$-derivatives of the Hamiltonian, therefore we do not have to specify smooth gauge(s) choice on $|n(\mathbf{R})\rangle$ over $\mathcal{S}$.

Degeneracy and two-level system From Eq. (1.22), we see that a degeneracy involving only two states, that we denote $|+(\mathbf{R})\rangle$ and $|-(\mathbf{R})\rangle$, at some point $\mathbf{R}^*$, *i.e.* $E_+(\mathbf{R}*) = E_-(\mathbf{R}^*)$, plays an major rôle in $\mathbf{V}_+$: for $\mathbf{R}$ near $\mathbf{R}^*$, $\mathbf{V}_+$ may be approximated by

$$\mathbf{V}_+ = \mathrm{Im}\frac{\langle +(\mathbf{R})|\left(\nabla H(\mathbf{R}^*)\right)|-(\mathbf{R})\rangle\times\langle -(\mathbf{R})|\left(\nabla H(\mathbf{R}^*)\right)|+(\mathbf{R})\rangle}{\left(E_+(\mathbf{R})-E_-(\mathbf{R})\right)^2}. \tag{1.23}$$

We notice that $\mathbf{V}_- = -\mathbf{V}_+$. This situation is important for us because the systems we study in this manuscript are generally concerned (depending on the value of the parameters) with degeneracies involving two energy bands.

Dirac points as sources of Berry curvature As an important application of the Eq. (1.23), let us consider the Hamiltonian which describes Dirac-fermions

$$H = \mathbf{R}\cdot\sigma, \tag{1.24}$$

with $\mathbf{R} = (X, Y, Z)$ a three-dimensional vector of parameters and $\sigma = (\sigma_x, \sigma_y, \sigma_z)$ and σ_x,σ_y and σ_z are the three Pauli matrices. We briefly show that the Berry phase along some paths in parameter space is non-vanishing and we explain that this potentially leads to non-trivial topological systems. Later (see Sec. 1.2.4 and Sec. 1.2.5) we show that simple systems on the honeycomb and on the kagome lattice show Dirac-fermions. Therefore systems on these lattices may have non-trivial topological properties, which explains our interest for these systems.

From Hamiltonian in Eq. (1.24), we notice that the only degeneracy occurs at $\mathbf{R} = 0$ and that $\nabla H = \sigma$. Using the actions of the Pauli matrices on the eigenstates $|+\rangle$ and $|-\rangle$, we find

$$\mathbf{V}_+ = \frac{\mathbf{R}}{2|\mathbf{R}|^3}. \tag{1.25}$$

We realize here that $\mathbf{V}_+$ is analogue to the magnetic field generated by a magnetic monopole at $\mathbf{R} = 0$. Then we deduce that the Berry phase is half of the solid angle Ω subtended by $\mathcal{C}$ at the degeneracy point $\mathbf{R} = 0$.

Link with condensed matter systems and topology Here we consider a Dirac-fermions system (see previous paragraph) and we assume that $\mathcal{C}$ is a path at $Z = 0$. Then, along $\mathcal{C}$, the Hamiltonian evolves in the two-dimensional parameter space $\{X, Y\}$. Here we have in mind the analogy with the two-dimensional Brillouin zone of (two-dimensional) translation-invariant systems. If $\mathcal{C}$ encircles the degeneracy point (called Dirac point) at $X = 0$ and $Y = 0$, then the solid angle Ω is $\pm 2\pi$, giving $\pm\pi$ for the Berry phase. Indeed, the two-dimensional plane which contains $\mathcal{C}$ (at $Z = 0$) also contains the Dirac point since the later appears at $\mathbf{R} = 0$. Then, $\Omega = \pm 2\pi$ which is the solid angle subtended by $\mathcal{C}$ at the degeneracy point $\mathbf{R} = 0$.

For an isolated energy band associated to a two-dimensional translation-invariant system, the Berry phase along the boundary of the first Brillouin zone is 2π times an integer number called the Chern number (see Sec. 1.3.2). It is related to the topological properties of the system (see Sec. 1.3.1 and Sec. 1.3.4). Let us again consider an energy band $|+\rangle$ which get degenerate with another band $|-\rangle$ at a Dirac point when the Z parameter vanishes. Simon ([54]) has proven that the Chern number associated to the band $|+\rangle$ at $Z \neq 0$ (*i.e.* when the Dirac point degeneracy is lifted) is the sum of the Berry phases along small path surrounding the Dirac points at $Z = 0$.

Summary about the relevance of the Berry phase concept To sum up, the Berry phase is a very important concept in topology because it links the appearance of topological phases with two-levels degenerate systems, and explains that the degeneracy can be thought of as sources of topology. This is particularly relevant for band systems in which degeneracy characterized by Dirac Fermions can appear by varying the system's parameters. As we saw, this is the case for the hexagonal lattice (honeycomb and kagome) systems we introduced. This is why here we introduce this Berry phase concept.

1.1.3 Integer Quantum Hall effect

The Quantum Hall effect, appearing at low temperatures in two-dimensional electron gas with a perpendicular magnetic field, is the quantized counterpart of the Hall effect. The later was discovered by E. Hall, in 1879, who applied a perpendicular magnetic field and a longitudinal electric current in a two-dimensional conductor (he used a gold leaf mounted on a plate of glass) and measured a non-vanishing transverse (compared to the direction of the current) voltage [55]. The transverse resistivity, denoted ρ_{xy} is therefore non-vanishing, it is called the Hall resistivity and also denoted ρ_H and its value characterizes the Hall effect. Its inverse is called the Hall conductivity and denoted σ_H. In the classical version of the Hall effect, we have $\sigma_H = ne/B$, with n the electron density, e the electron charge and B the amplitude of the magnetic field.

80 years after Hall's results, in the sixties, and during the following decades, the realization of the MOSFET[1], played an important role in the discovery of the quantum Hall effect. Indeed, it enabled to design a two-dimensional electron gas and to study the interdependence between in-plane electric fields, in-plane currents and perpendicular (to the plane) magnetic fields. Some years after the first realization of the MOSFET it became possible to investigate physical effects described by quantum theory in this device [56–60]; low temperatures (few

[1]MOSFET stands for Metal–Oxide–Semiconductor Field-Effect Transistor. It is the basic building block of modern electronics and one of the most manufactured device in Human history.

Kelvins) and large (perpendicular) magnetic fields (with order of magnitude 10 T) were reachable. Then it was relevant to think about the quantum consequences in the Hall effect.

When a perpendicular magnetic field (we denote its amplitude B) is applied to a two-dimensional gas in the quantum limit, the cyclotron orbits of the electrons are quantized and the Schrödinger equation leads to highly degenerate energy levels (called Landau levels [61]). The latter have energy $E_n = \hbar\omega_c(n + 1/2)$, with n is a positive integer and the cyclotron frequency $\omega_c = eB/m$, e and m being the electric charge and the mass of the electron. This is valid if the temperature is low compared to the energy difference between each Landau levels, *i.e.* such that $k_B T \ll \hbar\omega_c$, with k_B the Boltzmann constant. The number of states in each Landau level is given by

$$N_L = \frac{\phi}{\phi_0} = \frac{eAB}{2\pi\hbar}, \tag{1.26}$$

with ϕ the total magnetic flux through the sample, $\phi_0 = 2\pi\hbar/e$ and A the surface of the sample. From this, let us define the filling factor ν, $\nu = N/N_L$, with N the total number of particle in the system (this is the density of states in the two-dimensional electron gas at vanishing magnetic field times the surface of the sample). We shall mention here that the disorder present in the physical systems broadens each Landau levels, *i.e.* the density of states is a sum of peaks of finite width around the energies E_n.

In 1980, von Klitzing *et al.* found that the Hall conductivity σ_H, at integer filling factor ν (*i.e.* when the density of states at the Fermi energy is close to zero), was in fact quantized in units of e^2/h [6], with an accuracy of few parts in 10^6:

$$\sigma_H = \nu e^2/h. \tag{1.27}$$

This is called the integer quantum Hall effect; the accuracy of the measure is nowadays few parts in 10^{10} [62]. When the disorder in the system is small, we observe plateaus in the value of σ_H when varying B, as shown in Fig. 1.1(a). Let us mention that few years before von Klitzing *et al.*'s result, Ando *et al.* had concluded that σ_H, at integer filling factor, was quantized up to some (possibly important) correction term proportional to σ_{xx}/B [63], with

σ_{xx} the longitudinal conductivity. Also, there was already some experimental studies of σ_H, however not accurate enough to observe the plateaus in σ_H [64]. In Fig. 1.1(a), we observe that the later goes to zero when the Fermi energy lies between two Landau levels and that it is non-vanishing when the Fermi energy is inside a Landau level (with the highest value when the Landau level is half-filled). This is what we may expect from usual band theory. In the following section we focus on the understanding of the integer quantum Hall effect via an elegant explanation due to Laughlin.

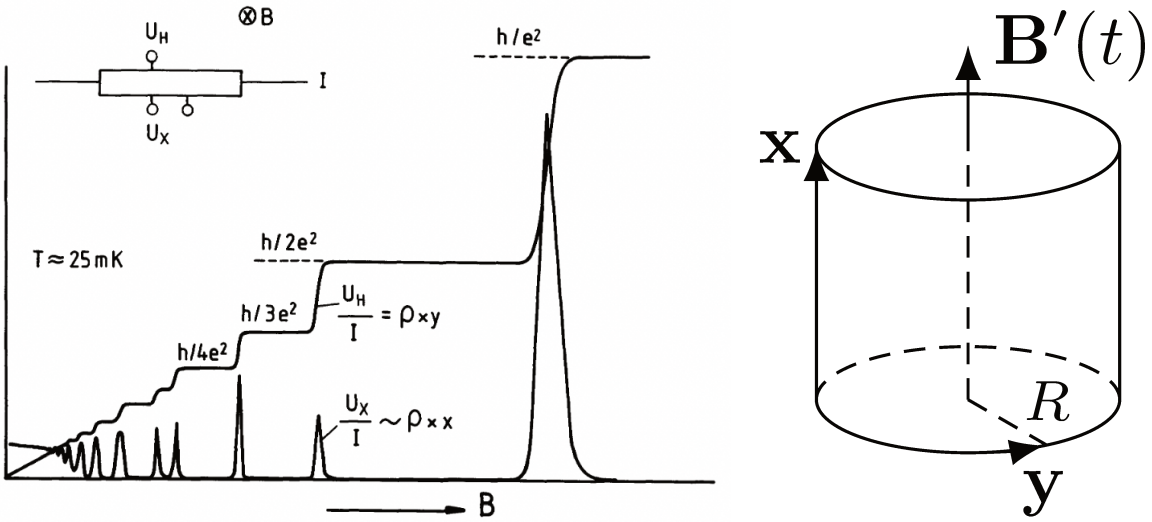

Figure 1.1: (a) Longitudinal resistivity σ_{xx} and transverse resistivity σ_{xy} as a function of the amplitude B of the perpendicular magnetic field applied to a two-dimensional electron gas. In the upper left par of the figure is briefly sketch the system, with the magnetic field $\mathbf{B}$, the longitudinal current amplitude I, and the measured difference of potential U_x and U_y respectively in the longitudinal and in the transverse direction of the two-dimensional sample. This figure is taken from Ref. [65]. (b) Cylinder geometry used to show the quantization of the transverse conductivity σ_{xy} through Laughlin argument in Sec. 1.1.4. Here a two-dimentional electron gas is confined on the surface of the cylinder and a flux $\Delta\Phi$ is adiabatically inserted thanks to the axial magnetic field $\mathbf{B}'(t)$. In a quantum Hall system, a uniform and constant magnetic field $\mathbf{B}$ is applied in the radial direction of the cylinder, *i.e.* perpendicular to the surface of the cylinder, at each points in the surface.

1.1.4 Laughlin argument and edge states

The quantization of the Hall conductivity Here we describe the argument presented by Laughlin in Ref. [7], showing that the quantum Hall conductivity is quantized in units of e^2/h. This was the first theoretical understanding of the integer quantum Hall effect in terms of a topological argument. With this argument we understand that the phase of the quantum state describing the system plays an important role for the topological properties. It therefore makes a connection with previous section about the Berry phase concept and with the following sections and chapters dealing with topological systems.

Let us consider a two-dimensional electron gas confined at the surface of a cylinder (see Fig. 1.1(b)), which is very convenient because of translation invariance in the **y** direction (we may also call it the longitudinal direction) of the sample [66]. We want to study the transverse conductivity σ_{xy}, for this we choose to study the relation between an electric field generated in the **y** direction and the current in the **x** direction (we may also call it the transverse direction). The electric field $\mathbf{E}$ results from a time-dependent magnetic flux $\Phi(t)$ through the cylinder and is given by Faraday's law $\oint d\mathbf{l} \cdot \mathbf{E} = \partial_t \Phi$, with $d\mathbf{l}$ an infinitesimal element in the longitudinal direction. The magnetic flux $\Phi(t)$ results from a magnetic field $\mathbf{B}'(t)$ along the axis of the cylinder. We denote the flux $\Delta\Phi$ inserted from time $t = 0$ to time $t = T$, *i.e.* $\Delta\Phi = \Phi(t = T) - \Phi(t = 0)$, we assume that the system is a bulk insulator and, from time $t = 0$ to time $t = T$, we assume that a charge ΔQ is transferred from the lower edge to the upper edge, *i.e.* in the **x** direction. We therefore write the transverse current $I = \Delta Q/T$. The transverse conductivity then reads

$$\sigma_{xy} = \frac{I}{\oint d\mathbf{l} \cdot E} = \frac{\Delta Q}{T \partial_t \Phi} = \frac{\Delta Q}{\Delta \Phi}. \tag{1.28}$$

In the last equation, the value of ΔQ depends on the value of $\Delta\Phi$ so that σ_{xy} is a constant. Laughlin noticed that at some specific value of $\Delta\Phi$, $\Delta\Phi = h/e$, ΔQ must be an integer number times the electron charge, and then σ_{xy} must be quantized in units of $e^2/\hbar$. To understand this, let us look at the Hamiltonian of the free electron two-dimensional gas on

the surface of cylinder with the magnetic field $\mathbf{B}'$ along the axis of the cylinder. We choose the following gauge for the magnetic vector potential $\mathbf{A}' = \mathbf{e}_y B' R/2$ with $\mathbf{e}_y$ a unit vector in the $\mathbf{y}$ direction, B' the amplitude of the magnetic field and R the radial distance as sketch in Fig. 1.1(b). The Hamiltonian is

$$H = \frac{1}{2m}\left(\mathbf{p} - e\mathbf{A}'\right)^2 = \frac{1}{2m}p_x^2 + \frac{1}{2m}\left(p_y - e\frac{\Delta\Phi}{L}\right)^2, \tag{1.29}$$

with $\mathbf{p}$ the momentum operator, m the electron mass, $B'R^2\pi = \Delta\Phi$ and $L = 2\pi R$.

Now, consider $\Delta\Phi = h/e$. When Φ goes from 0 to h/e, we see that it is similar to the variation h/L in $p_y = \hbar k_y$, *i.e* a variation $2\pi/L$ in k_y. From this, we deduce that (i) the spectrum and the eigenvectors of H are the same at $t = 0$ and at $t = T$. However, the momentum of the occupied states have all change by one increment $2\pi/L$. Therefore, if the bulk of the system is insulating, there can be a transfer of charges only between the edges, and from (i) we know that it must be an integer number of electron charge(s): $\Delta Q = ze$ with z an integer. Then we find

$$\sigma_{xy} = ze^2/\hbar. \tag{1.30}$$

Edge states The transfer of charges between the edges of the system means that some states, localized at the edges, must cross the Fermi level so that a charge can be accepted or donated (depending on the edge) at the Fermi energy. Because we consider a uniform system and from the relative orientation of the axes x and y, we know that $\sigma_{xy} = -\sigma_{yx}$. In fact, considering a voltage along $\mathbf{x}$, computing the resulting current along $\mathbf{y}$, and using the same argument we used in the previous paragraphs, we also find that σ_{yx} is quantized (the proof appears this way in Ref.[7]), in agreement with $\sigma_{xy} = -\sigma_{yx}$. This shows that the state localized at one edge of the system carry a chiral current; the state localized at the other edge carry a current in the opposite direction. Halperin ([67]) showed that this state is robust against weak disorder in the system; the reason being that there is no state available for backscattering. Halperin ([67]) also showed, from energy and particle number conservation

and considering weak disorder in the system, that there must also exist delocalized (also called extended) states below the Fermi energy, in the bulk, that contribute to the electron transport from one edge to the other during the adiabatic insertion of the flux.

Application to the quantum Hall effect In a quantum Hall system, a uniform and constant magnetic field $\mathbf{B}$ is applied perpendicular to the two-dimensional electron gas; in the cylinder geometry it would be radial, perpendicular to the surface of the cylinder. Considering this radial magnetic field $\mathbf{B}$ and the axial magnetic field $\mathbf{B}'$ (which produces the electric field we need to study the quantum Hall effect), we choose the total magnetic vector potential $\mathbf{A} + \mathbf{A}' = \mathbf{e}_y\,(B'R/2 - Bx)$, with B the amplitude of the magnetic field $\mathbf{B}$. It yields the Hamiltonian

$$H = \frac{1}{2m}p_x^2 + \frac{1}{2m}\left(p_y - e\frac{\Delta\Phi}{L} + eBx\right)^2. \tag{1.31}$$

We see that the Laughlin argument stays valid because translation invariance in the $\mathbf{y}$ direction is preserved. Eq. (1.31) is the Hamiltonian of a one-dimensional harmonic oscillator along the $\mathbf{x}$ direction; along the $\mathbf{y}$ direction it describes a free particle moving in a periodic space. The eigenenergies are given by $E_n = \hbar\omega_c(n + 1/2)$, with n a positive integer and each energy level is called a Landau level. The wavefunctions are the product of harmonic oscillator states, centered at x_0 (x_0 is given Eq. (1.32)) and localized in real space over a length corresponding to the so-called magnetic length $l_B = \sqrt{\hbar/eB}$, and plane waves in y. The center of the harmonic oscillator states is given by

$$x_0 = \frac{\Delta\Phi}{BL} - \frac{\hbar k_y}{eB} = \frac{h}{eBL}\left(\frac{\Delta\Phi}{\Phi_0} - n_y\right), \tag{1.32}$$

with $\Phi_0 = h/e$ and n_y is an integer given by $k_y = 2\pi n_y/L$. We see that inserting the flux $\Delta\Phi = h/e$, which is equivalent to a variation $2\pi/L$ in k_y is also equivalent to a variation of the center of the harmonic oscillator states. Now suppose that the Fermi level lies between two Landau levels and add a confining potential in the $\mathbf{x}$ direction, necessarily present in

the real system. This results (see [67]) in the crossing of the Fermi energy only by states localized at the edges in the **x** direction (and extended in the **y** direction) and the bulk is insulating. From this, we conclude that inserting the flux $\Delta\Phi = h/e$ corresponds to a charge transfer between the edges along the **x** direction. Following the convention on the orientation of the **x** axis in Fig. 1.1(b), here we find that inserting $\Delta\Phi = h/e$ increases x_0, therefore there is a transfer of charge from the lower to the upper edge. At the lower edge, a hole is created at the Fermi level, while at the upper edge an electron occupied a state above the Fermi level. This explains why ΔQ and then σ_H are quantized and not vanishing in the quantum Hall effect. When the filling factor $\nu = N/N_L$ (N and N_L are defined in the previous section Sec. 1.1.3) increases by an integer number, the number of Landau levels crossing the Fermi energy (at the edges of the sample) increases by the same integer number, so does σ_H. Taking into account the narrow localization of the Landau levels in energy space, this explains the behavior of the Hall conductivity in Fig. 1.1(a).

1.2 Systems with lattice translation symmetry

In this section we specify the general formalism we use to describe (non-interacting) lattice translation-invariant systems, and we remind Bloch's theorem and the definition of the Wannier functions which are important for the understanding of the topological phases. As examples of lattice translation-invariant systems, we introduce two simple tight-binding models on the honeycomb lattice and on the kagome lattice. These models are the elementary building blocks of the models we study in this manuscript.

1.2.1 Tight-binding model and momentum space Hamiltonian

Here we introduce some of the formalism and notations we use throughout this manuscript. We consider a non-interacting two-dimensional system with (real-space) translation symmetry. It is described by a Bravais lattice and a basis (also called "motif"). The former is

mathematically represented by a set $\mathcal{S}_r$ which contains all the lattice translation vectors. The latter describes the arrangement of the inequivalent sites (in a unit cell) that we distinguish by a "color". Non-interacting two dimensional systems we study are described by a generic lattice Hamiltonian H of the form

$$H = \sum_{(\mathbf{r},\mathbf{r}')\in\mathcal{S}_r^2} \sum_{\alpha,\alpha'} \sum_{(\sigma,\sigma')\in\{\uparrow,\downarrow\}^2} h_{\mathbf{r},\mathbf{r}',\alpha,\alpha',\sigma,\sigma'} c^\dagger_{\mathbf{r},\alpha,\sigma} c_{\mathbf{r}',\alpha',\sigma'}. \tag{1.33}$$

Here α and α' are the index associated to the color of the site and the associated sum runs over all the colors in a unit cell. σ and σ' are indices associated to the spin degree of freedom. The matrix made of the components $h_{\mathbf{r},\mathbf{r}',\alpha,\alpha',\sigma,\sigma'}$, has size $2NN_c \times 2NN_c$ and is hermitian, with N the total number of Bravais lattice sites and N_c the number of colors. $c^\dagger_{\mathbf{r},\alpha,\sigma}$ and $c_{\mathbf{r},\alpha,\sigma}$ are respectively creation and annihilation operators for a spin σ particle at a lattice site described by translation vector $\mathbf{r}$ and color α. In this manuscript we consider either fermionic or bosonic operators, which, we remind, satisfy the commutation relations

$$\{c^\dagger_{\mathbf{r},\sigma}, c_{\mathbf{r}',\sigma'}\} = c^\dagger_{\mathbf{r},\sigma} c_{\mathbf{r}',\sigma'} + c_{\mathbf{r}',\sigma'} c^\dagger_{\mathbf{r},\sigma} = \delta_{\mathbf{r},\mathbf{r}'}\delta_{\alpha,\alpha'}\delta_{\sigma,\sigma'} \quad \text{(Fermions)}, \tag{1.34a}$$

$$\left[c^\dagger_{\mathbf{r},\sigma}, c_{\mathbf{r}',\sigma'}\right] = c^\dagger_{\mathbf{r},\sigma} c_{\mathbf{r}',\sigma'} - c_{\mathbf{r}',\sigma'} c^\dagger_{\mathbf{r},\sigma} = \delta_{\mathbf{r},\mathbf{r}'}\delta_{\alpha,\alpha'}\delta_{\sigma,\sigma'} \quad \text{(Bosons)}, \tag{1.34b}$$

with δ the Kronecker delta function. In the following, we consider systems for which the matrix h couples the same sites in the lattice, the nearest neighbors in the lattice and possibly the next-nearest neighbors in the lattice. For instance, in the simple model we review in Sec. 1.2.4, h only couples the nearest neighbors in the lattice. It derives from a tight-binding approximation for a crystal, which consist in considering that the electron orbitals are localized near the atomic sites. Then, from a simple Hamiltonian made of the kinetic term $-\dfrac{\hbar^2}{2m}\nabla^2$ for the electrons with mass m and of a crystal lattice potential term, h is shown to depend on three overlap integrals, which namely gives an on-site potential term and a nearest neighbor hopping term [68].

Momentum space description is very convenient for translation-invariant systems and is

widely used in this manuscript, with the following notations

$$H = \sum_{\mathbf{k}\in\mathcal{S}_k} \sum_{\alpha,\alpha'} \sum_{(\sigma,\sigma')\in\{\uparrow,\downarrow\}^2} \tilde{h}_{\mathbf{k},\alpha,\alpha',\sigma,\sigma'} c^\dagger_{\mathbf{k},\alpha,\sigma} c_{\mathbf{k},\alpha',\sigma'}. \tag{1.35}$$

where $\mathbf{k}$ belongs to the set $\mathcal{S}_k$ which contains all the reciprocal lattice vectors and which is called the Brillouin zone. Here a is the lattice spacing, *i.e.* the smallest distance between two sites in the Bravais lattice. $c^\dagger_{\mathbf{k},\alpha,\sigma}$ and $c_{\mathbf{k},\alpha',\sigma'}$ are the Fourier transforms of the operators $c^\dagger_{\mathbf{r},\alpha,\sigma}$ and $c_{\mathbf{r},\alpha,\sigma}$. The Hamiltonian decouples into a sum over the momentum space vectors $\mathbf{k}$ of a $2N_c \times 2N_c$ hermitian matrix made of the components $\tilde{h}_{\mathbf{k},\alpha,\alpha',\sigma,\sigma'}$. This makes the description Eq. (1.35) very convenient.

1.2.2 Bloch's theorem and eigenstates of the Hamiltonian in momentum space

Bloch, in 1928, gave a general solution of the Schrödinger equation associated to a particle moving in a space-periodic potential [46]. His result, know as Bloch's theorem, is very important in condensed matter physics. Here we show a derivation of this theorem. It enables to introduce some notations (namely concerning the eigenenergies and the eigenvectors associated to a non-interacting translation invariant Hamiltonian) that we will use a lot throughout this manuscript.

Let us consider a single particle (fermion or boson) Hamiltonian $\hat{H} = \dfrac{\hat{\mathbf{p}}^2}{2m} + U(\hat{\mathbf{r}})$, with the periodic potential $U(\mathbf{r}+\mathbf{R}) = U(\mathbf{r})$, $\mathbf{R} \in \mathcal{S}_r$ being a translation vector in the Bravais lattice. Bloch's theorem states that translation symmetry imposes that each solution $|\psi_{n,\mathbf{k}}\rangle$ of the Schrödinger equation $\hat{H}\,|\psi_{n,\mathbf{k}}\rangle = E_{n,\mathbf{k}}\,|\psi_{n,\mathbf{k}}\rangle$ satisfy

$$\langle \mathbf{r}|\psi_{n,\mathbf{k}}\rangle = \psi_{n,\mathbf{k}}(\mathbf{r}) = \mathrm{e}^{i\mathbf{k}\cdot\mathbf{r}} u_{n,\mathbf{k}}(\mathbf{r}), \tag{1.36}$$

with $u_{n,\mathbf{k}}(\mathbf{r}+\mathbf{R}) = u_{n,\mathbf{k}}(\mathbf{r})$. Each solution $|\psi_{n,\mathbf{k}}\rangle$ is identified by two quantum numbers, n is called the (energy) band index and $\mathbf{k}$ is an eigenvalue of the momentum operator $\hat{\mathbf{k}}$. $|\mathbf{r}\rangle$ are the eigenstates of the position operator $\hat{\mathbf{r}}$. Let us briefly give a proof of this theorem.

We define the real space translation operator $\hat{T}_{\mathbf{R}}$ such that $\hat{T}_{\mathbf{R}}\,|\mathbf{r}\rangle = |\mathbf{r}+\mathbf{R}\rangle$ with $\mathbf{R} \in \mathcal{S}_r$. Acting with $\langle\mathbf{r}|\,\hat{T}^{\dagger}_{\mathbf{R}} = \langle\mathbf{r}+\mathbf{R}|$ on an arbitrary wave function which we then expand in a Taylor series, and using the real space representation of the operator $\hat{\mathbf{k}}$, we find that [69]

$$\hat{T}_{\mathbf{R}} = \mathrm{e}^{-i\hat{\mathbf{k}}\cdot\mathbf{R}} = \sum_{\mathbf{k}} \mathrm{e}^{-i\mathbf{k}\cdot\mathbf{R}}\,|\mathbf{k}\rangle\,\langle\mathbf{k}|\,, \tag{1.37}$$

with $|\mathbf{k}\rangle$ the eigenstates of the momentum operator $\hat{\mathbf{k}}$. The system is invariant under an arbitrary translation $\mathbf{R}$, therefore its associated Hamiltonian shall commute with the translation operator $\hat{T}_{\mathbf{R}}$. This is directly checked from the Hamiltonian $\hat{H}$ because $\mathbf{p} = \hbar\mathbf{k}$ and $U(\mathbf{r}+\mathbf{R}) = U(\mathbf{r})$. Therefore there exist a common basis of eigenvectors $|\psi\rangle$ that simultaneously diagonalizes $\hat{T}_{\mathbf{R}}$ and $\hat{H}$. Let us consider one of these eigenvectors that we denote $|\psi\rangle$. We write

$$\hat{H}\,|\psi\rangle = E\,|\psi\rangle\,, \tag{1.38a}$$

$$\hat{T}^{\dagger}_{\mathbf{R}}\,|\psi\rangle = t_{\mathbf{R}}\,|\psi\rangle\,. \tag{1.38b}$$

Moreover, we have

$$\langle\mathbf{k}|\,\hat{T}^{\dagger}_{\mathbf{R}}\,|\psi\rangle = \mathrm{e}^{i\mathbf{k}\cdot\mathbf{R}}\,\langle\mathbf{k}|\psi\rangle = t_{\mathbf{R}}\,\langle\mathbf{k}|\psi\rangle\,, \tag{1.39}$$

and either $\langle\mathbf{k}|\psi\rangle = 0$ or $\langle\mathbf{k}|\psi\rangle \neq 0$ in which case $t_{\mathbf{R}} = \mathrm{e}^{i\mathbf{k}\cdot\mathbf{R}}$. Therefore, if $\mathbf{k}' \neq \mathbf{k}$, then $\langle\mathbf{k}'|\psi\rangle = 0$ otherwise $t_{\mathbf{R}} = \mathrm{e}^{i\mathbf{k}'\cdot\mathbf{R}}$ which is incompatible with $t_{\mathbf{R}} = \mathrm{e}^{i\mathbf{k}\cdot\mathbf{R}}$. In other words, each eigenvectors $|\psi\rangle$ may have non vanishing overlap with only one ket $|\mathbf{k}\rangle$ so that it can be labeled by the momentum space vector $\mathbf{k}$. Besides, several eigenvectors $|\psi\rangle$ may overlap with the same ket $|\mathbf{k}\rangle$ so we introduce an index n to differentiate them. We therefore write $|\psi_{n,\mathbf{k}}\rangle$ instead of $|\psi\rangle$ and the corresponding Hamiltonian eigenvalue $E_{n,\mathbf{k}}$.

Now Eq. (1.38b) reads

$$\hat{T}^{\dagger}_{\mathbf{R}}\,|\psi_{n,\mathbf{k}}\rangle = \mathrm{e}^{i\mathbf{k}\cdot\mathbf{R}}\,|\psi_{n,\mathbf{k}}\rangle\,. \tag{1.40}$$

Using $\langle\mathbf{r}|\,\hat{T}^{\dagger}_{\mathbf{R}} = \langle\mathbf{r}+\mathbf{R}|$ we find

$$\psi_{n,\mathbf{k}}\,(\mathbf{r}+\mathbf{R}) = \mathrm{e}^{i\mathbf{k}\cdot\mathbf{R}}\psi_{n,\mathbf{k}}\,(\mathbf{r})\,. \tag{1.41}$$

Let us define $u_{n,\mathbf{k}}(\mathbf{r}) = \mathrm{e}^{-i\mathbf{k}\cdot\mathbf{r}}\psi_{n,\mathbf{k}}(\mathbf{r})$. From Eq. (1.41), we see that $u_{n,\mathbf{k}}(\mathbf{r}+\mathbf{R}) = u_{n,\mathbf{k}}(\mathbf{r})$ which proves Bloch's theorem.

In anticipation of further sections, where we are interested in quantities depending on $|u_{n,\mathbf{k}}\rangle$ rather than $|\psi_{n,\mathbf{k}}\rangle$, we note that

$$\mathrm{e}^{-i\mathbf{k}\cdot\hat{\mathbf{r}}}\hat{H}\mathrm{e}^{i\mathbf{k}\cdot\hat{\mathbf{r}}}\,|u_{n,\mathbf{k}}\rangle = E_{n,\mathbf{k}}\,|u_{n,\mathbf{k}}\rangle\,, \tag{1.42}$$

with

$$\mathrm{e}^{-i\mathbf{k}\cdot\hat{\mathbf{r}}} = \sum_{\mathbf{r}} \mathrm{e}^{-i\mathbf{k}\cdot\mathbf{r}}\,|\mathbf{r}\rangle\,\langle\mathbf{r}|\,. \tag{1.43}$$

To get Eq. (1.42), we used $\hat{H}\,|\psi_{n,\mathbf{k}}\rangle = E_{n,\mathbf{k}}\,|\psi_{n,\mathbf{k}}\rangle$, Bloch theorem Eq. (1.36) and the identity $1 = \sum_{\mathbf{r}}|\mathbf{r}\rangle\,\langle\mathbf{r}|$.

1.2.3 Wannier functions

Here we briefly introduce the Wannier functions [47] and some associated properties in one-dimensional system. These functions are useful to understand the relation between the Chern number and the charge polarization (in two-dimensional time-reversal breaking systems) and they are also useful to understand the relation between the $\mathbb{Z}_2$ invariant and the time-reversal polarization (in two-dimensional systems with time-reversal symmetry). We consider an isolated energy band indexed by the number n.

The Wannier functions, which we denote $|w_{n,\mathbf{R}}\rangle$, where $\mathbf{R}$ specify the position of the associated unit cell, are given by

$$|w_{n,\mathbf{R}}\rangle = \frac{V}{(2\pi)^d}\int_{\mathrm{BZ}} d^dk\,\mathrm{e}^{i\mathbf{k}\cdot\mathbf{R}}\mathrm{e}^{-i\phi_n(\mathbf{k})}\,|\psi_{n,\mathbf{k}}\rangle\,, \tag{1.44}$$

where the integral is over the Brillouin zone (BZ), d is the dimension of the system (we consider $d = 1$ or 2 in the following), V is the volume of the real-space unit cell and $|\psi_{n,\mathbf{k}}\rangle$ is the normalized Bloch eigenvector associated to the band n. $|\psi_{n,\mathbf{k}}\rangle$ is defined up to an overall phase, therefore Eq. (1.44) leaves some freedom on the definition of the Wannier states. Here, we made this degree of freedom explicit with the introduction of the phase $\phi_n \in \mathbb{R}$.

Following from the orthogonality of the Bloch eigenvectors, the Wannier functions $|w_{n,\mathbf{R}}\rangle$ form a complete and orthogonal set of functions that span the same Hilbert space as do the Bloch eigenvectors associated to the band n.

In one-dimension systems, it is possible to find exponentially localized (on the lattice sites) Wannier functions [70]. The spread of the Wannier functions depends on the choice of the phase $\phi_n(k_x)$; the choice $\phi_n(k_x) = -i\int_0^{k_x} dk'_x \mathcal{A}_n(k'_x)$ maximally localizes the Wannier functions around each (atomic) site [71]. $\mathcal{A}_n(k_x)$ is the Berry gauge field associated to the band n and it is defined in Sec.1.3.2.

1.2.4 Graphene

As a first example, we review a simple tight-binding model on the honeycomb lattice. This model is important for several reasons. A very fundamental and general reason why graphene is interesting is that several other allotropes of carbon are directly related to graphene [72]. For instance graphite is made of graphene stacks, fullerene [73–75] has a structure in space which occupies the surface of a sphere and each carbon atom has three σ-bonds with neighboring atoms and a carbon nanotube [76] is a sheet of graphene wrapped in a cylinder geometry. These materials have been the focus of an important scientific and technological interest [77, 78]. More specifically, graphene, characterized by Dirac fermions at the degenerate energy points, has interesting topological properties. As we saw in Sec. 1.1.2, degeneracies in two-level systems are source of Berry curvature flux and may lead to topologically non trivial systems. Numerous experimental and theoretical studies of the Berry phase in two-dimensional graphite or in other physical platforms where the graphene model has relevance (*e.g.* cold atom and light systems) has been realized [79–92], in particular from the time graphene is experimentally accessible [72]. A bit more generally speaking, topological systems related to graphene (we will introduce some in the rest of this manuscript) have attracted and still attract a lot of attention in the scientific community [11, 78, 93–105]. Here, we review a simple tight-binding graphene model; it proves helpful to study the

Haldane model presented in Chapter 2, which is itself helpful before studying the current theoretical description of the quantum spin Hall effect presented in Sec. 1.4.

Graphene [72, 78] is a two-dimensional material made of carbon atoms which disposition in space forms a honeycomb lattice (see Fig. 1.2(a)). Each carbon atom has three sp^2 orbitals (hybridization between one s orbital, one p_x orbital and one p_y orbital) which contributes to three σ-bonds with three other carbon atoms. This yields the honeycomb structure. The overlapping between the p_z orbitals (called π-bonds) at the nearest neighbors carbon atoms results in the essential low energy properties of graphene. It is well described by a tight-binding model on the honeycomb lattice with associated Hamiltonian

$$H = t_1 \sum_{\langle i,j \rangle} c_i^\dagger c_j, \tag{1.45}$$

where $c_i^\dagger$ is the creation operator for a particle at site i. $t_1 \in \mathbb{R}$, and the associated sum runs over all the nearest neighbors i and j. In the following, we will consider half-filling because each p_z orbital contains one electron.

The honeycomb lattice has two inequivalent sites in the unit cell (that we label by two "colors", A and B) and its Bravais lattice is hexagonal (see Fig. 1.2(a)). Let us write the creation operators $c_i^\dagger$ as $c_{\mathbf{r},\alpha}^\dagger$ where $\alpha = \{A, B\}$ indicates the color at the corresponding position given by the real-space vector $\mathbf{r}$. We define the Fourier transforms of these real space creation operators $c_{\mathbf{r},\alpha}^\dagger$, with $\alpha = \{A, B\}$:

$$c_{\mathbf{k},\alpha}^\dagger = \sum_{\mathbf{r} \in S_\alpha} \mathrm{e}^{i\mathbf{k}\cdot\mathbf{r}} c_{\mathbf{r},\alpha}^\dagger. \tag{1.46}$$

We also define $\sigma^x, \sigma^y, \sigma^z$ the three Pauli matrices acting in sub-lattice space. In Fourier space the Hamiltonian reads

$$H = \sum_{\mathbf{k}} \Psi_{\mathbf{k}}^\dagger h_{\mathbf{k}} \Psi_{\mathbf{k}}, \tag{1.47a}$$

$$h_{\mathbf{k}} = t_1 \sum_{i=1}^{3} \left[\cos(\mathbf{k}\cdot\mathbf{a}_i)\sigma_x + \sin(\mathbf{k}\cdot\mathbf{a}_i)\sigma_y \right], \tag{1.47b}$$

with $\Psi_{\mathbf{k}}^{\dagger} = \left(c_{\mathbf{k},A}^{\dagger}, c_{\mathbf{k},B}^{\dagger}\right)$. The displacement vectors $\mathbf{a}_i$, $i \in \{1,2,3\}$ and $\mathbf{b}_i$, $i \in \{1,2,3\}$ are defined in Fig. 1.2(a).

The graphene model has two energy bands $E_{\pm,\mathbf{k}}$ given by [106]

$$E_{\pm}(\mathbf{k}) = \pm|h_1(\mathbf{k})|, \tag{1.48}$$

with

$$h_1(\mathbf{k}) = t_1 \sum_{i=1}^{3} \exp(-i\mathbf{k}\cdot\mathbf{a}_i). \tag{1.49}$$

To anticipate the comparison with the results of the following section, we note that

$$E_{\pm}(\mathbf{k}) = \pm t_1 \sqrt{3 + 2\sum_{i=1}^{3} \cos(\mathbf{k}\cdot\mathbf{b}_i)}\,. \tag{1.50}$$

These energy bands are represented in Fig. 1.2(d). The associated eigenvectors are given by

$$|u_{\pm,\mathbf{k}}\rangle = \left(c_{A,\mathbf{k}}^{\dagger} \pm \mathrm{e}^{-i\varphi(\mathbf{k})} c_{B,\mathbf{k}}^{\dagger}\right)|0\rangle\ , \tag{1.51}$$

with $\mathrm{e}^{-i\varphi(\mathbf{k})} = \dfrac{\mathrm{e}^{i\mathbf{k}\cdot\mathbf{a}_3} h_1(\mathbf{k})^*}{|h_1(\mathbf{k})|}$. Both bands cross at both inequivalent points $\mathbf{K} = \dfrac{\mathbf{g}_3 - \mathbf{g}_2}{3}$ and $\mathbf{K}' = \dfrac{\mathbf{g}_2 - \mathbf{g}_3}{3}$ in the Brillouin zone (sketched in see Fig. 1.2(c)), with $\mathbf{g}_2$ and $\mathbf{g}_3$ defined by $-\mathbf{g}_2\cdot\mathbf{b}_2 = 2\pi$, $\mathbf{g}_2\cdot\mathbf{b}_3 = 0$, $\mathbf{g}_3\cdot\mathbf{b}_2 = 0$, and $\mathbf{g}_3\cdot\mathbf{b}_3 = 2\pi$. When the bands cross, the dispersion relation around $\mathbf{K}$ and $\mathbf{K}'$ is linear: for small $\mathbf{k}$, we have

$$h_1(\mathbf{K}+\mathbf{k}) = v_F(-k_x + ik_y), \quad \text{and} \quad h_1(\mathbf{K}'+\mathbf{k}) = v_F(k_x + ik_y), \tag{1.52}$$

with $v_F = \dfrac{3}{2}t_1$ the so-called Fermi velocity (in units of the lattice spacing), $k_x = \mathbf{k}\cdot\mathbf{e}_x$, $k_y = \mathbf{k}\cdot\mathbf{e}_y$, $\mathbf{e}_x = -\dfrac{1}{\sqrt{3}}(\mathbf{b}_2 + \mathbf{b}_3)$ and $\mathbf{e}_y = \dfrac{1}{3}(\mathbf{b}_2 - \mathbf{b}_3)$. This leads to

$$E_{\pm}(\mathbf{K}+\mathbf{k}) = E_{\pm}(\mathbf{K}'+\mathbf{k}) = \pm v_F|\mathbf{k}| + \mathcal{O}\left(|\mathbf{k}|^2\right), \tag{1.53}$$

with $|\mathbf{k}| = \sqrt{k_x^2 + k_y^2}$. A linear dispersion relation is reminiscent of massless Dirac Fermions therefore $\mathbf{K}$ and $\mathbf{K}'$ are called the Dirac points. At half-filling, the low energy excitations of

the model are described by the terms in Eq. (1.47a) near $\mathbf{K}$ and $\mathbf{K}'$. The effective Hamiltonian then reads [107]

$$H_0 = \int_{\mathbf{k}} \tilde{\Psi}^\dagger_{\mathbf{k}} h_{0,\mathbf{k}} \tilde{\Psi}_{\mathbf{k}}, \tag{1.54a}$$

$$h_{0,\mathbf{k}} = v_F \left(-k_x \sigma_x \tau_z + k_y \sigma_y\right), \tag{1.54b}$$

with $\tilde{\Psi}^\dagger_{\mathbf{k}} = \left(\Psi^\dagger_{\mathbf{K}+\mathbf{k}}, \Psi^\dagger_{\mathbf{K}'+\mathbf{k}}\right)$ and with τ_z the third Pauli matrix acting in the basis of kets with two components $\Psi^\dagger_{\mathbf{K}+\mathbf{k}}$ and $\Psi^\dagger_{\mathbf{K}'+\mathbf{k}}$. The integration runs over $\mathbf{k}$ such that $|\mathbf{k}| \ll 2\pi/a$.

Finally, let us notice that this graphene tight-binding model respects chiral symmetry, time-reversal symmetry and inversion symmetry.

1.2.5 Kagome tight-binding model

The kagome (shown in Fig. 1.2(b)) lattice shares common properties with the honeycomb lattice. Namely, as we show in this section, a simple tight-binding model on this lattice is characterized by Dirac fermions, as the graphene tight-binding model considered in the last section. Glancing back at Sec. 1.1.2, we deduce that the kagome lattice is potentially interesting to build non-trivial topological systems. In relation with the Berry phase concept, the kagome-lattice systems are interesting because they are a good platform for the quantum anomalous Hall effect. The (classical) anomalous Hall effect has been observed by E. Hall one hundred and forty years ago [108] and its quantized version has been theoretically and experimentally studied since Haldane's work in 1988 (see Ref. [5] or Sec. 2.1 of Chapter 2). Though it has attracted a lot of attention in the scientific community [4, 5, 109–112], the understanding of the anomalous Hall effect is still not complete. The quantum anomalous Hall effect appears in ferromagnetic topological materials, making the kagome-systems particularly interesting for the study of this effect. Indeed there are a lot of magnetic materials which atom structure is (or is similar to) the kagome lattice [27, 36–38, 113–116] while this is not the case for the honeycomb lattice. Moreover, in the kagome systems the band gap and the ferromagnetic Curie temperature is usually larger than in the honeycomb systems,

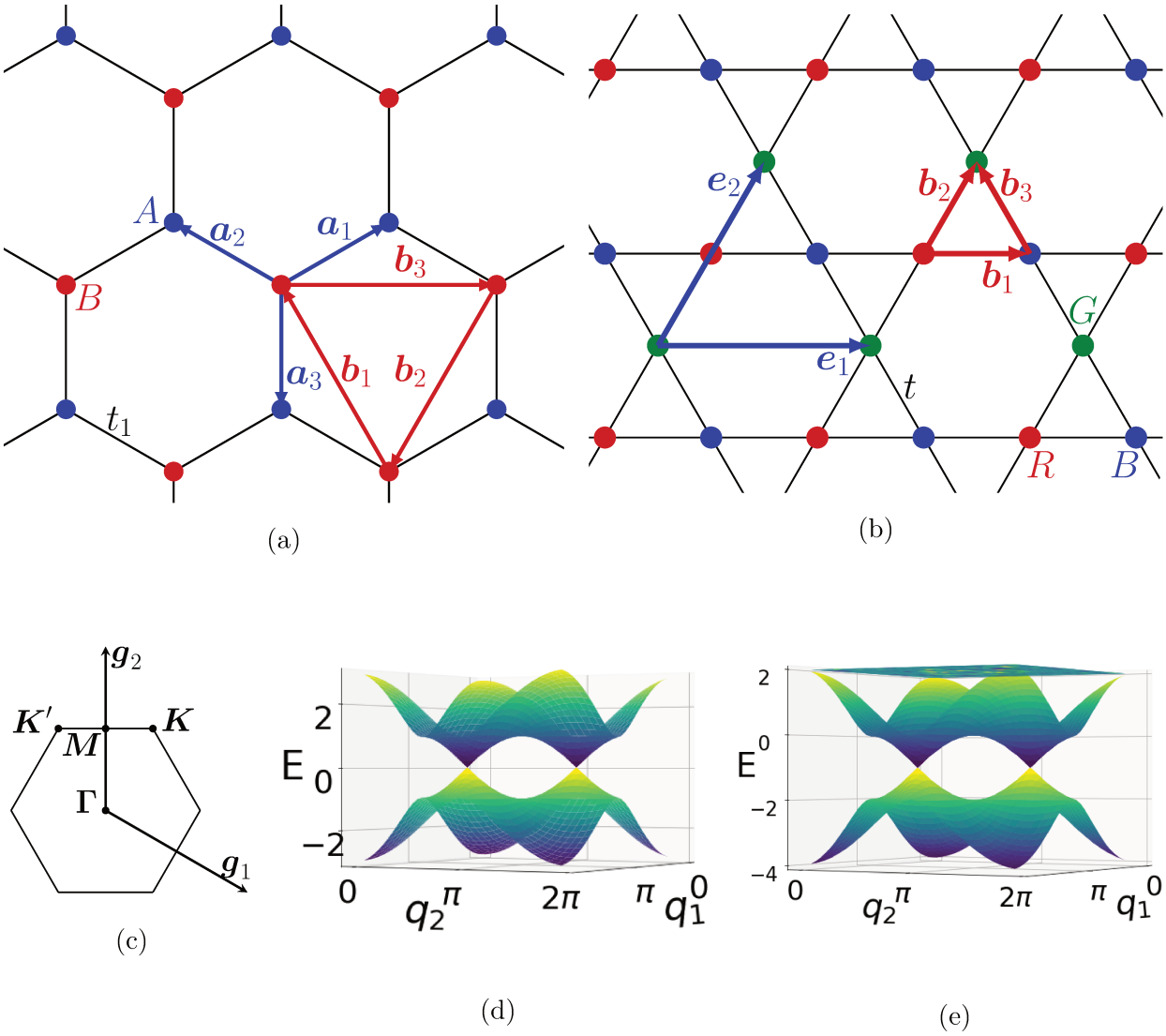

Figure 1.2: (a) Honeycomb lattice representation and definition of the sub-lattices A and B, of the nearest neighbors hopping amplitudes and of the displacement vectors $\mathbf{a}_i$, $i \in \{1,2,3\}$ and $\mathbf{b}_i$, $i \in \{1,2,3\}$. (b) Kagome lattice representation and definition of the sub-lattices R, B and G, of the nearest neighbors hopping amplitudes and of the displacement vectors $\mathbf{b}_i$, $i \in \{1,2,3\}$ and $\mathbf{e}_i$, $i \in \{1,2\}$. (c) Brillouin zone and high-symmetry points for the honeycomb and the kagome lattice which Bravais lattice is hexagonal. For the honeycomb lattice, in Sec. 1.2.4, we called $\mathbf{g}_3$ the vector called $\mathbf{g}_1$ in this figure. Dispersion relations for (d) the graphene model Eq (1.45) and (e) the tight-binding kagome model Eq (1.55).

therefore non-negligible topological properties should be measurable at higher temperatures [36]. This is very important for practical applications.

We consider a tight-binding model on the kagome lattice with only nearest-neighbor hopping term. We show that it shares some properties with the graphene model we described in previous section, namely linear dispersion relation near the Dirac points. The Hamiltonian reads

$$H = -t \sum_{\langle i,j \rangle} c_i^\dagger c_j, \tag{1.55}$$

where $c_i^\dagger$ is the creation operator for a particle at site i. $t_1 \in \mathbb{R}$, and the associated sum runs over all the nearest neighbors i and j.

The kagome lattice has three inequivalent sites in the unit cell (that we label by three "colors", R, B and G) and its Bravais lattice is hexagonal (see Fig. 1.2(b)). Let us write the creation operators $c_i^\dagger$ as $c_{\mathbf{r},\alpha}^\dagger$ where $\alpha = \{R, B, G\}$ indicates the color at the corresponding position given by the real-space vector $\mathbf{r}$. As we did in the previous section, we define the Fourier transforms

$$c_{\mathbf{k},\alpha}^\dagger = \sum_{\mathbf{r} \in S_\alpha} \mathrm{e}^{i\mathbf{k}\cdot\mathbf{r}} c_{\mathbf{r},\alpha}^\dagger. \tag{1.56}$$

In Fourier space the Hamiltonian reads

$$H = \sum_{\mathbf{k}} \Psi_{\mathbf{k}}^\dagger h_{\mathbf{k}} \Psi_{\mathbf{k}}, \tag{1.57a}$$

$$h_{\mathbf{k}} = -2t \begin{pmatrix} 0 & \cos(\mathbf{k}\cdot\mathbf{b}_1) & \cos(\mathbf{k}\cdot\mathbf{b}_2) \\ \cos(\mathbf{k}\cdot\mathbf{b}_1) & 0 & \cos(\mathbf{k}\cdot\mathbf{b}_3) \\ \cos(\mathbf{k}\cdot\mathbf{b}_2) & \cos(\mathbf{k}\cdot\mathbf{b}_3) & 0 \end{pmatrix}, \tag{1.57b}$$

with $\Psi_{\mathbf{k}}^\dagger = \left(c_{\mathbf{k},R}^\dagger, c_{\mathbf{k},B}^\dagger, c_{\mathbf{k},G}^\dagger\right)$. The displacement vectors $\mathbf{b}_i$, $i \in \{1, 2, 3\}$ are defined in Fig. 1.2(b).

Now we investigate the energy spectrum [31, 39] associated to the model we consider here and we show the similarities with the graphene. We have

$$\det\left(h_{\mathbf{k}} - \lambda \mathbb{I}\right) = (\lambda - 2t)(-\lambda^2 - 2t\lambda + 4t^2 f(\mathbf{k})), \tag{1.58}$$

with $f(\mathbf{k}) = 2\prod_{i=1}^{3}\cos\mathbf{k}\cdot\mathbf{b}_i$, $-1/4 \leq f(\mathbf{k}) \leq 2$. This yields one flat energy band $E_u = 2t$ and two dispersive bands

$$E_m = -t\left(1 - \sqrt{1+4f(\mathbf{k})}\right), \tag{1.59a}$$

$$E_l = -t\left(1 + \sqrt{1+4f(\mathbf{k})}\right), \tag{1.59b}$$

with $E_l \leq E_m \leq E_u$ and degeneracies appear in the spectrum only at $f(\mathbf{k}) = -1/4$ and at $f(\mathbf{k}) = 2$ in which cases we respectively have $E_l = E_m = -t$ and $E_m = E_u$. Graphical representation of the energy spectrum is given in Fig. 1.2(e). We have checked that hexagon-localized states associated to alternating values of the phase 0 and π are eigenstates with energies corresponding to the flat band [117, 118]. Such localized states are made possible because of the specific geometry of the kagome lattice; destructive interference processes occur in each triangle connected to the hexagon(s) where the state is localized. The equality $f(\mathbf{k}) = -1/4$ is obtained at both inequivalent points $\mathbf{K} = \dfrac{\mathbf{g}_1 - \mathbf{g}_2}{3}$ and $\mathbf{K}' = \dfrac{\mathbf{g}_2 - \mathbf{g}_1}{3}$ in the Brillouin zone (sketched in see Fig. 1.2(c)), with $\mathbf{g}_1$ and $\mathbf{g}_2$ defined by $\mathbf{g}_1\cdot\mathbf{e}_1 = 2\pi$, $\mathbf{g}_1\cdot\mathbf{e}_2 = 0$, $\mathbf{g}_2\cdot\mathbf{e}_1 = 0$, and $\mathbf{g}_2\cdot\mathbf{e}_2 = 2\pi$ and the vectors $\mathbf{e}_i$, $i \in \{1,2\}$ are defined in Fig. 1.2(b). Both lowest bands of the spectrum are in fact identical to both energy bands of the graphene (up to a global energy shift). Indeed we have $f(\mathbf{k}) = \sum_{i=1}^{3}\cos^2\mathbf{k}\cdot\mathbf{b}_i - 1$ and defining $\mathbf{e}_3 = \mathbf{e}_2 - \mathbf{e}_1$ so that $\mathbf{e}_i = 2\mathbf{b}_i$, $i \in \{1,2,3\}$, we find

$$1 + 4f(\mathbf{k}) = 3 + 2\sum_{i=1}^{3}\cos\mathbf{k}\cdot\mathbf{e}_i. \tag{1.60}$$

From this we deduce that for small $\mathbf{k}$ around $\mathbf{K}$ and $\mathbf{K}'$, we have

$$E_m(\mathbf{K}+\mathbf{k}) = E_m(\mathbf{K}'+\mathbf{k}) = -t\left(1 - \frac{3}{2}|\mathbf{k}|\right) + \mathcal{O}\left(|\mathbf{k}|^2\right), \tag{1.61a}$$

$$E_l(\mathbf{K}+\mathbf{k}) = E_l(\mathbf{K}'+\mathbf{k}) = -t\left(1 + \frac{3}{2}|\mathbf{k}|\right) + \mathcal{O}\left(|\mathbf{k}|^2\right), \tag{1.61b}$$

with $|\mathbf{k}| = \sqrt{k_x^2 + k_y^2}$, $k_x = \mathbf{k}\cdot\mathbf{e}_x$, $k_y = \mathbf{k}\cdot\mathbf{e}_y$, $\mathbf{e}_x = -\dfrac{1}{\sqrt{3}}(\mathbf{e}_1 - \mathbf{e}_2)$ and $\mathbf{e}_y = -\dfrac{1}{3}(\mathbf{e}_1 + \mathbf{e}_2)$. At 1/3 filling, the low energy excitations of the model are described by linear relation dispersion relation and one can identify $v_F = \dfrac{3}{2}t$ as for the graphene case.

1.3 Chern number and link with measurable observables in topological systems

We now make the connection between the Berry phase and observables such as the Hall conductivity (Sec. 1.3.1) and the charge polarization (Sec. 1.3.4) in two-dimensional systems. This leads us to introduce and study a topological invariant, the (first) Chern number (Sec. 1.3.2), characterizing these two-dimensional systems; systems with non-vanishing Chern number are called Chern insulators. We also explain the connection between the Chern number and the presence of the chiral edge states which energy cross the bulk gap in an open geometry (Sec. 1.3.3). This concepts are widely used throughout this manuscript, either for the study of Chern insulators (see Chapters 2, 3 and 4), or for the understanding of time-reversal invariant topological insulators (see Sec. 1.4 and Chapters 3 and 5).

1.3.1 Hall conductivity and TKNN integer

Here we compute the Hall conductivity using the Kubo formula, as Thouless, Kohmoto, Nightingale, and den Nijs did in 1982 [8]. As we will see, it has a direct link with the Berry phase concept and in particular with Eq. (1.22). This section therefore provides another way to understand how the Berry phase concept is related to the Hall conductivity and the topological properties of the system. It shows the quantization of the Hall conductivity in the QHE and it leads naturally to the introduction of the Chern number which is the invariant characterizing two-dimensional topological systems.

We consider a lattice translation-invariant two-dimensional system. Note that if a magnetic field is applied to the system, considering the magnetic unit cell instead of the "usual" unit cell (as long as we study a "spinless" system) and magnetic translation operators instead of "usual" translation operators restores the translation-invariance [10]. This lattice translation-invariant system is described by Bloch states. We assume a small electric field with amplitude ϵ_y applied in one direction of the system (call it the $\mathbf{y}$ direction); to be more

specific we consider this electric field as an adiabatic perturbation of the Bloch Hamiltonian. Let us compute the transverse conductance $\sigma_{x,y}$ defined by

$$e\langle j_x\rangle_y = \sigma_{x,y}\epsilon_y, \tag{1.62}$$

where $\langle j_x\rangle_y$ is the expectation value of the current density operator in the direction perpendicular to the $\mathbf{y}$ direction, resulting from the electric field perturbation and e is the electron charge. The response to the perturbation may be evaluated using linear response theory (see for instance [119]) which leads to the so-called Kubo formula (see App. D)

$$\langle j_x\rangle_y = i\hbar eV \sum_{E_m<\mu<E_n} \frac{\langle m|\, j_x\,|n\rangle\,\langle n|\, j_y\,|m\rangle - \langle n|\, j_x\,|m\rangle\,\langle m|\, j_y\,|n\rangle}{(E_n - E_m)^2}\epsilon_y, \tag{1.63}$$

where $|n\rangle$ and $|m\rangle$ are eigenstates of the system and E_n and E_m their energies, j_y is the current density operator in the $\mathbf{y}$ direction, V is the volume of a unit cell, E_F is the Fermi energy and $\hbar$ is the reduced Planck constant. This gives

$$\sigma_{x,y} = i\hbar e^2 V \sum_{E_m<\mu<E_n} \frac{\langle m|\, j_x\,|n\rangle\,\langle n|\, j_y\,|m\rangle - \langle n|\, j_x\,|m\rangle\,\langle m|\, j_y\,|n\rangle}{(E_n - E_m)^2}. \tag{1.64}$$

Let us apply it to the Bloch system we want to describe. We identify $V\,\langle n|\, j_x\,|m\rangle = \langle n|\, v_x\,|m\rangle = \langle n|\,(\partial_{k_x}H)\,|m\rangle/\hbar$ and $V\,\langle n|\, j_y\,|m\rangle = \langle n|\, v_y\,|m\rangle = \langle n|\,\left(\partial_{k_y}H\right)|m\rangle/\hbar$ which gives

$$\sigma_{x,y} = \frac{ie^2}{\hbar V} \sum_{E_m<\mu<E_n} \frac{\langle m|\,(\partial_{k_x}H)\,|n\rangle\,\langle n|\,\left(\partial_{k_y}H\right)|m\rangle - \langle n|\,(\partial_{k_x}H)\,|m\rangle\,\langle m|\,\left(\partial_{k_y}H\right)|n\rangle}{(E_n - E_m)^2}. \tag{1.65}$$

Then we use the eigenvalue equation

$$H\,|m\rangle = E_m\,|m\rangle\,, \tag{1.66}$$

and the action of ∂_{k_j}, $j = \{x, y\}$ on

$$\langle n|\, H\,|m\rangle = 0,\ \forall\,|n\rangle \neq |m\rangle\,, \tag{1.67}$$

to get

$$\langle n|\,\left(\partial_{k_j}H\right)|m\rangle = (E_m - E_n)\,\langle n|\,\left(\partial_{k_j}\,|m\rangle\right) = (E_n - E_m)\,\left(\partial_{k_j}\,\langle n|\right)|m\rangle\,. \tag{1.68}$$

Reporting this result in Eq. (1.65) gives

$$\sigma_{xy} = \frac{e^2}{i\hbar V} \sum_{E_m<E_F<E_n} \left(\langle \partial_{k_x} m|n\rangle \langle n|\partial_{k_y} m\rangle - \langle \partial_{k_y} m|n\rangle \langle n|\partial_{k_x} m\rangle \right). \tag{1.69}$$

The eigenstates of the Hamiltonian form a complete set and the Fermi energy is supposed to lie between two bands, therefore $\sum_{E_m<E_F<E_n}(|m\rangle\langle m| + |n\rangle\langle n|) = 1$, therefore

$$\sigma_{xy} = \frac{e^2}{i\hbar V} \sum_{E_m<E_F} \left(\langle \partial_{k_x} m|\partial_{k_y} m\rangle - \langle \partial_{k_y} m|\partial_{k_x} m\rangle \right). \tag{1.70}$$

Transforming this last equation into a sum over the filled bands with index m gives

$$\sigma_{xy} = \frac{e^2}{h} \sum_{\text{filled bands}} C_m. \tag{1.71}$$

with

$$C_m = \frac{1}{2\pi i} \int_{\text{BZ}} d^2\mathbf{k} \cdot [\nabla \times \mathbf{A}_m], \tag{1.72}$$

the so-called Chern number associated to the m^{th} energy band (the integral in the formula runs over all momentum in the Brillouin zone), and

$$d^2\mathbf{k} \cdot [\nabla \times \mathbf{A}_m] = d^2k \left(\langle \partial_{k_x} m|\partial_{k_y} m\rangle - \langle \partial_{k_y} m|\partial_{k_x} m\rangle \right). \tag{1.73}$$

Eq. (1.71) was first obtained by Thouless, Kohmoto, Nightingale, and den Nijs [8], and is often referred as the TKNN formula. Defining

$$\sigma_{xy} = \sum_{\text{filled bands}} \sigma_{xy,m}, \tag{1.74}$$

we see that each band n is associated with a Hall conductivity proportional to the associated Chern number

$$\sigma_{xy,n} = \frac{e^2}{h} C_n. \tag{1.75}$$

Thouless, *et al.* originally derived the TKNN formula for a two-dimensional crystal with perpendicular uniform magnetic field and they showed that what we called C_n here is quantized. This formula is in fact directly applicable to a two-dimensional crystal with vanishing magnetic field in the unit cell, first introduced by Haldane [5] few years later.

Comparing Eq. (1.72) with Eq. (1.22), we see that 2π times the Chern number is the integral of the Berry curvature over the two-dimensional Brillouin zone, *i.e.* the Berry phase accumulated by a particle around a close path being the boundary of the first Brillouin zone.

In the next section we explain that C_n, that is called the Chern number, is a mathematical object used to characterized the topology of a two-dimensional manifold and is quantized.

1.3.2 Chern number

Here we show the quantization of the Chern number, which explains the quantization of the Hall conductivity. The derivation presented here follows Ref. [10] and is also useful for the computation of topological invariants in further sections of this manuscript.

As introduced in the previous section the Chern number characterizing an arbitrary isolated Bloch energy band with associated Bloch eigenvector $\Psi_{\mathbf{k}}(\mathbf{r}) = \mathrm{e}^{i\mathbf{k}.\mathbf{r}} u_{\mathbf{k}}(\mathbf{r})$ reads

$$C = \frac{1}{2i\pi} \int_{\mathrm{BZ}} d^2k \, [\nabla_{\mathbf{k}} \times \mathbf{A}_{\mathbf{k}}] \cdot \mathbf{e}_z, \tag{1.76}$$

with the so-called Berry gauge field $\mathbf{A}_{\mathbf{k}} = \int d^2r u^*_{\mathbf{k}}(\mathbf{r}) \nabla_{\mathbf{k}} u_{\mathbf{k}}(\mathbf{r}) = \langle u_{\mathbf{k}} | \nabla_{\mathbf{k}} | u_{\mathbf{k}} \rangle$. Because the BZ is a torus, if we can find a gauge choice such that $\mathbf{A}_{\mathbf{k}}$ is uniquely and smoothly defined over all the BZ, then, using the Stokes' theorem, we find that C is vanishing. Therefore, a non-trivial topology comes from the impossibility of finding such a gauge choice that makes $\mathbf{A}_{\mathbf{k}}$ uniquely and smoothly defined.

Under a gauge transformation $u_{\mathbf{k}}(\mathbf{r}) \to u_{\mathbf{k}}(\mathbf{r}) \mathrm{e}^{if(\mathbf{k})}$, with f a smooth function of $\mathbf{k}$ and independent of $\mathbf{r}$, we have $\mathbf{A}_{\mathbf{k}} \to \mathbf{A}_{\mathbf{k}} + i\nabla_{\mathbf{k}} f(\mathbf{k})$, so $C \to C$. Now, suppose that the BZ is divided into 2 domains denoted $\mathcal{D}_{\mathrm{I}}$ and $\mathcal{D}_{\mathrm{II}}$, where the respective gauge choices $|u_{\mathbf{k},\mathrm{I}}\rangle$ and $|u_{\mathbf{k},\mathrm{II}}\rangle$ are unique and smooth. We define $\varphi(\mathbf{k})$ a smooth function of $\mathbf{k}$ such that $|u_{\mathbf{k},\mathrm{I}}\rangle = \mathrm{e}^{i\varphi(\mathbf{k})} |u_{\mathbf{k},\mathrm{II}}\rangle$ and we define $\mathbf{A}_{\mathbf{k},\mathrm{I}} = \langle u_{\mathbf{k},\mathrm{I}} | \nabla_{\mathbf{k}} | u_{\mathbf{k},\mathrm{I}} \rangle$ and $\mathbf{A}_{\mathbf{k},\mathrm{II}} = \langle u_{\mathbf{k},\mathrm{II}} | \nabla_{\mathbf{k}} | u_{\mathbf{k},\mathrm{II}} \rangle$ which are both uniquely and smoothly defined fields respectively inside $\mathcal{D}_{\mathrm{I}}$ and $\mathcal{D}_{\mathrm{II}}$. Then we have

$$C = \frac{1}{2i\pi} \left(\int_{\mathcal{D}_{\mathrm{I}}} d^2k \, [\nabla_{\mathbf{k}} \times \mathbf{A}_{\mathbf{k},\mathrm{I}}] \cdot \mathbf{e}_z + \int_{\mathcal{D}_{\mathrm{II}}} d^2k \, [\nabla_{\mathbf{k}} \times \mathbf{A}_{\mathbf{k},\mathrm{II}}] \cdot \mathbf{e}_z \right). \tag{1.77}$$

We call Γ the boundary between $\mathcal{D}_{\rm I}$ and $\mathcal{D}_{\rm II}$ and we have, from Stokes' theorem

$$C = \pm\frac{1}{2i\pi}\left(\oint_\Gamma d\mathbf{k}\cdot\mathbf{A}_{\mathbf{k},\rm I} - \oint_\Gamma d\mathbf{k}\cdot\mathbf{A}_{\mathbf{k},\rm II}\right). \tag{1.78}$$

Note that the sign in the previous equation depends on the choice of the domains $\mathcal{D}_{\rm I}$ and $\mathcal{D}_{\rm II}$ and on the orientation of the one-dimensional integral over Γ on the BZ. Applications of this formula to specific topological systems are detailed in Chapter 4, Sec. 1.1.4 and in Chapter 5, Sec. 1.1.4. Using $\mathbf{A}_{\mathbf{k},\rm I} = \mathbf{A}_{\mathbf{k},\rm II} + i\nabla_{\mathbf{k}}\varphi(\mathbf{k})$, we find [10]

$$C = \pm\frac{1}{2\pi}\oint_\Gamma d\mathbf{k}\cdot\nabla_{\mathbf{k}}\varphi(\mathbf{k}). \tag{1.79}$$

Along Γ, the kets $|u_{\mathbf{k},\rm II}\rangle$ and $|u_{\mathbf{k},\rm I}\rangle = \mathrm{e}^{i\varphi(\mathbf{k})}|u_{\mathbf{k},\rm II}\rangle$ are unique functions of $\mathbf{k}$ and the phase $\varphi(\mathbf{k})$ is a smooth function of $\mathbf{k}$, therefore the integral in the last formula is an integer times 2π and C is an integer. We conclude that the Hall conductivity Eq. (1.75) is quantized (in units of e^2/h).

1.3.3 Bulk-boundary correspondence

In the previous sections, we showed that a quantized value of the Hall conductivity is related to an integer value of the Chern number, which is a bulk invariant. The quantized value of the Hall conductivity is also related to the presence of the chiral edge states which energy cross the bulk gap in an open geometry (see Sec. 1.1.4). Here we explain that these edge states are in fact necessarily appearing at the interface between two systems characterized by different Chern numbers. We use the notations introduced in Sec. 1.1.2.

Let us consider an adiabatic evolution of the Hamiltonian $H(\mathbf{R})$ in parameter space; the energies of the system vary continuously. As long as an energy band n stays isolated (no crossing with other bands) a quantity (that we denote $C_n(\mathbf{R})$) computed from the energy states associated to this band can only vary continuously. Therefore, in this case, a number which is constrained to be an integer can not vary. However, if during the evolution of $\mathbf{R}$, the energy band crosses another one and after the crossing an isolated energy band reappears,

then, there is no constrain of a continuous relation between both $C_n(\mathbf{R})$ associated to the isolated band before and after the crossing. In other words, taking $C_n(\mathbf{R})$ to be the Chern number tells us that it can vary only if the bulk gap closes.

Now we consider an interface (where the parameters $\mathbf{R}$ vary slowly) between a Chern insulator and a trivial insulator. Both of these systems, away from the interface region, are characterized by gapped bulk bands. On the other hand, from the previous paragraph, we know that at the interface region, the gap has to close so that the topological invariant characterizing the Chern insulator and the trivial insulator can be different. This is realized thanks to states which are localized at the interface and which connect the bulk bands below and above the gap. If we further assume that the system is described by a Dirac Hamiltonian at the gap closing points, looking for an edge solution of the Schrödinger equation gives a chiral propagating mode along the interface [2, 66].

This bulk-boundary correspondence is generalizable to an interface between two insulators characterized by different values (say I_1 and I_2) of a topological bulk invariant (integer). In such system, $I_1 - I_2$ edges states are predicted [2, 120, 121].

1.3.4 Charge polarization

The modern microscopic theory of charge polarization is quite recent and is a rich subject. We refer the interested reader to the Ref. [122].

Here we would like to give another perspective on the relation between the Chern number and the charge polarization [123] which is the number of charge pumped during a cycle such as the one described in Sec. 1.1.4. Let us first consider a one-dimensional system with associated Hamiltonian H, space coordinate x and momentum coordinate k_x. We consider an energy band labeled by quantum number n.

The Polarization is given by the center of charge of the Wannier states (in units of the

electron charge e) [48, 68, 122, 124]

$$P = \langle w_{n,X}| \, x \, |w_{n,X}\rangle = \frac{1}{2i\pi} \int_{-\pi}^{\pi} dk_x \, \mathcal{A}_n(k_x) + X, \tag{1.80}$$

with $\mathcal{A}_n(k_x) = \langle u_{n,k_x}| \, \partial_{k_x} \, |u_{n,k_x}\rangle$. Let us impose that the Bloch eigenvectors $|\psi_{n,k_x}\rangle$ are defined continuously from $k_x = -\pi$ to $k_x = \pi$ and that $|\psi_{n,k_x+\pi}\rangle = |\psi_{n,k_x-\pi}\rangle$ (note that this however implies that $u_{n,k_x+\pi}(x) = \mathrm{e}^{-i2\pi x} u_{n,k_x-\pi}(x)$). Then from the expression of the Berry field (see under Eq. (1.76) for instance) we see that $\mathcal{A}_n(k_x + \pi) = \mathcal{A}_n(k_x - \pi)$ and the last integral (right-hand side of Eq. (1.80)) can be taken on a closed loop. Now we parametrize the Hamiltonian with say time t and we consider an adiabatic evolution of H, from an initial time t_0 to a final time t_1. We assume that the Bloch eigenvectors $|\psi_{n,k_x}(t)\rangle$ are defined continuously between t_0 and t_1 for all value of k_x. We have

$$P(t_1) - P(t_0) = \frac{1}{2i\pi} \left[\oint dk_x \, \mathcal{A}_n(k_x, t_1) - \oint dk_x \, \mathcal{A}_n(k_x, t_0) \right], \tag{1.81}$$

which, gives after application of Stokes' theorem [48]

$$P(t_1) - P(t_0) = \frac{1}{2i\pi} \int_{t_0}^{t_1} dt \oint dk_x F(t, k_x), \tag{1.82}$$

with the Berry curvature $F(t, k_x) = \langle \partial_t u_{n,k_x}(t) | \partial_{k_x} u_{n,k_x}(t) \rangle + c.c.$ and "$c.c.$" denotes the complex conjugate. The experimental access to the polarization in perovskite crystals made possible to check that Eq.(1.82) leads to consistent physical results [125–128]. In most experiments, we access the polarization through its derivatives (*e.g.* via the permittivity, the piezoelectric tensor, the Born charge [122]). The change in the polarization expressed in Eq. (1.81) is therefore connected to experimental measurements.

We now consider a two-dimensional real-space system and we write its Hamiltonian in momentum space

$$H = \sum_{k_y} \mathcal{H}(k_y), \tag{1.83a}$$

$$\mathcal{H}(k_y) = \sum_{k_x} \sum_{\alpha,\alpha'} \tilde{h}_{\mathbf{k},\alpha,\alpha'} c^{\dagger}_{\mathbf{k},\alpha} c_{\mathbf{k},\alpha'}, \tag{1.83b}$$

with $\mathcal{H}(k_y) = \mathcal{H}(k_y + 2\pi)$. In the thermodynamic limit where the number of unit cell goes to infinity so that k_y (and k_x) varies continuously, taking $t = k_y$ and considering a periodic pumping cycle, *i.e.* $t_0 = k_{y,0}$ and $t_1 = k_{y,1} = k_{y,0} + 2\pi$, gives

$$P(k_{y,1}) - P(k_{y,0}) = \frac{1}{2i\pi} \int d^2k \, [\nabla_{\mathbf{k}} \times \mathbf{A}_{\mathbf{k}}] \cdot \mathbf{e}_z, \tag{1.84}$$

where we identify the famous form of the Berry curvature for two-dimensional systems $[\nabla_{\mathbf{k}} \times \mathbf{A}_{\mathbf{k}}] \cdot \mathbf{e}_z$. The change in the polarization during a periodic pumping cycle, in units of the electron charge e, is the Chern number. In other words, during such a periodic pumping cycle, the center of charge of the Wannier functions is shifted by the value of the Chern number (remind that we set the lattice parameter to unity $a = 1$).

1.4 Time-reversal invariant topological insulators

In this section we introduce two-dimensional topological spin systems which are time-reversal invariant. This is particularly useful for Chapter 5 where we study such systems. As we explain in the following section, the key physical ingredient of the topological band theory introduced here is the spin-orbit coupling; its description and its relation with topology is also useful for the chapter 4. Time-reversal symmetry plays a major role for the topological properties of the systems studied here. The time-reversal operator is introduced in App. B and some proofs of statements used in this section can also be found in this appendix.

The topological phase we study in this section is called a quantum spin Hall phase and was first envisaged to exist in graphene by Kane and Mele who theoretically described it in Ref. [11]. Almost at the same time, Bernevig *et al* [12, 13] independently studied a similar model realizable in mercury cadmium telluride (HgCdTe) semiconductor quantum wells. This enabled the first experimental observation of the quantum spin Hall phase few years later [14].

The quantum spin Hall effect is the quantized version of the spin Hall effect. A spin Hall state is characterized by electrons moving in a direction which depends on their spin

direction [129, 130]. In a spin Hall system under an applied electric current, the Hall voltage (difference in the Fermi levels at both edges of the sample) is vanishing but the spin Hall voltage (difference in the Fermi levels for each spin at both edges of the sample) is finite. The spin Hall effect appears in systems with strong spin-orbit coupling. A microscopic model with spin-orbit coupling which shows a quantized spin Hall conductance has been formulated in years following the first studies about the spin Hall effect [11–13]. It leads to a topological band theory describing topological insulators [2, 131]. This was also a major step towards the realization of the quantum anomalous Hall effect, introduced in a theoretical model almost two decades earlier [5].

In the following section we review Kane and Mele's model [11]. Then, in section 1.4.2, we study a topological pump for a time-reversal invariant system and we make the connection with the topological invariant which characterizes these systems.

1.4.1 Kane and Mele model

The Kane-Mele model [11] is a spin model on the honeycomb lattice. Kane and Mele introduced this model to describe graphene with spin-orbit coupling at low energy. Then they constructed an effective tight-binding model which, at low energy, is identical to the former model.

Spin-orbit coupling in the low energy effective model We want to build a low-energy topological spin model on the honeycomb lattice; our starting point is two spin copies (one spin up copy, one spin down copy) of the low energy graphene model. Let us define

$$\Psi_{\mathbf{k}}^{\dagger} = \left(\tilde{\Psi}_{\mathbf{k},\uparrow}^{\dagger}, \tilde{\Psi}_{\mathbf{k},\downarrow}^{\dagger}\right), \tag{1.85a}$$

$$\tilde{\Psi}_{\mathbf{k},\sigma}^{\dagger} = \left(c_{\mathbf{K}+\mathbf{k},A,\sigma}^{\dagger}, c_{\mathbf{K}+\mathbf{k},B,\sigma}^{\dagger}, c_{\mathbf{K}'+\mathbf{k},A,\sigma}^{\dagger}, c_{\mathbf{K}'+\mathbf{k},B,\sigma}^{\dagger}\right), \ \sigma \in \{\uparrow,\downarrow\}, \tag{1.85b}$$

where $c^\dagger_{\mathbf{k},L,\sigma}$ is the creation operator for a particle with momentum $\mathbf{k}$, color $L = \{A, B\}$, and spin $\sigma = \{\uparrow, \downarrow\}$. The extension of the Hamiltonian in Eq. (1.54) is

$$H_0 = \int_{\mathbf{k}} \tilde{\Psi}^\dagger_{\mathbf{k}} h_{0,\mathbf{k}} \tilde{\Psi}_{\mathbf{k}}, \tag{1.86a}$$

$$h_{0,\mathbf{k}} = v_F \mathbb{I} \left(-k_x \sigma_x \tau_z + k_y \sigma_y\right), \tag{1.86b}$$

with $\mathbb{I}$ the identity in spin space. In this system, we want to open a topological gap at each Dirac point and we want to keep the system time-reversal invariant, because in such a system, the edge modes are protected by time-reversal symmetry as we explain in App. B. From the expression of $h_{0,\mathbf{k}}$ we see that a gap can be opened only thanks to a term proportional to σ_z (third Pauli matrix acting in sub-lattice space).

Let us consider one Dirac point, say $\mathbf{K}$. We can open an identical gap for both spin polarizations with a term proportional to $\sigma_z \mathbb{I}_s$, where the identity matrix acts in the spin space. We have $\theta \sigma_z \mathbb{I}_s \theta^{-1} = \sigma_z \mathbb{I}_s$ (see App. B) so time-reversal symmetry imposes that at the other Dirac point $\mathbf{K}'$, we take the same term $\sigma_z \mathbb{I}_s$. However we know that for a spinless system a Semenoff mass term $\sigma_z \mathbb{I}_m$ ($\mathbb{I}_m$ is the identity in the $(\mathbf{K}, \mathbf{K}')$ space) gives a trivial phase. Here for a spin model it would just yield two spin copies of trivial topological systems, so the whole system would also be trivial. Another way to open a gap is to consider, at one Dirac point (say $\mathbf{K}$), opposite masses for both spin polarizations, *i.e.* a term $\sigma_z s_z$, where s_z is the third Pauli matrix acting in spin space. We want to impose that the system is time-reversal invariant. A time-reversal transformation flips the spin (in the spin Pauli matrix language it gives $\theta s_z \theta^{-1} = -s_z$ so $\theta \sigma_z s_z \theta^{-1} = -\sigma_z s_z$) and it sends the Bloch Hamiltonian at $\mathbf{k} = \mathbf{K}$ to the Bloch Hamiltonian at $-\mathbf{k} = \mathbf{K}'$:

$$\theta h(\mathbf{k} = \mathbf{K}) \theta^{-1} = h(-\mathbf{k} = \mathbf{K}'). \tag{1.87}$$

Therefore the system is time-reversal invariant if we set

$$h(\mathbf{K}') = -h(\mathbf{K}), \tag{1.88}$$

i.e. the term opening the gap must be proportional to $\sigma_z\tau_z s_z$, where τ_z acts in the $(\mathbf{K}, \mathbf{K}')$ space. We denote it H_{SO} and we write its amplitude λ_{SO};

$$H_{SO} = \lambda_{SO} \int_{\mathbf{k}} \Psi^\dagger_{\mathbf{k}} \sigma_z \tau_z s_z \Psi_{\mathbf{k}} \,, \tag{1.89}$$

This is a spin-orbit coupling term since it couples spin and momentum quantum numbers. This is the extension of the (effective low-energy) Haldane mass term $\sigma_z\tau_z$ for a time-reversal invariant spin system.

This term is referred to as "intrinsic" spin-orbit coupling because its physical origin comes from the motion of the electrons in the potential created by the atoms forming the lattice (as we explain in the paragraph "Lattice model"). It is invariant under the $\mathbf{z} \to -\mathbf{z}$ transformation, called mirror symmetry about the plane.

In their seminal paper [11], Kane and Mele also considered a Rashba spin-orbit term; alone it is not sufficient to open a gap but it may vary the gap yielded by H_{SO} through the coupling of both spin species. It is given by

$$H_R = \lambda_R \int_{\mathbf{k}} \Psi^\dagger_{\mathbf{k}} \left(\sigma_x \tau_z s_y - \sigma_y s_x\right) \Psi_{\mathbf{k}} \,. \tag{1.90}$$

As for the intrinsic spin-orbit coupling term, we study the lattice version of this term in the next paragraph.

Lattice model The total spin Hamiltonian $H = H_0 + H_{SO}$ is found to be the low-energy limit of two spin copies of the Haldane model (at $\phi = \pi/2$ and $M = 0$), where the sign of the t_2 term depends on the spin degree of freedom:

$$t_1 \sum_{\substack{\langle i\,,j\rangle \\ \alpha\neq\beta}} c^\dagger_{i,\alpha} \mathbb{I} c_{j,\beta} + i t_2 \sum_{\substack{\langle\langle i\,,j\rangle\rangle \\ \alpha}} \nu_{i\,j} c^\dagger_{i,\alpha} s_z c_{j,\alpha}, \tag{1.91}$$

where we can also write explicitly $c^\dagger_{i,\alpha} = \left(c^\dagger_{i,\alpha,\uparrow}, c^\dagger_{i,\alpha,\downarrow}\right)$. The t_1 term is the graphene Hamiltonian H_0 and at low energy the t_2 term gives the spin-orbit term H_{SO}. In graphene, the physical origin of the t_2 term is the spin orbit coupling between a particle's spin and its

motion (characterized by the momentum $\mathbf{p} = \hbar\mathbf{k}$) in the lattice potential V (due to the atoms) [11, 109, 132], given by [133]

$$(\boldsymbol{\nabla} V \times \mathbf{p}) \cdot \mathbf{s} \propto \mathbf{L} \cdot \mathbf{s}, \tag{1.92}$$

where $\mathbf{L}$ is the angular momentum operator and in graphene $\mathbf{L} \cdot \mathbf{s}$ reduces to $L_z s_z$ because the system is invariant under mirror reflection about the lattice plane. As we mentionned in Sec. 1.2.4, two types of orbitals are found in graphene, the sp^2 orbitals which contribute to the σ-bonds and p_z orbitals which are the one we took into account to describe the low energy properties of graphene. The amplitude $\langle R_i(\mathbf{r})| L_z s_z |R_j(\mathbf{r})\rangle$ of the term in Eq. (1.92) between two p_z orbitals $|R_i(\mathbf{r})\rangle$ and $|R_j(\mathbf{r})\rangle$ centered at two nearest-neighbor sites i and j is vanishing. Indeed, consider a vertical reflection plane along the bond between i and j; under a mirror transformation about this plane, L_z is odd and the p_z orbitals are unchanged. Therefore $\langle R_i(\mathbf{r})| L_z s_z |R_j(\mathbf{r})\rangle$ vanishes. If i and j are next-nearest neighbors, the lattice is not invariant under the mirror transformation about vertical reflection plane along the i-j bond. Although Kane and Mele first estimated the amplitude of this term to be ≈ 1 meV, it was shown few years later ([134, 135]) that this term in graphene is actually very small (10^{-3} meV) compared to the relevant energies of the system (remind that the nearest neighbor hopping term has amplitude ~ 1 eV). The quantum spin Hall effect was also predicted to happen in HgCdTe ([12, 13]) where the amplitude of the spin-orbit coupling is large ([2, 136–138]); this effect was then experimentally observed [14, 139–141].

Hamiltonian in Eq. (1.91) is time-reversal symmetric so it is characterized by a topological $\mathbb{Z}_2$ invariant, as we argue in Sec. 1.4.2. Moreover, it is inversion symmetric, so it is possible to compute ν from the method presented in Sec. 3.3.2. In fact, ν can also be computed as a difference of Chern numbers associated to both spin energy band since the Hamiltonian in Eq. (1.91) does not contain spin mixing terms. From Eq. (1.91), we see that we have two spin-copies of the Haldane model at vanishing Semenoff mass. These two copies experience an effective opposite magnetic density (in terms of the Haldane model), therefore the total

polarization is vanishing but the difference in polarization between both Kramers' partner is a topological invariant. This difference is the difference between the Chern numbers associated to both Kramers' partner. If the system has open boundary, at each edge of the system, two edge modes (forming a Kramers' pair) are localized, they propagate along the edge in opposite directions and they are associated to opposite spin polarizations. This gives a quantized spin Hall conductivity σ^s_{xy} which relates the difference in the spin currents along the edges and an applied electric field in the direction perpendicular to the edges. For instance, in a system with translation invariance along the $\mathbf{x}$ direction, we have $J_\uparrow - J_\downarrow = \sigma^s_{xy} E_y$, where J_σ is the current along the $\mathbf{x}$ direction associated to the σ spin species when a small electric field E_y is applied in the $\mathbf{y}$ direction. As we explain in App. B, in the momentum space, the energy associated to both partners of a Kramers' pair cross at the time reversal invariant points. Time-reversal symmetry protects this crossing; single-particle scattering terms (which could open a gap) between both partners of the Kramers' edge pair are necessarily (because of time-reversal invariance) vanishing. The energy associated to two modes localized at different edges can also cross at other points in momentum space; the gap can not open here because the scattering between modes localized at different edges of the (bulk insulating) system is not possible.

The lattice version of the Rashba spin-orbit coupling term, which corresponds to a term $(\mathbf{s} \times \mathbf{p}) \cdot \mathbf{e}_z$, with $\mathbf{e}_z$ a unit vector along the $\mathbf{z}$ direction, reads

$$i\lambda_{\mathrm{R}} \sum_{\langle i\,,\,j \rangle} c_i^\dagger \left(\sigma_x d^y_{i,\,j} - \sigma_y d^x_{i,\,j} \right) c_j. \tag{1.93}$$

It arises when mirror symmetry about the two-dimensional lattice plane is broken and since it mixes the spin degree of freedom, the $\mathbb{Z}_2$ invariant can not be obtained as simply as we discussed in the previous paragraph. However, small values of λ_{R} (such that the band gap does not close) do not destroy the topological phase, as we can see from the phase diagram of the model Fig. 1.3. Starting in the topological phase at $\lambda_{\mathrm{R}} = 0$ and varying λ_{R}, the spin Hall conductivity σ^s_{xy} is not conserved (and not quantized) but the topological $\mathbb{Z}_2$ phase is

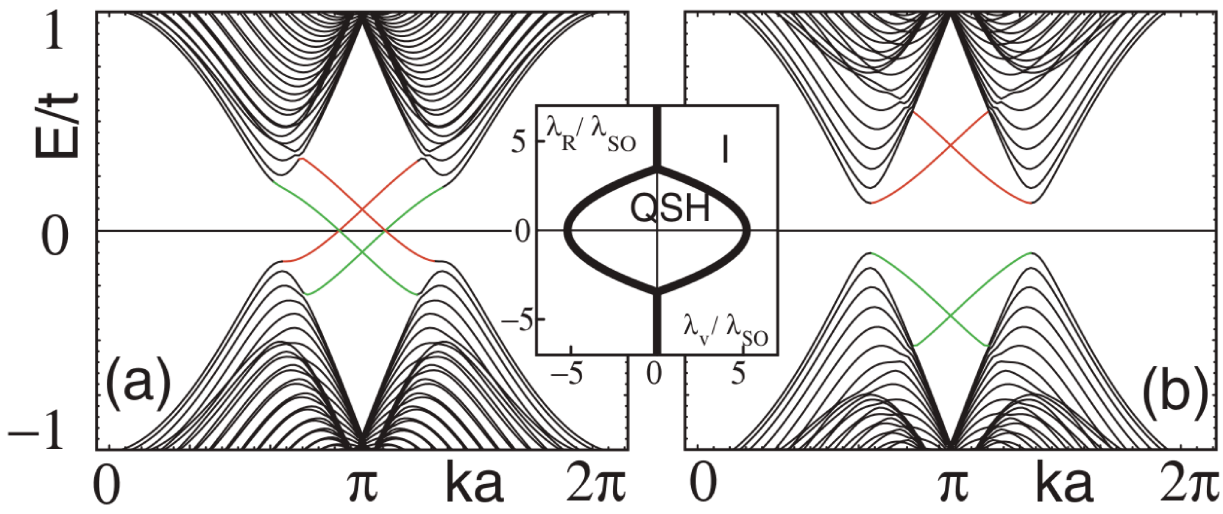

Figure 1.3: Energy spectrum in (a) the topological phase and (b) the trivial phase of the Kane and Mele model. The inset shows the phase diagram as a function of the amplitude of the Semenoff mass and of the Rashba spin-orbit amplitude, both in units of the amplitude of the intrinsic spin orbit coupling. This figure is taken from Ref. [144].

conserved as long as the gap does not get closed [11, 142–144]. In open geometries, at each edge of the system, in the topological phase, two edge modes (forming a Kramers' pair) are localized and they propagate along the edge in opposite direction but they can not be labelled by a spin quantum number. Again, as we explained in the last paragraph, the edge states are robust because of conserved time-reversal invariance which protects their crossing.

1.4.2 $\mathbb{Z}_2$ topological invariant

During a pumping protocol, the variation of the center of charge of the Wannier states associated with one isolated energy band is related the Chern number of the band (see Sec. 1.3.4). In a (topological) time-reversal invariant system, from Kramers' theorem, we know that the system is composed of a set of pairs of (time-reversed) energy bands. In momentum space, each energy band in a pair cross at the time-reversal symmetric points of the BZ, *i.e.* such that $\mathbf{k} = -\mathbf{k}$. The Chern number is defined for a set of well isolated energy bands only. In a time-reversal invariant system, the Chern numbers associated to each Kramers' pair are vanishing. This can be explained without calculation: if the Chern

number would be nonvanishing, it means that the system would present physical properties breaking time-reversal symmetry (*e.g.* chiral edge modes) which is in contradiction with the fact that we consider a time-reversal invariant system. Therefore the Chern number is necessarily vanishing and can not characterize the topology of a time-reversal invariant system.

In a time-reversal invariant system, Fu and Kane [48] showed that the variation of the center of charge of the Wannier states is related to the topological properties and can be used to build a topological invariant. To be more specific, here, what matters is the difference between the center of charge of the Wannier states associated to both states of a Kramers' pair. Let us review this in a formal way.

$\mathbb{Z}_2$ pumping protocol for time-reversal invariant systems We consider a one-dimensional time-reversal invariant system with associated Hamiltonian H, space coordinate x and momentum coordinate k_x. Moreover, we consider an isolated (Kramers') pair of energy bands, and we label each band by the indices I and II. We assume that there is no other degeneracy in the energy spectrum than those imposed by time-reversal invariance $\theta H \theta^{-1} = H$ (which appear at $k_x = \{0, \pi, -\pi\}$). The band I eigenstate $|u^{\mathrm{I}}_{-k_x}\rangle$ (at $-k_x$) is the time-reversal transform of the band II eigenstate $|u^{\mathrm{II}}_{k_x}\rangle$, up to a $U(1)$ phase factor:

$$|u^{\mathrm{I}}_{-k_x}\rangle = \mathrm{e}^{i\xi_{k_x}} \theta \, |u^{\mathrm{II}}_{k_x}\rangle \,, \tag{1.94}$$

with ξ_{k_x} a real number. $\theta^2 = -1$ gives

$$|u^{\mathrm{II}}_{-k_x}\rangle = -\mathrm{e}^{i\xi_{-k_x}} \theta \, |u^{\mathrm{I}}_{k_x}\rangle \,. \tag{1.95}$$

We introduce, by analogy with Sec. 1.3.4, the polarization associated to the band $s = \{\mathrm{I}, \mathrm{II}\}$ eigenstate [48]

$$P^s = \frac{1}{2\pi} \int_{-\pi}^{\pi} dk_x \, A^s(k_x), \tag{1.96}$$

with $A^s(k_x) = i \langle u^s_{k_x} | \partial_{k_x} | u^s_{k_x} \rangle$. We notice that $P^{\mathrm{I}} = P^{\mathrm{II}}$ modulo an integer. Indeed, using Eq. (1.94) and $\langle \theta u^{\mathrm{II}}_{k_x} | \partial_{k_x} | \theta u^{\mathrm{II}}_{k_x} \rangle = - \langle u^{\mathrm{II}}_{k_x} | \partial_{k_x} | u^{\mathrm{II}}_{k_x} \rangle$ we find

$$A^{\mathrm{I}}(-k_x) = -i \langle u^{\mathrm{I}}_{-k_x} | \partial_{k_x} | u^{\mathrm{I}}_{-k_x} \rangle = A^{\mathrm{II}}(k_x) + \partial_{k_x} \xi_{k_x}, \tag{1.97}$$

therefore

$$\begin{aligned} P^{\mathrm{I}} - P^{\mathrm{II}} &= \frac{1}{2\pi} \int_0^\pi dk_x \left[A^{\mathrm{I}}(k_x) + A^{\mathrm{I}}(-k_x) - A^{\mathrm{II}}(k_x) - A^{\mathrm{II}}(-k_x) \right] \\ &= \frac{1}{2\pi} \int_0^\pi dk_x \partial_{k_x} \left(\xi_{k_x} - \xi_{-k_x} \right) = \frac{1}{2\pi} \left(\xi_\pi - \xi_{-\pi} \right). \end{aligned} \tag{1.98}$$

$k_x = \pi$ and $k_x = -\pi$ being the same points of the Brillouin zone, and the kets $|u^{\mathrm{s}}_{k_x}\rangle$ being uniquely defined, we know that $\mathrm{e}^{i\xi_{-\pi}} = \mathrm{e}^{i\xi_\pi}$, which means that $(\xi_\pi - \xi_{-\pi})$ is equal to 2π times an integer. In other words, for a time-reversal invariant system, the Wannier state associated to the band s has the same center of charge (up to a lattice constant) than the Wannier state associated to the time-reversed partner of the band s. The value of $P^{\mathrm{I}} - P^{\mathrm{II}}$ is not a gauge invariant (*e.g.* consider a simple gauge transformation $|u^{\mathrm{s}}_{k_x}\rangle \to \mathrm{e}^{ik_x} |u^{\mathrm{s}}_{k_x}\rangle$). The complete set of Wannier functions associated to the band s states, $\{|w^{\mathrm{s}}_X\rangle\}$, is a set of functions which centers of charge run over all the lattice positions. The set of centers of charge associated to the set of Wannier functions $\{|w^{\mathrm{s}}_X\rangle\}$ is invariant under a gauge transformation because of the periodic boundary conditions. It is possible to choose the gauge such that $P^{\mathrm{I}} - P^{\mathrm{II}}$, the difference between the centers of charge of $|w^{\mathrm{I}}_0\rangle$ and $|w^{\mathrm{II}}_0\rangle$ (more generally it is the difference between the centers of charge of $|w^{\mathrm{I}}_X\rangle$ and $|w^{\mathrm{II}}_X\rangle$), is exactly vanishing (not up to an integer). With this in mind, let us now discuss a pumping protocol for the system; it will naturally lead us to define a topological invariant for a time-reversal invariant system.

As we did in Sec. 1.3.4, we consider an adiabatic evolution of H, from an initial time $t = 0$ to a final time $T/2$ (T is one period; $H(0) = H(T)$). We assume that the Bloch eigenvectors are defined continuously between 0 and $T/2$ for all value of k_x. We assume that H is time-reversal invariant at $t = 0$ and $T/2$ while it breaks time-reversal invariance for each time between $t = 0$ and $T/2$. At the time-reversal points $t = 0$ and $T/2$, we know that a pair of

Wannier states is localized over each lattice site, because of time-reversal symmetry. Let us assume that we choose the gauge as we discuss previously, such that $|w_X^{\mathrm{I}}\rangle$ and $|w_X^{\mathrm{II}}\rangle$ have the same center of charge X at time $t = 0$, *i.e.* $P^{\mathrm{I}}(0) - P^{\mathrm{II}}(0) = 0$. During the pumping protocol time-reversal symmetry is broken so the Wannier states are not required to be localized by pairs. At the end of the pumping protocol (at time $T/2$), both partners of a "Wannier pair" which had the same center of charge at $t = 0$ can:

(i) be associated with the same center of charge; in this case $|w_X^{\mathrm{I}}\rangle$ and $|w_X^{\mathrm{II}}\rangle$ keep the same center of charge X, or

(ii) be associated with the same center of charge up to one lattice constant; in this case $|w_X^{\mathrm{I}}\rangle$ has for instance center of charge $X - 1/2$ and $|w_X^{\mathrm{II}}\rangle$ has center of charge $X + 1/2$ and $|w_X^{\mathrm{I}}\rangle$ form a pair with $|w_{X-1}^{\mathrm{II}}\rangle$ and $|w_X^{\mathrm{II}}\rangle$ form a pair with $|w_{X+1}^{\mathrm{I}}\rangle$. We say that the Wannier states "switch partners" (see Fig. 1.4).

In both cases, the sum of the centers of charge is constant from $t = 0$ to $T/2$ because the total Chern number is vanishing.

If the one-dimensional system has open boundary conditions, at $T/2$ and at each end of the system, it appears one occupied Wannier state for a Wannier pair. Therefore each edge yields two degenerate states, and the ground state for a system with two edges (cylinder geometry) is composed of four degenerate states (see Fig. 1.5). This is unusual for noninteracting topological phases: threading half a flux in the system changes the degeneracy of the ground state (see [66]).

Let us define $P_\theta(t) = P^{\mathrm{I}}(t) - P^{\mathrm{II}}(t)$. We notice that, for the pumping protocol discussed in the previous paragraphs, the number Δ defined such that $\Delta = P_\theta(T/2) - P_\theta(0) \bmod 2$ is a gauge invariant because a gauge transformation would transform $P_\theta(T/2)$ and $P_\theta(0)$ equally (look at Eq. (1.98)). Both topologically distinct pumping processes that we referred as case (i) and (ii) are characterized by a different value of Δ. In the case (i) both partners of a "Wannier pair" keep the same center of charge therefore $\Delta = 0$ while in the case (ii), the

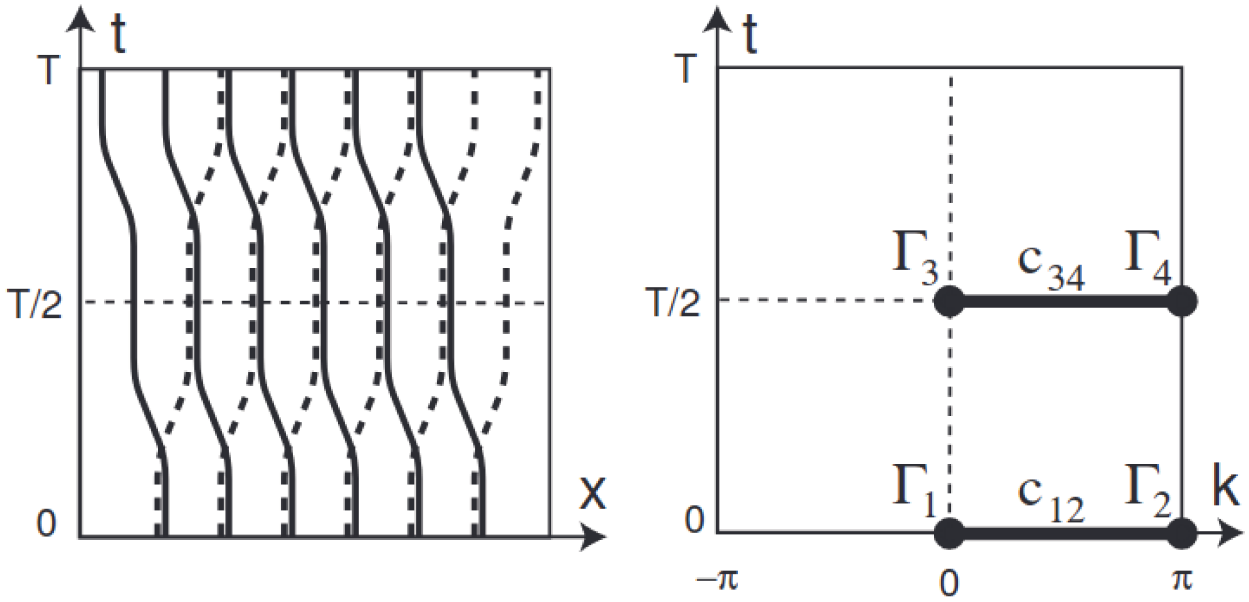

(a) (b)

Figure 1.4: Switching of the Wannier pairs centers during a pumping cycle of period T in a topological system. Fig. (a) shows how the positions of the Wannier centers move when performing a pumping cycle. $t = 0$, $t = T/2$ are both times for which the system is time-reversal invariant. Fig. (b) shows the two-dimentional space of the system; the Γ points are the time-reversal invariant points. This figure is taken from Ref. [48].

Wannier states "switch partners" so $\Delta = 1$. Δ defines a $\mathbb{Z}_2$ topological invariant.

Similarly to what we did in Sec. 1.3.4, for a two-dimensional real-space system, the variation of the time coordinate is replaced by the variation of the k_y momentum coordinate and the pumping protocol defines a topological invariant for a two-dimensional system. Note that this protocol involves only half of the BZ because $k_y = 0$ and $k_y = \pi$ are the time-reversal invariant points. This is consistent with the fact that the other half of the BZ encodes the same information because of time-reversal symmetry. In general, it is not an easy task to compute this $\mathbb{Z}_2$ invariant. In the rest of this section, following Ref. [48], we give a formulation of this invariant which appears under a $U(2)$ symmetric form and which explicitly shows its $\mathbb{Z}_2$ character.

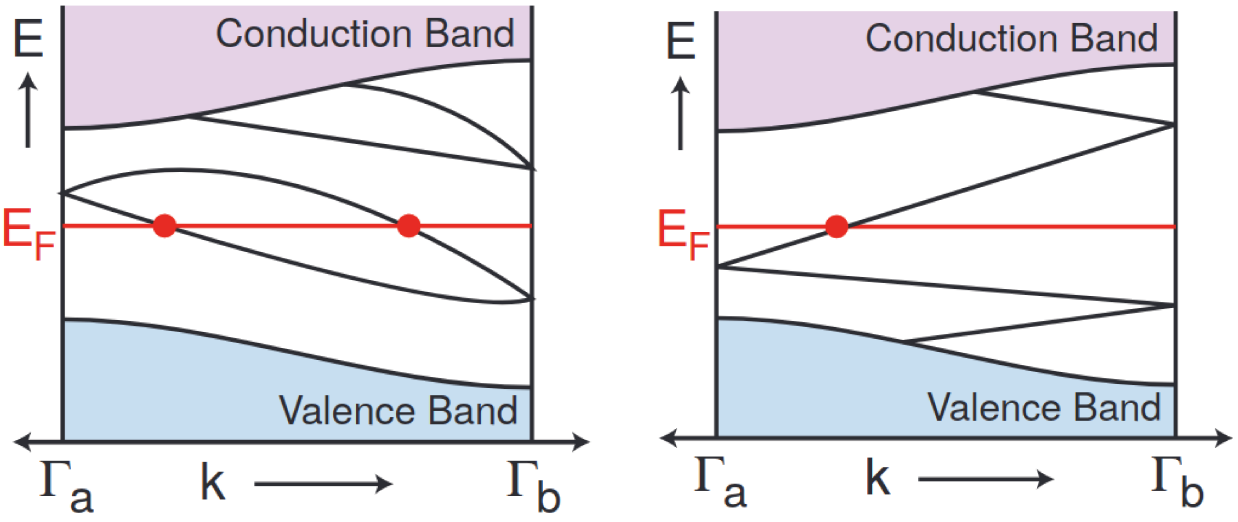

Figure 1.5: Dispersion relation for a cylinder geometry, between two time-reversal points in the BZ. The bulk bands and only the energy of the modes at one edge are sketched. Γ_a and Γ_b are inequivalent time-reversal invariant momenta corresponding respectively to what we call $t = 0$ and $t = T/2$ in the text. When going from one time-reversal invariant point to the other, either (a) the modes keep the same partner, the occupation does not change and the ground state degeneracy remains the same, or (b) the edge modes switch partners which results in a half-filled time-reversal pair at Γ_b and changes the ground state degeneracy. This figure is taken from Ref. [2].

Time-reversal polarization and $\mathbb{Z}_2$ invariant Under a $U(2)$ transformation $|u^s_{k_x}\rangle \to \sum_{s'} U_{s,s'} |u^{s'}_{k_x}\rangle$, with U a unitary matrix, the many-body wave function (which is the Slater determinant of the two states) is unchanged. In P^{I}'s (P^{II}'s) expression, as it is written in Eq. (1.96), only $|u^{\mathrm{I}}_{k_x}\rangle$ ($|u^{\mathrm{II}}_{k_x}\rangle$) is appearing so P^{I} (P^{II}) seems to break the $U(2)$ symmetry. Let us find an expression where P^s appears under a more $U(2)$ symmetric form. We have

$$P^{\mathrm{I}} = \frac{1}{2\pi} \int_0^\pi dk_x \, \left(A^{\mathrm{I}}(k_x) + A^I(-k_x) \right), \tag{1.99}$$

and using Eq. (1.94) and $\langle \theta u^{\mathrm{II}}_{k_x} | \, \partial_{k_x} \, | \theta u^{\mathrm{II}}_{k_x} \rangle = - \langle u^{\mathrm{II}}_{k_x} | \, \partial_{k_x} \, | u^{\mathrm{II}}_{k_x} \rangle$ we find

$$A^{\mathrm{I}}(-k_x) = -i \langle u^{\mathrm{I}}_{-k_x} | \, \partial_{k_x} \, | u^{\mathrm{I}}_{-k_x} \rangle = A^{\mathrm{II}}(k_x) + \partial_{k_x} \xi_{k_x}, \tag{1.100}$$

which leads to

$$P^{\mathrm{I}} = \frac{1}{2\pi} \left(\int_0^\pi dk_x \, A(k_x) + \xi_\pi - \xi_0 \right), \tag{1.101}$$

with $A(k_x) = A^{\rm I}(k_x) + A^{\rm II}(k_x)$. A very similar computation leads to

$$P^{\rm II} = \frac{1}{2\pi}\left(\int_{-\pi}^{0} dk_x\, A(k_x) - \xi_\pi + \xi_0\right), \tag{1.102}$$

Let us write $\xi_\pi - \xi_0$ as the Pfaffian of a unitary matrix $w(k_x)$. This is important to get an expression explicitly independent of the representation given by Eq. (1.94) and to show that $P^{\rm I}$ does not break the $U(2)$ symmetry. The components of $w(k_x)$ are the projections of the time-reversed partner of an eigenstate at k_x over an eigenstate at $-k_x$:

$$w_{s,{\rm s'}}(k_x) = \langle u^{s}_{-k_x} | \theta u^{\rm s'}_{k_x} \rangle\,. \tag{1.103}$$

At the time-reversal points $k_x = 0$ and $k_x = \pi$, $w(k_x)$ is antisymmetric. Indeed, using $k_x = -k_x$ for time-reversal invariant points, writing $\theta = MK$, with M a unitary matrix, K the complex conjugation operator, and using $M = -M^T$, we find

$$w_{s,{\rm s'}}(k_x) = \sum_{m,n} \left(u^{s}_{k_x}\right)^*_m M_{m,n} \left(u^{\rm s'}_{k_x}\right)^*_n = -\sum_{m,n} \left(u^{\rm s'}_{k_x}\right)^*_n M_{n,m} \left(u^{s}_{k_x}\right)^*_m = -w_{{\rm s'},s}(k_x). \tag{1.104}$$

Here we explicitly have

$$w_{s,{\rm s'}}(k_x) = \begin{pmatrix} 0 & {\rm e}^{-i\xi_{k_x}} \\ -{\rm e}^{-i\xi_{-k_x}} & 0 \end{pmatrix}, \tag{1.105}$$

For a two-dimensional matrix, the Pfaffian is the off-diagonal component: ${\rm Pf}\,[w(k_x)] = {\rm e}^{-i\xi_{k_x}}$. This gives

$$\xi_\pi - \xi_0 = i \log\left[\frac{{\rm Pf}\,[w(\pi)]}{{\rm Pf}\,[w(0)]}\right], \tag{1.106}$$

from which we write

$$P^{\rm I} - P^{\rm II} = \frac{1}{2\pi}\left(\int_0^{\pi} dk_x\, A(k_x) - \int_{-\pi}^{0} dk_x\, A(k_x) + 2i \log\left[\frac{{\rm Pf}\,[w(\pi)]}{{\rm Pf}\,[w(0)]}\right]\right). \tag{1.107}$$

From the explicit form of $w(k_x)$ Eq. (1.105), we can show that

$$P^{\rm I} - P^{\rm II} = \frac{1}{2i\pi}\left(\int_0^{\pi} dk_x\, {\rm Tr}\left[w^\dagger \partial_{k_x} w\right] + 2 \log\left[\frac{{\rm Pf}\,[w(\pi)]}{{\rm Pf}\,[w(0)]}\right]\right), \tag{1.108}$$

and

$$P^{\mathrm{I}} - P^{\mathrm{II}} = \frac{1}{2i\pi}\left(\int_0^\pi dk_x\, \partial_{k_x} \log\det\left[w(k_x)\right] + 2\log\left[\frac{\mathrm{Pf}\left[w(\pi)\right]}{\mathrm{Pf}\left[w(0)\right]}\right]\right). \tag{1.109a}$$

$$P^{\mathrm{I}} - P^{\mathrm{II}} = \frac{1}{2i\pi}\left(2\log\left[\frac{\sqrt{\det\left[w(\pi)\right]}}{\sqrt{\det\left[w(0)\right]}}\frac{\mathrm{Pf}\left[w(\pi)\right]}{\mathrm{Pf}\left[w(0)\right]}\right]\right). \tag{1.109b}$$

Let us here write $\sqrt{\det\left[w(\pi)\right]} = \mathrm{e}^{i\chi}$, $\chi \in]-\pi, \pi]$, such that its logarithm is on the principal branch and remind that $\det\left[w(\pi)\right] = \mathrm{Pf}\left[w(\pi)\right]^2$ which imposes that $\mathrm{Pf}\left[w(\pi)\right] = \mathrm{e}^{i(\chi+z\pi)}$, with z an integer. Each integer z mod 2 is equivalent because $\mathrm{e}^{i2n\pi} = 1$ with n an integer. If z is odd or even, $\mathrm{Pf}\left[w(\pi)\right]$ is respectively opposite or equal to $\sqrt{\det\left[w(\pi)\right]}$. Then we get

$$P^{\mathrm{I}} - P^{\mathrm{II}} = z \bmod 2, \tag{1.110}$$

which shows that $P^{\mathrm{I}} - P^{\mathrm{II}}$ is an integer defined modulo 2. This lead to the following definition for Δ:

$$(-1)^{\Delta} = \prod_{i=1}^{4} \frac{\sqrt{\det\left[w(\mathbf{\Gamma}_i)\right]}}{\mathrm{Pf}\left[w(\mathbf{\Gamma}_i)\right]}. \tag{1.111}$$

We understand that Δ is also an integer defined modulo 2 and since it is gauge invariant it is the $\mathbb{Z}_2$ topological invariant which characterizes the topological properties of the system. When using this formula it is essential that the wave functions evolve continuously during the pumping protocol (if we study a two-dimensional system, the wave functions must evolve continuously on the BZ), because it is essential for the pumping protocol that only one gauge choice is used. The same results can be found if we would have considered several Kramers' pairs (see Ref. [48]). We notice that if the system has extra-symmetries, the computation of ν may be simplified (see Chapter 3) and we also notice that several other formulations of this invariant has been proposed [144–148].

In the next chapter, we show explicit computations of the $\mathbb{Z}_2$ invariant for the Haldane model and for the simple kagome model studied in Sec. 3.1. This makes the connection between the general theory we introduced in this section and practical implementations of the $\mathbb{Z}_2$ invariant computation that we developed and which we use in Chapters 4 and 5.

1.5 Conclusion

In this chapter, we have introduced the general formalism we use throughout this manuscript. We have reviewed the important discoveries and concepts in topology in condensed matter which are relevant for the studies we present in the following.

The Berry phase is one of the most important concept in this regard and its connection with the integer quantum Hall effect, the Chern number and the properties of Chern insulators have been explained. We have tried to make clear the connection between topological invariant and physical observables. This concepts are widely used in this manuscript, either for the study of Chern insulators (see Chapters 2, 3 and 4), or for the understanding of time-reversal invariant topological insulators (Chapters 3 and 5). We also have reviewed two tight-binding models on the honeycomb and on the kagome lattice. These are the elementary building blocks of the models we study in the following.

Finally, we have reviewed the topological band theory describing time-reversal invariant topological systems and the associated topological $\mathbb{Z}_2$ invariant. This is particularly relevant for Chapter 5 where we study such systems. We have emphasized on the particularly important role of the spin-orbit coupling; its description and its relation with topology is also useful for the chapter 4.

Chapter 2

Haldane light system and local probe of the Chern number

In this chapter, we review the Haldane model [5], we develop a computation of the associated bands' Chern number and we propose a protocol to probe the Haldane topological phase diagram in a photonic system. An article related to the work presented in this chapter, whose authors are J.L. and Karyn Le Hur, is currently in preparation.

The Haldane model (1988) is a topological model for a Chern insulator without Landau levels on the honeycomb lattice [5]. It is characterized by a local magnetic flux density which respects the spatial translational symmetry of the lattice but breaks time-reversal symmetry. The total flux in the unit cell is vanishing. This is in contrast with the quantum Hall phase [6] (see Sec.1.1.3) which implies non-vanishing flux in the unit cell (because of the uniform external magnetic field). It was the first theoretical model predicting the quantum anomalous Hall effect. A quantum anomalous Hall phase is a phase characterized by non-vanishing Chern number in a system with vanishing total flux in the unit cell. Some of the topological properties associated to such a phase were described in Sec. 1.3.2 of Chapter 1. The Haldane model has had a huge impact in topology in condensed matter, and it led, a bit more than fifteen years later, to the birth of topological band theory. The kagome systems we study in Chapters 3, 5 and 4 are deeply related to the Haldane model.

The Haldane model has been realized in solid-state systems, in cold atom gases and in

photonic systems (coupled waveguides) [112, 149, 150]. One very convenient way to realize this model for artificial systems is to use Floquet engineering [149–154].

The most common way to probe the topological properties of a Chern insulator, in condensed matter systems, is to determine the Hall conductance from transport measurements [6, 155]. The topological properties of artificial systems have been measured in many different ways [15–18]. In cold atom gases, the measurement of the topological properties has been realized for instance, via transport measurements (measurement of the Hall drift) [150, 156], using interferometry [157–159], relying on the observation of chiral edge states [160, 161] or via a measurement of the Berry curvature [162]. Let us also mention that, for condensed matter systems and cold atom gases, it has been shown that the response to a circular drive on the system also enables to probe the topology [163–169]. In photonics systems several ways to measure the topological properties have also been studied. These systems gather for instance gyromagnetic photonic crystal [170–173], arrays of coupled waveguides [149, 174, 175] optomechanical systems [176, 177] and cavity and circuit quantum electrodynamics (cQED) [33, 178–182]. These artificial systems enable to build artificial fields [17, 183].

We are here interested in a Haldane boson model in cQED systems [18, 180, 181]. Several cQED systems have been realized and in some cases the topological properties have been measured [33, 178, 179]. An example of cQED system leading to an effective photon kagome lattice Hamiltonian was proposed in Ref. [33]. In this system the microwave resonators (which are series of LC circuits) are arranged in a honeycomb array and coupled together via Josephson ring circulators.

In Ref. [30], a protocol to probe the topological properties of a one-dimensional LC circuit system is proposed. In this work, the authors considered a transmission line (capacitively) coupled to a single cell in the chain. They showed how one can rebuild the Zak phase (which is the topological invariant characterizing the one-dimensional system the authors studied) from the reflection coefficient. In this chapter, we consider a local light probe with capacitive

coupling to a Haldane boson model in cQED. We show one can measure the Chern number from the reflection coefficient at specific energy points.

This chapter is organized as follows. In Sec. 2.1, we review the Haldane model for a boson system. First, we explain that the Haldane model is a valid simple choice for a honeycomb tight-binding model which breaks time-reversal symmetry and which have vanishing total flux in the unit cell. We write the associated Hamiltonian and we give its momentum-space representation, along with some important remarks on the energy dispersion relation.

In Sec. 2.2, we perform an explicit analytical computation of the bands' Chern numbers for the Haldane model, starting from Eq. (1.79) of Chapter 1. We explicitly show how the sign of the "mass function" determines both band's Chern numbers. Such a computation does not appear explicitly in the literature, to the best of our knowledge. Both first sections, Sec. 2.1 and Sec. 2.2, are written for a boson system to avoid introducing other definitions in Sec. 2.3, however the results obtained in both first sections do not depend on the statistics.

In Sec. 2.3, we consider a local capacitive probe on the lattice and the reflection coefficient which relates an input voltage and an output voltage in this probe. We show that the sign of the "bulk gap function" is encoded in this reflection coefficient at the energy of the Dirac point at which the band gap is the narrowest. In the system we consider, which is made of resonators of frequency amplitude in the GHz range, the sign of the "bulk gap function" is measurable via microwave light.

2.1 Haldane model

In this section, we introduce the Haldane model for a light system. First, we explain that, for a honeycomb tight-binding model which breaks time-reversal symmetry and which have vanishing total flux in the unit cell, a valid simple choice contains real nearest neighbor hopping terms and complex next-nearest neighbor hopping terms. Then we write the Haldane Hamiltonian and introduce the notations which we use in this chapter.

2.1.1 Breaking time-reversal symmetry while having a vanishing total flux in the unit cell

As explained in Sec. 1.2.4 of Chapter 1, breaking time-reversal symmetry is necessary to open a gap in the system and therefore to possibly obtain topological energy bands. A non-vanishing local magnetic flux density $\mathbf{B}(\mathbf{r})$ with vanishing total flux in the unit cell [5] breaks time-reversal invariance, because the time reversal operator send $\mathbf{B}(\mathbf{r})$ to its opposite. We can impose that $\mathbf{B}(\mathbf{r})$ respects the symmetries of the lattice. Then, the vector potential $\mathbf{A}(\mathbf{r})$ which derives from $\mathbf{B}(\mathbf{r})$ can be chosen to have the same periodicity than the lattice.

The honeycomb lattice is such if the magnetic flux is vanishing in a unit cell, it is vanishing in an hexagon (see Fig. 2.2(b)). Moreover, all the nearest-neighbor closed paths in the lattice are made of an integer number of hexagons and therefore are associated to zero magnetic flux. Therefore the nearest neighbor hopping terms (deriving from the $\mathbf{B}(\mathbf{r})$ field that respects the symmetries of the lattice) shall not give rise to a topologically non-trivial lattice model. Another way to reach this conclusion is to notice that all the valid choices of nearest neighbor hopping terms are equivalent, up to a local U(1) gauge transformation, to the "bare" choice where all the nearest neighbor hopping terms are real. The latter is associated to a topologically trivial lattice model so we deduce that it is the same for all the valid choices of nearest neighbor hopping terms.

The smallest area enclosed by the next-nearest neighbors is smaller than the area of a unit cell. Therefore it is possible to choose $\mathbf{B}(\mathbf{r})$ such that a closed path along the next-nearest neighbors encircle a region threaded by a non-vanishing flux while the total flux in the unit cell is vanishing (see Fig. 2.2(b)). Then the next nearest neighbor terms, associated to complex amplitudes, break the time-reversal symmetry and may yield a topological system. In both next subsections, we review the lattice Hamiltonian of the Haldane model and investigate the associated dispersion relation. The computation of the topological invariant for the bulk bands in performed in Sec. 2.2.

2.1.2 Haldane Hamiltonian for a photonic system

We consider a circuit quantum electrodynamic (cQED) system made of an array of resonators coupled together in such a way that the system is described by an effective photon lattice Haldane Hamiltonian H. Such a photonic system is permanently driven to compensate for the photon decay processes that necessarily happen [18]. A photonic system has positive energy eigenvalues; usually, in such a system, the on-site energies are large (denoted $\hbar\Omega_0$ here, usually $\sim$ GHz order of magnitude) compared to the hopping amplitudes on the effective lattice (*e.g.* can be $\sim$ 10 MHz to $\sim$ 100 MHz) [33, 184, 185]. The effective photon lattice Haldane Hamiltonian H reads

$$H = t_1 \sum_{\substack{\langle i\,,j\rangle \\ \alpha\neq\beta}} c^\dagger_{i,\alpha} c_{j,\beta} + t_2 \sum_{\substack{\langle\langle i\,,j\rangle\rangle \\ \alpha}} \mathrm{e}^{i\nu_{i\,j}\phi} c^\dagger_{i,\alpha} c_{j,\alpha} + \sum_i \left(\hbar\Omega_0 + \xi_\alpha M\right) c^\dagger_{i,\alpha} c_{i,\alpha}, \tag{2.1}$$

where $c^\dagger_{i,\alpha}$ is the creation operator for a color-α boson at site i. $t_1 \in \mathbb{R}$, $t_2 \in \mathbb{R}$ and the associated sums respectively runs over all the nearest neighbors (therefore α and β are different colors) and all the next-nearest neighbors i and j with color $\alpha = \{A, B\}$. $\phi \in \mathbb{R}$ and $\nu_{i\,j} = +1\,(-1)$ if the associated $c^\dagger_{i,\alpha} c_{j,\alpha}$ term displaces a particle clockwise (counter-clockwise) along the triangle made by the α-color sites in the concerned hexagon of the lattice (see Fig. 2.2(a)). $M \in \mathbb{R}$, $\xi_A = +1$ and $\xi_B = -1$ and the associated sum runs over all sites of the lattice. This term is a color-alternate mass term first studied by Semenoff who also considered the real nearest neighbors terms in the honeycomb lattice [186]. Varying the amplitude M, we show in Sec. 2.2 that the Semenoff term enables to study the transition from a trivial insulator to a Chern insulator (topological phase with finite Chern number). $\hbar\Omega_0$ is chosen such that all the energies associated to H are positive. In Ref. [5], Haldane considered fermions and no $\hbar\Omega_0$ term; in fact the first part of this chapter (Secs. 2.1 and 2.2) does not depend on the statistics and the term $\hbar\Omega_0$ has almost no effect (just a shift of the Fermi energy) but we already specify the statistics and consider the term $\hbar\Omega_0$ so that we do not have to change notations.

2.1.3 Momentum space and dispersion relation

A Fourier transformation gives a formulation of H in momentum space

$$H = \sum_{\mathbf{k}} \Psi_{\mathbf{k}}^{\dagger} h_{\mathbf{k}} \Psi_{\mathbf{k}}, \tag{2.2a}$$

$$h_{\mathbf{k}} = \hbar\Omega_0 \mathbb{I} + 2t_2 \cos\phi \left[\sum_{i=1}^{3} \cos(\mathbf{k}\cdot\mathbf{b}_i)\right] \mathbb{I} + t_1 \sum_{i=1}^{3} [\cos(\mathbf{k}\cdot\mathbf{a}_i)\sigma_x + \sin(\mathbf{k}\cdot\mathbf{a}_i)\sigma_y] + \left[M - 2t_2 \sin\phi \sum_{i=1}^{3} \sin(\mathbf{k}\cdot\mathbf{b}_i)\right] \sigma_z, \tag{2.2b}$$

with $\Psi_{\mathbf{k}}^{\dagger} = \left(c_{\mathbf{k},A}^{\dagger}, c_{\mathbf{k},B}^{\dagger}\right)$, defined in Sec. 1.2.4 and $\mathbf{a}_i$, $i \in \{1,2,3\}$ and $\mathbf{b}_i$, $i \in \{1,2,3\}$ defined in Fig. 2.2. We remind that the three Pauli matrices $\sigma^x, \sigma^y, \sigma^z$ act in sub-lattice space. We notice that the σ_z term of equation (2.2b) opens a gap and the t_2 term breaks time reversal symmetry.

The Haldane model is characterized by two energy bands in momentum space $E_{1,\mathbf{k}}$ and $E_{2,\mathbf{k}}$ given by

$$E_{1,\mathbf{k}} = h_0(\mathbf{k}) - \sqrt{|h_1(\mathbf{k})|^2 + h_2(\mathbf{k})^2}, \qquad \text{and} \qquad E_{2,\mathbf{k}} = h_0(\mathbf{k}) + \sqrt{|h_1(\mathbf{k})|^2 + h_2(\mathbf{k})^2}, \tag{2.3}$$

with

$$h_0(\mathbf{k}) = \hbar\Omega_0 + 2t_2 \cos\phi \sum_{i=1}^{3} \cos(\mathbf{k}\cdot\mathbf{b}_i), \tag{2.4a}$$

$$h_2(\mathbf{k}) = M - 2t_2 \sin\phi \sum_{i=1}^{3} \sin(\mathbf{k}\cdot\mathbf{b}_i), \tag{2.4b}$$

$$h_1(\mathbf{k}) = t_1 \sum_{i=1}^{3} \exp(-i\mathbf{k}\cdot\mathbf{a}_i). \tag{2.4c}$$

From Eqs. (2.3), we see that a band crossing appears at $h_1(\mathbf{k}) = h_2(\mathbf{k}) = 0$. $h_1(\mathbf{k}) = 0$ is reached at both inequivalent points $\mathbf{K} = \dfrac{\mathbf{g}_3 - \mathbf{g}_2}{3}$ and $\mathbf{K}' = \dfrac{\mathbf{g}_2 - \mathbf{g}_3}{3}$ in the Brillouin zone (see Fig. 2.3(a)), with $\mathbf{g}_2$ and $\mathbf{g}_3$ defined by $-\mathbf{g}_2\cdot\mathbf{b}_2 = 2\pi$, $\mathbf{g}_2\cdot\mathbf{b}_3 = 0$, $\mathbf{g}_3\cdot\mathbf{b}_2 = 0$, and $\mathbf{g}_3\cdot\mathbf{b}_3 = 2\pi$. Moreover, we have $h_2(\mathbf{K}) = 0$ if $M = +3\sqrt{3}t_2\sin\phi$ and $h_2(\mathbf{K}') = 0$ if $M = -3\sqrt{3}t_2\sin\phi$. When the bands cross, the dispersion relation around $\mathbf{K}$ and $\mathbf{K}'$ is linear. The $\mathbf{K}$ and $\mathbf{K}'$ are called the Dirac points. The energies for several values of M are represented in Fig. 2.1.

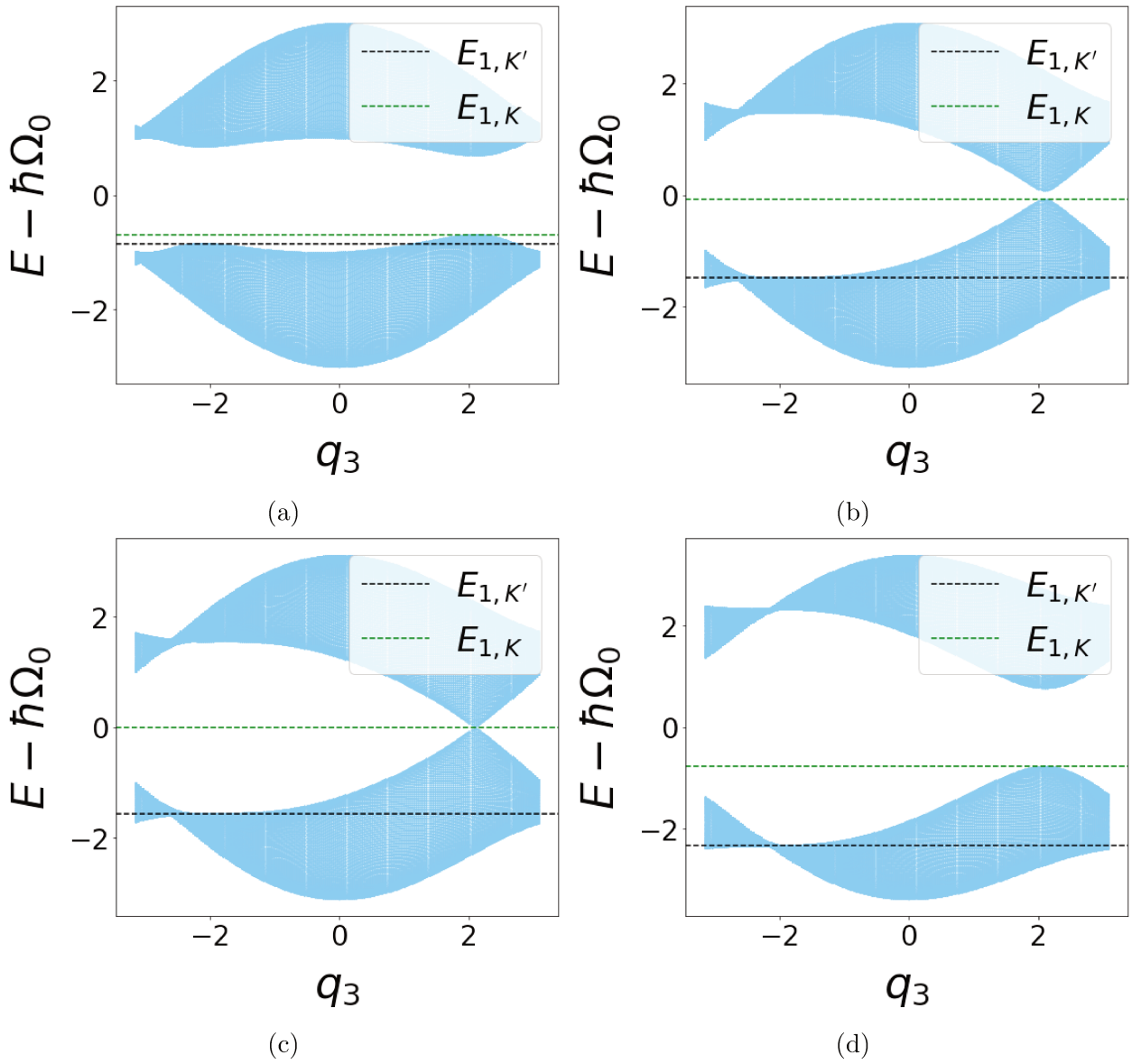

Figure 2.1: Energies of the Haldane model as a function of $q_3 = a\mathbf{k} \cdot \mathbf{g}_3$, with a the lattice spacing. The energies are expressed in units of t_1. The values of the lowest band energy at both Dirac points, $E_{1,\mathbf{K}}$ and $E_{1,\mathbf{K}'}$, are shown. The parameters considered are $\phi = \pi/2$, $t_2 = 0.15t_1$ and (a) $M = 0.1 \times 3\sqrt{3}t_2$, (b) $M = 0.9 \times 3\sqrt{3}t_2$, (c) $M = 3\sqrt{3}t_2$ and (d) $M = 2 \times 3\sqrt{3}t_2$.

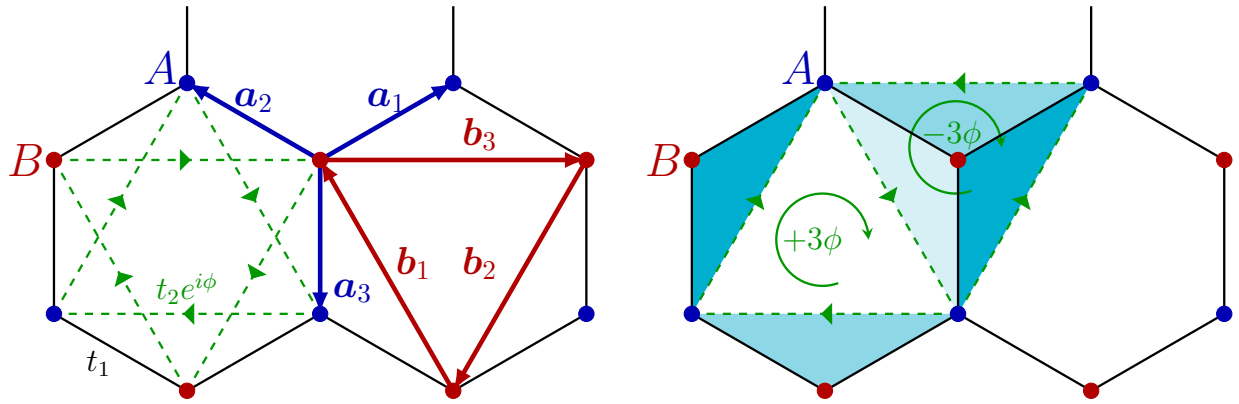

(a) (b)

Figure 2.2: (a) Honeycomb lattice representation and definition of the sub-lattices A and B, of the nearest neighbors and next-nearest neighbors hopping amplitudes and of the displacement vectors $\mathbf{a}_i$, $i \in \{1,2,3\}$ and $\mathbf{b}_i$, $i \in \{1,2,3\}$. (b) Magnetic fluxes in the unit cell, which contains one "up" triangle (associated to a flux $+3\phi$ and delimited here by a green dashed line with arrow) and one "down" triangle (associated to a flux -3ϕ and delimited here by a green dashed line with arrow). The regions shaded with the same color are equivalent up to a lattice translation and are threaded by the same magnetic flux. This shows that the magnetic flux in an hexagon is vanishing.

2.2 Smooth Berry gauge fields and topological properties of the Haldane model

In this section, using Eq. (1.79) of Chapter 1, we show an analytical computation of the bands' Chern numbers for the Haldane model introduced in Sec. 2.1. We identify how the change of sign of the function h_2 (see Eq. (2.4)) at the Dirac points results in the variation of the topological properties of the model. In Sec. 2.3, we show that this can be measured via a local capacitive probe on the lattice.

2.2.1 Hamiltonian and eigenvectors

In Sec. 1.2.2 of Chapter 1, we reminded that the real-space periodic part of the Bloch eigenvector satisfy

$$\mathrm{e}^{-i\mathbf{k}\cdot\hat{\mathbf{r}}}\hat{H}\mathrm{e}^{i\mathbf{k}\cdot\hat{\mathbf{r}}}\left|u_{n,\mathbf{k}}\right\rangle = E_{n,\mathbf{k}}\left|u_{n,\mathbf{k}}\right\rangle, \tag{2.5}$$

i.e. the kets $|u_{n,\mathbf{k}}\rangle$'s are the eigenvectors of

$$\mathrm{e}^{-i\mathbf{k}\cdot\hat{\mathbf{r}}} H \mathrm{e}^{i\mathbf{k}\cdot\hat{\mathbf{r}}} = \sum_{\mathbf{k}} \Psi_{\mathbf{k}}^{\dagger} \tilde{h}_{\mathbf{k}} \Psi_{\mathbf{k}}, \tag{2.6}$$

with

$$\tilde{h}_{\mathbf{k}} = t_1 \left[1 + \cos(\mathbf{k}\cdot\mathbf{b}_1) + \cos(\mathbf{k}\cdot\mathbf{b}_2)\right] \sigma^x + t_1 \left[\sin(\mathbf{k}\cdot\mathbf{b}_1) - \sin(\mathbf{k}\cdot\mathbf{b}_2)\right] \sigma^y, \tag{2.7}$$

which we also write

$$\mathrm{e}^{-i\mathbf{k}\cdot\hat{\mathbf{r}}} H \mathrm{e}^{i\mathbf{k}\cdot\hat{\mathbf{r}}} = \sum_{\mathbf{k}} \tilde{\Psi}_{\mathbf{k}}^{\dagger} h_{\mathbf{k}} \tilde{\Psi}_{\mathbf{k}}, \tag{2.8}$$

with $\tilde{\Psi}_{\mathbf{k}}^{\dagger} = \left(c_{\mathbf{k},A}^{\dagger}, \mathrm{e}^{i\mathbf{k}\cdot\mathbf{a}_3} c_{\mathbf{k},B}^{\dagger}\right)$. In other words, $|u_{i,\mathbf{k}}\rangle$, $i = \{1, 2\}$ is the eigenvector of $h_{\mathbf{k}}$ in the basis $\left(c_{A,\mathbf{k}}^{\dagger}, \mathrm{e}^{i\mathbf{k}\cdot\mathbf{a}_3} c_{B,\mathbf{k}}^{\dagger}\right)$. Let us define the coefficients $a_i(\mathbf{k})$ and $\tilde{b}_i(\mathbf{k})$ such that

$$|u_{i,\mathbf{k}}\rangle = \left(a_i(\mathbf{k}) c_{A,\mathbf{k}}^{\dagger} + \tilde{b}_i(\mathbf{k}) \mathrm{e}^{i\mathbf{k}\cdot\mathbf{a}_3} c_{B,\mathbf{k}}^{\dagger}\right) |0\rangle \ , \tag{2.9}$$

with

$$|a_i(\mathbf{k})|^2 + \left|\tilde{b}_i(\mathbf{k})\right|^2 = 1. \tag{2.10}$$

From the relation $h_{\mathbf{k}} |u_{i,\mathbf{k}}\rangle = E_i |u_{i,\mathbf{k}}\rangle$, we get

$$\tilde{b}_i(\mathbf{k}) = \frac{h_1(\mathbf{k})^*}{h_2(\mathbf{k}) - h_0(\mathbf{k}) + E_{i,\mathbf{k}}} a_i(\mathbf{k}), \tag{2.11}$$

with h_0, h_1 and h_1 defined in Sec. 2.1.3. It is useful to define $b_i(\mathbf{k}) = \tilde{b}_i(\mathbf{k}) \mathrm{e}^{i\mathbf{k}\cdot\mathbf{a}_3}$, so that $a_i(\mathbf{k})$ and $b_i(\mathbf{k})$ are the components of the eigenvectors in the basis $\left(c_{A,\mathbf{k}}^{\dagger}, c_{B,\mathbf{k}}^{\dagger}\right)$,

$$|u_{i,\mathbf{k}}\rangle = \left(a_i(\mathbf{k}) c_{A,\mathbf{k}}^{\dagger} + b_i(\mathbf{k}) c_{B,\mathbf{k}}^{\dagger}\right) |0\rangle \ , \tag{2.12}$$

with

$$|a_i(\mathbf{k})|^2 + |b_i(\mathbf{k})|^2 = 1, \tag{2.13}$$

and the relation between the components of the eigenvectors reads

$$b_i(\mathbf{k}) = \frac{\mathrm{e}^{i\mathbf{k}\cdot\mathbf{a}_3} h_1(\mathbf{k})^*}{h_2(\mathbf{k}) - h_0(\mathbf{k}) + E_{i,\mathbf{k}}} a_i(\mathbf{k}). \tag{2.14}$$

2.2.2 Gauge choices, unique and smooth Berry gauge fields

Let us describe two gauge choices G_I and G_{II} for the eigenvectors that we respectively write $|u_{i,\mathbf{k},I}\rangle$ and $|u_{i,\mathbf{k},II}\rangle$. Then we show how these choices enable to define the Bloch eigenvectors so that we can compute the bands' Chern numbers using Eq. (1.79) from Sec. 1.3.2 of Chapter 1.

Gauge choices We define both following gauge choices:

(i) *Gauge choice G_I*: the coefficient $a_i(\mathbf{k})$ is real. More precisely, we choose

$$a_i(\mathbf{k}) = \rho_i(\mathbf{k})\,, \tag{2.15}$$

with

$$\rho_i(\mathbf{k}) = \frac{h_2(\mathbf{k}) - h_0(\mathbf{k}) + E_{i,\mathbf{k}}}{R_i(\mathbf{k})}, \tag{2.16}$$

and $R_i(\mathbf{k}) = \left[2\left(h_2(\mathbf{k})^2 + |h_1(\mathbf{k})|^2 + (-1)^i h_2(\mathbf{k})\sqrt{|h_1(\mathbf{k})|^2 + h_2(\mathbf{k})^2}\right)\right]^{1/2}$, and we have

$$b_i(\mathbf{k}) = \lambda_i(\mathbf{k})\mathrm{e}^{-i\varphi(\mathbf{k})}\,, \tag{2.17}$$

with

$$\lambda_i(\mathbf{k}) = \frac{|h_1(\mathbf{k})|}{R_i(\mathbf{k})} \quad \text{and} \quad \mathrm{e}^{-i\varphi(\mathbf{k})} = \frac{\mathrm{e}^{i\mathbf{k}\cdot\mathbf{a}_3} h_1(\mathbf{k})^*}{|h_1(\mathbf{k})|}. \tag{2.18}$$

(ii) *Gauge choice G_{II}*: the coefficient $b_i(\mathbf{k})$ is real. We choose

$$b_i(\mathbf{k}) = \lambda_i(\mathbf{k}), \tag{2.19}$$

and we have

$$a_i(\mathbf{k}) = \rho_i(\mathbf{k})\mathrm{e}^{i\varphi(\mathbf{k})}. \tag{2.20}$$

Let us notice that $h_1(\mathbf{k})$ is vanishing only at the Dirac points $\mathbf{K}$ and $\mathbf{K}'$ and that we have $h_2(\mathbf{k}) - h_0(\mathbf{k}) + E_{i,\mathbf{k}} = h_2(\mathbf{k}) + (-1)^i\sqrt{|h_1(\mathbf{k})|^2 + h_2(\mathbf{k})^2}$. From this, we see that $h_2(\mathbf{k}) - h_0(\mathbf{k}) + E_{i,\mathbf{k}}$ (and therefore R) may be vanishing only at the Dirac points $\mathbf{K}$ and $\mathbf{K}'$. We

$\lvert M\rvert$	$< 3\sqrt{3}t_2\lvert\sin\phi\rvert$	$> 3\sqrt{3}t_2\lvert\sin\phi\rvert$
$\mathrm{sgn}(h_2(\mathbf{K}))$	$\mathrm{sgn}(\sin\phi)$	$\mathrm{sgn}(M)$
$\mathrm{sgn}(h_2(\mathbf{K}'))$	$-\mathrm{sgn}(\sin\phi)$	$\mathrm{sgn}(M)$

Table 2.1: Table giving the sign of $h_2(\mathbf{K})$ and $h_2(\mathbf{K}')$ as a function of M and $\mathrm{sgn}(\sin\phi)$.

$(-1)^i\,\mathrm{sgn}(\sin\phi)$	$\lim_{\mathbf{k}\to\mathbf{K}}[\rho_i(\mathbf{k})]$	$\lim_{\mathbf{k}\to\mathbf{K}'}[\rho_i(\mathbf{k})]$	$\lim_{\mathbf{k}\to\mathbf{K}}[\lambda_i(\mathbf{k})]$	$\lim_{\mathbf{k}\to\mathbf{K}'}[\lambda_i(\mathbf{k})]$
$+1$	0	$\mathrm{sgn}(\sin\phi)$	1	0
-1	$-\mathrm{sgn}(\sin\phi)$	0	0	1

Table 2.2: Table giving the values of of $\rho_i(\mathbf{k})$ and $\lambda_i(\mathbf{k})$ at the Dirac points in the case $\lvert M\rvert< 3\sqrt{3}t_2\lvert\sin\phi\rvert$, as a function of the sign of the Semenoff mass M and of the index of the energy band i.

have

$$\lim_{h_1\to 0}\left(h_2(\mathbf{k})-h_0(\mathbf{k})+E_{i,\mathbf{k}}\right)=\lim_{h_1\to 0}\left(|h_2|\big(\mathrm{sgn}\,(h_2)+(-1)^i\big)+(-1)^i\frac{|h_1|^2}{|h_2|}\right), \tag{2.21a}$$

$$\lim_{h_1\to 0} R=\lim_{h_1\to 0}\left[2h_2(\mathbf{k})^2\left(1+(-1)^i\,\mathrm{sgn}\,(h_2)\right)+2|h_1(\mathbf{k})|\big(1+(-1)^i h_2(\mathbf{k})/2\big)\right]^{1/2}. \tag{2.21b}$$

The sign of h_2 at both Dirac points is given in Table 2.1 as a function of M and ϕ.

Smooth Berry gauge fields and Chern numbers We are looking for the zeros of $\rho_i(\mathbf{k})$ and $\lambda_i(\mathbf{k})$, which potentially yield (depending on the gauge choice) non-smooth definition of the Berry gauge field $\mathbf{A}_\mathbf{k}$. Here we need to distinguish the cases $|M|< 3\sqrt{3}t_2|\sin\phi|$, $|M|= 3\sqrt{3}t_2|\sin\phi|$ and $|M|> 3\sqrt{3}t_2|\sin\phi|$.

(i) In the case $|M|< 3\sqrt{3}t_2|\sin\phi|$, we gathered the values of of $\rho_i(\mathbf{k})$ and $\lambda_i(\mathbf{k})$ at the Dirac points in Table 2.2. From this table, we see that it is impossible to apply gauge choice G_I or gauge choice G_{II} everywhere in the BZ because $\rho_i(\mathbf{k})$ and $\lambda_i(\mathbf{k})$ are vanishing at one of the Dirac points. It follows that it is impossible to find a unique and smooth phase for the ket $|u_{i,\mathbf{k}}\rangle$ and therefore it is impossible to find a unique and smooth Berry gauge field $\mathbf{A}_\mathbf{k}$ everywhere in the BZ. Let us split the BZ into two non-overlapping domains [10]. One

domain, which we call the $\mathcal{D}_I$ domain contains $\mathbf{K}$ and the other one, the $\mathcal{D}_{II}$ domain, contains $\mathbf{K}'$, as if is sketched in Fig. 2.3(a). The boundary between $\mathcal{D}_I$ and $\mathcal{D}_{II}$ do not contain neither $\mathbf{K}$ nor $\mathbf{K}'$. We also define P a closed path along this boundary (see Fig. 2.3(a)), surrounding once $\mathbf{K}$ (and also $\mathbf{K}'$ since the BZ is a torus).

Now, for $(-1)^i \operatorname{sgn}(\sin\phi) = +1$, we apply G_I for the points contained in $\mathcal{D}_{II}$ and G_{II} for the points contained in $\mathcal{D}_I$ while for $(-1)^i \operatorname{sgn}(\sin\phi) = -1$, we apply G_I for the points contained in $\mathcal{D}_I$ and G_{II} for the points contained in $\mathcal{D}_{II}$. Then the phase of $|u_{i,\mathbf{k},I}\rangle$ (the eigenstate in $\mathcal{D}_I$) and $|u_{i,\mathbf{k},II}\rangle$ (the eigenstate in $\mathcal{D}_{II}$) and the Berry gauge fields $\mathbf{A}_{i,\mathbf{k},I} = \langle u_{i,\mathbf{k},I}| \nabla_{\mathbf{k}} |u_{i,\mathbf{k},I}\rangle$ and $\mathbf{A}_{i,\mathbf{k},II} = \langle u_{i,\mathbf{k},II}| \nabla_{\mathbf{k}} |u_{i,\mathbf{k},II}\rangle$ are uniquely and smoothly defined respectively on $\mathcal{D}_I$ and $\mathcal{D}_{II}$. As we did in Sec. 1.3.2 of Chapter 1, we write the Chern number associated to the j^{th} band (remind that $j = 1$ or $j = 2$)

$$C_j = \frac{1}{2i\pi}\left(\int_{\mathcal{D}_\text{I}} d^2k\,[\nabla_{\mathbf{k}} \times \mathbf{A}_{j,\mathbf{k},\text{I}}]\cdot\mathbf{e}_z + \int_{\mathcal{D}_\text{II}} d^2k\,[\nabla_{\mathbf{k}} \times \mathbf{A}_{j,\mathbf{k},\text{II}}]\cdot\mathbf{e}_z\right). \tag{2.22}$$

Using Stokes' theorem and considering the specific choice of path P shown in Fig. 2.3(a) leads to

$$C_j = \frac{1}{2i\pi}\left(\oint_\text{P} d\mathbf{k}\cdot\mathbf{A}_{j,\mathbf{k},\text{I}} - \oint_\text{P} d\mathbf{k}\cdot\mathbf{A}_{j,\mathbf{k},\text{II}}\right). \tag{2.23}$$

Along P, we have $|u_{j,\mathbf{k},I}\rangle = \mathrm{e}^{i(-1)^j \operatorname{sgn}(\sin\phi)\varphi(\mathbf{k})}\,|u_{j,\mathbf{k},II}\rangle$. We choose $\varphi(\mathbf{k})$ so that it is smooth along the whole P path and we obtain

$$C_j = \frac{(-1)^j \operatorname{sgn}(\sin\phi)}{2\pi}\oint_\text{P} d\mathbf{k}\cdot\nabla_{\mathbf{k}}\varphi(\mathbf{k}). \tag{2.24}$$

C_i is found by studying how $\varphi(\mathbf{k})$ evolves when moving along P. Generally speaking, when the P path surround a $\varphi(\mathbf{k})$'s divergence (here at the $\mathbf{K}$ or $\mathbf{K}'$ point), the accumulated phase increases or decreases by $\pm 2\pi z$, $z \in \mathbb{Z}$, which gives a quantized value of C, as expected. Here, from the expression of $\varphi(\mathbf{k})$ (see Eq. (2.18)) and from the expression of $h_1(\mathbf{k})$ (see Eq. (2.4c)), we find that $\varphi(\mathbf{k})$ changes by -2π when moving along the entire closed path P. One can also easily build intuition from Eq. (1.52) for a small path around $\mathbf{K}$ or $\mathbf{K}'$. This

gives

$$C_i = (-1)^{i+1} \operatorname{sgn}(\sin\phi). \tag{2.25}$$

(ii) If $|M| = 3\sqrt{3}t_2|\sin\phi|$ then the bands cross at $\mathbf{K}$ or $\mathbf{K}'$ so the Chern number is not defined.

(iii) In the case $|M| > 3\sqrt{3}t_2|\sin\phi|$, we gathered the values of $\rho_i(\mathbf{k})$ and $\lambda_i(\mathbf{k})$ at the Dirac points in Table 2.3. At both Dirac points, either $\rho_i(\mathbf{k})$ or $\lambda_i(\mathbf{k})$ are non-vanishing, therefore it is possible to find a unique and smooth phase for the ket $|u_{i,\mathbf{k}}\rangle$ everywhere in the BZ which leads to a unique and smooth Berry gauge field $\mathbf{A}_\mathbf{k}$. Depending on the value of $(-1)^i \operatorname{sgn}(M)$, we apply gauge choice G_I or G_{II} for all the points of the BZ, and then we can show that the associated wave function $|u_{i,\mathbf{k},I}\rangle$ or $|u_{i,\mathbf{k},II}\rangle$ (and its phase) is uniquely and smoothly defined, as is the Berry gauge field $\mathbf{A}_{i,\mathbf{k},III} = \langle u_{i,\mathbf{k},III}| \nabla_\mathbf{k} |u_{i,\mathbf{k},III}\rangle$. Because the BZ is a torus, we find that the Chern numbers C_i are vanishing.

This gives the phase diagram of the Haldane phase diagram shown in Fig. 2.3(b): in the case $|M| < 3\sqrt{3}t_2|\sin\phi|$, we have $C_i = (-1)^{i+1} \operatorname{sgn}(\sin\phi)$ while if $|M| > 3\sqrt{3}t_2|\sin\phi|$, the Chern numbers C_i are vanishing. Moreover we showed (see namely Eq. (2.21)) that the sign of h_2 at the Dirac points (see Table 2.1) indicates the value of C_i. To be more specific, the discontinuity in the value of C_i at the transition arises from a discontinuity in $\operatorname{sgn}(h_2(\mathbf{K}))\operatorname{sgn}(h_2(\mathbf{K}'))$: at $|M| < 3\sqrt{3}t_2|\sin\phi|$, $\operatorname{sgn}(h_2(\mathbf{K}))\operatorname{sgn}(h_2(\mathbf{K}')) = -1$ while at $|M| > 3\sqrt{3}t_2|\sin\phi|$, $\operatorname{sgn}(h_2(\mathbf{K}))\operatorname{sgn}(h_2(\mathbf{K}')) = +1$. In other words, when the sign of h_2 is opposite at the Dirac points, the system is a Chern insulator, while when the sign of h_2 is the same at the Dirac points, the system is a trivial insulator. In the following section, we show how the sign of h_2 at the Dirac points can be measured in a Haldane light system via a local capacitive probe on the lattice.

$(-1)^i \operatorname{sgn}(M)$	$\lim_{\mathbf{k}\to\mathbf{K}} [\rho_i(\mathbf{k})]$	$\lim_{\mathbf{k}\to\mathbf{K}'} [\rho_i(\mathbf{k})]$	$\lim_{\mathbf{k}\to\mathbf{K}} [\lambda_i(\mathbf{k})]$	$\lim_{\mathbf{k}\to\mathbf{K}'} [\lambda_i(\mathbf{k})]$
$+1$	$\operatorname{sgn}(M)$	$\operatorname{sgn}(M)$	0	0
-1	0	0	1	1

Table 2.3: Table giving the values of of $\rho_i(\mathbf{k})$ and $\lambda_i(\mathbf{k})$ at the Dirac points in the case $|M| > 3\sqrt{3}t_2|\sin\phi|$, as a function of the sign of the Semenoff mass M and of the index of the energy band i.

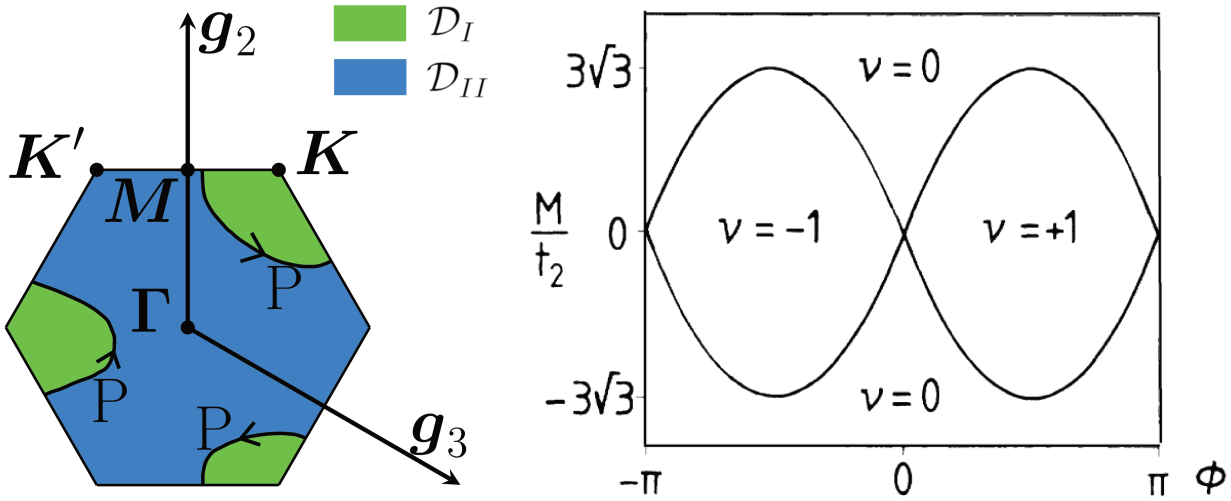

(a) (b)

Figure 2.3: (a) Definition of the Brillouin zone for the honeycomb lattice and of the $\mathcal{D}_I$ and $\mathcal{D}_{II}$ domains, each associated to a specific gauge choice for the eigenvectors of the Bloch Hamiltonian considered in Sec. 2.2. Lowest band Chern number phase diagram of the Haldane model (this figure is taken from Ref. [5]).

2.3 Haldane light system and local response to capacitively coupled probes

Here we present a protocol for the measurement of the topological properties of a Haldane model in a circuit quantum electrodynamics (cQED) setup. This protocol involves a local probe with capacitive coupling to the system and it relies on the measure of the reflection coefficient which relates an input voltage signal and an output voltage signal in this probe. The results may be expanded to a kagome lattice system, although more tedious.

2.3.1 Capacitive coupling with a transmission line

In this section we consider a resonator (light) probe which is coupled to the Haldane photonic system described in Sec. 2.1.2. We assume a capacitive coupling between the probe and the system. We write H_{prb} the Hamiltonian associated to the probe and H_{cpl} the Hamiltonian describing the coupling between the system and the probe.

Probe The probe is a resonator with a certain number of (relevant) modes, each mode q being characterized by the frequency $\omega_q > 0$. The probe is coupled to the system at position $\mathbf{R}_0$. The lattice site at position $\mathbf{R}_0$ belongs to the sublattice A or B; in each case we respectively define $j_0 = j(\mathbf{R}_0) = 1$ or $j_0 = j(\mathbf{R}_0) = 2$. We write the Hamiltonian associated to the probe

$$H_{\text{prb}} = \sum_q \omega_q b^\dagger_{\mathbf{R}_0,q} b_{\mathbf{R}_0,q}, \tag{2.26}$$

with $b_{\mathbf{R}_0,q}$ the annihilation operators for the mode q of the probe at $\mathbf{R}_0$.

Coupling We assume a capacitive coupling between the probe and the resonator at lattice site at $\mathbf{R}_0$. The associated Hamiltonian reads

$$H_{\text{cpl}} = \left(c_{\mathbf{R}_0} + c^\dagger_{\mathbf{R}_0}\right) \sum_q g_q \left(b_{\mathbf{R}_0,q} + b^\dagger_{\mathbf{R}_0,q}\right), \tag{2.27}$$

where we wrote $c^\dagger_{\mathbf{R}_0}$ the creation operator for a boson at site $\mathbf{R}_0$. The coupling amplitude g_q is assumed not to depend on the position of the probe. Let us define $g = \max_q(g_q)$. In the following, we consider that g is small compared to the energies $E_{i,\mathbf{k}}$ of the system.

2.3.2 Response function and topological properties

Here we investigate the relation between an input voltage $\langle V^{\text{in}}_{\mathbf{R}_0}[\omega]\rangle$ at frequency ω in the probe at $\mathbf{R}_0$ and the resulting output voltage $\langle V^{\text{out}}_{\mathbf{R}_0}[\omega]\rangle$ (still in the probe at $\mathbf{R}_0$), with $\langle V^{\text{in}}_{\mathbf{R}_0}[\omega]\rangle$ and $\langle V^{\text{out}}_{\mathbf{R}_0}[\omega]\rangle$ the Fourier transforms with respect to the time variable t of respectively (see

App. C)

$$V^{\text{in}}_{\mathbf{R}_0}(t) = \sum_q g_q \left(\mathrm{e}^{-i\omega_q(t-t_i)} b_{\mathbf{R}_0,q}(t_i) + h.c. \right), \tag{2.28}$$

and

$$V^{\text{out}}_{\mathbf{R}_0}(t) = \sum_q g_q \left(\mathrm{e}^{-i\omega_q(t-t_f)} b_{\mathbf{R}_0,q}(t_f) + h.c. \right). \tag{2.29}$$

t_i is an initial time in distant past and t_f is a final time in the distant future. We show that for a frequency ω corresponding to the energy at one of both Dirac points, this relation between $\langle V^{\text{in}}_{\mathbf{R}_0}[\omega] \rangle$ and $\langle V^{\text{out}}_{\mathbf{R}_0}[\omega] \rangle$ can be used to evaluate the sign of h_2 and therefore to rebuild the Haldane phase diagram. We also mention the connection with the energy density of states. For explicit definitions and demonstrations we refer to App. C.

Relation between $\langle V^{\text{in}}_{\mathbf{R}_0}[\omega] \rangle$ and $\langle V^{\text{out}}_{\mathbf{R}_0}[\omega] \rangle$

In App. C, we computed the relation between the output voltage operator in a probe at a certain position on the lattice and the input voltage operators associated to an ensemble of probes on the lattice. Here, considering only one probe at $\mathbf{R}_0$, and taking the average values of these operators in the driven probe's state gives

$$\langle V^{\text{out}}_{\mathbf{R}_0}[\omega] \rangle = (1 + iJ[\omega]\chi_{\mathbf{R}_0,\mathbf{R}_0}) \langle V^{\text{in}}_{\mathbf{R}_0}[\omega] \rangle + \mathcal{O}(g^4), \tag{2.30}$$

where we remind that $\langle V^{\text{in}}_{\mathbf{R}_0}[\omega] \rangle$ and $\langle V^{\text{out}}_{\mathbf{R}_0}[\omega] \rangle$ are first order terms in g and with

$$J[\omega] = 2\sqrt{2}\pi \sum_q g_q^2 \left[\delta(\omega - \omega_q) - \delta(\omega + \omega_q) \right], \tag{2.31}$$

and

$$\chi_{\mathbf{R}_0,\mathbf{R}_0} = \frac{1}{\sqrt{2}N} \sum_{\substack{i=1 \\ \mathbf{k}}}^{2} \left(\frac{\left(\beta^i_{j_0,\boldsymbol{k}} \alpha^{j_0}_{i,\boldsymbol{k}}\right)^*}{-\omega - E_{i,\mathbf{k}} + i0^+} - \frac{\beta^i_{j_0,\boldsymbol{k}} \alpha^{j_0}_{i,\boldsymbol{k}}}{-\omega + E_{i,\mathbf{k}} + i0^+} \right), \tag{2.32}$$

where N is the number of lattice sites and $E_{i,\mathbf{k}}$ is defined in Eq. (2.3). $\alpha^1_{i,\mathbf{k}}$ and $\alpha^2_{i,\mathbf{k}}$ are respectively the coefficients $a_i(\mathbf{k})$ and $\tilde{b}_i(\mathbf{k})$ appearing in Eq. (2.11):

$$\alpha^2_i = \frac{h_1(\mathbf{k})^*}{h_2(\mathbf{k}) - h_0(\mathbf{k}) + E_{i,\mathbf{k}}} \alpha^1_i, \tag{2.33}$$

from which we write the eigenvectors of the matrix $h_{\mathbf{k}}$ (defined in Eq. (2.2b))

$$|\Phi_{i,\mathbf{k}}\rangle = \Phi^\dagger_{i,\mathbf{k}}|0\rangle = \left(\alpha^1_{i,\mathbf{k}} c^\dagger_{A,\mathbf{k}} + \alpha^2_{i,\mathbf{k}} c^\dagger_{B,\mathbf{k}}\right)|0\rangle\,, \tag{2.34}$$

and the coefficients $\beta^j_{i,\boldsymbol{k}}$ are defined by

$$a^\dagger_{j,\boldsymbol{k}}|0\rangle = \sum_{i=1}^{2} \beta^i_{j,\boldsymbol{k}} \Phi^\dagger_{i,\boldsymbol{k}}|0\rangle\,. \tag{2.35}$$

Using Eqs. (2.33) and (2.34), we obtain

$$\beta^i_{j_0,\boldsymbol{k}}\alpha^{j_0}_{i,\boldsymbol{k}} = \frac{1}{2} + \frac{(-1)^{j_0+i+1}h_2(\mathbf{k})}{2\sqrt{|h_1(\mathbf{k})|^2+h_2(\mathbf{k})^2}}, \tag{2.36}$$

which is a real number.

The sign of h_2 at the Dirac points

Now, we transform the variable $\mathbf{k}$ into a continuous variable, *i.e.* we consider the large number of lattice sites limit, and we use

$$\begin{aligned}\iint_{\mathrm{BZ}} dk_1dk_2 \frac{\beta^i_{j_0,\boldsymbol{k}}\alpha^{j_0}_{i,\boldsymbol{k}}}{-\omega \pm E_{i,\boldsymbol{k}} + i0^+} = \mathrm{P}\left[\int_{\mathbb{R}} \frac{dE}{-\omega \pm E} \iint_{\mathrm{BZ}} dk_1dk_2 \beta^i_{j_0,\boldsymbol{k}}\alpha^{j_0}_{i,\boldsymbol{k}}\delta(E - E_{i,\mathbf{k}})\right] \\ - i\pi \iint_{\mathrm{BZ}} dk_1dk_2 \beta^i_{j_0,\boldsymbol{k}}\alpha^{j_0}_{i,\boldsymbol{k}}\delta(-\omega \pm E_{i,\mathbf{k}}),\end{aligned} \tag{2.37}$$

where P denotes the principal value. We obtain

$$\begin{aligned}\sqrt{2}(2\pi)^2\chi_{\mathbf{R}_0,\mathbf{R}_0} = &-\sum_{i=1}^{2} \mathrm{P}\left[\int_{\mathbb{R}} \frac{dE}{-\omega + E} \iint_{\mathrm{BZ}} dk_1dk_2 \beta^i_{j_0,\boldsymbol{k}}\alpha^{j_0}_{i,\boldsymbol{k}}\delta(E - E_{i,\mathbf{k}})\right] \\ &+ \sum_{i=1}^{2} \mathrm{P}\left[\int_{\mathbb{R}} \frac{dE}{-\omega - E} \iint_{\mathrm{BZ}} dk_1dk_2 \beta^i_{j_0,\boldsymbol{k}}\alpha^{j_0}_{i,\boldsymbol{k}}\delta(E - E_{i,\mathbf{k}})\right] \\ &+ i\pi \sum_{i=1}^{2} \iint_{\mathrm{BZ}} dk_1dk_2 \beta^i_{j_0,\boldsymbol{k}}\alpha^{j_0}_{i,\boldsymbol{k}}\delta(-\omega + E_{i,\mathbf{k}}) \\ &- i\pi \sum_{i=1}^{2} \iint_{\mathrm{BZ}} dk_1dk_2 \beta^i_{j_0,\boldsymbol{k}}\alpha^{j_0}_{i,\boldsymbol{k}}\delta(-\omega - E_{i,\mathbf{k}}).\end{aligned} \tag{2.38}$$

Let us denote $1 + iJ[\omega]\chi_{\mathbf{R}_0,\mathbf{R}_0} = R(\omega)$. From Eq. (2.30) and because $J[\omega]$ is of order 2 in g, we have

$$\left|\langle V^{\mathrm{out}}_{\mathbf{R}_0}[\omega]\rangle\right| = \mathrm{Re}\left[R(\omega)\right]\left|\langle V^{\mathrm{in}}_{\mathbf{R}_0}[\omega]\rangle\right| + \mathcal{O}(g^4), \tag{2.39}$$

with $\left|\langle V^{\rm out}_{\mathbf{R}_0}[\omega]\rangle\right|^2 = \langle V^{\rm out}_{\mathbf{R}_0}[\omega]\rangle \left(\langle V^{\rm out}_{\mathbf{R}_0}[\omega]\rangle\right)^*$ and the same holds for $\langle V^{\rm in}_{\mathbf{R}_0}[\omega]\rangle$ and $\mathrm{Re}\,[R(\omega)]$ reads

$$\begin{aligned}\mathrm{Re}\,[R(\omega)] =& 1 - \frac{J[\omega]\pi}{\sqrt{2}(2\pi)^2}\sum_{i=1}^{2}\iint_{\rm BZ} dk_1 dk_2 \beta^i_{j_0,\boldsymbol{k}}\alpha^{j_0}_{i,\boldsymbol{k}}\delta(-\omega + E_{i,\mathbf{k}}) \\ &+ \frac{J[\omega]\pi}{\sqrt{2}(2\pi)^2}\sum_{i=1}^{2}\iint_{\rm BZ} dk_1 dk_2 \beta^i_{j_0,\boldsymbol{k}}\alpha^{j_0}_{i,\boldsymbol{k}}\delta(\omega + E_{i,\mathbf{k}}).\end{aligned} \tag{2.40}$$

$\left|\langle V^{\rm out}_{\mathbf{R}_0}[\omega]\rangle\right|$ and $\left|\langle V^{\rm in}_{\mathbf{R}_0}[\omega]\rangle\right|$ are respectively the amplitudes of the average output and input voltages in the probe at frequency ω.

Let us consider a probe with one relevant mode $\omega_0 > 0$ and an average input voltage in the probe which is a cosine function of time with amplitude V_0 (and frequency ω_0) to fix the ideas. It gives two delta peaks in the frequency space at $-\omega_0$ and $+\omega_0$. Therefore $\left|\langle V^{\rm out}_{\mathbf{R}_0}[\omega]\rangle\right|$ is non-vanishing only for $\omega = -\omega_0$ or $\omega = +\omega_0$. The average output voltage at $-\omega_0$ and $+\omega_0$ is then respectively given by $\mathrm{Re}\,[R(-\omega_0)]\,V_0/2$ and $\mathrm{Re}\,[R(+\omega_0)]\,V_0/2$. $J[\omega]$ reads

$$J[\omega] = 2\sqrt{2}\pi g^2\left[\delta(\omega-\omega_0) - \delta(\omega+\omega_0)\right], \tag{2.41}$$

therefore we have (remind that the energies $E_{i,\mathbf{k}}$ are positive numbers)

$$\mathrm{Re}\,[R(-\omega_0)] = \mathrm{Re}\,[R(+\omega_0)] = 1 - \frac{g^2}{2}\sum_{i=1}^{2}\iint_{\rm BZ} dk_1 dk_2 \beta^i_{j_0,\boldsymbol{k}}\alpha^{j_0}_{i,\boldsymbol{k}}\delta(-\omega_0 + E_{i,\mathbf{k}}). \tag{2.42}$$

Now let us assume that $\omega_0 = E_{j_0,\boldsymbol{k}_0}$ with $\boldsymbol{k}_0$ an arbitrary wave-vector in the BZ. We have

$$\beta^{j_0}_{j_0,\boldsymbol{k}}\alpha^{j_0}_{j_0,\boldsymbol{k}} = \frac{1}{2} - \frac{h_2(\mathbf{k})}{2\sqrt{|h_1(\mathbf{k})|^2 + h_2(\mathbf{k})^2}}. \tag{2.43}$$

We notice that at the Dirac points, $|h_1| = 0$ so $2\beta^{j_0}_{j_0,\boldsymbol{k}}\alpha^{j_0}_{j_0,\boldsymbol{k}} = 1 - \mathrm{sgn}(h_2)$. Therefore, if $E_{j_0,\boldsymbol{k}_0}$ is non-degenerate at $\mathbf{k}_0 = \mathbf{K}$ or $\mathbf{k}_0 = \mathbf{K}'$, $\mathrm{Re}\,[R(\omega)]$ can be used to probe the sign of h_2 respectively at $\mathbf{k} = \mathbf{K}$ or $\mathbf{k} = \mathbf{K}'$. For instance, from Fig. 2.1, we observe that, at $\phi = \pi/2$ and $t_2 = 0.15t_1$, for $M > 0$, $E_{j_0,\boldsymbol{K}}$, $j_0 \in \{1,2\}$ is non-degenerate. In fact, at $t_2 \lesssim 0.15t_1$, for $\sin\phi > 0$ and $M/t_2 > 0$, $E_{j_0,\boldsymbol{K}}$, $j_0 \in \{1,2\}$ is non-degenerate and for $\sin\phi > 0$ and $M/t_2 < 0$, $E_{j_0,\boldsymbol{K}'}$, $j_0 \in \{1,2\}$ is non-degenerate.

In Fig. 2.4, we show a numerical evaluation of $1 - \mathrm{Re}\,[R(\omega)]$ from Eq. (2.42), for $\sin\phi > 0$ and for $E_{1,\boldsymbol{K}'} - 0.02t_1 \leq \omega \leq E_{1,\boldsymbol{K}'} + 0.02t_1$ and $E_{1,\boldsymbol{K}} - 0.02t_1 \leq \omega \leq E_{1,\boldsymbol{K}} + 0.02t_1$ (the "optical probe bandwidth" is four percent of the amplitude of the nearest neighbor hopping terms of the Haldane effective boson model) respectively in the cases $M/t_2 > 0$ and $M/t_2 < 0$. We considered a 50×50 unit cells periodic Haldane model described by the Hamiltonian in Eq. (2.2). It confirms that $\mathrm{Re}\,[R(\omega)]$ gives the sign of h_2, at $\mathbf{K}$ or $\mathbf{K}'$ respectively for $M/t_2 > 0$ and $M/t_2 < 0$.

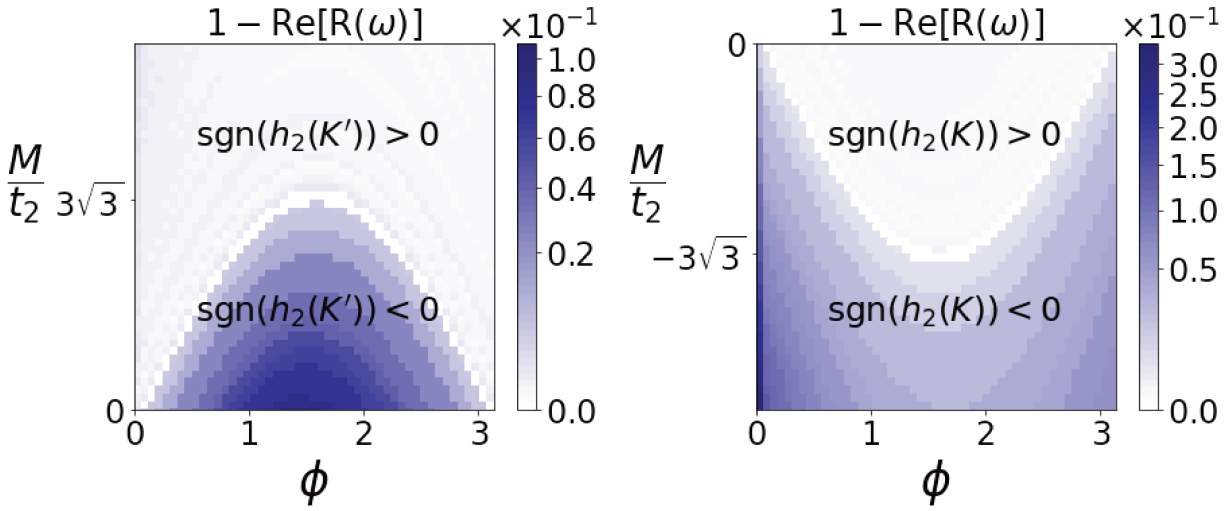

(a) (b)

Figure 2.4: The quantity $1 - \mathrm{Re}\,[R(\omega)]$ computed from Eq. (2.42), for $\sin\phi > 0$ and for (a) $M/t_2 > 0$, $E_{1,\boldsymbol{K}'} - 0.02t_1 \leq \omega \leq E_{1,\boldsymbol{K}'} + 0.02t_1$ and for (b) $M/t_2 < 0$, $E_{1,\boldsymbol{K}} - 0.02t_1 \leq \omega \leq E_{1,\boldsymbol{K}} + 0.02t_1$. We considered a 50×50 unit cells periodic Haldane model described by the Hamiltonian in Eq. (2.2) and we have chosen $t_2 = 0.15t_1$. $1 - \mathrm{Re}\,[R(\omega)]$ is given in units of g^2, where g is the amplitude of the coupling between the probe's mode and the system, and the color scale is logarithmic.

Remarks

Let us briefly mention few points about this protocol.

(i) For smaller systems, down to $\sim$ 30 unit cell systems, the quantity $1 - \mathrm{Re}\,[R(\omega)]$ computed from Eq. (2.40) still gives a good approximation of the Haldane phase diagram.

(ii) From Eq. (2.36), we notice that the density of states can be measured by summing the responses $1 - \mathrm{Re}\,[R(\omega)]$ for both energies $\omega = E_{1,\boldsymbol{K}}$ and $\omega = E_{2,\boldsymbol{K}}$ with a probe at $j_0 = 1$ (sublattice A) or $j_0 = 2$ (sublattice B). The density of states can also be measured by summing the responses $1 - \mathrm{Re}\,[R(\omega)]$ for both energies $\omega = E_{i,\boldsymbol{K}}$ with a probe at $j_0 = 1$ (sublattice A) and $\omega = E_{i,\boldsymbol{K}}$ with a probe at $j_0 = 2$ (sublattice B), for $i = 1$ (lowest energy band) or $i = 2$ (highest energy band).

(iii) If the input is created at a site on the sublattice (A or B) and the output is measured at a site on the other sublattice (respectively B or A), we have

$$\beta^{i}_{j_0,\boldsymbol{k}}\alpha^{\overline{j_0}}_{i,\boldsymbol{k}} \propto \frac{h_1(\mathbf{k})}{2\sqrt{|h_1(\mathbf{k})|^2+h_2(\mathbf{k})^2}}, \tag{2.44}$$

where $\overline{j_0} = 2(1)$ if $j_0 = 1(2)$. At the Dirac points, h_1 is vanishing, therefore the measure here does not help to rebuild the topological phase diagram.

(iv) Other reflection/transmission measures have been proposed in the litterature. For instance, in Ref. [187], the reflection coefficient gives the (Hofstatter) energy spectrum. This differs from our system namely from the coupling considered. In this Ref. [187], the authors (see the "Supplementary Information" file) have considered that each resonator mode couples to a single running wave in the probing waveguides. This is different from the (capacitive) coupling we considered.

(v) Numerical computations of $1 - \mathrm{Re}\,[R(\omega)]$ for nearest-neighbor tight binding topological models on the kagome lattice (for several configurations of the chemical potentials) show that it is also possible to evaluate the topological properties with this capacitive-coupling light probe. The details of the analytical computations are more complicated than for the honeycomb lattice (because the kagome lattice has three sites per unit cell) but it seems possible to show analytically that this capacitive-coupling light probe indeed is informative about the value of the Chern number. For this computation, the explicit analytical computation of the bands' Chern numbers, as we showed in this chapter for the Haldane model, is helpful. We perform this computation in the following chapter. More generally, it should be

possible to make a clear link between the Chern number and the response function computed in this section, for an arbitrary lattice model. We are currently working on this.

(vi) We also considered a protocol to probe the Chern number for a Haldane (fermion) model with a capacitively coupled probe, described by the coupling

$$c^{\dagger}_{\mathbf{R}_0} c_{\mathbf{R}_0} \sum_q g_q \left(b_{\mathbf{R}_0,q} + b^{\dagger}_{\mathbf{R}_0,q} \right), \tag{2.45}$$

where $c_{\mathbf{R}_0}$ is a fermion annihilation operator (and $b_{\mathbf{R}_0,q}$ is still a boson annihilation operator). We computed the response function which is given by the particle-hole Green's function. Evaluating the topological properties for such a fermion system with this capacitive-coupled light probe protocol is *a priori* more complicated but maybe not impossible. We are currently working on this.

2.4 Conclusion

In this chapter, we have introduced a boson Haldane model. We have explicitly computed the Chern number phase diagram starting from Eq. (1.79) of Chapter 1. In the following chapters, this method is extended to the Chern number's computation for the kagome topological systems we consider. We have shown that the sign, at both Dirac points, of the function that we called h_2 (its expression is given in Eq. (2.4)) indicates the value of both bands' Chern number. h_2 depends on the Semenoff mass term M and on the amplitude t_2 associated to the next-nearest neighbors hopping terms of the Haldane model.

In Sec. 2.3, we have considered a local probe with capacitive coupling to the Haldane system, for the regime of small coupling amplitudes. We have explicitly computed the reflection coefficient, which relates an input voltage and an output voltage in this probe, as a function of the system's parameters. We show that the sign of the "mass function" ($h_2(\mathbf{K})$ or $h_2(\mathbf{K}')$ depending on the sign of $M/t_2 \sin\phi$) is encoded in this reflection coefficient at the energy of the Dirac point at which the band gap is the narrowest. Since the Chern number is determined from the sign of h_2 at the Dirac points, the measure of the reflection coefficient

(for an input of energy equal to the energy of the Dirac point at which the band gap is the narrowest) determines the Chern number phase diagram. In the system we consider, which is made of resonators of frequency amplitude in the GHz range, the sign of the "mass function" h_2 is measurable via microwave light.

Numerical computations indicate that evaluating the topological properties in kagome Chern insulating boson system, with this capacitive-coupling light probe protocol is also possible. Therefore it should be possible to realize such a measure for instance in the cQED system proposed in Ref. [33] which leads to an effective photon kagome lattice Hamiltonian.

Chapter 3

Kagome topological models and computation of the topological invariants

In this Chapter, we introduce a topological nearest-neighbor tight binding model on the kagome lattice and we develop an analytical computation of the associated lowest band Chern number. To the best of our knowledge this explicit computation does not appear in the literature before our publication [188]. We also consider two spin copies of this kagome system and we compute the associated $\mathbb{Z}_2$ invariant [48, 189, 190] at 2/3 filling. These computations are extended, in Chapter 5, to the case of different chemical potential configurations. We also investigate the topological properties of small noisy kagome systems, thanks to numerical computations of local observables.

As we mentioned in Chapter 1, Sec. 1.2.5, the kagome lattice is particularly interesting for studying topological effects in lattice models. Indeed, Dirac points appear in a simple nearest-neighbor tight-binding model on the kagome lattice. The quantum anomalous Hall effect on the kagome lattice has attracted much attention [31–38]. The computation of Chern number has been performed, for instance, by studying the contribution of each Berry phase flux coming from the Dirac cones, by the investigation of the edges states, or numerically, *e.g.* using a method where one does not have to worry about the arbitrary gauge of the eigenvectors resulting from the numerical computation [191]. In materials, the spin-orbit

interaction plays an essential role for the appearance of the quantum anomalous Hall effect. In several kagome materials, the spin-orbit interaction has relatively high amplitude and opens a topological gap (at least at some points in the Brillouin zone) [25, 26, 36, 37, 192]. Several time-reversal invariant kagome systems with intrinsic spin-orbit interaction have also been studied [39–42, 193].

This chapter is organized as follows. In Sec. 3.1, we explain that a kagome tight-binding model with complex nearest neighbor hopping terms breaks time-reversal symmetry and have vanishing total flux in the unit cell. We compute the associated energy spectrum and briefly review [34] an analytical computation of the edge modes. In Sec. 3.2, we study the topological properties of this kagome tight-binding model. First, we develop an analytical computation of the lowest band Chern number, starting from Eq. (1.79) of Chapter 1. Then, we numerically investigate the local density of states and the chiral currents in small noisy systems. We also review another method for the determination of the Chern number, based on the splitting of the energy bands in weak magnetic fields [34, 194]. Such computations and methods are used in the following Chapters.

Eventually, in Sec. 3.3, we compute the $\mathbb{Z}_2$ invariant at 2/3 filling and we show the appearance of edge states for time-reversal invariant kagome systems with spin and inversion symmetries. Because the system conserves the spin in the out-of-plane direction, the $\mathbb{Z}_2$ invariant can be deduced from the Chern number computation [48, 189], as we explain in Sec. 3.3.1. The system has also inversion symmetry, enabling us to use another method to obtain the $\mathbb{Z}_2$ invariant [190]. This enables us to check the results obtained from the former method.

3.1 Simple topological model on the kagome lattice

Here we introduce and study a topologically non-trivial lattice model with a local magnetic flux density $\mathbf{B}(\mathbf{r})$, which, as described in Sec. 2.1.1, respects the symmetries of the lattice and

for which the total flux in the unit cell is vanishing. This model is the topological building block of the models we study in Chapters 4 and 5.

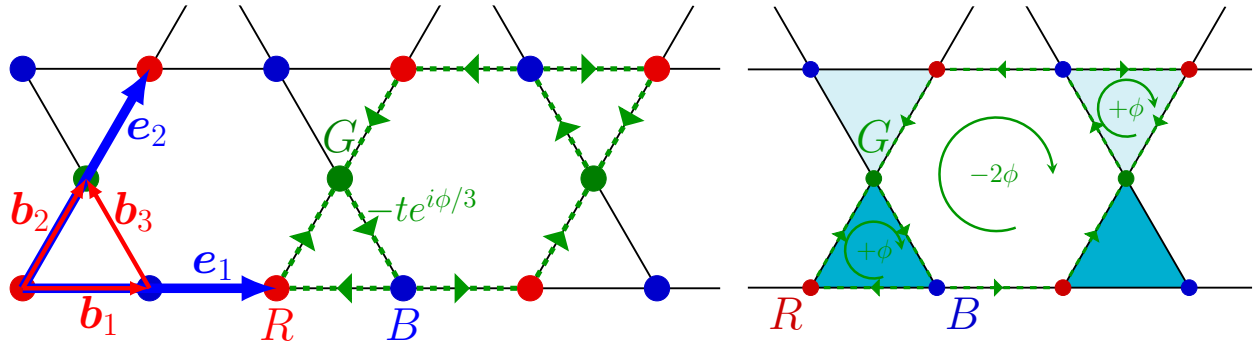

Figure 3.1: (a) Kagome lattice representation and definition of the sub-lattices R, G and B, of the nearest neighbors hopping amplitudes and of the displacement vectors $\mathbf{e}_i$, $i \in \{1, 2\}$ and $\mathbf{b}_i$, $i \in \{1, 2, 3\}$. (b) Magnetic fluxes in the unit cell, which contains one hexagon (associated to a flux -2ϕ and delimited here by a green dashed line with arrow), one "up" triangle (associated to a flux $+\phi$ and delimited here by a green dashed line with arrow) and one "down" triangle (associated to a flux $+\phi$ and delimited here by a green dashed line with arrow). The regions shaded with the same color are equivalent up to a lattice translation and are threaded by the same magnetic flux.

3.1.1 Breaking time-reversal symmetry while having a vanishing total flux in the unit cell

The kagome lattice has three inequivalent sites in the unit cell that we label by three "colors", R, G and B as shown in Fig. 3.1. Its Bravais lattice is hexagonal. The kagome lattice is such that a unit cell contains an hexagon, a triangle "up" and a triangle "down". Therefore, as we can see in Fig. 3.1b, it is possible to choose $\mathbf{B}(\mathbf{r})$ such that there is a finite non-zero flux through each hexagon and triangle. Then the nearest neighbor terms, contrarily as in the honeycomb lattice, break the time-reversal symmetry (which opens a gap) and may yield a topological system, although the total flux in the unit cell is vanishing. The nearest neighbor hopping amplitudes are complex and the contribution of the magnetic flux density is given by the so-called Peierls phases $\exp\left(i\frac{q}{\hbar}\int \mathbf{dl}\cdot\mathbf{A}(\mathbf{r})\right)$, with $\mathbf{dl}$ the oriented infinitesimal element

along the hopping path.

This leads us to consider the following simple, although possibly topological, Hamiltonian

$$H = -t \sum_{\langle ij \rangle} \mathrm{e}^{-i\phi\nu_{ij}/3} c_i^\dagger c_j, \tag{3.1}$$

with $t \in \mathbb{R}$ and $\phi \in \mathbb{R}$. $c_i^\dagger$ is the creation operator for a particle at site i. The sum runs over i and j nearest neighbors and $\nu_{ij} = +1(-1)$ if $c_i^\dagger c_j$ makes the particle jumping counter-clockwise (clockwise) inside the triangle of the kagome lattice containing sites i and j (see Fig. 3.1a).

As we argue in Chapter 4 (see in particular Sec. 4.1.2), Hamiltonian in Eq. (3.1) is relevant in topological kagome materials; spin-orbit coupling being the physical origin of the time-reversal symmetry breaking. Hamiltonian in Eq. (3.1) is also relevant for light and cold atom systems (see respectively Refs. [33, 34, 182] and Chapter 5).

3.1.2 Hamiltonian in momentum space and energies

In Fourier space the Hamiltonian reads

$$H = \sum_{\mathbf{k}} \Psi_{\mathbf{k}}^\dagger h_{\mathbf{k}} \Psi_{\mathbf{k}}, \tag{3.2a}$$

$$h_{\mathbf{k}} = -2t \begin{pmatrix} 0 & \mathrm{e}^{i\phi/3}\cos(\mathbf{k}\cdot\mathbf{b}_1) & \mathrm{e}^{-i\phi/3}\cos(\mathbf{k}\cdot\mathbf{b}_2) \\ \mathrm{e}^{-i\phi/3}\cos(\mathbf{k}\cdot\mathbf{b}_1) & 0 & \mathrm{e}^{i\phi/3}\cos(\mathbf{k}\cdot\mathbf{b}_3) \\ \mathrm{e}^{i\phi/3}\cos(\mathbf{k}\cdot\mathbf{b}_2) & \mathrm{e}^{-i\phi/3}\cos(\mathbf{k}\cdot\mathbf{b}_3) & 0 \end{pmatrix}, \tag{3.2b}$$

with $\Psi_{\mathbf{k}}^\dagger = \left(c_{\mathbf{k},R}^\dagger, c_{\mathbf{k},B}^\dagger, c_{\mathbf{k},G}^\dagger\right)$ defined in Sec. 1.2.5 and the displacement vectors $\mathbf{b}_i$, $i \in \{1,2,3\}$ defined in Fig. 3.1a. The eigenenergies are given by (see also [195])

$$E_l = -4t\sqrt{\frac{1+f(\mathbf{k})}{3}}\cos\frac{\theta(\mathbf{k})}{3}, \tag{3.3a}$$

$$E_m = -4t\sqrt{\frac{1+f(\mathbf{k})}{3}}\cos\frac{\theta(\mathbf{k})-2\pi}{3}, \tag{3.3b}$$

$$E_u = -4t\sqrt{\frac{1+f(\mathbf{k})}{3}}\cos\frac{\theta(\mathbf{k})+2\pi}{3}, \tag{3.3c}$$

with $f(\mathbf{k}) = 2\prod_{\alpha=1}^{3}\cos\mathbf{k}\cdot\mathbf{b}_\alpha$ and $0 \leq \theta(\mathbf{k}) \leq \pi$ defined by

$$\theta(\mathbf{k}) = \arccos\frac{3^{3/2}f(\mathbf{k})\cos\phi}{2\left(1+f(\mathbf{k})\right)^{3/2}}\,. \tag{3.4}$$

We have $E_l \leq E_m \leq E_u$ and the equality is reached when time-reversal symmetry is preserved ($\phi = 0$ or $\phi = \pi$). The topological invariant associated to the different energy bands is computed in Sec. 3.2.1.

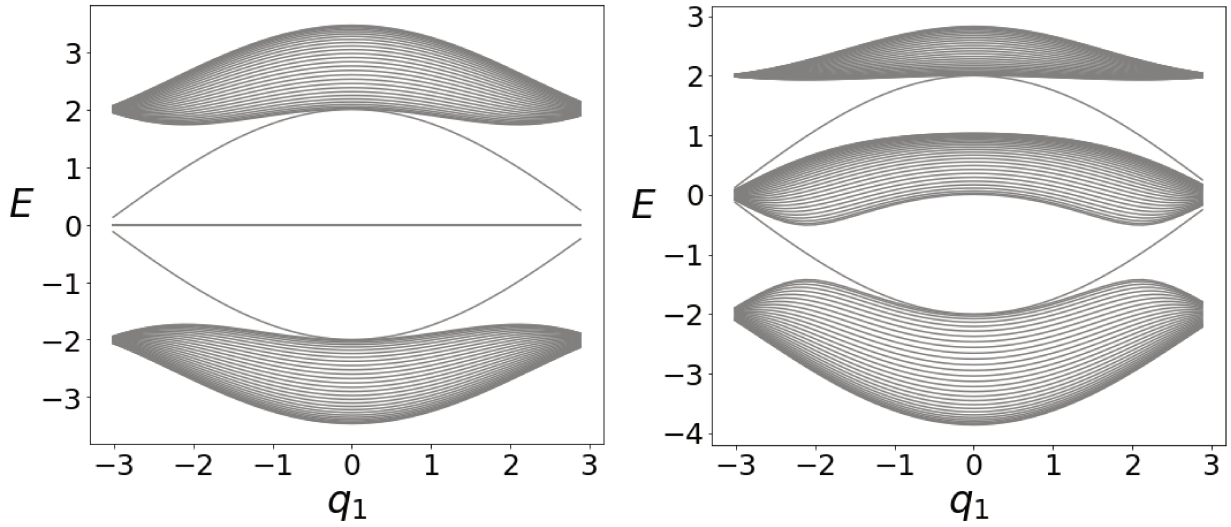

(a) (b)

Figure 3.2: Energies for the system described by the Hamiltonian in Eq. (3.1) for a cylinder geometry. We considered a system with periodicity along the direction $\boldsymbol{e}_1$ (see Fig. 3.1(a)) and open boundary conditions along the direction $\boldsymbol{e}_2$ with line edges formed by the lattice site B and R. Figures (a) and (b) differ by the value of the flux taken, respectively $\phi = \pi/2$ and $\phi = 3\pi/4$.

3.1.3 Edge states

Here we evaluate the eigenenergies E_Ψ and the eigenstates Ψ of the Hamiltonian in Eq. (3.1) for a lattice cylinder geometry. We considered a system with periodicity along the direction $\boldsymbol{e}_1$ (see Fig. 3.1(b)) and open boundary conditions along the direction $\boldsymbol{e}_2$ with line edge formed by the lattice site B and R. We apply a partial Fourier transform on the Hamiltonian H. A numerical computation gives the eigenenergies and the local density of states given

by $\rho(E,\boldsymbol{r}) \equiv \sum_\Psi \delta(E-E_\Psi)|\langle \boldsymbol{r}|\Psi\rangle|^2$. It satisfies the following normalization condition : $\int dE \sum_{\boldsymbol{r}\in\boldsymbol{R}} \rho(E,\boldsymbol{r}) = N$, with $\boldsymbol{R}$ the ensemble of all possible lattice sites and N their total number. The eigenenergies are represented in Fig. 3.2 (for two different values of the flux ϕ) and the numerical evaluation of the local density of states shows that the states which dispersion relation link the bulk bands are indeed edge states.

The energy and the expression of these edge modes can be analytically determined as shown in Ref. [34]. Let us briefly review this. We write the eigenstates as a superposition of localized states on each atom :

$$\Psi_\sigma(q_1) \equiv \sum_{\alpha=R,B,G} \sum_m \phi_{\alpha,m,\sigma}(q_1)\,|\alpha,m\rangle\,, \tag{3.5}$$

where m labels the unit cells along the direction $\boldsymbol{e}_2$. We assume that $\phi_{G,m}(q_1)=0$ (because along the edge there is no color G atom; we can also build intuition from the numerical evaluation of the local density of states) and we use the ansatz

$$\phi_{B,R}(m) = \lambda^m \phi_{B,R}(0). \tag{3.6}$$

It gives the energies of the two edge modes $E_\pm$ and the associated values of $\lambda_\pm$, in agreement with the numerical solution:

$$E_\pm = \pm 2r\cos\left(\frac{q_1}{2}\right), \tag{3.7a}$$

$$\lambda_+ = -\cos\left(\frac{\phi}{2}-\frac{q_1}{4}\right)\Big/\cos\left(\frac{\phi}{2}+\frac{q_1}{4}\right), \tag{3.7b}$$

$$\lambda_- = \sin\left(\frac{\phi}{2}-\frac{q_1}{4}\right)\Big/\sin\left(\frac{\phi}{2}+\frac{q_1}{4}\right). \tag{3.7c}$$

If the Fermi energy lies in the bulk gap, this predicts one eigenmode located at each edge of the system; $|\lambda_\pm|>1$ or $|\lambda_\pm|<1$ determines which mode is localized at which edge.

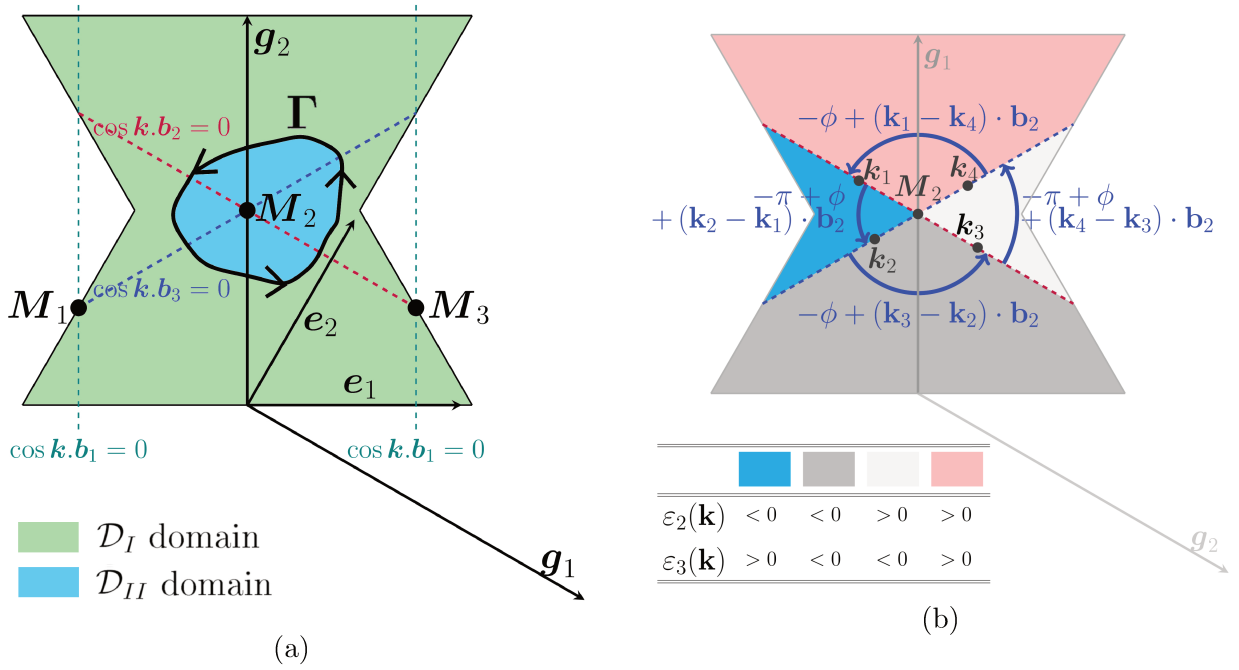

Figure 3.3: (a) Choice of two domains in the Brillouin zone, each associated to a specific gauge choice for the eigenvectors of the Hamiltonian in Eq. (3.10a). (b) Sign of $\varepsilon_2(\mathbf{k})$ and $\varepsilon_3(\mathbf{k})$ ($\varepsilon_\alpha = -2t\cos(\mathbf{k}\cdot\mathbf{b}_\alpha)$) in the BZ and the related evolution of $\varphi(\mathbf{k})$ along several portions of the Γ path (shown in figure (a)), for $\mathrm{sgn}(\sin\phi) > 0$.

3.2 Topological properties of a simple model on the kagome lattice

In this section, we investigate the topological properties of the kagome system introduced in Sec. 3.1. In Sec. 3.2.1, we develop an analytical computation of the Chern number starting from Eq. (1.79) of Chapter 1. Such a computation does not appear explicitly in the literature before our publication [188], to the best of our knowledge. This computation is generalized to a kagome model with different configurations of non-vanishing chemical potentials in Chapter 5. In Sec. 3.2.2 we study the topological properties of the model introduced in Sec. 3.1 through local observables in small noisy systems. For these systems, we perform numerical computation of the local density of states, of the currents and of the density of states under small magnetic fields.

3.2.1 Computation of the Chern number from a smooth field approach

Here we compute the Chern number associated to lowest energy band of the kagome-lattice model with Hamiltonian

$$H = -t \sum_{\langle ij \rangle} \mathrm{e}^{-i\phi\nu_{ij}/3} c_i^\dagger c_j, \tag{3.8}$$

described in Sec. 3.1. We remind that the Chern number is well-defined if the energy band is isolated from the others, which here means that $\phi \notin \{0, \pi\}$. The computation of the other bands' Chern number is similar.

Gauge transformation and Hamiltonian

We remind that in Fourier space the Hamiltonian reads

$$H = \sum_{\mathbf{k}} \Psi_{\mathbf{k}}^\dagger h_{\mathbf{k}} \Psi_{\mathbf{k}}, \tag{3.9a}$$

$$h_{\mathbf{k}} = -2t \begin{pmatrix} 0 & \mathrm{e}^{i\phi/3}\cos(\mathbf{k}\cdot\mathbf{b}_1) & \mathrm{e}^{-i\phi/3}\cos(\mathbf{k}\cdot\mathbf{b}_2) \\ \mathrm{e}^{-i\phi/3}\cos(\mathbf{k}\cdot\mathbf{b}_1) & 0 & \mathrm{e}^{i\phi/3}\cos(\mathbf{k}\cdot\mathbf{b}_3) \\ \mathrm{e}^{i\phi/3}\cos(\mathbf{k}\cdot\mathbf{b}_2) & \mathrm{e}^{-i\phi/3}\cos(\mathbf{k}\cdot\mathbf{b}_3) & 0 \end{pmatrix}, \tag{3.9b}$$

with $\Psi_{\mathbf{k}}^\dagger = \left(c_{\mathbf{k},R}^\dagger, c_{\mathbf{k},B}^\dagger, c_{\mathbf{k},G}^\dagger\right)$. In the following, we rather use

$$H = \sum_{\mathbf{k}} \Psi_{\mathbf{k}}^\dagger h_{\mathbf{k}} \Psi_{\mathbf{k}}, \tag{3.10a}$$

$$h_{\mathbf{k}} = -2t \begin{pmatrix} 0 & \cos(\mathbf{k}\cdot\mathbf{b}_1) & \cos(\mathbf{k}\cdot\mathbf{b}_2) \\ \cos(\mathbf{k}\cdot\mathbf{b}_1) & 0 & \mathrm{e}^{i\phi}\cos(\mathbf{k}\cdot\mathbf{b}_3) \\ \cos(\mathbf{k}\cdot\mathbf{b}_2) & \mathrm{e}^{-i\phi}\cos(\mathbf{k}\cdot\mathbf{b}_3) & 0 \end{pmatrix}, \tag{3.10b}$$

for the computation of the Chern number. This differs by the $U(1)$ local gauge transformation

$$\Psi_{\mathbf{k}}^\dagger = \left(c_{\mathbf{k},R}^\dagger, c_{\mathbf{k},B}^\dagger, c_{\mathbf{k},G}^\dagger\right) \to \left(c_{\mathbf{k},R}^\dagger, \mathrm{e}^{-i\phi/3} c_{\mathbf{k},B}^\dagger, \mathrm{e}^{i\phi/3} c_{\mathbf{k},G}^\dagger\right). \tag{3.11}$$

The Chern number is invariant under this transformation. We use Eq. (3.10b) instead of Eq. (3.9b) because it simplifies a bit the computations and because it describes one spin copy of the $\gamma = 0$ limit of the system we study in Chapter. 5.

Energies and eigenvectors

Let us denote E the energy of the lowest band and we remind that

$$E = -2\sqrt{\frac{4t^2\left[1+f(\mathbf{k})\right]}{3}}\cos\frac{\theta(\mathbf{k})}{3}, \tag{3.12}$$

with $f(\mathbf{k}) = 2\prod_{\alpha=1}^{3}\cos\mathbf{k}\cdot\mathbf{b}_\alpha$ and $0 \leq \theta(\mathbf{k}) \leq \pi$ defined by

$$\theta(\mathbf{k}) = \arccos\frac{3^{3/2}f(\mathbf{k})\cos\phi}{2\left(1+f(\mathbf{k})\right)^{3/2}}. \tag{3.13}$$

As we saw to the section Sec 2.2, the kets $|u_{n,\mathbf{k}}\rangle$'s are the eigenvectors of

$$\mathrm{e}^{-i\hat{\mathbf{k}}\cdot\hat{\mathbf{r}}}H\mathrm{e}^{i\hat{\mathbf{k}}\cdot\hat{\mathbf{r}}} = \sum_{\mathbf{k}}\Psi_{\mathbf{k}}^{\dagger}\tilde{h}_{\mathbf{k}}\Psi_{\mathbf{k}}, \tag{3.14}$$

with, here,

$$\tilde{h}_{\mathbf{k}} = -2t\begin{pmatrix} 0 & \mathrm{e}^{-i\mathbf{k}\cdot\mathbf{b}_1}\cos(\mathbf{k}\cdot\mathbf{b}_1) & \mathrm{e}^{-i\mathbf{k}\cdot\mathbf{b}_2}\cos(\mathbf{k}\cdot\mathbf{b}_2) \\ \mathrm{e}^{i\mathbf{k}\cdot\mathbf{b}_1}\cos(\mathbf{k}\cdot\mathbf{b}_1) & 0 & \mathrm{e}^{-i\mathbf{k}\cdot\mathbf{b}_3}\mathrm{e}^{i\phi}\cos(\mathbf{k}\cdot\mathbf{b}_3) \\ \mathrm{e}^{i\mathbf{k}\cdot\mathbf{b}_2}\cos(\mathbf{k}\cdot\mathbf{b}_2) & \mathrm{e}^{i\mathbf{k}\cdot\mathbf{b}_3}\mathrm{e}^{-i\phi}\cos(\mathbf{k}\cdot\mathbf{b}_3) & 0 \end{pmatrix}, \tag{3.15}$$

which we also write

$$\mathrm{e}^{-i\hat{\mathbf{k}}\cdot\hat{\mathbf{r}}}H\mathrm{e}^{i\hat{\mathbf{k}}\cdot\hat{\mathbf{r}}} = \sum_{\mathbf{k}}\tilde{\Psi}_{\mathbf{k}}^{\dagger}h_{\mathbf{k}}\tilde{\Psi}_{\mathbf{k}}, \tag{3.16}$$

with $\tilde{\Psi}_{\mathbf{k}}^{\dagger} = \left(c_{\mathbf{k},R}^{\dagger}, \mathrm{e}^{i\mathbf{k}\cdot\mathbf{b}_1}c_{\mathbf{k},B}^{\dagger}, \mathrm{e}^{i\mathbf{k}\cdot\mathbf{b}_2}c_{\mathbf{k},G}^{\dagger}\right)$. We write

$$|u_{\mathbf{k}}\rangle = \frac{\left(r(\mathbf{k})c_{R,\mathbf{k}}^{\dagger} + b(\mathbf{k})c_{B,\mathbf{k}}^{\dagger} + g(\mathbf{k})c_{G,\mathbf{k}}^{\dagger}\right)|0\rangle}{\sqrt{|r(\mathbf{k})|^2 + |b(\mathbf{k})|^2 + |g(\mathbf{k})|^2}}, \tag{3.17}$$

the eigenvector of $h(\mathbf{k})$ (defined in Eq. (3.10b)), in the basis $\left(c_{\mathbf{k},R}^{\dagger}, \mathrm{e}^{i\mathbf{k}\cdot\mathbf{b}_1}c_{\mathbf{k},B}^{\dagger}, \mathrm{e}^{i\mathbf{k}\cdot\mathbf{b}_2}c_{\mathbf{k},G}^{\dagger}\right)$, which is also the eigenvector of $\tilde{h}(\mathbf{k})$ in $\left(c_{\mathbf{k},R}^{\dagger}, c_{\mathbf{k},B}^{\dagger}, c_{\mathbf{k},G}^{\dagger}\right)$. From this relation, we get the $r(\mathbf{k})$, the $b(\mathbf{k})$ and the $g(\mathbf{k})$ coefficients.

Gauge choices, unique and smooth Berry gauge fields

We describe two gauge choices G_I and G_{II} for the eigenvectors that we respectively write $|u_{\mathbf{k},I}\rangle$ and $|u_{\mathbf{k},II}\rangle$. We will see later that these choices enable to correctly define the Bloch eigenvectors over the BZ.

(i) *Gauge choice* G_I: the coefficient $g(\mathbf{k})$ is real. More precisely, we choose

$$g(\mathbf{k}) = \rho(\mathbf{k})\,, \tag{3.18}$$

with

$$\rho(\mathbf{k})e^{i\varphi(\mathbf{k})} = -e^{i\mathbf{k}\cdot\mathbf{b}_2}\left[\frac{E\varepsilon_2(\mathbf{k})}{2\varepsilon_1(\mathbf{k})} + \frac{1}{2}e^{-i\phi}\varepsilon_3(\mathbf{k})\right]\,, \tag{3.19}$$

where $\rho(\mathbf{k})$ and $\varphi(\mathbf{k})$ are both real numbers and where we defined $\varepsilon_\alpha = -2t\cos(\mathbf{k}\cdot\mathbf{b}_\alpha)$. Then we have

$$r(\mathbf{k}) = -\frac{E^2 - \varepsilon_3^2(\mathbf{k})}{2\varepsilon_1(\mathbf{k})}e^{-i\varphi(\mathbf{k})}\,, \tag{3.20}$$

and

$$b(\mathbf{k}) = \frac{E^2 - \varepsilon_2^2(\mathbf{k})}{\rho_1(\mathbf{k})}\rho(\mathbf{k})e^{-i\varphi_1(\mathbf{k})}\,, \tag{3.21}$$

with

$$\rho_1(\mathbf{k})e^{i\varphi_1(\mathbf{k})} = e^{-i\mathbf{k}\cdot(\mathbf{b}_1-\mathbf{b}_2)}\left[E\varepsilon_3(\mathbf{k})e^{-i\phi} + \varepsilon_1(\mathbf{k})\varepsilon_2(\mathbf{k})\right]\,, \tag{3.22}$$

where $\rho_1(\mathbf{k})$ and $\varphi_1(\mathbf{k})$ are both real numbers.

(ii) *Gauge choice* G_{II}: the coefficient $r(\mathbf{k})$ is real. We choose

$$g(\mathbf{k}) = \rho(\mathbf{k})e^{i\varphi(\mathbf{k})}. \tag{3.23}$$

Then we have

$$r(\mathbf{k}) = -\frac{E^2 - \varepsilon_3^2(\mathbf{k})}{2\varepsilon_1(\mathbf{k})}, \tag{3.24}$$

and

$$b(\mathbf{k}) = \frac{E^2 - \varepsilon_2^2(\mathbf{k})}{\rho_1(\mathbf{k})}\rho(\mathbf{k})e^{i[\varphi(\mathbf{k})-\varphi_1(\mathbf{k})]}\,. \tag{3.25}$$

We introduce the three nonequivalent high symmetry $\mathbf{M}$ points, $\mathbf{M}_1 = -\frac{1}{2}\mathbf{g}_1$, $\mathbf{M}_2 = \frac{1}{2}\mathbf{g}_2$ and $\mathbf{M}_3 = \frac{1}{2}(\mathbf{g}_1 + \mathbf{g}_2)$ (see Fig. 3.3). We have $\rho(\mathbf{k}) = 0$ at the $\mathbf{M}_2$ point. We have $\rho_1(\mathbf{k}) = 0$ at the $\mathbf{M}_2$ and the $\mathbf{M}_1$ points. Here, it is impossible to find a unique and smooth gauge everywhere in the BZ. Then we split the BZ into two non-overlapping domains where we apply different gauge choices [10] (see Fig. 3.3(a)). One domain, which we call the $\mathcal{D}_{II}$

domain, contains the point where $\rho(\mathbf{k})$ vanishes. The other one, the $\mathcal{D}_I$ domain, contains all the points where $E^2 - \varepsilon_3^2(\mathbf{k})$ vanishes or $\varepsilon_1(\mathbf{k})$ vanishes. The boundary between $\mathcal{D}_I$ and $\mathcal{D}_{II}$ do not contain any of the $\rho(\mathbf{k}) = 0$, $E^2 - \varepsilon_3^2(\mathbf{k}) = 0$ and $\varepsilon_1(\mathbf{k}) = 0$ points. We also define Γ a closed path along this boundary, surrounding once the $\mathbf{M}_2$ point, as sketched in Fig. 3.3(a). Now, we apply G_I gauge choice for the points contained in $\mathcal{D}_I$ and G_{II} gauge choice for the points contained in $\mathcal{D}_{II}$. Then the associated wave function $|u_{\mathbf{k},I}\rangle$ and $|u_{\mathbf{k},II}\rangle$ (and its phase) and the Berry gauge fields $\mathbf{A}_{\mathbf{k},I} = \langle u_{\mathbf{k},I}| \nabla_{\mathbf{k}} |u_{\mathbf{k},I}\rangle$ and $\mathbf{A}_{\mathbf{k},II} = \langle u_{\mathbf{k},II}| \nabla_{\mathbf{k}} |u_{\mathbf{k},II}\rangle$ are uniquely and smoothly defined respectively on $\mathcal{D}_I$ and $\mathcal{D}_{II}$.

As we did in Sec. 1.3.2 of Chapter 1, we write the Chern number

$$C = \frac{1}{2i\pi} \left(\int_{\mathcal{D}_\mathrm{I}} d^2k \, [\nabla_{\mathbf{k}} \times \mathbf{A}_{\mathbf{k},\mathrm{I}}] \cdot \mathbf{e}_z + \int_{\mathcal{D}_\mathrm{II}} d^2k \, [\nabla_{\mathbf{k}} \times \mathbf{A}_{\mathbf{k},\mathrm{II}}] \cdot \mathbf{e}_z \right). \tag{3.26}$$

Using Stokes' theorem and considering the specific choice of path Γ shown in Fig. 3.3(a) leads to

$$C = \frac{1}{2i\pi} \left(- \oint_\mathrm{P} d\mathbf{k} \cdot \mathbf{A}_{\mathbf{k},\mathrm{I}} + \oint_\mathrm{P} d\mathbf{k} \cdot \mathbf{A}_{\mathbf{k},\mathrm{II}} \right). \tag{3.27}$$

Along Γ, we have $|u_{\mathbf{k},I}\rangle = \mathrm{e}^{-i\varphi(\mathbf{k})} |u_{\mathbf{k},II}\rangle$. We choose $\varphi(\mathbf{k})$ so that it is smooth along the whole Γ path and we obtain

$$C = \frac{1}{2\pi} \oint_\Gamma d\mathbf{k} \cdot \nabla_{\mathbf{k}} \varphi(\mathbf{k}). \tag{3.28}$$

Now, we find C by studying (analytically) how $\varphi(\mathbf{k})$ evolves when moving along Γ. Generally speaking, when the Γ path surround a $\varphi(\mathbf{k})$'s divergence (here at the $\mathbf{M}_2$ point), the accumulated phase increases or decreases by $\pm 2\pi z$, $z \in \mathbb{Z}$, which gives a quantized C, as expected. Here, from the expression of $\varphi(\mathbf{k})$ (see Eq. (3.19)), we find that $\varphi(\mathbf{k})$ changes by $-2\pi \mathrm{sgn}\,(\sin\phi)$ when moving along the entire closed path Γ. This gives

$$C = -\mathrm{sgn}\,(\sin\phi)\,, \; \phi \in]0, \pi[. \tag{3.29}$$

We have performed this computation by (i) determining the value of $\rho(\mathbf{k})e^{i\varphi(\mathbf{k})}$ along the lines $\varepsilon_2(\mathbf{k}) = 0$ and $\varepsilon_3(\mathbf{k}) = 0$ (remind that $\varepsilon_\alpha = -2t\cos(\mathbf{k}\cdot\mathbf{b}_\alpha)$) in the BZ (see Table 3.1) and (ii)

	$\boldsymbol{k}_1$	$\boldsymbol{k}_2$	$\boldsymbol{k}_3$	$\boldsymbol{k}_4$
$E(\mathbf{k})$	< 0	< 0	< 0	< 0
$\varepsilon_1(\mathbf{k})$	< 0	< 0	< 0	< 0
$\varepsilon_2(\mathbf{k})$	0	< 0	0	> 0
$\varepsilon_3(\mathbf{k})$	> 0	0	< 0	0
$\rho(\mathbf{k})e^{i\varphi(\mathbf{k})}$	$-\frac{\varepsilon_3}{2}\Big\|_{\mathbf{k}_1} e^{i(\mathbf{k}_1\cdot\mathbf{b}_2-\phi)}$	$-\frac{E\varepsilon_2}{2\varepsilon_1}\Big\|_{\mathbf{k}_2} e^{i\mathbf{k}_2\cdot\mathbf{b}_2}$	$-\frac{\varepsilon_3}{2}\Big\|_{\mathbf{k}_3} e^{i(\mathbf{k}_3\cdot\mathbf{b}_2-\phi)}$	$-\frac{E\varepsilon_2}{2\varepsilon_1}\Big\|_{\mathbf{k}_4} e^{i\mathbf{k}_4\cdot\mathbf{b}_2}$

Table 3.1: Value of $\rho(\mathbf{k})e^{i\varphi(\mathbf{k})}$ (see Eq. (3.19)) along the lines $\varepsilon_2(\mathbf{k}) = 0$ and $\varepsilon_3(\mathbf{k}) = 0$ (remind that $\varepsilon_\alpha = -2t\cos(\mathbf{k}\cdot\mathbf{b}_\alpha)$) in the Brillouin Zone. As it is sketched in Fig. 3.3(b), the points $\boldsymbol{k}_1$ and $\boldsymbol{k}_3$ belong to the line $\varepsilon_2(\mathbf{k}) = 0$ and the points $\boldsymbol{k}_2$ and $\boldsymbol{k}_4$ belong to the line $\varepsilon_3(\mathbf{k}) = 0$.

studying the sign of $\varepsilon_2(\mathbf{k})$ and $\varepsilon_3(\mathbf{k})$ in the BZ (see Fig. 3.3(b)). As an example, the evolution of $\varphi(\mathbf{k})$ along several portions of the Γ path is shown in Fig. 3.3(b), for $\mathrm{sgn}\,(\sin\phi) > 0$.

From Eq. (3.29), we conclude that all flux $\phi \in]0, \pi[$, the lowest band associated to the model introduced in Sec. 3.1 has non-vanishing Chern number. If the Fermi energy lies in the gap above the lowest band, the system is a Chern insulator, and as we saw it is characterized by one chiral edge mode.

3.2.2 Topological properties observable in small systems with disorder

Here we show that the local density of states and chiral currents show topological features in a noisy 3×3 unit cells system. We also review a method for the computation of the Chern number which relies on the splitting of the energy bands under a weak magnetic field. We show that this method also constitutes a way to probe the topological properties in small noisy systems.

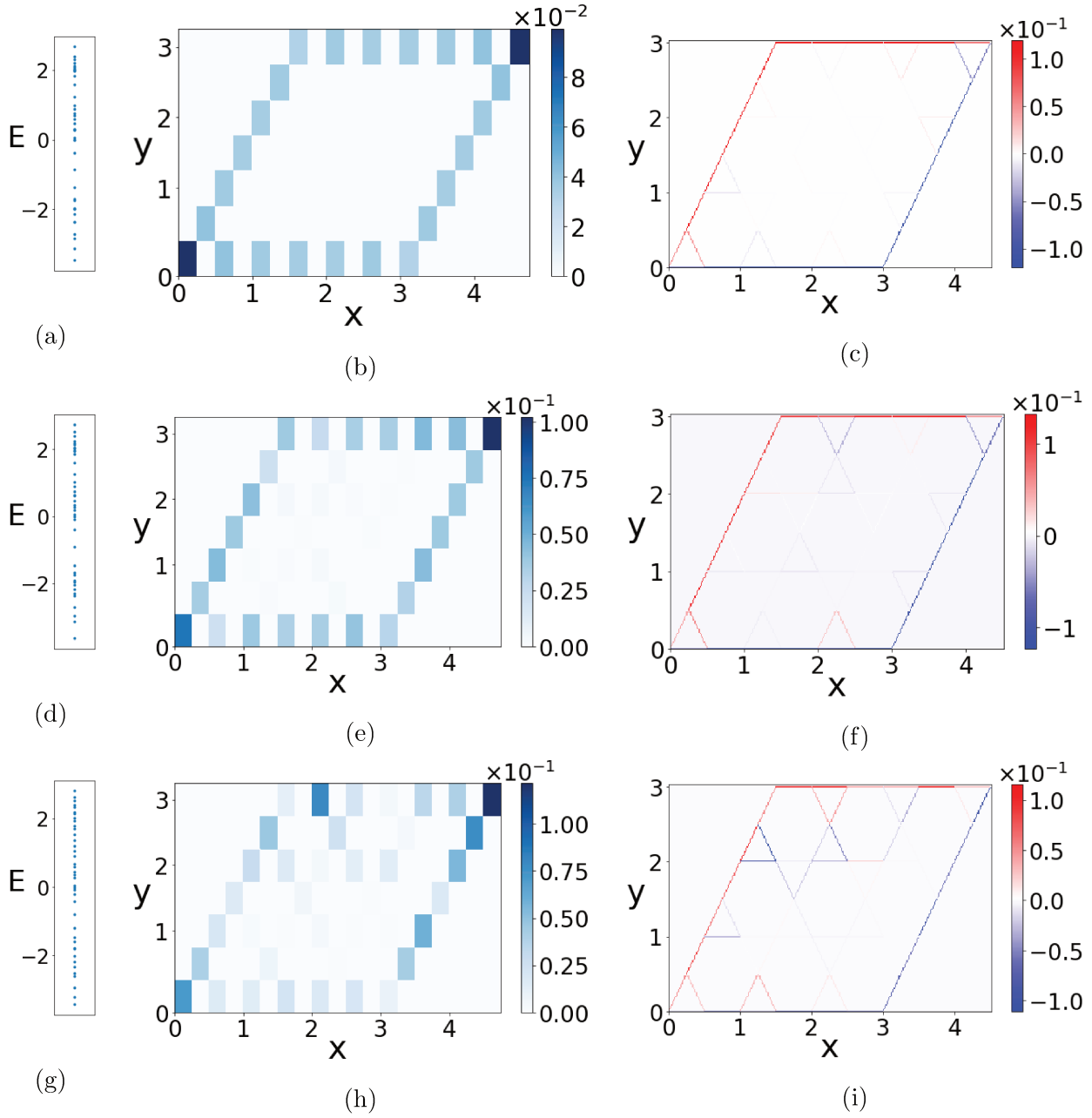

Figure 3.4: Energies (in units of t, Figs. (a), (d) and (g)), local density of states (at $E \approx 1.25\mathbb{E}(t)$, Figs. (b), (e) and (h)) and lattice currents (in units of t/a in Figs. (c), (f) and (i)) in a 9 unit cells kagome system for increasing values of Gaussian noise amplitudes, from top to bottom row: no noise, 10 percent noise, 20 percent noise (see Sec. 3.2.2 for details). We chose $\mathbb{E}(\phi) = 3\pi/4$. For the right panel figures, the color blue or red refers to the current orientation. Along an horizontal path, if the particles moves left (right) the color is blue (red). For non-horizontal path, if the particle moves up (down), the color is red (blue).

Local density of states and chiral currents

Here we compute the energies, the local density of states and the currents for the system described by Eq. (3.8)), in a plane geometry composed of 9 unit cells and adding noise on the parameters. The local density of states reads $\rho(E, \boldsymbol{r}) \equiv \sum_\Psi \delta(E - E_\Psi)|\langle \boldsymbol{r}|\Psi\rangle|^2$ and satisfies the normalization condition $\int dE \sum_{\boldsymbol{r}\in\boldsymbol{R}} \rho(E, \boldsymbol{r}) = N$, where the sum runs over all the eigenstates Ψ of the system, with $\boldsymbol{R}$ the ensemble of all possible lattice sites and $N = 40$ their total number. The current operator between two lattice sites m and n is given by $j_{mn} \equiv -ic_m^\dagger t_{mn} c_n + H.c.$, where t_{mn} is the hopping amplitude (complex term, $-te^{\pm i\phi/3}$ in our case) between m and n.

Numerical evaluation of the local density of states and of the currents shows that for values of the Fermi energy lying between two bulk bands, we observe edge modes (see Figs. 3.4(a) and 3.4(b)) and the localization at the edges of the current expectation value $\sum_\Psi \delta(E - E_\Psi) \langle\Psi| j_{mn} |\Psi\rangle$ (see Fig. 3.4(c)).

We also numerically investigated the effect of Gaussian noise on the chemical potential μ (which is zero everywhere in the ideal case Eq. (3.8)), on the amplitude of the hopping term t and on the flux ϕ. Results are shown in Figs. 3.4(d)-3.4(i) for increasing values of the noise. For Figs. 3.4(d)-3.4(f) and Figs. 3.4(g)-3.4(i) the noise on μ and t is a gaussian distribution with standard deviation respectively equals to $0.1\,\mathbb{E}(t)$ and $0.2\,\mathbb{E}(t)$, where $\mathbb{E}(t)$ is the average value of t; the noise on ϕ is a gaussian distribution with standard deviation respectively equals to $0.1\,\mathbb{E}(\phi)$ and $0.2\,\mathbb{E}(\phi)$ where $\mathbb{E}(\phi)$ is the average value of ϕ. We refer to these amplitudes of noise respectively as "Gaussian noise with amplitude 10 percent" and "Gaussian noise with amplitude 20 percent". We observe that these rather small systems show density of states localized at the edges and chiral currents up to rather large values of Gaussian noise.

Splitting of the energy bands under a weak magnetic field and noise

Here we consider a weak magnetic field $\mathcal{B} = \mathcal{B}\hat{\mathbf{z}}$ orthogonal to the kagome lattice plane. Let us call the energy bands when $\mathcal{B} = 0$ the "parents bands". Under a weak magnetic field, each parent band i ($i = 1$, 2 and 3 label respectively the lowest, the middle and the highest energy bands) is split into a certain number of subbands that we denote D_i. There is a relation between this number, the amplitude of the magnetic field and the Chern number C_i associated to the i^{th} parent band [34, 194]. We introduce $f = qn_\phi$ where $n_\phi = \dfrac{\mathcal{B}a^2}{h/e}$ is the number of flux quanta in the system and q is the area of the first magnetic Brillouin zone. In the following, we choose $\mathcal{B}$ such that $1/f$ is an integer. Then we have:

$$C_i = D_i - \frac{1}{f}. \tag{3.30}$$

We implemented the effect of the magnetic field for the Hamiltonian in Eq. (3.8) for a cylinder geometry (periodic boundary conditions only in one direction of the lattice) and for a square geometry (periodic boundary conditions in both directions of the lattice). We also considered the same gaussian noise than the one considered in the previous section, with a smaller amplitude: the noise on μ and t is a gaussian distribution with standard deviation respectively equals to $0.01\,\mathbb{E}\,(t)$ and the noise on ϕ is a gaussian distribution with standard deviation respectively equals to $0.01\,\mathbb{E}\,(\phi)$. We call this noise "Gaussian noise with amplitude 1 percent". We investigated systems of sizes 10×5 unit cells and 10×10 unit cells for the cylinder geometry and 27×27 units cells for the square geometry; the density of states $\rho(E) \equiv \sum_\Psi \delta(E - E_\Psi)/N$ in such systems are reported in Fig. 3.5 (for $\mathbb{E}\,(\phi) > 0$). In the last equation, the sum runs over all the eigenstates Ψ of the system, and $N = 40$ is the total number of lattice sites. We see that we have $D_1 = 4$ subbands, $D_2 = 5$ subbands and $D_3 = 6$ subbands, which gives, considering that we used $1/f = 5$, $C_1 = -C_3 = -1$, and $C_2 = 0$.

It seems that larger noises makes ineffective the method for probing the Chern number. Keeping the same system sizes or smaller, maybe if one would optimize the detection of

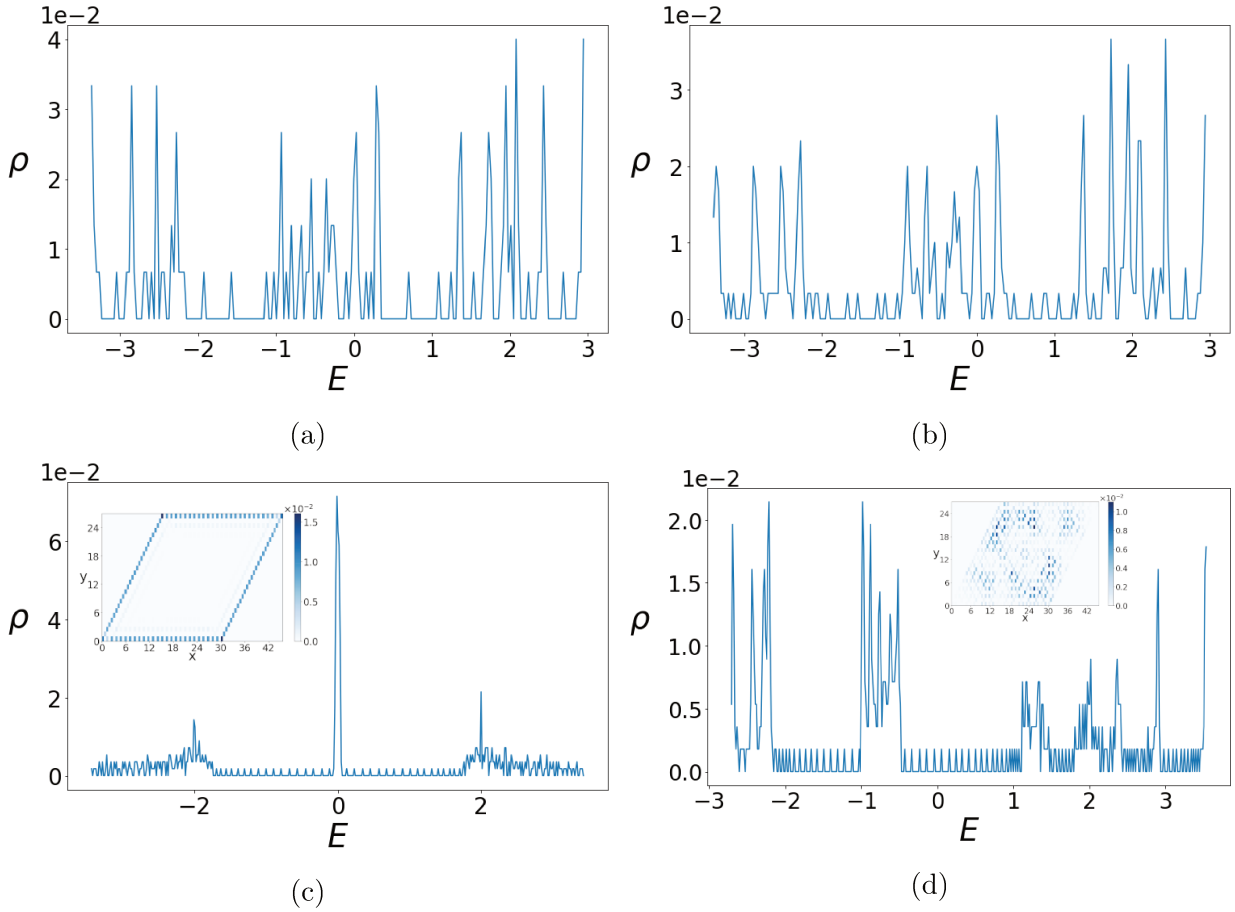

Figure 3.5: Splitting of the energy bands for the system described by Eq. (3.8) under a weak magnetic field ($1/f = 5$, see text) on open noisy systems with non-vanishing Chern numbers. (a) and (b) show the density of states $\rho(E)$ at $1/f = 5$ for a cylinder geometry of size respectively 5×10 and 10×10 (number of unit cells in the translation invariant direction $\times$ numbers of unit cells in the direction perpendicular to the edges of the system). (c) Density of states (here at vanishing magnetic field), for a square geometry of size 27×27 unit cells. (d) Density of states $\rho(E)$ under a weak magnetic field ($1/f = 5$), for a square geometry of size 27×27 unit cells. The insets in Fig.(c) and (d) show the local density of states. For all the figures, we considered a "Gaussian noise with amplitude 1 percent" (see text in Sec. 3.2.2) and we considered $\mathbb{E}(\phi) = \pi/2$.

the density of states pics the method would still be efficient up to, say Gaussian noise with amplitude 5 percent. However, it seems out of reach that this method works at Gaussian noise with amplitudes 10 or 20 percent, which are yet values at which we know that the local density of states and the currents still shows topological properties for such small systems

(see Fig. 3.5(c) and previous subsection).

3.3 Computation of the $\mathbb{Z}_2$ number with spin and inversion symmetries

In this section, we consider two spin copies of the two-dimensional Hamiltonian in Eq. (3.8), with opposite flux associated to each spin copies (this is required to conserve time-reversal symmetry, see Sec. 1.4):

$$H = -t \sum_{\langle ij \rangle} c_i^\dagger \mathrm{e}^{-i\phi s_z \nu_{ij}/3} c_j, \tag{3.31}$$

with $c_i^\dagger = \left(c_{i,\uparrow}^\dagger, c_{i,\downarrow}^\dagger\right)$ and s_z is the third Pauli matrix acting in spin space, as we defined in Sec. 1.4. We compute the $\mathbb{Z}_2$ in such a system, relying either on the conservation of the spin number along the out-of-plane direction or on the conservation of the inversion symmetry.

3.3.1 $\mathbb{Z}_2$ number and edge states for systems with conserved spin number along the out-of-plane direction

$\mathbb{Z}_2$ number If the Hamiltonian commutes with the spin operator along the out-of-plane axis (which is the case for the system we consider here), $s_z/2$, then each band can be labeled by $\sigma = \{\uparrow, \downarrow\}$ which identify the eigenvalues of $s_z/2$. We are interested by the value of the $\mathbb{Z}_2$ number when the Fermi level lies in the bulk gap between the lowest bands and the middle bands. The procedure to obtain the $\mathbb{Z}_2$ number if the Fermi level lies in the bulk gap between the middle bands and the highest bands or if the Fermi level lies above the highest bands is similar. Let us denote the σ-band Chern number C_σ and we call it the spin-σ Chern number. When s_z is conserved, the $\mathbb{Z}_2$ number is the difference between both spin Chern numbers (see Sec. 1.4.1 or Refs. [48, 189]):

$$\nu = \frac{1}{2}\left(C_\uparrow - C_\downarrow\right) \bmod 2 = C_\uparrow \bmod 2. \tag{3.32}$$

From Eq. (3.29), we deduce that

$$\nu = 1 \, \forall \phi \in]0, \pi[, \tag{3.33a}$$

$$\nu = 0 \, \forall \phi \in \{0, \pi\}. \tag{3.33b}$$

Edge states As we explained in Sec. 1.4, the $\nu = 1$ phase is associated with opposite-spin counter-propagating modes at each edge of the system. We can also extend the results of the "edge state" paragraph of Sec. 3.1, by performing the same analysis for each spin σ species, and labelling each quantity by σ (namely $\phi \to \phi_\sigma$ and $\lambda_\pm \to \lambda_{\pm,\sigma}$). In Fig. 3.6, we show the energy dispersion relation for a system described by the Hamiltonian in Eq. (3.31) in a cylinder geometry. Counter-propagating modes which connect the bulk bands appear clearly and the numerical evaluation of the associated local density of state shows their localization at the edges of the system. We also have $\lambda_{-,\uparrow} = \dfrac{1}{\lambda_{-,\downarrow}}$ because of the replacement $\phi_\uparrow = -\phi_\downarrow$ and $\lambda_{-,\uparrow}(q_1) = \dfrac{1}{\lambda_{-,\uparrow}(-q_1)}$ so we get $\lambda_{-,\uparrow}(q_1) = \lambda_{-,\downarrow}(-q_1)$ which shows that opposite spin species with opposite velocities are localized at each edge of the system.

3.3.2 Computation of the $\mathbb{Z}_2$ invariant in inversion symmetric systems

Here we use the invariance of the topological number under a $U(1)$ local gauge transformation, so we consider two spin copies of the Hamiltonian in Eq. (3.10b), with opposite flux associated to each spin copies. The purpose of this section is to show another way of computing the $\mathbb{Z}_2$ invariant. We use this method in Chapter 5 to check the results obtained from the method introduced in the previous sections.

For a two-dimensional system

For a two-dimensional system invariant under inversion symmetry ($\mathbf{r} \to -\mathbf{r}$), the Z_2 topological invariant ν (defined for time reversal invariant Hamiltonian, *i.e.* $B = 0$) is given by

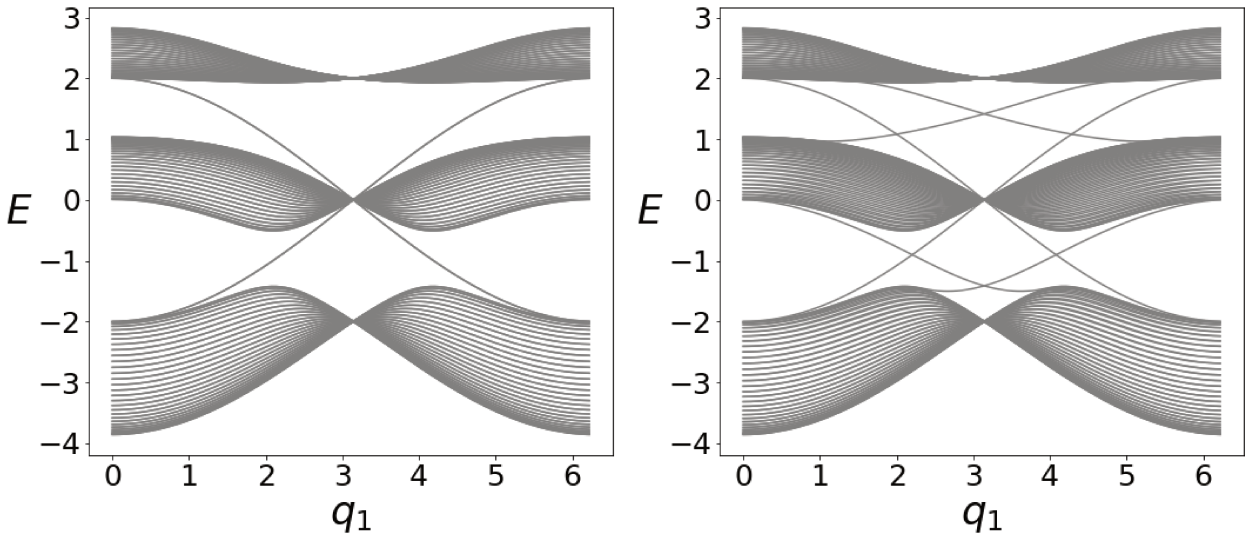

(a) (b)

Figure 3.6: Dispersion relation for the spin system considered in Sec. 3.3.1, associated to the Hamiltonian (3.31), in a cylinder geometry with flux $\phi = 3\pi/4$ and for different boundary shapes. Below the dispersion relations figures, we show a sketch (it is taken from Ref. [34]) of small systems with the boundary shape considered for the computation of the energies: (a) corresponds to the line-line boundaries while (b) corresponds to the line-armchair boundaries. The numerical computation shows that the edge modes which appear in (a) are degenerate twice (for all the momenta q_1) while the edge modes which appear in (a) are degenerate twice only for few specific values of the momenta q_1 (namely the time-reversal invariant momenta). In both figures, there are therefore two time-reversed pairs of edge modes; these pairs are localized at opposite edges of the system.

[39, 190]

$$(-1)^{\nu} = \prod_{\substack{n_1=0,1 \\ n_2=0,1}} \delta_{(n_1,n_2)}, \tag{3.34}$$

with $\delta_{(n_1,n_2)} = \prod_{m=1}^{N} p_{2m}\left(\Gamma_{(n_1,n_2)}\right)$ is the product of the parity eigenvalues p_{2m}, at $\Gamma_{(n_1,n_2)}$, associated to each occupied Kramer's degenerate pair (p_{2m} and p_{2m-1} are identical). The $\Gamma_{(n_1,n_2)}$ points are the time-reversal invariant points, *i.e.* the points such that $H(\Gamma_{(n_1,n_2)}) = \Theta H(\Gamma_{(n_1,n_2)})\Theta^{-1}$. These points can be written

$$\Gamma_{(n_1,n_2)} = \frac{1}{2}\left(n_1 \boldsymbol{g}_1 + n_2 \boldsymbol{g}_2\right), \tag{3.35}$$

with $\boldsymbol{g}_1$ and $\boldsymbol{g}_2$ both reciprocal lattice basis vectors. These points correspond to the so-called $\mathbf{\Gamma}$ point and to the three $\mathbf{M}$ points.

For a topological model on the kagome lattice

As in Sec. 3.3.1, we are interested by the value of the $\mathbb{Z}_2$ number when the Fermi level lies in the bulk gap between the lowest bands and the middle bands. We rely on the Eq. (3.34); we first need the parity eigenvalues p_{2m} associated to each of the four $\Gamma_{(n_1,n_2)}$ points so we need to express the Hamiltonian and the momentum space parity operator at these points. Eq. (3.34) only implies the parity eigenvalues associated to one of the lowest band, because the parity eigenvalues associated to the other band are identical. Here, as we mentioned in the previous section, each band can be label by $\sigma = \{\uparrow, \downarrow\}$ which identify the eigenvalues of $s_z/2$. Therefore, in the following, we consider separately each of both diagonal H_σ parts of the Hamiltonian $H = \sum_\sigma H_\sigma$.

The parity operator can be defined in real space by

$$P\left(c_{R,\boldsymbol{r}}, c_{B,\boldsymbol{r}}, c_{G,\boldsymbol{r}}\right) = \left(c_{R,-\boldsymbol{r}}, c_{B,-\boldsymbol{r}-\boldsymbol{e}_1}, c_{G,-\boldsymbol{r}-\boldsymbol{e}_2}\right). \tag{3.36}$$

A Fourier transformation of the fermionic operators enables to see that, in momentum space, the parity operator reads

$$P_{\boldsymbol{k}} = \mathrm{diag}\left(1, \mathrm{e}^{-i\boldsymbol{e}_1\boldsymbol{k}}, \mathrm{e}^{-i\boldsymbol{e}_2\boldsymbol{k}}\right). \tag{3.37}$$

Therefore, at the $\mathbf{\Gamma}_{(0,0)}$ point, $P_{\mathbf{\Gamma}_{(0,0)}}$ is diagonal so $\delta_{(0,0)} = 1$ and at the other points we have $P_{\mathbf{\Gamma}_{(1,0)}} = \mathrm{diag}\,(1,-1,1)$, $P_{\mathbf{\Gamma}_{(0,1)}} = \mathrm{diag}\,(1,1,-1)$, and $P_{\mathbf{\Gamma}_{(1,1)}} = \mathrm{diag}\,(1,-1,-1)$.

Now we need to evaluate the lowest energy associated eigenvectors of $\mathcal{H}_\sigma(\mathbf{k})$ at $\mathbf{\Gamma}_{(1,0)}$,

$\mathbf{\Gamma}_{(0,1)}$, and $\mathbf{\Gamma}_{(1,1)}$. This is straightforward here since we have

$$\mathcal{H}_\sigma(\mathbf{\Gamma}_{(1,0)})=\begin{pmatrix} 0 & 0 & -2t \\ 0 & 0 & 0 \\ -2t & 0 & 0 \end{pmatrix}, \tag{3.38a}$$

$$\mathcal{H}_\sigma(\mathbf{\Gamma}_{(0,1)})=\begin{pmatrix} 0 & -2t & 0 \\ -2t & 0 & 0 \\ 0 & 0 & 0 \end{pmatrix}, \tag{3.38b}$$

$$\mathcal{H}_\sigma(\mathbf{\Gamma}_{(1,1)})=\begin{pmatrix} 0 & 0 & 0 \\ 0 & 0 & -2te^{is_z\phi} \\ 0 & -2te^{-is_z\phi} & 0 \end{pmatrix}. \tag{3.38c}$$

We denote the lowest energy eigenvalue $E_l(\boldsymbol{k})$ and we write the $|u_{\sigma,\boldsymbol{k}}\rangle$ the σ spin species associated eigenvector

$$|u_{\sigma,\boldsymbol{k}}\rangle = \frac{\left(r_\sigma(\boldsymbol{k})c^\dagger_{R,\mathbf{k},\sigma} + b_\sigma(\boldsymbol{k})c^\dagger_{B,\mathbf{k},\sigma} + g_\sigma(\boldsymbol{k})c^\dagger_{G,\mathbf{k},\sigma}\right)|0\rangle}{\sqrt{|r_\sigma(\boldsymbol{k})|^2 + |b_\sigma(\boldsymbol{k})|^2 + |g_\sigma(\boldsymbol{k})|^2}}. \tag{3.39}$$

At the points $\mathbf{\Gamma}_{(1,0)}$, $\mathbf{\Gamma}_{(0,1)}$ and $\mathbf{\Gamma}_{(1,1)}$ the smallest energy eigenvalues are $E_l = -2t$ and the associated eigenvector are proportional to

(i) $(-1, 0, 1)$ at the $\mathbf{\Gamma}_{(1,0)}$ point,

(ii) $(-2t/(\lambda + E_l), 1, 0)$ at the $\mathbf{\Gamma}_{(0,1)}$ point,

(iii) $(0, 2te^{is_z\phi}/(\lambda - E_l), 1)$ at the $\mathbf{\Gamma}_{(1,1)}$ point.

Applying the parity operator on the eigenvectors, we find that the system studied here is a topological insulator. Of course, this is valid when $\phi \neq \{0, \pi\}$ which is the condition for which the system is insulating. These results are sum up in table 3.2.

3.4 Conclusion

We have adapted several methods for the computation of the Chern number for a topological model on the kagome lattice. These models are the elementary topological building blocks of the models we study in the following chapters.

(n_1, n_2)	Eigenvalues E_l	$(r_\sigma(\boldsymbol{k}), b_\sigma(\boldsymbol{k}), g_\sigma(\boldsymbol{k}))$	Parity operator	$(-1)^\nu$
$(1,0)$	$-2t$	$(-1,0,1)$	$\mathrm{diag}(1,-1,1)$	
$(0,1)$	$-2t$	$(-1,1,0)$	$\mathrm{diag}(1,1,-1)$	-1
$(1,1)$	$-2t$	$(0,-\mathrm{e}^{is_z\phi},1)$	$\mathrm{diag}(1,-1,-1)$	

Table 3.2: Table summarizing the computation of the Z_2 topological invariant ν for an inversion and time-reversal symmetric system. (n_1, n_2) are defined in Eq. (3.35), and the eigenvector's coefficient $(r_\sigma(\boldsymbol{k}), b_\sigma(\boldsymbol{k}), g_\sigma(\boldsymbol{k}))$ is defined in Sec. 3.39.

First, using Eq. (1.79) of Chapter 1, we have explicitly performed the computation of the lowest band's Chern number in a kagome system. We notice that this computation is more involved because the kagome lattice contains three colors per unit cell. Again, when the system is topologically non-trivial, we made two different gauge choices for two complementary domains in the Brillouin zone, but here, one of both domains contains one of the time-reversal invariant momenta. We also computed the $\mathbb{Z}_2$ invariant relying on spin and inversion symmetry [48, 189, 190] and we commented on the appearance of edge states for two spin copies of the kagome system introduced in Sec. 3.1. In Chapter 5, we use these methods for the computation of the $\mathbb{Z}_2$ invariant for different sets of chemical potentials.

We also showed the robustness of the topological properties in small (9×9 unit cells) square systems against Gaussian noise on the parameters: even for large values of the noise, the local density of states and the chiral currents show topological features. We compared this with another probe of the topological features: under a weak out-of-plane magnetic field, each ("parent") energy bands is split into a number of subbands that depends on the "parent band's" Chern number [34, 194]. From the numerical evaluation of the density of states, at magnetic field $1/f = 5$ (see Sec. 3.2.2), we achieved to retrieve the bands' Chern number from this method only for systems of size larger than about 30×30 unit cells and with Gaussian noise amplitude smaller than about 1 percent.

Chapter 4

A magnetic and topological kagome system

In this chapter, we propose a model on the kagome lattice which, under the variation of an external parameter, shows a transition from a magnetic Chern insulator, to an in-plane magnetic order possibly associated to a quantum spin Hall phase [193]. The external parameter is either the temperature or the pressure; we justify that the model we study is associated to a disordered phase at high values of this external parameter.

We apply this model to the Weyl semimetal $Co_3Sn_2S_2$ which has recently attracted much attention [25–28, 38, 43]. The crystal structure of this material shows two-dimensional stacked sheets of cobalt atoms which are arranged in a kagome lattice inside each sheet. Under a variation of external parameters, such as the temperature or the pressure, this material shows a magnetic transition, from an out-of-plane ferromagnetic phase at low temperature and low pressure going through an {out-of-plane ferromagnetic + in-plane antiferromagnetic} phase and possibly (depending on the temperature and the pressure) reaching a paramagnetic phase. In this material, a large anomalous Hall effect is observed, with Hall conductivity correlated to the ferromagnetic fraction [26, 27].

The magnetic and topological properties depend on the Coulomb-interaction strength [196–198], which has been estimated around 4eV in $Co_3Sn_2S_2$ [28]. On the other hand, spin-orbit coupling plays an essential role for the appearance of the anomalous Hall effect and its

quantized version [4, 109, 112]. It appears that Kagome materials are good candidates for investigating physical effect due to spin-orbit coupling. Indeed, spin-orbit coupling is found to open non-negligible gaps in diverse kagome materials, *e.g.* gaps of amplitudes ~ 30 meV in Fe_3Sn_2 [37] and in $TbMn_6Sn_6$ [192], ~ 20 meV in $Cs_2Mn_3F_{12}$ [36]. In $Co_3Sn_2S_2$, spin-orbit coupling also has large amplitude and is deeply related to the anomalous Hall properties [25–28, 38, 199].

A very common framework for studying magnetic ordered phases is the Heisenberg spin model. This model shows interesting phases on triangular lattices, because these lattices are frustrated. On the kagome lattice, the classical limit of the Heisenberg model, which shows a large ground state degeneracy [200–205] and its quantum limit [206–216] have been extensively studied. Diverse numerical and analytical approaches have been employed to tackle Heisenberg models on the kagome lattice, for instance, spin-wave theory and high-temperature expansions [200, 201], Monte Carlo methods [202, 203], exact diagonalization [210, 217, 218], density-matrix renormalization-group computations [213, 215, 219]. The ground state at the isotropic (antiferromagnetic) Heisenberg point on the kagome lattice seems to be a spin-liquid phase.

In the model we develop here, the magnetic properties are described by an anisotropic Ising ferromagnetic Heisenberg model on the kagome lattice. We study this model first evaluating the classical ground states and then using a spin wave approach to investigate the stability. Exact diagonalization study of this model has been performed in Ref. [220]. In the model we introduce in this chapter, the magnetic properties result from a channel associated to localized spins on the kagome lattice, while the topological properties result from a channel associated to itinerant electrons on this same lattice. Both channels are coupled via a ferromagnetic Hund's coupling.

At the microscopic level, one channel contains half-filled orbitals, in which the spin particles experience a large on-site Hubbard interaction which gives rise to Mott physics. In this

limit of a large Hubbard interaction, perturbation theory gives an antiferromagnetic nearest neighbor effective spin Hamiltonian and each particle is considered to be localized on each kagome lattice site. We study these localized spin particles in the limit of large spin. The other channel contains low-energy mobile electrons which are coupled to the first channel via a large Hund's coupling [216, 221, 222] that we consider to occur along the out-of-plane direction. We consider a double-exchange mechanism [221, 223–226] which induces nearest neighbor ferromagnetic J_z coupling between the localized spins. The low-energy electronic properties of our model are given by mobile electrons which are described by a tight-binding model with spin-orbit coupling [11, 36, 227, 228].

4.1 Hamiltonian

In this section, we first build an effective spin model for the description of the half-filled orbitals (denoted O_S) in which the spin particles experience a large Hubbard interaction (or with small exchange integral between neighbors, *i.e.* strong localization around the atomic centers). This results in a Mott state with localized spin particles. Then we write the Hamiltonian for the mobile electrons and their coupling with the localized spins.

4.1.1 Localized spins

We first consider a simple microscopic model with a nearest neighbor hopping term and a Hubbard interaction term for the spins in the orbitals O_S. The former term reads

$$-t_S \sum_{\langle ij\rangle,\sigma} C^\dagger_{i\sigma} C_{j\sigma}, \tag{4.1}$$

where t_S is a real parameter, the sum runs over all lattice nearest neighbors, and $C_{i\sigma}$ is the annihilation operator of a spin σ particle in the orbital O_S centered at the lattice site i. The Hubbard interaction term reads

$$U \sum_i n_{i\uparrow} n_{i\downarrow}, \tag{4.2}$$

with $U \gg t$, $n_{i\sigma} = C^\dagger_{i\sigma} C_{i\sigma}$, where the sum runs over all lattice sites and over both spin polarizations $\sigma = \{\uparrow, \downarrow\}$.

Effective spin Hamiltonian We use perturbation theory to get an effective Hamiltonian $\mathcal{H}_{\text{eff}}$ (see App. F) in the strong interaction limit, *i.e.* U is large compared to t_S. We denote

$$\mathcal{H}_0 = U \sum_i n_{i\uparrow} n_{i\downarrow}, \tag{4.3a}$$

$$V = -t_S \sum_{\langle ij \rangle, \sigma} C^\dagger_{i\sigma} C_{j\sigma}, \tag{4.3b}$$

We consider that the orbitals are half-filled, *i.e.* $N_S = N$, with N_S the total number of spin particles in the orbitals O_S and N the number of lattice sites. The ground states of $\mathcal{H}_0$ are states with exactly one particle at each sub-lattice sites. These states are linear combinations of the $\sim 2^N$ states $|\sigma_1 \dots \sigma_N\rangle$, with $\sigma_i = \{\uparrow, \downarrow\}$, for $i \in [1 \dots N]$. The first order terms (with respect to t_S/U) of the effective Hamiltonian, $\langle \psi' | V | \psi \rangle$, where $|\psi\rangle$ and $|\psi'\rangle$ belong to the ground state subspace (denoted S_0), vanish. Indeed, $V|\psi\rangle$ are linear combination of states with two particles on some site i and zero particle of some site j. The second order terms of $\mathcal{H}_{\text{eff}}$ are

$$\langle \psi' | \mathcal{H}_{\text{eff}} | \psi \rangle = t_S^2 \sum_{|m\rangle \notin \mathcal{H}_I} \sum_{\substack{\langle ij \rangle, \langle kl \rangle, \\ \sigma, \sigma'}} \frac{\langle \psi' | C^\dagger_{i\sigma'} C_{j\sigma'} | m \rangle \langle m | C^\dagger_{k\sigma} C_{l\sigma} | \psi \rangle}{-E_m}, \tag{4.4}$$

with $|m\rangle$ the eigenstates of $\mathcal{H}_0$ which do not belong to the ground states subspace S_0 and E_m the corresponding eigenenergy. The numerator of the equation (4.4) is non vanishing only if $|m\rangle = C^\dagger_{k\sigma} C_{l\sigma} |\psi\rangle$ and if $|m\rangle = C^\dagger_{j\sigma'} C_{i\sigma'} |\psi'\rangle$ so if $k = j$ and $l = i$ and for these states $E_m = U$. Therefore we have

$$\mathcal{H}_{\text{eff}} = -\frac{t_S^2}{U} \sum_{\substack{\langle ij \rangle, \\ \sigma, \sigma'}} C^\dagger_{i\sigma'} C_{j\sigma'} C^\dagger_{j\sigma} C_{i\sigma}. \tag{4.5}$$

Using the fermionic anti-commutation relations we get

$$C^\dagger_{i\sigma'} C_{j\sigma'} C^\dagger_{j\sigma} C_{i\sigma} = -C^\dagger_{i\sigma'} C_{i\sigma} C^\dagger_{j\sigma} C_{j\sigma'} + \delta_{\sigma\sigma'} n_{i\sigma},$$

and using $\sum_\sigma n_{i\sigma} \overset{\text{def}}{=\!=} n_i = 1$ ($\mathcal{H}_{\text{eff}}$ acts on a ground state), we get

$$\sum_\sigma C^\dagger_{i\sigma} C_{j\sigma} C^\dagger_{j\sigma} C_{i\sigma} = -2 S^z_i S^z_j + \frac{1}{2},$$

and

$$\sum_{\substack{\sigma\sigma' \\ \sigma\neq\sigma'}} C^\dagger_{i\sigma'} C_{j\sigma'} C^\dagger_{j\sigma} C_{i\sigma} = -2 \left(S^x_i S^x_j + S^y_i S^y_j \right),$$

where $S^r_i = \frac{1}{2} C^\dagger_{i,\sigma} \sigma^r_{\sigma,\sigma'} C_{i,\sigma'}$ (implicit summation on repeated indices) and $\sigma^r_{\sigma,\sigma'}$, $r = \{x, y, z\}$ are the Pauli matrices. This gives, up to the constant energy term $-J_{t_S}/4$,

$$\mathcal{H}_{\text{eff}} = \sum_{\langle ij \rangle} \left[J_{t_S} S^z_i S^z_j + J_{t_S} \left(S^x_i S^x_j + S^y_i S^y_j \right) \right], \tag{4.6}$$

with $J_{t_S} = \dfrac{4t_S^2}{U} > 0$.

Let us mention that, if we also consider a nearest-neighbor spin-orbit coupling term for the orbitals O_S, the effective Hamiltonian reads, up to the constant energy term $-(J_{t_S} + J_{\lambda_S})/4$,

$$\mathcal{H}_{\text{eff}} = \sum_{\langle ij \rangle} \left[\left(J_{t_S} + J_{\lambda_S} \right) S^z_i S^z_j + \left(J_{t_S} - J_{\lambda_S} \right) \left(S^x_i S^x_j + S^y_i S^y_j \right) \right], \tag{4.7}$$

with $J_{\lambda_S} = \dfrac{4{\lambda_S}^2}{U} > 0$ and λ_S is the amplitude of the spin-orbit coupling term given by

$$-i\lambda_S \sum_{\langle ij \rangle, \sigma} \nu_{ij} C^\dagger_{i\sigma} \sigma^z_{\sigma\sigma'} C_{j\sigma'}, \tag{4.8}$$

the sum runs over all nearest-neighbors i and j and $\nu_{ij} = +1$ or -1 if, respectively, the particle jumps counter clockwise or clockwise inside the considered triangle of the kagome lattice. The presence of this term has no important consequence on the study performed in the following. In $Co_3Sn_2S_2$, band-structure numerical calculations indicate that spin-orbit coupling has a negligible effect on the magnetic properties [229].

This Hamiltonian, valid in the strong interaction limit, acts on the ground state where there is one electron per site. As we discussed in the introduction of this Chapter, we

treat these localized spins classically in the limit of large spin S. These spins are coupled to itinerant electrons via a large Hund's coupling [216, 221, 222] in the **z** direction. This leads to a double-exchange mechanism [221, 223, 224] which induces nearest neighbor coupling (its amplitude is denoted $-J_H$) between the localized spins that we assume to be of ferromagnetic ($J_H > 0$). The total spin Hamiltonian then reads

$$\mathcal{H}_S = \sum_{\langle ij \rangle} \left[-J_z S_i^z S_j^z + J_{xy} \left(S_i^x S_j^x + S_i^y S_j^y \right) \right], \tag{4.9}$$

with $-J_z = -J_H + J_{t_S} + J_{\lambda_S}$ and $J_{xy} = J_{t_S} - J_{\lambda_S}$. In the following we consider $J_H > J_{t_S} + J_{\lambda_S}$, *i.e.* $J_z > 0$.

We notice that this model breaks continuous rotational symmetry and may show spontaneous magnetization (with finite temperature phase transition) in the **z** direction for finite temperature, particularly for the "Ising ferromagnetic" regime $J_{xy}/J_z < 1$, contrarily to the isotropic Heisenberg model for which the lower critical dimension is 2 [230]. In fact, at zero temperature, we show in the Sec. 4.2.1 that because of the geometry of the kagome lattice, the transition point is $J_{xy}/J_z = 2$, the classical ground state being ferromagnetic for $J_{xy}/J_z < 2$.

4.1.2 Itinerant electrons and Hund's coupling

Here we write the Hamiltonian associated to the itinerant spins and their coupling with the localized spin in the orbitals O_S. The itinerant electrons are assumed to belong to orbitals (denoted O_i) with large spatial extension around the lattice site and the amplitude of the Hubbard interaction in these orbitals is much smaller than in the O_S orbitals. Here we write a microscopic model for the itinerant electrons where we take into account a nearest neighbor hopping term, a nearest neighbor spin-orbit coupling term and a ferromagnetic Hund's coupling between the itinerant electrons and the localized spins. In $Co_3Sn_2S_2$, ab-initio band-structure calculations suggest that the states near the Fermi energy are mainly associated to the cobalt 3d orbitals [229, 231, 232].

Nearest-neighbors hopping term The nearest neighbor hopping term (denoted H_t), which results from the exchange integral between the orbitals O_i at nearest neighbor sites, reads

$$H_t = -t_i \sum_{\langle ij \rangle, \sigma} c^\dagger_{i\sigma} c_{j\sigma}, \tag{4.10}$$

where t is a real parameter, the sum runs over all lattice nearest neighbors, and $c_{i\sigma}$ is the annihilation operator of a spin σ polarized itinerant electron in the orbital O_e centered at the atomic site i. The sum runs over all lattice nearest-neighbors i and j and over both spin polarizations for α.

Nearest neighbor spin orbit coupling The spin-orbit coupling term, which takes into account the coupling between an itinerant electron's spin and its motion in the lattice potential, is $L_z s_z$ because the system is invariant under mirror reflection about the lattice plane (see Refs. [11, 36, 109, 133, 228] and also Sec. 1.4.1). The kagome lattice is not invariant under the mirror transformation about vertical reflection plane along a nearest-neighbor bond, so the nearest-neighbor spin orbit coupling is a priori not vanishing. We write this term H_{SO}, its amplitude λ_i, and we have

$$H_{SO} = -i\lambda_i \sum_{\langle ij \rangle, \alpha, \beta} \nu_{ij} c^\dagger_i \sigma^z c_j = -i\lambda_i \sum_{\langle ij \rangle} \nu_{ij} \left(c^\dagger_{i\uparrow} c_{j\uparrow} - c^\dagger_{i\downarrow} c_{j\downarrow} \right), \tag{4.11}$$

with $c^\dagger_i = \left(c^\dagger_{i,\uparrow}, c^\dagger_{i,\downarrow} \right)$, σ^z is the third Pauli matrix acting in spin space, the sum runs over all nearest-neighbors i and j and $\nu_{ij} = +1$ or -1 if, respectively, the electron jumps counter clockwise or clockwise inside the considered triangle of the kagome lattice. In fact, it is shown in many kagome systems that this term is indeed not vanishing and that its amplitude is large and has important electronic consequences [36, 37, 192, 199].

Ferromagnetic Hund's coupling We define $\boldsymbol{s}_i = (s^x_i, s^y_i, s^z_i)$ the spin operator acting on the itinerant electron spins and $\boldsymbol{S}_i = (s^x_i, s^y_i, s^z_i)$ the spin operator acting on the localized spins. As we already mentionned, we consider a strong Hund's coupling in the $\hat{\boldsymbol{z}}$ direction

between the localized spins and the itinerant electron spins. The associated Hamiltonian is denoted H_h and reads

$$H_h = -h_c \sum_i S_i^z s_i^z = -\frac{h_c}{2} \sum_i S_i^z \left(c_{i\uparrow}^\dagger c_{i\uparrow} - c_{i\downarrow}^\dagger c_{i\downarrow} \right), \tag{4.12}$$

where h_c is the (real) amplitude of the coupling.

4.2 Magnetic order in the large spin S limit

In Sec. 4.2.1, we determine the classical ground state from a minimization of the energy associated to this spin Hamiltonian. In Sec. 4.2.2, we investigate the stability of this ground state against quantum fluctuations in the large spin limit.

4.2.1 Energy minimization and classical magnetic state

We now compute the ground state of this spin Hamiltonian in the classical limit of large spin S. We write the value of the spin operators in the classical ground state $\langle S_i^x \rangle = S \sin\theta_i \cos\varphi_i$, $\langle S_i^y \rangle = S \sin\theta_i \sin\varphi_i$, and $\langle S_i^z \rangle = S \cos\theta_i$, with $\theta_i \in [0, \pi]$, and $\varphi_i \in [0, 2\pi]$ and S is the norm of the spins in the classical ground state. In this limit, we obtain

$$\mathcal{H}_S = S^2 \sum_{\langle ij \rangle} \left[-J_z \cos\theta_i \cos\theta_j + J_{xy} \sin\theta_i \sin\theta_j \cos(\phi_i - \phi_j) \right]. \tag{4.13}$$

We determine the classical ground state from a minimization of the energy associated to this spin Hamiltonian. The magnetic state results from the competition between ferromagnetism in the **z** direction and antiferromagnetism in the xy plane.

The energy reaches its minima in the parameter space made up of the θ_i at all the lattice sites i if we have

$$\theta_i = \theta_j = \{0, \pi/2, \pi\}, \tag{4.14}$$

or

$$\frac{-J_z}{J_{xy}} = \frac{\tan\theta_j}{\tan\theta_i} \cos(\phi_i - \phi_j) = \frac{\tan\theta_i}{\tan\theta_j} \cos(\phi_i - \phi_j) \qquad \forall (\theta_i, \theta_j) \in (]0, \pi/2[\cup]\pi/2, \pi[)^2, \tag{4.15}$$

for all j such that i and j are nearest-neighbor sites. The last condition, when considering the nearest neighbours in a triangle of the kagome lattice, gives $\theta_i = \theta_j \overset{\text{def}}{=\!=} \theta$. Therefore, gathering both conditions (4.14) and (4.15) gives $\theta_i = \theta_j \overset{\text{def}}{=\!=} \theta,\ \forall(\theta_i, \theta_j) \in ([0, \pi])^2$.

Now, given this constraint (all the angles θ_i are the same for the minimum energy), we look for the configuration(s) of the angles ϕ_i which minimize(s) the energy. First let us seek this condition for an arbitrary triangle of the lattice and then try to extend it to all the nearest-neighbors in the lattice. When the angles are well defined, *i.e.* for all $\theta \notin \{0, \pi\}$, the energy reaches its minima in the parameter space made up of the ϕ_i at the three lattice sites i forming a triangle of the lattice, for all j such that i and j are nearest-neighbor sites, if we have

$$\phi_i - \phi_j = \pm\frac{2\pi}{3},\ \forall\theta \notin \{0, \pi\}, \tag{4.16}$$

with the same sign for all ordered pair (i, j) nearest neighbors inside a triangle. It is possible to fix this condition for every other triangles of the lattice. Given the condition Eq. (4.16) on the values of the parameters ϕ_i, the energy reads

$$E = S^2 \sum_{\langle ij \rangle} \left[(-J_z) \cos^2\theta - \frac{J_{xy}}{2} \sin^2\theta \right] = 2S^2 N \left[\left(-J_z + \frac{1}{2} J_{xy} \right) \cos^2\theta - \frac{1}{2} J_{xy} \right],\ \forall\theta \notin \{0, \pi\}, \tag{4.17a}$$

$$E = S^2 \sum_{\langle ij \rangle} (-J_z) = -2S^2 N J_z,\ \text{if}\ \theta \in \{0, \pi\}, \tag{4.17b}$$

with N the number of lattice sites. The solutions which minimize the energy in the θ parameter space are given by

(i) if $J_{xy} > 2J_z$, writing $-J_z = -\frac{1}{2} J_{xy} + \delta$, with $\delta \in]0, J_{xy}/2[$, we have

$$E = 2S^2 N \left(\delta \cos^2\theta - \frac{J_{xy}}{2} \right),\ \forall\theta \in [0, \pi], \tag{4.18}$$

and we deduce that E reaches its minimum at $\theta = \pi/2$ and is $E = -S^2 N J_{xy}$.

(ii) if $J_{xy} < 2J_z$, replacing δ by $-\delta$, we see that E reaches its minimum at $\theta \in \{0, \pi\}$ and is $E = -2S^2 N J_z$.

(iii) if $J_{xy} = 2J_z$, then $E = -S^2 N J_{xy}$ for all θ.

The transition between ferromagnetism along the $\hat{z}$ axis and in-plane antiferromagnetism, at $J_{xy} = 2J_z$, is discontinuous.

The classical limit for $J_{xy}/J_z > 2$ has therefore vanishing out-of plane magnetic order but 120° spin ordering in the XY plane and each configuration is invariant under a global shift of the parameters ϕ_i. This order is characterized by both following constraints: zero total spin in each triangle of the lattice and each spin lies in the XY plane. Determining the Néel ground state is not trivial because several inequivalent in-plane (XY) configurations satisfy this ordering [200]. Studies performed for the antiferromagnetic Heisenberg model show that the antiferromagnetic ground state is highly degenerate and has finite entropy per site at $T = 0$ [200–202, 233–235]. This systems, similarly to the model we study here, have ground state characterized by zero total spin in each triangle of the lattice (*i.e.* coplanar 120° spins in each triangle of the lattice), however, there is no constraint that each spin lies in the XY plane. Therefore, local distortions of the spin configuration are allowed and the spin wave energy spectrum shows a flat band at zero energy [200–202]. This is not the case for the present situation. In the next section, we study the spin wave excitations, of the classical phases we just obtained.

4.2.2 Spin-wave analysis

Here, we are interested in the stability of the classical magnetic phases (determined in the previous section) against spin wave excitations. We compute the energies of the spin waves in the harmonic approximation (linear spin wave theory).

Ferromagnetic phase From Eq. (4.13) and using $S_i^x = \left(S_i^+ + S_i^-\right)/2$ and $S_i^y = -i\left(S_i^+ - S_i^-\right)/2$ we write

$$\mathcal{H}_S = \sum_{\langle ij \rangle} \left[-J_z S_i^z S_j^z + \frac{J_{xy}}{2} \left(S_i^+ S_j^- + S_i^- S_j^+ \right) \right], \tag{4.19}$$

In the ferromagnetic state, the spins order along the **z** axis so we write the Holstein-Primakoff transformation as follows

$$S_i^z = S - a_i^\dagger a_i, \tag{4.20a}$$

$$S_i^- = a_i^\dagger \sqrt{2S - a_i^\dagger a_i}, \tag{4.20b}$$

$$S_i^+ = \sqrt{2S - a_i^\dagger a_i}\, a_i, \tag{4.20c}$$

with s the spin norm and a_i a boson spin-wave annihilation operator at site i. We consider the large spin S limit of this transformation and we rewrite it, to second order in the boson operators $a_i^\dagger$ and a_i (harmonic approximation)

$$S_i^z = S - a_i^\dagger a_i, \tag{4.21a}$$

$$S_i^- = \sqrt{2S}\, a_i^\dagger, \tag{4.21b}$$

$$S_i^+ = \sqrt{2S}\, a_i, \tag{4.21c}$$

Now we use the previous transformation to write the formulation of $\mathcal{H}_S$ in a spin-wave harmonic approximation. It reads, after a Fourier transformation (so considering periodic boundary conditions)

$$\mathcal{H}_S = -2NJ_zS^2 + 2J_zS \sum_{\mathbf{k}} \left(2\delta_{\alpha,\beta} + \gamma_F \Lambda_{\alpha,\beta}\right) a_\alpha^\dagger(\mathbf{k}) a_\beta(\mathbf{k}), \tag{4.22}$$

with $\gamma_F = J_{xy}/J_z$ ($\gamma_F \in [0,2]$), $a_\alpha(\mathbf{k})$ is the momentum space boson spin-wave annihilation operator associated to the color α spin sub-lattice (in the ferromagnetic phase), $\delta_{\alpha,\beta}$ is the Krönecker delta function and the Λ matrix reads

$$\Lambda = \begin{pmatrix} 0 & \cos\mathbf{k}\cdot\mathbf{b}_1 & \cos\mathbf{k}\cdot\mathbf{b}_2 \\ \cos\mathbf{k}\cdot\mathbf{b}_1 & 0 & \cos\mathbf{k}\cdot\mathbf{b}_3 \\ \cos\mathbf{k}\cdot\mathbf{b}_2 & \cos\mathbf{k}\cdot\mathbf{b}_3 & 0 \end{pmatrix}, \tag{4.23}$$

where $\mathbf{b}_i$, $i \in 1,2,3$ are the three vectors (previously defined) joining the nearest neighbor sites on the kagome lattice (see for instance Fig. 3.1(a) of Chapter 3). The eigenvalues of Λ

are

$$\lambda_1 = -1, \tag{4.24a}$$

$$\lambda_2 = \frac{1}{2}\left(1 + \sqrt{1 + 4f(\mathbf{k})}\right), \tag{4.24b}$$

$$\lambda_3 = \frac{1}{2}\left(1 - \sqrt{1 + 4f(\mathbf{k})}\right), \tag{4.24c}$$

with $f(\mathbf{k}) = 2\prod_{\alpha=1}^{3} \cos \mathbf{k} \cdot \mathbf{b}_\alpha$. Let us call

$$\upsilon_\mu(\mathbf{k}) = (\upsilon_{\mu,1}, \upsilon_{\mu,2}, \upsilon_{\mu,3}), \tag{4.25}$$

the normalized eigenvectors of Λ ($\mu \in \{1, 2, 3\}$), and we define

$$d_\mu(\mathbf{k}) = \sum_\alpha \upsilon_{\mu,\alpha} a_\beta(\mathbf{k}), \tag{4.26}$$

Then we have

$$\mathcal{H}_S = -2NJ_zS^2 + 2J_zS \sum_{\mathbf{k}} \left(2 + \gamma_F \lambda_\mu\right) d_\mu^\dagger(\mathbf{k}) d_\mu(\mathbf{k}), \tag{4.27}$$

The three spin wave branches with energies $\epsilon_\mu(\mathbf{k}) = 2J_zS\left(2 + \gamma_F\lambda_\mu\right)$ are sketched in Figs. 4.1(a) and 4.1(c) for different values of γ_F. We remind that the energy of the so called classical state is

$$\left(S^2 \sum_{i,j} -J_z \cos^2\theta - \frac{J_{xy}}{2}\sin^2\theta\right)\Bigg|_{\theta=0} = -2NJ_zS^2, \tag{4.28}$$

with N the number of spins in the system. For all values γ_F, except $\gamma_F = 2$ (transition point), we observe a finite gap between the lowest energy associated to the spin wave excitations and the energy associated to the classical state. $\lambda_1 = -1$ so ϵ_1 is a flat band and because $\lambda_1 \leq \lambda_3 \leq \lambda_2$, ϵ_1 is associated to the lowest energy states. Moreover, we have checked that hexagon-localized excitations associated to alternating values 0 and π of the azimuthal angles are eigenstates with energies corresponding to the flat band [200]. The energy of the spin wave excitations for the lowest dispersive band, for second order in small $|\mathbf{k}|$ is given by $\epsilon_2(\mathbf{k}) = 2J_zS\left(2 - \gamma_F + \frac{\gamma_F}{2}|\mathbf{k}|^2\right)$. This quadratic dispersion relation is shown in Figs. 4.1(b) and (d).

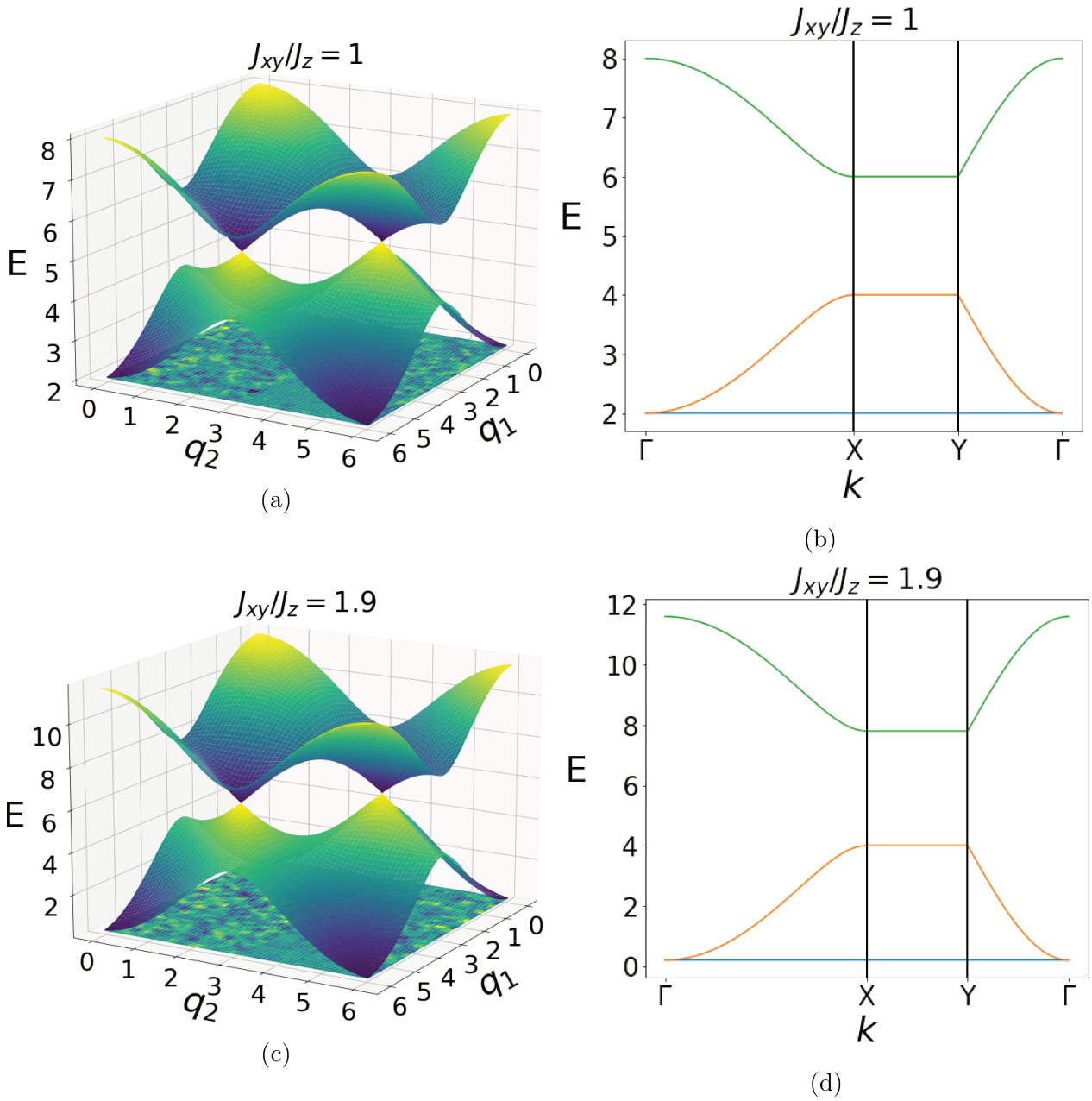

Figure 4.1: Spin wave spectrum in the harmonic approximation for the ferromagnetic phase (computed from Eq. (4.27)). The energy is expressed in $J_z S$ units. Figures on the first row are associated to $J_{xy}/J_z = 1$ and figures on the second row to $J_{xy}/J_z = 1.9$. Vectors $\boldsymbol{q}_1$ and $\boldsymbol{q}_2$ are dual to the unit vectors $\boldsymbol{e}_1$ and $\boldsymbol{e}_2$ of Fig. 3.1(a) of Chapter 3. We took periodic boundary conditions, the Brillouin zone (BZ) is therefore a torus. On the first column, we represented the spectrum for the whole BZ, whereas the second column's figures are cuts along the ΓXY lines of the BZ ($\Gamma = (0, 0)$, $X = (0, \pi)$, $Y = (\pi/2, \pi)$).

Antiferromagnetic phase The procedure we follow is detailed in [200]. We remind that the classical antiferromagnetic phase is characterized by a spin order in the XY plane with angles between nearest neighbor spins $\phi_i - \phi_j = \pm 2\pi/3$. The sign of $\phi_i - \phi_j$ is fixed for the three ordered pairs $(\phi_1 - \phi_2,\, \phi_2 - \phi_3,\, \phi_3 - \phi_1)$ in each triangle of the lattice. It is convenient for the study to rewrite the Hamiltonian (given by Eq. (4.9)) in a so-called rotating frame $(x_i,\, y_i,\, \mathrm{z})$, in which one axis (say y_i axis) is aligned with the local spin at site i and the $\mathbf{z}$ axis remains the same. This is done thanks to the following transformation

$$S_i^y = \cos\phi_i S_i^{y_i} - \sin\phi_i S_i^{x_i}, \tag{4.29a}$$

$$S_i^x = \cos\phi_i S_i^{x_i} - \sin\phi_i S_i^{y_i}, \tag{4.29b}$$

and H now reads

$$H = \sum_{\langle ij \rangle} \left[-J_z S_i^z S_j^z + J_{xy} \cos\left(\phi_i - \phi_j\right) \left(S_i^{x_i} S_j^{x_j} - S_i^{y_i} S_j^{y_j} \right) + J_{xy} \sin\left(\phi_i - \phi_j\right) \left(S_i^{x_i} S_j^{y_j} - S_i^{y_i} S_j^{x_j} \right) \right]. \tag{4.30}$$

We can now perform the Holstein-Primakoff transformation, writing S the spin norm and a_i a boson spin-wave annihilation operator at site i,

$$S_i^{y_i} = S - a_i^\dagger a_i, \tag{4.31a}$$

$$S_i^+ = a_i^\dagger \sqrt{2S - a_i^\dagger a_i}, \tag{4.31b}$$

$$S_i^- = \sqrt{2S - a_i^\dagger a_i}\, a_i, \tag{4.31c}$$

where, because of the respective orientation of the axis in the frame $(x_i,\, y_i,\, \mathrm{z})$, $S_i^\pm = S_i^z \pm S_i^{x_i}$. As we did for the ferromagnetic phase, we consider the large S limit and we keep only terms up to second order in the bosonic operators. Because the sign of $\phi_i - \phi_j$ is fixed for the three ordered pairs in each triangle of the lattice, the $S_i^{x_i} S_j^{y_j} - S_i^{y_i} S_j^{x_j}$ term in Eq. (4.30) is canceled out when performing the $\langle i, j \rangle$ summation in each triangle of the lattice. H then

reads

$$H = -NJ_{xy}S^2 + \frac{SJ_{xy}}{2}\sum_{\langle i,j\rangle}\left[\left(\frac{1}{2}-\gamma_{AF}\right)\left(a_i a_j + a_i^\dagger a_j^\dagger\right) - \left(\frac{1}{2}+\gamma_{AF}\right)\left(a_i^\dagger a_j + a_i a_j^\dagger\right) + 2a_i^\dagger a_i\right], \tag{4.32}$$

with $J_z = \gamma_{AF} J_{xy}$, $\gamma_{AF} \in [0, 1/2]$. Now, we restrict our analysis to the $\mathbf{q} = 0$ configuration [200] for which the magnetic unit cell contains three sites and corresponds to the kagome lattice unit cell. In fact, this calculation would yield the same result for the $\sqrt{3}\times\sqrt{3}$ unit cell, as in Ref. [200] analysis, where only including further nearest neighbor terms lifts the degeneracy between both configurations. A Fourier transform of H gives

$$H = -NJ_{xy}S^2 + SJ_{xy}\sum_{\mathbf{k}}\Bigg\{\left[2\delta_{\alpha,\beta} - \left(\frac{1}{2}+\gamma_{AF}\right)\Lambda_{\alpha,\beta}\right]a_\alpha^\dagger(\mathbf{k})a_\beta(\mathbf{k}) \tag{4.33}$$

$$+\frac{1}{2}\left(\frac{1}{2}-\gamma_{AF}\right)\Lambda_{\alpha,\beta}\left(a_\alpha(\mathbf{k})a_\beta(-\mathbf{k}) + a_\alpha^\dagger(\mathbf{k})a_\beta^\dagger(-\mathbf{k})\right)\Bigg\}, \tag{4.34}$$

where $a_\alpha(\mathbf{k})$ is the momentum space boson spin-wave annihilation operator associated to the color α spin sub-lattice (in the antiferromagnetic phase), and the matrix Λ is the same than in the ferromagnetic phase (see Eq. (4.23)). Here we obtain

$$H = -NJ_{xy}S^2 + SJ_{xy}\sum_{\mathbf{k},\mu}\Bigg\{\left[2-\left(\frac{1}{2}+\gamma_{AF}\right)\lambda_\mu\right]d_\mu^\dagger(\mathbf{k})d_\mu(\mathbf{k}) \tag{4.35}$$

$$+\frac{1}{2}\left(\frac{1}{2}-\gamma_{AF}\right)\lambda_\mu\left(d_\mu(\mathbf{k})d_\mu(-\mathbf{k}) + d_\mu^\dagger(\mathbf{k})d_\mu^\dagger(-\mathbf{k})\right)\Bigg\}. \tag{4.36}$$

Now we define the coordinate operator $Q_\mu(\mathbf{k})$ and the momentum operator $P_\mu(\mathbf{k})$ such that

$$Q_\mu(\mathbf{k}) = \frac{i}{\sqrt{2}}\left(d_\mu(-\mathbf{k}) - d_\mu^\dagger(\mathbf{k})\right), \tag{4.37a}$$

$$P_\mu(\mathbf{k}) = \frac{1}{\sqrt{2}}\left(d_\mu(-\mathbf{k}) + d_\mu^\dagger(\mathbf{k})\right), \tag{4.37b}$$

$$\left[P_\mu(\mathbf{k}), Q_\nu^\dagger(\mathbf{q})\right] = -i\delta_{\mathbf{k}+\mathbf{q},0}\delta_{\mu,\nu}, \tag{4.37c}$$

Then, using $\sum_\mu \lambda_\mu = 0$, we have

$$H = -NJ_{xy}S^2 - NJ_{xy}S + SJ_{xy}\sum_{\mathbf{k},\mu}\left[\left(1-\gamma_{AF}\lambda_\mu\right)P_\mu(\mathbf{k})P_\mu^\dagger(\mathbf{k}) + \left(1-\frac{1}{2}\lambda_\mu\right)Q_\mu(\mathbf{k})Q_\mu^\dagger(\mathbf{k})\right], \tag{4.38}$$

and we see that we get a well-known harmonic oscillator Hamiltonian. Therefore we define two normal modes operators $b_\mu(\mathbf{k})$ and $b_\mu^\dagger(\mathbf{k})$ such that

$$Q_\mu(\mathbf{k}) = \sqrt{\frac{c_1}{2c_0}}\left(b_\mu(\mathbf{k}) + b_\mu^\dagger(\mathbf{k})\right), \tag{4.39a}$$

$$P_\mu(\mathbf{k}) = -i\sqrt{\frac{c_0}{2c_1}}\left(b_\mu(\mathbf{k}) - b_\mu^\dagger(\mathbf{k})\right), \tag{4.39b}$$

$$\left[b_\mu(\mathbf{k}), b_\nu^\dagger(\mathbf{q})\right] = \delta_{\mathbf{k},\mathbf{q}}\delta_{\mu,\nu}, \tag{4.39c}$$

with c_0 and c_1 two constant terms. We take $c_0 = \sqrt{1 - \frac{1}{2}\lambda_\mu}$, $c_1 = \sqrt{1 - \gamma_{AF}\lambda_\mu}$ and we find

$$H = -NJ_{xy}S^2 - NJ_{xy}S + \sum_{\mathbf{k},\mu}\epsilon_\mu(\mathbf{k})\left(b_\mu^\dagger(\mathbf{k})b_\mu(\mathbf{k}) + \frac{1}{2}\right), \tag{4.40}$$

with

$$\epsilon_\mu(\mathbf{k}) = J_{xy}S\sqrt{2\left(2 - \lambda_\mu\right)\left(1 - \gamma_{AF}\lambda_\mu\right)}, \tag{4.41}$$

which explicitly reads

$$\epsilon_1 = 2J_{xy}S\sqrt{\frac{3}{2}\left(1 + \gamma_{AF}\right)}, \tag{4.42a}$$

$$\epsilon_2(\mathbf{k}) = 2J_{xy}S\sqrt{1 + f(\mathbf{k})\gamma_{AF} - \frac{1 + \gamma_{AF}}{4}\left(1 + \sqrt{1 + 4f(\mathbf{k})}\right)} \tag{4.42b}$$

$$\epsilon_3(\mathbf{k}) = 2J_{xy}S\sqrt{1 + f(\mathbf{k})\gamma_{AF} - \frac{1 + \gamma_{AF}}{4}\left(1 - \sqrt{1 + 4f(\mathbf{k})}\right)}, \tag{4.42c}$$

The $\mathbf{k}$-dependency of these energies is represented in Fig. 4.2. Let us compare with the energy of the classical antiferromagnetic state which is

$$\left(S^2\sum_{i,j} -J_z\cos^2\theta - \frac{J_{xy}}{2}\sin^2\theta\right)\Bigg|_{\theta=\pi/2} = -NJ_{xy}S^2, \tag{4.43}$$

Here we have $-1/4 \leq f(\mathbf{k}) \leq 2$ so the flat band ϵ_1 is the higher energy band. Hexagon-localized excitations associated to alternating values of the spin S_i^z components with opposite signs are eigenstates with energies corresponding to the flat band [200]. The energy in the lowest dispersive band for small $|\mathbf{k}|$ is given by $\epsilon_3(\mathbf{k}) = 2J_{xy}s\sqrt{1 - 2\gamma_{AF}}|\mathbf{k}|$. This linear dispersion relation is clearly shown in Figs. 4.2(b) and (d). From Eq. (4.40), we see that

there is an energy shift Δ between the classical state energy and the lowest energy associated to the normal mode ($b_\mu^\dagger(\mathbf{k})$) particles. At the transition we have $\Delta = 0$, but for $\gamma_{AF} < 1/2$ (*i.e.* $J_{xy} > 2J_z$), we see (Fig. 4.4(a)) that $\Delta < 0$, reaching $\Delta_{E,\min} \approx 0.043 J_{xy}$ per spin for $\gamma_{AF} \to 0$. This negative energy shift destabilizes the classical state characterized by $\phi_i - \phi_j = 2\pi/3$. In fact, for $J_{xy}/J_z > 2$, Changlani *et al.* [220] found a spin liquid phase using exact diagonalization [236, 237] for a 36 sites system. This seems to be consistent with the spin liquid phase found for the Heisenberg isotropic point on the kagomé lattice [211–215].

Results of Refs. [220, 238] also show a long range ordered ferromagnetic phase at $J_{xy}/J_z < 2$ and a long range order in-plane antiferromagnetic phase (at $J_{xy}/J_z > 2$) when next nearest neighbor spin exchange is added. This is in general relevant for real systems, for instance in $Co_3Sn_2S_2$ further than nearest neighbor spin exchange seem to play a non negligible role [239, 240]. In this Weyl semi-metal, in the ferromagnetic phase, ferromagnetic spin exchange between the kagome plane has also non-negligible amplitude [239, 240]. Then it seems probable that in the antiferromagnetic phase, these couplings are also non negligible. Since there is no frustration between the planes, this should stabilize both the ordered phases we observed. The anisotropic Heisenberg model with ferromagnetic spin exchange term J_z along the $\mathbf{z}$ direction and antiferromagnetic spin exchange term J_{xy} in the XY plane has also been studied on the triangular lattice [241]. A long range ferromagnetic order at $J_{xy}/J_z < 2$ and an antiferromagnetic in-plane 120° order at $J_{xy}/J_z > 2$, stable against spin-wave fluctuations, at small temperature, was found.

4.3 Consequence of the magnetism on the topological properties of the low-energy channel

In this section we describe a temperature or a pressure-induced magnetic and topological transition. First we describe how varying the temperature or the pressure can be understood

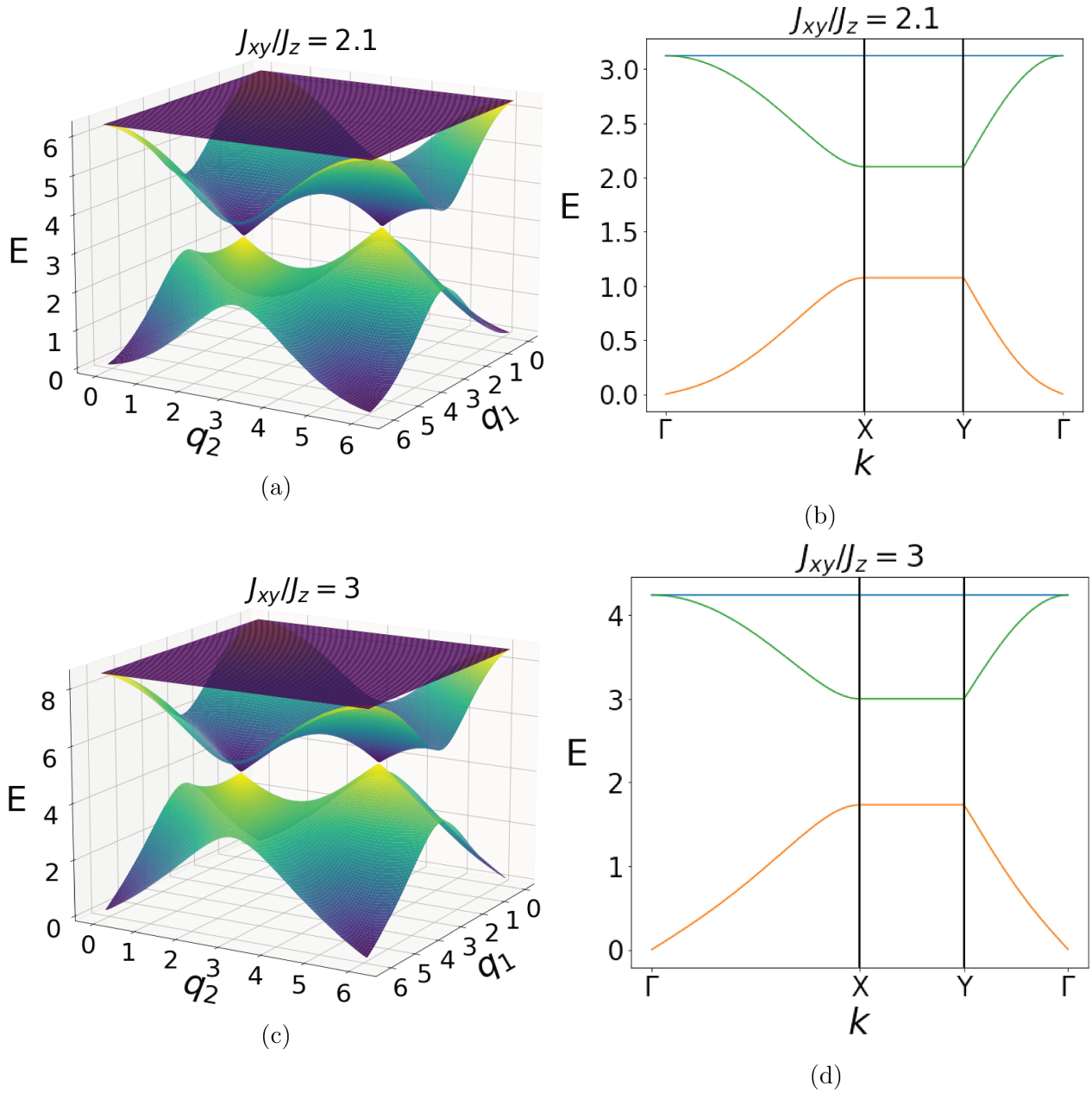

Figure 4.2: Spin wave spectrum (computed from Eq. (4.41)) in the harmonic approximation for the antiferromagnetic phase. The energy is expressed in $J_z S$ units. Figures on the first row are associated to $J_{xy}/J_z = 2.1$ and figures on the second row to $J_{xy}/J_z = 3$. Vectors $\boldsymbol{q}_1$ and $\boldsymbol{q}_2$ are dual unit vectors $\boldsymbol{e}_1$ and $\boldsymbol{e}_2$ of Fig. 3.1(a) of Chapter 3. We considered periodic boundary conditions, the Brillouin zone (BZ) is therefore a torus. On the first column, we represented the spectrum for the whole BZ, whereas the second column's figures are cuts along the ΓXY lines of the BZ ($\Gamma = (0, 0)$, $X = (0, \pi)$, $Y = (\pi/2, \pi)$).

in our model as varying the ratio J_{xy}/J_z. This leads to a magnetic phase transition, from a ferromagnetic phase at low temperature or ambient pressure to a spin liquid phase (or an in-plane antiferromagnetic phase if further spin exchange nearest neighbor terms are considered) and then to a disordered phase at high temperature or pressure. The ferromagnetic phase is associated with quantum anomalous Hall effect while the in-plane ordered phase is associated with a metal behavior or a quantum spin Hall effect depending on the values of the Hund's coupling amplitude and of the Fermi level. We have been inspired from the Weyl semimetal $Co_3Sn_2S_2$, in which a magnetic and topological phase transition as the temperature or the pressure varies [27, 229]. It is believed that the anomalous Hall effect which is observed in the Weyl semimetals results from the QAH effect happening in each layer [38, 155, 242–245]. This justifies a comparison between the phase transition associated to the two-dimensional model we study and the phase transition in $Co_3Sn_2S_2$.

4.3.1 Temperature or pressure phase transition

Here we consider the effect of either a variation of the temperature or a variation of the pressure in the model we built. This gives two different physical origins for the variation of J_{xy}/J_z leading to a magnetic transition.

Temperature effect

Starting in the ferromagnetic phase $J_{xy}/J_z < 2$ and approaching the transition point $J_{xy}/J_z = 2$ we saw that the amplitude of the gap between the energy of the classical state and the lowest energy of the spin wave excitations goes to zero. Moreover, the lowest energy spin wave excitations are degenerate and associated to a flat band. The entropy S_F associated to such degenerate states, at finite temperature T, results in a free energy term $-TS_F$ that should lower the flat band energy given by Eq. (4.27). Therefore, before the transition point, for $J_{xy}/J_z < 2$, this energy becomes smaller than the classical ground state energy $-2NJ_zS^2$ and it destabilizes the ferromagnetic order. In other words, when T increases, the value of

J_{xy}/J_z at the transition should be decreased, from $J_{xy}/J_z = 2$ at zero temperature to some value $J_{xy}/J_z < 2$ at finite temperature. Here we notice that the parameters J_z and J_{xy} are fixed. In the following, we choose to describe this situation by keeping the transition point fixed $J_{xy}/J_z = 2$ while varying the ratio J_{xy}/J_z as the external parameter (the temperature) varies. The later does not appear explicitly in the following but is responsible for this transition.

Above a certain temperature T_m such that $k_B T_m \sim J_{xy}$, the magnetic order disappears because the Boltzmann weights of the ordered configurations decrease (classical phase transition from a Ginzburg-Landau theory). Above a temperature T_t such that $k_B T_t \sim \Delta_{\lambda_i}$, where Δ_{λ_i} denotes the amplitude of the itinerant electrons gap (the gap is due to the spin-orbit coupling term), we expect that the topological order disappears. Indeed, the energy bands for the itinerant electrons disappear because transitions between states associated to different bands are possible at T_t. The exchange coupling amplitudes have been estimated around $10 - 20$ meV $= 100 - 200$ K in $Co_3Sn_2S_2$ [239, 240]. Spin-orbit gaps (appearing at certain points in momentum space), are of order $10 - 50$ meV $= 100 - 500$ K in $Co_3Sn_2S_2$ [199]. This seems consistent with the argument developed in this paragraph and with the magnetic and topological transition observed.

Pressure effect

In $Co_3Sn_2S_2$, it is also shown that a magnetic and topological transition is observed when the external (hydrostatic) pressure is varied [27, 229]. The increase of the pressure results in the reduction of the rhombohedral lattice parameter which closes the half-metallic gap [229]. For the model we built, we argue that the reduction of the rhombohedral lattice parameter results in the increase of the amplitude of the exchange integrals, in particular the one associated to the localized spins, t_S, which we assumed small when no external pressure is applied. This yields an increase of $J_{xy} = t_S^2/U$ compared to J_z, which would lead to a ferromagnetic-antiferromagnetic phase transition. This is valid as long as $t_S/U \ll 1$.

Above a certain pressure, the exchange integrals are so large that the O_S orbitals are not associated to localized particles and the energy gaps associated to the itinerant electrons go to zero, which results in a phase without magnetic and the topological order.

Gaussian distribution

Let us write R the ratio J_{xy}/J_z: $R = J_{xy}/J_z$. For both temperature and pressure induced transitions, we consider that we only have access to an effective distribution law for the random variable R which is a function of the external parameter P_E (being the temperature or the external pressure as we describe in the last section). We write $R_0\left(P_E\right)$ the mean value of R at P_E and its variance $\sigma^2\left(P_E\right)$.

As an example we consider a Gaussian law and write its probability density function

$$P(R) = \frac{1}{\sqrt{2\pi}\sigma} \exp\left(-\frac{(R-R_0)^2}{2\sigma^2}\right). \tag{4.44}$$

where, as we wrote, R_0 and σ^2 depend on P_E so $P(R)$ does also depend on P_E. We remind that $R > 0$. We want to impose

$$\int_0^\infty dR P(R) \approx 1. \tag{4.45}$$

Then we assume that for all external parameter values P_E, $\sigma(P_E) \ll R_0(P_E)$.

4.3.2 Topological model for the itinerant electrons

Here we consider two topological phases for the itinerant electrons model introduced in Sec. 4.1.2. Let us define $t = \sqrt{t_i^2 + \lambda_i^2}$ and $\phi = 3\left[\arctan\left(\frac{\lambda_i}{t_i}\right) + \pi\right]$. This gives

$$-t\mathrm{e}^{-i\phi\sigma^z\nu_{ij}/3} = -(t_i - i\lambda_i\nu_{ij}\sigma^z), \tag{4.46}$$

The Hamiltonian associated to the itinerant electrons is

$$H = -t\sum_{\langle ij\rangle} c_i^\dagger \mathrm{e}^{-i\phi\sigma^z\nu_{ij}/3} c_j - \frac{h_c}{2}\sum_i S_i^z c_i^\dagger \sigma^z c_i, \tag{4.47}$$

We notice that we already computed the Chern numbers associated to the energy bands given by the first term $-t\sum_{\langle ij\rangle} c_i^\dagger \mathrm{e}^{-i\phi\sigma^z\nu_{ij}/3} c_j$ (see Chapter 3): we have $C = -\operatorname{sgn}(\sin\phi)$

($C = +\mathrm{sgn}(\sin\phi)$) for the lowest energy band associated to the spin $\uparrow$ ($\downarrow$) particles, $C = 0$ for the middle energy band associated to both spin $\uparrow$ particles and spin $\downarrow$ particles, and $C = \mathrm{sgn}(\sin\phi)$ ($C = -\mathrm{sgn}(\sin\phi)$) for the highest energy band associated to the spin $\uparrow$ ($\downarrow$) particles.

4.3.3 The magnetic transition yields a topological transition

Here we show how the magnetic order influences the topological order. In Sec. 4.2, we found that, in the large S (for the localized spins) limit, if $R < 2$, the localized spin show a ferromagnetic out-of-plane order while if $R > 2$ there is no out-of-plane order. This leads to two different topological phases associated to the itinerant electrons. In the following, we label by $l\sigma$, $m\sigma$ and $u\sigma$ respectively the lowest, the middle and the highest itinerant electron spin σ energy bands. Moreover, as we mentioned, both temperature and pressure induced transitions introduced in Sec. 4.3.1 are described by the variation of R.

Magnetic and topological transition

For $R < 2$, the Hund's coupling term acts like a magnetic field:

$$H_h = -h_c \sum_i S_i^z s_i^z = -h_c \sum_i \langle S_i^z \rangle s_i^z = -h_c S \sum_i s_i^z. \tag{4.48}$$

We consider that h_c is large enough so that the energy bands $l\uparrow$ and $m\uparrow$ lie below the bands $u\uparrow$, $l\downarrow$, $m\downarrow$ and $u\downarrow$ and that the Fermi level lies in the gap between the bands $l\uparrow$ and $m\uparrow$ and the other ones. This means that h_c has at least amplitude of the order t_i (the amplitude of the nearest neighbor hopping terms). Such a situation is shown in Fig. 4.3(a). The computation of the Chern number in Chapter 3 (see Eq. (3.29)) is directly applicable to the present case. We consider $\lambda_i > 0$ so $\phi > 0$. The lowest spin $\uparrow$ energy band is associated with Chern number -1 while the middle spin $\uparrow$ energy band is associated with Chern number 0 giving $C_\uparrow = -1$ (here $C_\downarrow = 0$ because all the spin $\downarrow$ bands are above the Fermi level) and a total Chern number $C = -1$.

For $R > 2$, the out-of-plane magnetic moments vanish, therefore the h_c term vanishes. The energy bands associated to the itinerant electrons have twofold spin degeneracy. Such a situation, with the Fermi level previously defined (Fig. 4.3(a)) is shown in Fig. 4.3(b). We see that a convenient choice of h_c and of E_F makes that the Fermi level lies between the degenerate energy bands $l\uparrow$, $l\downarrow$ and $m\uparrow$, $m\downarrow$. The computation of the topological invariant in Chapter 3 (see Eq. (3.32)) is directly applicable to the present case and we deduce that we a have a QSH state with $\nu = (C_\uparrow - C_\downarrow)/2 \bmod 2 = 1$ ($C_\uparrow$ and $C_\downarrow$ are the Chern numbers respectively associated to the spin $\uparrow$ and $\downarrow$ electrons) and vanishing total Chern number $C = C_\uparrow + C_\downarrow$.

Figs. 4.3(c) and (d) also show another choice for the values of h_c and of E_F for which we observe a QAH phase associated to ferromagnetism but no topological properties in the ("high temperature") antiferromagnetic phase.

(Gaussian) distribution on R

In the large S limit, for $R < 2$ (ferromagnetic order), $\langle S_i^z \rangle = S$ is non-vanishing, $C = -1$, $C_\uparrow = -1$ and $C_\downarrow = 0$ (giving $\nu = 0$) while for $R > 2$, there is no out-of-plane magnetic order $\langle S_i^z \rangle = 0$, $C = 0$, $C_\uparrow = -1$ and $C_\downarrow = 1$ (giving $\nu = 1$).

Writing $\mathbb{E}(\langle S_i^z \rangle)$, $\mathbb{E}(C)$, $\mathbb{E}(C_\uparrow)$ and $\mathbb{E}(C_\downarrow)$ the values of respectively $\langle S_i^z \rangle$, C, $C_\uparrow$ and $C_\downarrow$ averaged over the distribution $P(R)$ (see Eq. (4.44)), we obtain

$$\mathbb{E}(\langle S_i^z \rangle) = \int_0^\infty dR P(R) \langle S_i^z \rangle(R) = S \int_{1/2}^\infty dR P(R) = \frac{S}{2} \mathrm{erfc}\left[\frac{1}{\sqrt{2}\sigma} \left(\frac{1}{2} - R_0 \right) \right], \tag{4.49a}$$

$$\mathbb{E}(C) = -\frac{1}{2} \mathrm{erfc}\left[\frac{1}{\sqrt{2}\sigma} \left(\frac{1}{2} - R_0 \right) \right], \tag{4.49b}$$

$$\mathbb{E}(C_\uparrow) = -1, \tag{4.49c}$$

$$\mathbb{E}(C_\downarrow) = 1 - \frac{1}{2} \mathrm{erfc}\left[\frac{1}{\sqrt{2}\sigma} \left(\frac{1}{2} - R_0 \right) \right], \tag{4.49d}$$

where we denoted by "erfc[]" the complementary error function. $\mathbb{E}(\langle S_i^z \rangle)$ depends on the value of the external parameter P_E via R_0 and σ. These results are represented in Fig. 4.4(b).

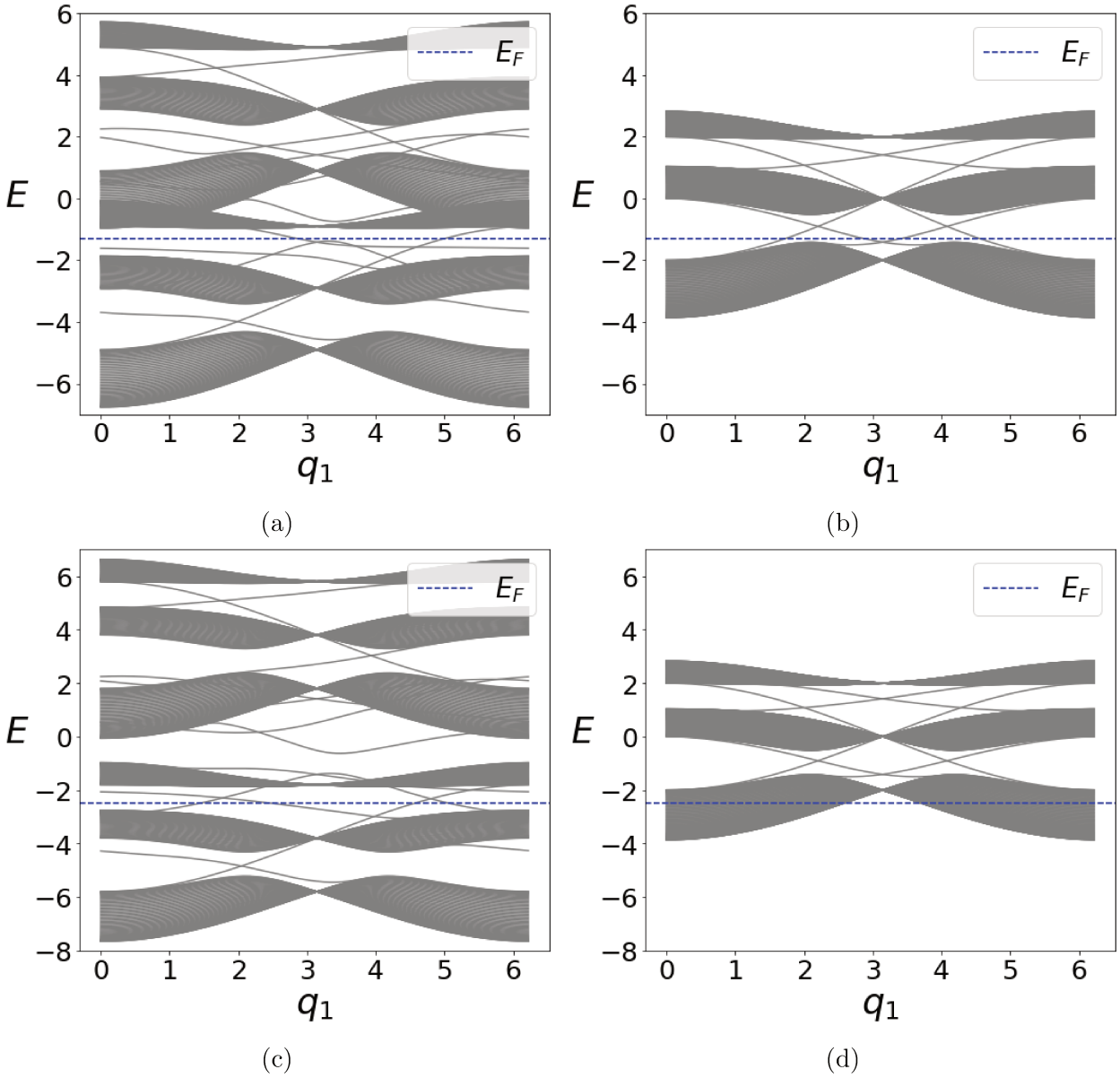

Figure 4.3: Dispersion relation for the itinerant electron channel Eq. (4.47), in a cylinder geometry with flux $\phi = 3\pi/4$ and for line-armchair boundary shape (see Chapter 3, Fig. 3.6). Figures on the left are associated to the ferromagnetic phase $\langle S_i^z \rangle \neq 0$ and figures on the right are associated to the in-plane magnetically ordered phase $\langle S_i^z \rangle = 0$. The energies are in units of t. Top row corresponds to a value of $h_c = 2.7t$ and we set the Fermi level at energy $E_F = -1.3t$. Bottom row corresponds to a value of $h_c = 3.8t$ and we set the Fermi level at energy $E_F = -2.5t$.

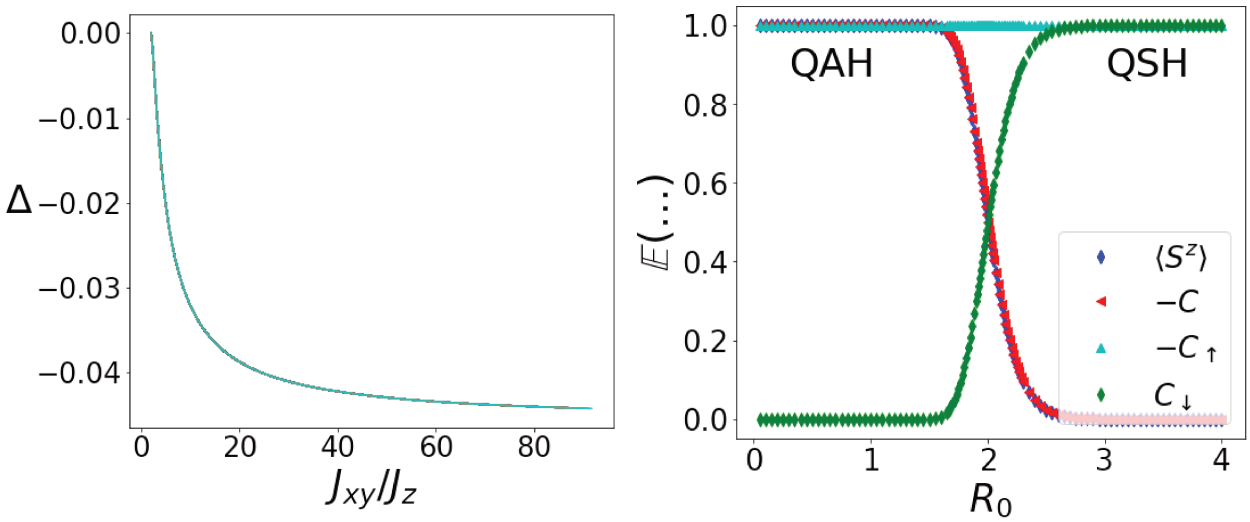

(a) (b)

Figure 4.4: (a) Energy shift Δ_E between the energy of the classical antiferromagnetic state and the lowest energy associated to the spin wave excitations, in units of SJ_{xy} per spin. (b) Values of $\langle S_i^z \rangle$, $-C$, $-C_\uparrow$ and $C_\downarrow$ averaged over the distribution $P(R)$ (see Eqs. (4.49)), as a function of the ratio J_{xy}/J_z. Here, we arbitrary took the standard deviation σ of the distribution in Eq. (4.44) to be $0.05J_{xy}$. Moreover, we considered $h_c = 2.7t$ and $E_F = -1.3t$, as in Figs. 4.3(a) and 4.3(b), which gives a QAH-QSH transition.

The order parameters are here statistical averages which may represent averages over all the two-dimensional layers of a three-dimensional sample, averages over over different time realizations or averages over different magnetic clusters in the sample.

4.4 Conclusion

In this chapter, we built a two-channel model on the kagome lattice to describe a transition from a magnetic Chern insulator, to an in-plane magnetic order with possible quantum spin Hall effect. One channel is associated with localized spin while the other contains itinerant electrons which are coupled to the former via a large Hund's ferromagnetic coupling [31, 216, 221, 222, 225, 226].

The localized spin channel is described by an anisotropic Heisenberg model with ferromagnetism along the **z** direction. The microscopic origin of this model is a large on-site Hubbard

interaction which gives rise to Mott physics and a double-exchange mechanism with the itinerant electrons [221, 223–226]. This results either in an out-of-plane ferromagnetic phase or in an in-plane ordered phase. The in-plane ordered phase is either a spin-liquid or a long range order phase if further nearest neighbor spin-exchange is considered [220].

The localized spins couple to the spins of the itinerant electrons through a ferromagnetic Hund's coupling term. The itinerant electrons are described by a nearest neighbors hopping term with spin-orbit coupling [11, 36, 227, 228]. In the ferromagnetic phase, the ferromagnetic Hund's coupling term acts like a magnetic field and for certain values of the chemical potential, the itinerant channel shows a quantum anomalous Hall effect. In the in-plane ordered magnetic phase, the itinerant electrons model is time-reversal invariant and, depending on the Fermi energy, is either associated to a quantum spin Hall phase or to a metallic phase.

We applied this model to the Weyl semimetal $Co_3Sn_2S_2$ in which a temperature and pressure dependent magnetic and topological transition is observed. On the one hand, at finite temperature, we argue that the ferromagnetic phase should be destabilized near the transition because of the finite entropy associated to the spin wave excitations. Therefore, increasing the temperature yields a magnetic transition and as a consequence it also results in a topological transition because, as we explained in the previous paragraph, the later is coupled to the former in our model. On the other hand, an increase of the pressure results in the reduction of the rhombohedral lattice parameter [229]. In our approach, we argued that this would results in the increase of the exchange integrals (hopping terms), which, consequently, varies the in-plane spin-exchange term in our model and yields a magnetic and topological transition.

Chapter 5

Time reversal symmetric topological insulators

In this chapter we study a new time-reversal invariant topological model for a two-dimensional kagome lattice system. It contains flux $L_z s_z$ and $L_y s_x$ nearest-neighbor terms, respectively reminiscent of intrinsic spin-orbit coupling (see Sec. 1.4.1) and Rashba spin-orbit coupling processes. We study this model for several on-site energy configurations. We show how the topological phase, resulting from the flux term, is tuned by varying the amplitude(s) of on-site energy terms and/or of the Rashba spin-orbit coupling term, at filling $n = 2/3$. In the last section of this chapter, we study the effect of Hubbard interactions on the topological properties for a specific on-site energy configuration and at vanishing Rashba spin-orbit coupling. The work reviewed in this chapter, which results from a collaboration involving Karyn Le Hur's group (Ecole Polytechnique, Palaiseau), and Walter Hofstetter's group (Goethe University, Frankfurt) was published in Refs. [188] and [246]. Walter Hofstetter's group was mainly concerned with the numerical investigation of the topological and magnetic phase diagram in the non-interacting case and in the interacting case. In this chapter we only briefly mention their numerical results; the interested reader is referred to both previous references.

My contribution in these publications essentially concerns analytical computations. In the non-interacting case, I determined, through several methods, the $\mathbb{Z}_2$ phase diagram for

different on-site energy configurations. In particular, I performed an explicit analytical computation of the spin Chern number using the method we developed in Chapter 3, Sec. 3.2.1; to the best of our knowledge this computation does not appear in the literature before our publication. In the interacting case, I determined the system's ground state, for a specific limit of the on-site energies' amplitude, at vanishing Rashba spin-orbit coupling. I used perturbation theory in the large Hubbard amplitude U limit and a mean-field method for smaller U.

In two-dimensional time-reversal invariant systems, the spin-orbit interaction is essential to obtain non-trivial topological properties (see Refs. [2, 11–14, 48, 144, 145] and section 1.4.1). Several topological insulators on the kagome lattice have been studied, for instance first and second nearest neighbors intrinsic spin-orbit interaction [39–41, 193], Rashba spin-orbit interaction [247] or intrinsic and Rashba spin-orbit coupling for the breathing kagome lattice [42]. Related to the quantum spin Hall phase, the quantum anomalous Hall phase on the kagome lattice has attracted much attention [31–38]. In several kagome materials, the spin-orbit interaction has relatively high amplitude and opens a topological gap (at least at some points in the Brillouin zone) [25, 26, 36, 37, 192].

Hubbard interactions [248] on the kagome lattice leads to very interesting phases, because of geometrical frustration in this lattice and the appearance of flat bands [117, 118, 249–260] and namely in the limit of large Hubbard interactions at half filling, spin models become relevants [261, 262] and have been extensively studied on the kagome lattice [200–205, 208–216, 218, 263–268]. Recently, materials showing interplay between topological and magnetic properties has attracted a lot of attention [20–24, 28, 29].

The experimental investigation of the model we study here is possibly reachable using cold atom gases; the impressive experimental progress in this domain has enabled the simulation of many topological and correlated condensed matter systems [269, 270]. Experimental realization of Bose-Einstein condensate in 1995 has been the starting point of intense research

activity focused on cold atom systems [269, 271–273]. Cold atom gases of fermions have been realized few years later [274–276], as well as optical lattice traps, which have enabled to study systems with spatial periodicity [277–280]. In particular, the kagome lattice has been experimentally realized by overlaying two optical triangular lattices [281] and there are also proposals based on other techniques [282, 283]. In cold atom gases, topological systems are implementable via artificial gauge potentials [80, 284–292]. Several topological systems have already been experimentally realized, for instance the Hofstadter Hamiltonian and the Haldane model [150, 156, 293, 294]. More specifically, topological models with spin-orbit coupling have been investigated theoretically on two-dimensional lattices [80, 291, 292, 295], have been engineered [296–300] and it has been shown such spin-orbit coupled systems are associated with spin Hall effect [301–303]. The simulation of Hubbard interactions in cold atom systems has been achieved experimentally for bosons [304–307] and fermions [268, 308–312]. These systems are very interesting for the study of Hubbard interactions since it is possible to tune the amplitude of the interaction thanks to Feshbach resonances.

This chapter is organized as follows. In Sec. 5.1, we compute the $\mathbb{Z}_2$ invariant at vanishing Rashba spin-orbit coupling. In this case, there is a simple link between the $\mathbb{Z}_2$ number and both Chern numbers associated to each spin polarized occupied bands (see [48, 189] or Chapter 1, Sec. 1.4). We compute these spin Chern numbers using an extension of the method introduced in Chapter 3, Sec. 3.2.1, for several on-site potential configurations. At vanishing Rashba spin-orbit coupling, the system is inversion symmetric therefore the $\mathbb{Z}_2$ number can also be computed from the eigenvalues of the parity operator at the time-reversal invariant points in the Brillouin zone [39, 42, 190], as we mentioned in Chapter 3, Sec. 3.3.2. We adapt this method for our system and compare the results we obtain with the one we obtained from the extension of the method introduced in Chapter 3, Sec. 3.2.1. We also use another method for the (numerical) computation of the spin Chern numbers at vanishing Rashba spin-orbit coupling, relying on the splitting of the energy bands under a

weak magnetic field [34, 194].

Then, in Sec. 5.2 we study the effect of the Rashba spin-orbit coupling; the topological phase diagram is readily obtained by adapting the argument introduced in Chapter 1, Sec. 1.3.3 and computing the energy gap phase diagram. We also numerically compute the energy spectrum, the local density of states and the currents in systems with open boundary conditions.

Eventually, in Sec. 5.3, we study the effect of Hubbard interactions (amplitude U) added to the topological model we introduce at vanishing Rashba spin-orbit coupling. We consider a specific on-site energy configuration. In this case, we use perturbation theory in the large U limit and a mean-field method for smaller U.

5.1 Quantum spin Hall phase on the kagome lattice with color-dependent chemical potentials

In this section, we study the effect of several on-site potential configurations for a time-reversal model on the kagome lattice with flux and conserved spin s_z. We describe the analytical computation of the $\mathbb{Z}_2$ number at filling $n = 2/3$, which means that the number of particles in the system is $1/3$ of the maximum number of particles that the system can host (which correspond to $n = 2$). First, we develop two methods for this computation. One method relies on the simple link between the $\mathbb{Z}_2$ number and both Chern numbers associated to each spin polarized occupied bands [48, 189]. The challenge here is to compute analytically these Chern numbers. The other method relies on the conservation of the inversion symmetry [190]: the $\mathbb{Z}_2$ number is the product of the parity eigenvalues at the high symmetry points of the BZ. These methods are applied to the different on-site potential cases (i), (ii) and (iii) described in Sec. 5.1.1, for arbitrary values of the phase ϕ and the on-site potentials amplitude λ.

5.1.1 Hamiltonian

In Sec. 1.4.1 we reviewed a $\mathbb{Z}_2$ topological time-reversal symmetric model on the honeycomb lattice. This model contains an intrinsic spin-orbit coupling term $L_z s_z$ (we also call it a flux term) which is essential for the emergence of topological energy bands.

Here we study the effect of such a $L_z s_z$ term along only one direction of the kagome lattice and written as an exponential phase factor. This makes it particularly relevant for a cold atom system where this spin-dependent "phase" term could be implemented using artificial gauge potential [288]. Keeping the notations we previously used for the description of the kagome lattice we write this $L_z s_z$ term

$$-t\sum_{\mathbf{r}} c^{\dagger}_{B,\mathbf{r}} e^{i\phi s_z} c_{G,\mathbf{r}} + c^{\dagger}_{B,\mathbf{r}+\mathbf{e}_3} e^{i\phi s_z} c_{G,\mathbf{r}} + H.c., \tag{5.1}$$

where t is the hopping amplitude for the fermions between neighboring sites in the lattice. $c^{\dagger}_{\alpha,\mathbf{r}} = \left(c^{\dagger}_{\alpha,\mathbf{r},\uparrow}, c^{\dagger}_{\alpha,\mathbf{r},\downarrow}\right)$ is the operator which creates a fermion at site $\mathbf{r}$ for $\alpha = R$, at site $\mathbf{r}+\mathbf{b}_1$ for $\alpha = B$, and at site $\mathbf{r}+\mathbf{b}_2$ for $\alpha = G$. We remind the definitions of the vectors $\mathbf{b}_\alpha$ and $\mathbf{e}_\alpha$ in Fig. 5.1(a) where we represented the flux term introduced in Eq. (5.1). The total flux in each unit cell is vanishing and a local flux which sign depends on the spin is inserted. If we consider each spin species separately, this flux term breaks time-reversal symmetry.

To vary the amplitude of the topological gap, we also consider an on-site potential term, which reads

$$\sum_{\mathbf{r}} \sum_{\alpha=R,B,G} \lambda_\alpha n_{\alpha,\mathbf{r}}, \tag{5.2}$$

with $n_{\alpha,\mathbf{r},\sigma} = c^{\dagger}_{\alpha,\mathbf{r},\sigma} c_{\alpha,\mathbf{r},\sigma}$ the density operator for the spin σ and we have $n_{\alpha,\mathbf{r}} = n_{\alpha,\mathbf{r},\uparrow} + n_{\alpha,\mathbf{r},\downarrow}$. In the following we consider several configurations for this on-site potential term: (i) $\lambda_B = -\lambda_R = \lambda$ and $\lambda_G = 0$, (ii) $\lambda_R = \lambda$ and $\lambda_B = \lambda_G = 0$, and (iii) $\lambda_B = \lambda$ et $\lambda_R = \lambda_G = 0$. The case $\lambda_G = \lambda$ and $\lambda_R = \lambda_B = 0$ is equivalent to the case (ii).

Along the directions $\mathbf{e}_1$ and $\mathbf{e}_2$ (see Fig. 5.1(a)), we consider real-amplitude $-t$ hopping

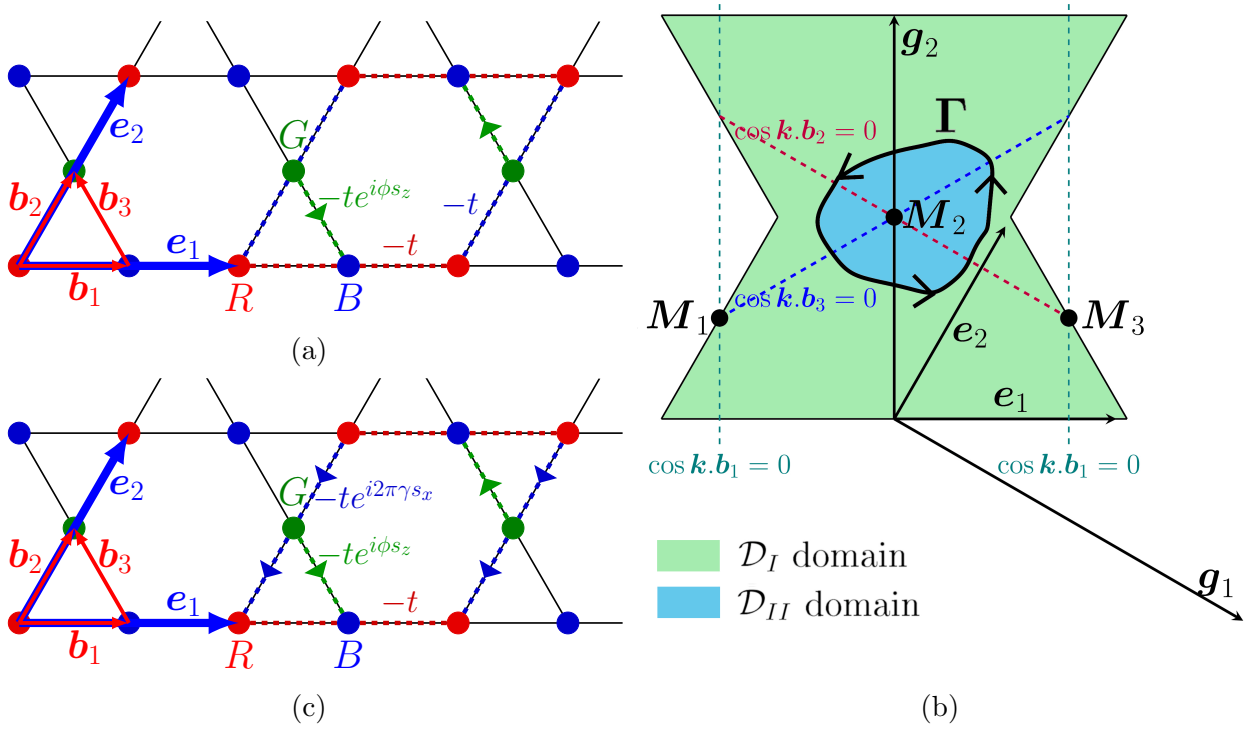

Figure 5.1: (a) and (c) Kagome lattice representation and respectively Hamiltonian in Eq. (5.3) and Hamiltonian in Eq. (5.41) hopping terms. The direction of the arrow is associated to a positive sign in the phase of exponential for the hopping terms between the sites G and B or R and G. (b) Definition of the Brillouin zone into two domains, each associated to a specific gauge choice for the eigenvectors of the Hamiltonian in Eq. (5.3).

terms and the complete Hamiltonian we study is then

$$\begin{aligned}\mathcal{H} &= -t\sum_{\mathbf{r}}\Big[c^{\dagger}_{R,\mathbf{r}}\mathbb{I}c_{B,\mathbf{r}} + c^{\dagger}_{R,\mathbf{r}+\mathbf{e}_1}\mathbb{I}c_{B,\mathbf{r}} + c^{\dagger}_{R,\mathbf{r}}\mathbb{I}c_{G,\mathbf{r}} + c^{\dagger}_{G,\mathbf{r}}\mathbb{I}c_{R,\mathbf{r}+\mathbf{e}_2} \\ &+ c^{\dagger}_{B,\mathbf{r}}e^{i\phi s_z}c_{G,\mathbf{r}} + c^{\dagger}_{B,\mathbf{r}+\mathbf{e}_3}e^{i\phi s_z}c_{G,\mathbf{r}} + H.c.\Big] + \sum_{\mathbf{r}}\sum_{\alpha=R,B,G}\lambda_\alpha n_{\alpha,\mathbf{r}}. \end{aligned} \tag{5.3}$$

We consider periodic boundary conditions in both directions of the lattice. A Fourier transformation gives

$$\mathcal{H} = \sum_{\mathbf{k}}\psi^{\dagger}_{\mathbf{k}}\begin{pmatrix}\mathcal{H}_{\uparrow}(\mathbf{k}) & 0\\ 0 & \mathcal{H}_{\downarrow}(\mathbf{k})\end{pmatrix}\psi_{\mathbf{k}}\,, \tag{5.4}$$

with

$$\mathcal{H}_\sigma(\mathbf{k}) = \begin{pmatrix} \lambda_R & \varepsilon_1(\mathbf{k}) & \varepsilon_2(\mathbf{k}) \\ \varepsilon_1(\mathbf{k}) & \lambda_B & e^{is_z\phi}\varepsilon_3(\mathbf{k}) \\ \varepsilon_2(\mathbf{k}) & e^{-is_z\phi}\varepsilon_3(\mathbf{k}) & \lambda_G \end{pmatrix}, \tag{5.5}$$

$$\psi^\dagger_{\mathbf{k}} = \left(c^\dagger_{R,\mathbf{k},\uparrow}, c^\dagger_{B,\mathbf{k},\uparrow}, c^\dagger_{G,\mathbf{k},\uparrow}, c^\dagger_{R,\mathbf{k},\downarrow}, c^\dagger_{B,\mathbf{k},\downarrow}, c^\dagger_{G,\mathbf{k},\downarrow}\right), \tag{5.6}$$

$\varepsilon_\alpha = -2t\cos(\mathbf{k}\cdot\mathbf{b}_\alpha)$, and $s_z = 1\,(-1)$ for $\sigma = \uparrow\ (\downarrow)$. We notice that if the on-site potential terms are vanishing, we obtain the Hamiltonian in Eq. (3.10b) studied in Chapter 3. As we mentioned in Chapter 3, this Hamiltonian only differs from the Hamiltonian describing two spin copies of Eq. (3.8) by a $U(1)$ local gauge transformation. It is obviously time-reversal invariant.

5.1.2 Computation of the $\mathbb{Z}_2$ invariant from the spin Chern numbers

We now compute the lowest band spin Chern numbers C_σ associated to the model described in the previous section (for different on-site energy configurations), by implementing the method described in Chapter. 3, Sec. 3.2.1 [10]. The $\mathbb{Z}_2$ invariant ν is then given by $\nu = C_\uparrow \bmod 2$ (see Sec. 3.3.1).

On-site potential configuration $\lambda_B = -\lambda_R = \lambda$ and $\lambda_G = 0$

Here we consider the case for which the on-site energies are such that $\lambda_B = -\lambda_R = \lambda$ and $\lambda_G = 0$. We compute ν for all flux ϕ and arbitrary onsite energy λ. Both lowest energy band (associated to opposite spin species) are described by the energy E given by

$$E = -2\sqrt{\frac{\lambda^2 + 4t^2\left[1 + f(\boldsymbol{k})\right]}{3}}\cos\frac{\theta(\boldsymbol{k})}{3}, \tag{5.7}$$

with $f(\boldsymbol{k}) = 2\prod_{\alpha=1}^{3}\cos\mathbf{k}\cdot\mathbf{b}_\alpha$ and $0 \leq \theta(\boldsymbol{k}) \leq \pi$ defined by

$$\theta(\boldsymbol{k}) = \arccos \frac{3^{3/2}\left(f(\boldsymbol{k})\cos\phi + \dfrac{\lambda\left(\varepsilon_2^2(\mathbf{k}) - \varepsilon_3^2(\mathbf{k})\right)}{8t^3}\right)}{2\left(1 + f(\boldsymbol{k}) + \left(\dfrac{\lambda}{2t}\right)^2\right)^{3/2}}. \tag{5.8}$$

From this we observe that the gap between the lowest band and the middle one only closes at $\lambda = \pm\sqrt{2}t$. It is valid for each spin species, to which associated middle band energy is given by

$$E_{\mathrm{m}} = -2\sqrt{\frac{\lambda^2 + 4t^2\left[1 + f(\boldsymbol{k})\right]}{3}}\cos\frac{\theta(\boldsymbol{k}) - 2\pi}{3}, \tag{5.9}$$

Let us remind that we denote the three nonequivalent high symmetry $\mathbf{M}$ points, $\mathbf{M}_1 = -\frac{1}{2}\mathbf{g}_1$, $\mathbf{M}_2 = \frac{1}{2}\mathbf{g}_2$ and $\mathbf{M}_3 = \frac{1}{2}(\mathbf{g}_1 + \mathbf{g}_2)$ (see Fig. 5.1(b)). At $\lambda = \sqrt{2}t$ the energy bands touch in reciprocal space at the $\mathbf{M}_3$ point, while at $\lambda = -\sqrt{2}t$ the energy bands touch at the $\mathbf{M}_1$ point, and we observe that

(i) at $\lambda \leq -\sqrt{2}t$, we have $E \leq \lambda$, with the equality occurring at the $\mathbf{M}_1$ point,

(ii) at $-\sqrt{2}t < \lambda < \sqrt{2}t$, we have $E < -|\lambda|$,

(iii) at $\lambda \geq \sqrt{2}t$, we have $E \leq -\lambda$, with the equality occurring at the $\mathbf{M}_3$ point.

In the following, we will only describe the computation of the lowest band Chern number for the case $\lambda < 0$ because the case $\lambda > 0$ can be studied following almost the same steps. Let us write

$$|u_{\sigma,\boldsymbol{k}}\rangle = \frac{\left(r_\sigma(\boldsymbol{k})c^\dagger_{R,\mathbf{k},\sigma} + b_\sigma(\boldsymbol{k})c^\dagger_{B,\mathbf{k},\sigma} + g_\sigma(\boldsymbol{k})c^\dagger_{G,\mathbf{k},\sigma}\right)|0\rangle}{\sqrt{|r_\sigma(\boldsymbol{k})|^2 + |b_\sigma(\boldsymbol{k})|^2 + |g_\sigma(\boldsymbol{k})|^2}}, \tag{5.10}$$

the lowest energy eigenvector of $\mathcal{H}_\sigma(\boldsymbol{k})$ in the basis $\left(c^\dagger_{\mathbf{k},R,\sigma}, \mathrm{e}^{i\mathbf{k}\cdot\mathbf{b}_1}c^\dagger_{\mathbf{k},B,\sigma}, \mathrm{e}^{i\mathbf{k}\cdot\mathbf{b}_2}c^\dagger_{\mathbf{k},G,\sigma}\right)$. We now determine the coefficients $r_\sigma(\boldsymbol{k})$, $b_\sigma(\boldsymbol{k})$ and $g_\sigma(\boldsymbol{k})$ for 3 gauge choices G_I, G_{II} and G_{III} on the eigenvectors that we respectively write $|u_{\sigma,\boldsymbol{k},I}\rangle$, $|u_{\sigma,\boldsymbol{k},II}\rangle$ and $|u_{\sigma,\boldsymbol{k},III}\rangle$. We will see later that these choices enable to correctly define the Bloch eigenvectors over the BZ.

(i) *Gauge choice* G_I: the coefficient $g_\sigma(\boldsymbol{k})$ is real. More precisely, we choose

$$g_\sigma(\boldsymbol{k}) = \rho_\sigma(\boldsymbol{k}), \tag{5.11}$$

with

$$\rho_\sigma(\boldsymbol{k})e^{i\varphi_\sigma(\boldsymbol{k})} = -e^{i\mathbf{k}\cdot\mathbf{b}_2}\left[\frac{(E-\lambda)\varepsilon_2(\mathbf{k})}{2\varepsilon_1(\mathbf{k})} + \frac{1}{2}e^{-is_z\phi}\varepsilon_3(\mathbf{k})\right], \tag{5.12}$$

where $\rho_\sigma(\boldsymbol{k})$ and $\varphi_\sigma(\boldsymbol{k})$ are both real numbers. Then we have

$$r_\sigma(\boldsymbol{k}) = -\frac{E(E-\lambda)-\varepsilon_3^2(\mathbf{k})}{2\varepsilon_1(\mathbf{k})}e^{-i\varphi_\sigma(\boldsymbol{k})}, \tag{5.13}$$

and

$$b_\sigma(\boldsymbol{k}) = \frac{E(E+\lambda)-\varepsilon_2^2(\mathbf{k})}{\rho_{1,\sigma}(\boldsymbol{k})}\rho_\sigma(\boldsymbol{k})e^{-i\varphi_{1,\sigma}(\boldsymbol{k})}, \tag{5.14}$$

with

$$\rho_{1,\sigma}(\boldsymbol{k})e^{i\varphi_{1,\sigma}(\boldsymbol{k})} = e^{-i\mathbf{k}\cdot(\mathbf{b}_1-\mathbf{b}_2)}\left[(E+\lambda)\varepsilon_3(\mathbf{k})e^{-is_z\phi} + \varepsilon_1(\mathbf{k})\varepsilon_2(\mathbf{k})\right], \tag{5.15}$$

where $\rho_{1,\sigma}(\boldsymbol{k})$ and $\varphi_{1,\sigma}(\boldsymbol{k})$ are both real numbers.

(ii) *Gauge choice* G_{II}: the coefficient $r_\sigma(\boldsymbol{k})$ is real. We choose

$$g_\sigma(\boldsymbol{k}) = \rho_\sigma(\boldsymbol{k})e^{i\varphi_\sigma(\boldsymbol{k})}. \tag{5.16}$$

Then we have

$$r_\sigma(\boldsymbol{k}) = -\frac{E(E-\lambda)-\varepsilon_3^2(\mathbf{k})}{2\varepsilon_1(\mathbf{k})}, \tag{5.17}$$

and

$$b_\sigma(\boldsymbol{k}) = \frac{E(E+\lambda)-\varepsilon_2^2(\mathbf{k})}{\rho_{1,\sigma}(\boldsymbol{k})}\rho_\sigma(\boldsymbol{k})e^{i[\varphi_\sigma(\boldsymbol{k})-\varphi_{1,\sigma}(\boldsymbol{k})]}. \tag{5.18}$$

(iii) *Gauge choice* G_{III}: the coefficient $b_\sigma(\boldsymbol{k})$ is real. We choose

$$g_\sigma(\boldsymbol{k}) = \rho_\sigma(\boldsymbol{k})e^{i\varphi_{1,\sigma}(\boldsymbol{k})}. \tag{5.19}$$

Then we have

$$r_\sigma(\boldsymbol{k}) = -\frac{E(E-\lambda)-\varepsilon_3^2(\mathbf{k})}{2\varepsilon_1(\mathbf{k})}e^{-i[\varphi_\sigma(\boldsymbol{k})-\varphi_{1,\sigma}(\boldsymbol{k})]}, \tag{5.20}$$

and

$$b_\sigma(\boldsymbol{k}) = \frac{E(E+\lambda)-\varepsilon_2^2(\mathbf{k})}{\rho_{1,\sigma}(\boldsymbol{k})}\rho_\sigma(\boldsymbol{k}). \tag{5.21}$$

Notice that $\varphi_\sigma(\boldsymbol{k})$ is well-defined (modulo 2π) for all $\boldsymbol{k}$ except when $\rho_\sigma(\boldsymbol{k}) = 0$ or when $\varepsilon_1(\mathbf{k}) = -2t\cos\mathbf{k}\cdot\mathbf{b}_1 = 0$ and $\varphi_{1,\sigma}(\boldsymbol{k})$ is well-defined for all $\boldsymbol{k}$ except when $\rho_{1,\sigma}(\boldsymbol{k}) = 0$.

Now we have to distinguish two different cases $\lambda < -\sqrt{2}t$ and $-\sqrt{2}t \leq \lambda \leq 0$. First, the $\lambda < -\sqrt{2}t$ case. In this case, $E \leq \lambda$. The points for which $\rho_\sigma(\boldsymbol{k}) = 0$ are the same than those for which $\rho_{1,\sigma}(\boldsymbol{k}) = 0$. These are the $\boldsymbol{M}_2 = \frac{1}{2}\mathbf{g}_2$ point at which $\cos\mathbf{k}\cdot\mathbf{b}_2 = \cos\mathbf{k}\cdot\mathbf{b}_3 = 0$, and the $\boldsymbol{M}_1$ point at which $\cos\mathbf{k}\cdot\mathbf{b}_1 = \cos\mathbf{k}\cdot\mathbf{b}_3 = 0$ and $E = \lambda$. In this case, we apply gauge choice G_{III} for all the points of the BZ; then the wave function $|u_{\sigma,\boldsymbol{k},III}\rangle$ (and its phase) is uniquely and smoothly defined, as is the Berry gauge field $\boldsymbol{A}_{\sigma,\boldsymbol{k},III} = \langle u_{\sigma,\boldsymbol{k},III}|\,\boldsymbol{\nabla}_{\boldsymbol{k}}\,|u_{\sigma,\boldsymbol{k},III}\rangle$. Because the BZ is a torus, we find that the lowest band Chern numbers C_σ, are both vanishing. A very similar proof can be done for the $\lambda > \sqrt{2}t$ case. We conclude that at $n = 2/3$ filling, for all flux $\phi \in]0,\pi[$, the phase associated to $\lambda_B = -\lambda_R = \lambda$ and $\lambda_G = 0$, $|\lambda| > \sqrt{2}t$ is a trivial insulator.

Now, let us study the $-\sqrt{2}t \leq \lambda \leq 0$ case which includes the $\lambda = 0$ case we studied in Chapter. 3, Sec. 3.2.1. In this case, $E < \lambda$. We have $\rho_\sigma(\boldsymbol{k}) = 0$ at the $\boldsymbol{M}_2$ point. We have $\rho_1(\boldsymbol{k}) = 0$ at the $\boldsymbol{M}_2$ and the $\boldsymbol{M}_1$ points. Here, it is impossible to find a unique and smooth gauge everywhere in the BZ. Extending the study of Chapter. 3, Sec. 3.2.1, we define the $\mathcal{D}_{II}$ domain, which contains the point where $\rho_\sigma(\boldsymbol{k})$ vanishes, and the $\mathcal{D}_I$ domain, which contains all the points where $E(E-\lambda) - \varepsilon_3^2(\mathbf{k})$ vanishes or $\varepsilon_1(\mathbf{k})$ vanishes (see Fig. 5.1(b)). The boundary between $\mathcal{D}_I$ and $\mathcal{D}_{II}$ do not contain any of the $\rho_\sigma(\boldsymbol{k}) = 0$, $E(E-\lambda) - \varepsilon_3^2(\mathbf{k}) = 0$ and $\varepsilon_1(\mathbf{k}) = 0$ points. We also define Γ a closed path along this boundary, surrounding once $\boldsymbol{M}_2$, as it is sketched in Fig. 5.1(b). We apply G_I gauge choice for the points contained in $\mathcal{D}_I$ and G_{II} gauge choice for the points contained in $\mathcal{D}_{II}$ and it yields unique and smooth Berry gauge fields on each domain $\mathcal{D}_I$ and $\mathcal{D}_{II}$. Along Γ, we have $|u_{\sigma,\boldsymbol{k},I}\rangle = \mathrm{e}^{-i\varphi_\sigma(\boldsymbol{k})}\,|u_{\sigma,\boldsymbol{k},II}\rangle$ and we define $\varphi_\sigma(\boldsymbol{k})$ so that it is smooth (along Γ). Here we have (this is the adaptation of Eq. (3.28) to the present case)

$$C_\sigma = \frac{1}{2\pi}\oint_\Gamma d\boldsymbol{k}\cdot\boldsymbol{\nabla}_{\boldsymbol{k}}\varphi_\sigma(\boldsymbol{k}). \tag{5.22}$$

Studying how $\varphi_\sigma(\boldsymbol{k})$ evolves when moving along Γ, we get

$$C_\sigma = -s_z \mathrm{sgn}\left(\sin\phi\right). \tag{5.23}$$

A very similar proof can be done for the $0 < \lambda < \sqrt{2}t$ case. We conclude that at $n = 2/3$ filling, for all flux $\phi \in]0, \pi[$, the phase associated to $\lambda_B = -\lambda_R = \lambda$ and $\lambda_G = 0$, $|\lambda| < \sqrt{2}t$ is a quantum spin Hall topological insulator $\nu = 1$.

This computation allows us to understand the discontinuous changes in the $\mathbb{Z}_2$ number. Let us denote $\max(E_l)$ the highest energy eigenvalue associated with the lowest band. When λ is such that $|\lambda| < \sqrt{2}t$, we have $\max(E_l) < -|\lambda|$. From the eigenvector's coefficients (see Eqs. (5.11)–(5.21)), we see that we can not define a continuous gauge choice in the whole BZ. At $|\lambda| = \sqrt{2}t$ the gap between the lowest and the middle energy bands closes. When λ is such that $|\lambda| > \sqrt{2}t$, $\max(E_l) = -|\lambda|$. It is now possible to define a continuous gauge choice in the whole BZ. When varying λ and crossing the $|\lambda| = \sqrt{2}t$ point, the fact that $\max(E_l)$ goes from $\max(E_l) < -|\lambda|$ to $\max(E_l) = -|\lambda|$ gives a discontinuity in the $\mathbb{Z}_2$ number. It is important to notice that when $|\lambda| > \sqrt{2}t$, $\max(E_l)$ is reached at either the high symmetry $\mathbf{M_1}$ point or the high symmetry $\mathbf{M_3}$ point. In Sec 5.1.3, we use a different method for computing the $\mathbb{Z}_2$ number. But as we shall see, this is still the fact that $\max(E_l)$ goes from $\max(E_l) < -|\lambda|$ to $\max(E_l) = -|\lambda|$ which yields a discontinuity in the parity eigenvalue (associated with the lowest band) at the high symmetry points, and this eventually gives a discontinuity in the $\mathbb{Z}_2$ number.

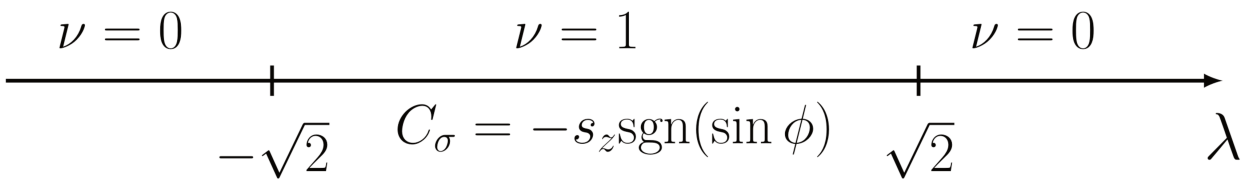

Figure 5.2: Topological phase diagram for the on-site energy configuration $\lambda_B = -\lambda_R = \lambda$, $\lambda_G = 0$.

On-site potential configuration $\lambda_R = \lambda$ and $\lambda_B = \lambda_G = 0$

Now we consider the case where one of the sublattices has a finite onsite energy, while on the other two sublattices the onsite energy vanishes, $\lambda_R = \lambda$ and $\lambda_B = \lambda_G = 0$. At $\gamma = 0$, we compute the $\mathbf{Z}_2$ number for all flux ϕ and arbitrary onsite energy λ at $n = 2/3$ filling. The computation is similar to the one we have done for the $\lambda_B = -\lambda_R = \lambda$ and $\lambda_G = 0$ case. We denote $\tilde{\lambda} = \lambda/3t$. Both lowest energy band (associated to opposite spin species) are described by the energy E given by

$$E = 2t\sqrt{\tilde{\lambda}^2 + \frac{4}{3}\left[1 + f(\boldsymbol{k})\right]}\cos\frac{\theta(\boldsymbol{k}) + 2\pi}{3}, \tag{5.24}$$

with $f(\boldsymbol{k}) = 2\prod_{\alpha=1}^{3}\cos\mathbf{k}\cdot\mathbf{b}_\alpha$ and $0 \leq \theta(\boldsymbol{k}) \leq \pi$ defined by

$$\theta(\boldsymbol{k}) = \arccos\frac{\tilde{\lambda}^3 + 2\tilde{\lambda}\left(1 + f(\boldsymbol{k}) - \frac{3}{4t^2}\varepsilon_3^2(\mathbf{k})\right) - 4f(\boldsymbol{k})\cos\phi}{\left[\tilde{\lambda}^2 + \frac{4}{3}\left[1 + f(\boldsymbol{k})\right]\right]^{3/2}}. \tag{5.25}$$

In this case, the gap between the lowest band and the middle one only closes for the parameter value $\lambda = -2t$, at the reciprocal space $\mathbf{M}_3$ point. It is valid for each spin species, to which associated middle energy band is given by

$$E_{\mathrm{m}} = 2t\sqrt{\tilde{\lambda}^2 + \frac{4}{3}\left[1 + f(\mathbf{k})\right]}\cos\frac{\theta(\mathbf{k}) - 2\pi}{3}. \tag{5.26}$$

We observe that

(i) for $\lambda \leq -2t$, we have $E \leq \lambda$, with the equality occurring at the $\mathbf{M}_3$ point,

(ii) for $\lambda > -2t$, we have $E < \lambda$.

Now we can proceed in the same way than in the last section. We keep the same notations for the coefficients of the eigenvectors and we introduce 3 gauge choices.

(i) *Gauge choice G_{IV}*: the coefficient $g_\sigma(\boldsymbol{k})$ is real. More precisely, we choose

$$g_\sigma(\boldsymbol{k}) = \rho_{2,\sigma}(\boldsymbol{k}), \tag{5.27}$$

with

$$\rho_{2,\sigma}(\boldsymbol{k})e^{i\varphi_{2,\sigma}(\boldsymbol{k})} = e^{i\mathbf{k}\cdot(\mathbf{b}_2 - \mathbf{b}_1)}\left[\frac{(-E + \lambda)\varepsilon_3(\mathbf{k})}{2\varepsilon_1(\mathbf{k})}e^{-is_z\phi} - \frac{1}{2}\varepsilon_2(\mathbf{k})\right], \tag{5.28}$$

where $\rho_{2,\sigma}(\boldsymbol{k})$ and $\varphi_{2,\sigma}(\boldsymbol{k})$ are both real numbers. Then we have

$$r_\sigma(\boldsymbol{k}) = \frac{E^2 - \varepsilon_3^2(\mathbf{k})}{\rho_{3,\sigma}} \rho_{2,\sigma} e^{-i\varphi_{3,\sigma}(\boldsymbol{k})}, \tag{5.29}$$

and

$$b_\sigma(\boldsymbol{k}) = -\frac{E(E-\lambda) - \varepsilon_2^2(\mathbf{k})}{2\varepsilon_1(\mathbf{k})} e^{-i\varphi_{2,\sigma}(\boldsymbol{k})}\,, \tag{5.30}$$

with

$$\rho_{3,\sigma}(\boldsymbol{k}) e^{i\varphi_{3,\sigma}(\boldsymbol{k})} = e^{i\mathbf{k}\cdot\mathbf{b}_2} \left[E\varepsilon_2(\mathbf{k}) + e^{-is_z\phi_\sigma} \varepsilon_1(\mathbf{k})\varepsilon_2(\mathbf{k}) \right]\,, \tag{5.31}$$

where $\rho_{3,\sigma}(\boldsymbol{k})$ and $\varphi_{3,\sigma}(\boldsymbol{k})$ are both real numbers.

(ii) *Gauge choice* G_V: the coefficient $b_\sigma(\boldsymbol{k})$ is real. We choose

$$g_\sigma(\boldsymbol{k}) = \rho_{2,\sigma}(\boldsymbol{k}) e^{i\varphi_{2,\sigma}(\boldsymbol{k})}. \tag{5.32}$$

Then we have

$$r_\sigma(\boldsymbol{k}) = \frac{E^2 - \varepsilon_3^2(\mathbf{k})}{\rho_{3,\sigma}} \rho_{2,\sigma} e^{i[\varphi_{2,\sigma}(\boldsymbol{k}) - \varphi_{3,\sigma}(\boldsymbol{k})]}, \tag{5.33}$$

and

$$b_\sigma(\boldsymbol{k}) = -\frac{E(E-\lambda) - \varepsilon_2^2(\mathbf{k})}{2\varepsilon_1(\mathbf{k})}\,. \tag{5.34}$$

(iii) *Gauge choice* G_{VI}: the coefficient $r_\sigma(\boldsymbol{k})$ is real. We choose

$$g_\sigma(\boldsymbol{k}) = \rho_{2,\sigma}(\boldsymbol{k}) e^{i\varphi_{3,\sigma}(\boldsymbol{k})}. \tag{5.35}$$

Then we have

$$r_\sigma(\boldsymbol{k}) = \frac{E^2 - \varepsilon_3^2(\mathbf{k})}{\rho_{3,\sigma}} \rho_{2,\sigma}, \tag{5.36}$$

and

$$b_\sigma(\boldsymbol{k}) = -\frac{E(E-\lambda) - \varepsilon_2^2(\mathbf{k})}{2\varepsilon_1(\mathbf{k})} e^{-i[\varphi_{2,\sigma}(\boldsymbol{k}) - \varphi_{3,\sigma}(\boldsymbol{k})]}\,. \tag{5.37}$$

When $\lambda < -2t$, gauge choice G_{VI} is applicable to the whole BZ. We conclude that at $n = 2/3$ filling, for all flux $\phi \in]0, \pi[$, our model with $\lambda_R = \lambda$ and $\lambda_B = \lambda_G = 0$, $\lambda < -2t$ is characterized by a trivial insulating phase.

When $\lambda > -2t$, we split the Brillouin zone into 2 non-overlapping domains: the $\mathcal{D}_V$ domain contains the point where $\rho_2(\boldsymbol{k})$ vanishes and the $\mathcal{D}_{IV}$ domain contains all the points where $E(E-\lambda)-\varepsilon_2^2(\mathbf{k})$ vanishes or $\varepsilon_1(\mathbf{k})$ vanishes. The application of gauge choice G_{IV} and G_V in respectively $\mathcal{D}_{IV}$ and $\mathcal{D}_V$ indicates us that at $n = 2/3$ filling, for all flux $\phi \in]0, \pi[$, our model with $\lambda_R = \lambda$ and $\lambda_B = \lambda_G = 0$, $\lambda > -2t$ is characterized by a quantum spin Hall phase $\nu = 1$.

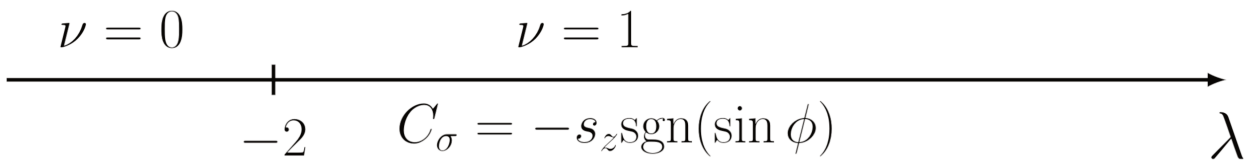

Figure 5.3: Topological phase diagram for the on-site energy configuration $\lambda_R = \lambda$, $\lambda_B = \lambda_G = 0$.

On-site potential configuration $\lambda_B = \lambda$ and $\lambda_R = \lambda_G = 0$

At $\gamma = 0$, we compute the $\mathbf{Z}_2$ number for all flux ϕ and arbitrary onsite energy λ. The computation is very similar to the one done at $\lambda_R = \lambda$ and $\lambda_B = \lambda_G = 0$. We can show that, for all flux $\phi \in]0, \pi[$, the $\lambda < -2t$ parameter space is characterized by a trivial insulating phase while the $\lambda > -2t$ parameter space is characterized by a quantum spin Hall phase $\nu = 1$.

5.1.3 Computation of the $\mathbb{Z}_2$ invariant using inversion symmetry

Now we check the results obtained in the previous section by using the method described in Chapter. 3, Sec. 3.3 [190]. We consider both configurations $\lambda_B = -\lambda_R = \lambda$, $\lambda_G = 0$ and $\lambda_R = \lambda$, $\lambda_B = \lambda_G = 0$ (this last case is identical to $\lambda_B = \lambda$ and $\lambda_R = \lambda_G = 0$ as we showed previously) and we compute the $\mathbb{Z}_2$ invariant associated to the Hamiltonian in Eq. (5.4) at $n = 2/3$ filling (Fermi level in the gap between both lowest energy bands and both middle energy bands). In this Hamiltonian, because both spin polarization are not coupled, we

consider separately each of both diagonal parts.

As we explained in Chapter. 3, Sec. 3.3, at the $\mathbf{\Gamma}_{(0,0)}$ point, $P_{\mathbf{\Gamma}_{(0,0)}}$ is diagonal and at the other points we have

$$P_{\mathbf{\Gamma}_{(1,0)}} = \mathrm{diag}\,(1,-1,1), \tag{5.38a}$$

$$P_{\mathbf{\Gamma}_{(0,1)}} = \mathrm{diag}\,(1,1,-1), \tag{5.38b}$$

$$P_{\mathbf{\Gamma}_{(1,1)}} = \mathrm{diag}\,(1,-1,-1). \tag{5.38c}$$

At $\mathbf{\Gamma}_{(1,0)}$, $\mathbf{\Gamma}_{(0,1)}$, and $\mathbf{\Gamma}_{(1,1)}$., we have

$$\mathcal{H}_\sigma(\mathbf{\Gamma}_{(1,0)}) = \begin{pmatrix} \lambda_R & 0 & -2t \\ 0 & \lambda_B & 0 \\ -2t & 0 & \lambda_G \end{pmatrix}, \qquad \mathcal{H}_\sigma(\mathbf{\Gamma}_{(0,1)}) = \begin{pmatrix} \lambda_R & -2t & 0 \\ -2t & \lambda_B & 0 \\ 0 & 0 & \lambda_G \end{pmatrix}, \tag{5.39a}$$

$$\mathcal{H}_\sigma(\mathbf{\Gamma}_{(1,1)}) = \begin{pmatrix} \lambda_R & 0 & 0 \\ 0 & \lambda_B & -2te^{is_z\phi} \\ 0 & -2te^{-is_z\phi} & \lambda_G \end{pmatrix}. \tag{5.39b}$$

On-site potentials $\lambda_B = -\lambda_R = \lambda$ and $\lambda_G = 0$

In the case $\lambda_B = -\lambda_R = \lambda$ and $\lambda_G = 0$, we have

(i) at the $\mathbf{\Gamma}_{(1,0)}$ point, for $\lambda < -\sqrt{2}t$, the smallest eigenvalue is $E = \lambda$ and the associated eigenvector is proportional to $(0,1,0)$ (coefficients $(r_\sigma(\boldsymbol{k}), b_\sigma(\boldsymbol{k}), g_\sigma(\boldsymbol{k}))$ defined in Eq. (5.10)), while for $\lambda > -\sqrt{2}t$, the smallest eigenvalue is $E = -\left(\lambda + \sqrt{16t^2+\lambda^2}\right)/2$, with associated eigenvector proportional to $\left(-2t/(\lambda + E_l), 0, 1\right)$.

(ii) at the $\mathbf{\Gamma}_{(0,1)}$ point, the smallest eigenvalue is $E = -\sqrt{4t^2+\lambda^2}$ and the eigenvector associated to it is proportional to $\left(-2t/(\lambda + E_l), 1, 0\right)$.

(iii) at the $\mathbf{\Gamma}_{(1,1)}$ point, if $\lambda > \sqrt{2}t$, then $E = -\lambda$ is the smallest eigenvalue and the associated eigenvector is proportional to $(1,0,0)$, while if $\lambda < \sqrt{2}t$, then the smallest eigenvalue is $E = \left(\lambda - \sqrt{16t^2+\lambda^2}\right)/2$, with associated eigenvector proportional to $\left(0, 2te^{is_z\phi}/(\lambda - E_l), 1\right)$.

Applying the parity operator and the eigenvectors, we find that the phases $\lambda > \sqrt{2}t$ and $\lambda < -\sqrt{2}t$ are trivial insulators while the phase $-\sqrt{2}t < \lambda < \sqrt{2}t$ is a quantum spin Hall phase $\nu = 1$. These results are summarized in Table 5.1.

On-site potentials $\lambda_R = \lambda$ and $\lambda_B = \lambda_G = 0$

In the case $\lambda_R = \lambda$ and $\lambda_B = \lambda_G = 0$, we have

(i) at the $\mathbf{\Gamma}_{(1,0)}$ point, the smallest eigenvalue is $E = \left(\lambda - \sqrt{16t^2 + \lambda^2}\right)/2$, with associated eigenvector proportional to $(-E/2t, 0, 1)$ (coefficients $(r_\sigma(\boldsymbol{k}), b_\sigma(\boldsymbol{k}), g_\sigma(\boldsymbol{k}))$ defined in Eq. (5.10)).

(ii) at the $\mathbf{\Gamma}_{(0,1)}$ point, the smallest eigenvalue is $E = \left(\lambda - \sqrt{16t^2 + \lambda^2}\right)/2$, with associated eigenvector proportional to $(-E/2t, 1, 0)$.

(iii) at the $\mathbf{\Gamma}_{(1,1)}$ point, if $\lambda < -2t$, then $E = \lambda$ is the smallest eigenvalue and the associated eigenvector is proportional to $(1, 0, 0)$, while if $\lambda > -2t$, then the smallest eigenvalue is $E = -2t$, with associated eigenvector proportional to $(0, -\mathrm{e}^{is_z\phi}, 1)$.

Applying the parity operator on the eigenvectors, we find that the phase $\lambda < -2t$ is a trivial insulator while the phase $\lambda > -2t$ is a quantum spin Hall phase $\nu = 1$. These results are summarized in Table 5.2.

5.1.4 Splitting of the energy bands under a weak magnetic field

The determination of the spin Chern number may be performed using the method introduced in Chapter 3, Sec. 3.2.2 [34, 194] which rely on the determination of the energy spectrum under a weak magnetic field $\mathcal{B} = \mathcal{B}\hat{\mathbf{z}}$ orthogonal to the Kagome lattice plane. Let us show to which extend it is applicable to the present model described by the Hamiltonian in Eq. (5.4).

Hamiltonian in Eq. (5.4) decouples into two spin independent parts. Spin up and spin down part are associated to opposite energy bands' Chern number. Here we only consider the spin up part of the Hamiltonian.

We implement the effect of the magnetic field in the Hamiltonian. We compute the

λ	(n_1, n_2)	Eigenvalues E	$(r_\sigma(\boldsymbol{k}), b_\sigma(\boldsymbol{k}), g_\sigma(\boldsymbol{k}))$	Parity operator	$(-1)^\nu$
$\lambda < -\sqrt{2}t$	$(1,0)$	λ	$(0, t, 0)$	$\mathrm{diag}(1,-1,1)$	
	$(0,1)$	$-\sqrt{4t^2+\lambda^2}$	$\left(-2t^2/(\lambda+E), t, 0\right)$	$\mathrm{diag}(1,1,-1)$	$+1$
	$(1,1)$	$\left(\lambda - \sqrt{16t^2+\lambda^2}\right)/2$	$(0, 2t^2 e^{is_z\phi}/(\lambda - E), t)$	$\mathrm{diag}(1,-1,-1)$	
$\lvert\lambda\rvert < \sqrt{2}t$	$(1,0)$	$-\left(\lambda + \sqrt{16t^2+\lambda^2}\right)/2$	$\left(-2t^2/(\lambda+E), 0, t\right)$	$\mathrm{diag}(1,-1,1)$	
	$(0,1)$	$-\sqrt{4t^2+\lambda^2}$	$\left(-2t^2/(\lambda+E), t, 0\right)$	$\mathrm{diag}(1,1,-1)$	-1
	$(1,1)$	$\left(\lambda - \sqrt{16t^2+\lambda^2}\right)/2$	$(0, 2t^2 e^{is_z\phi}/(\lambda - E), t)$	$\mathrm{diag}(1,-1,-1)$	
$\lambda > \sqrt{2}t$	$(1,0)$	$-\left(\lambda + \sqrt{16t^2+\lambda^2}\right)/2$	$\left(-2t^2/(\lambda+E), 0, t\right)$	$\mathrm{diag}(1,-1,1)$	
	$(0,1)$	$-\sqrt{4t^2+\lambda^2}$	$\left(-2t^2/(\lambda+E), t, 0\right)$	$\mathrm{diag}(1,1,-1)$	$+1$
	$(1,1)$	$-\lambda$	$(t, 0, 0)$	$\mathrm{diag}(1,-1,-1)$	

Table 5.1: Table summarizing the computation of the Z_2 topological invariant ν for an inversion and time-reversal symmetric system. In this example, we took the chemical potentials to be $\lambda_B = -\lambda_R = \lambda$ and $\lambda_G = 0$. (n_1, n_2) define the time-reversal invariant momenta (see Chapter 3, Sec. 3.3.2), and the eigenvector's coefficients $(r_\sigma(\boldsymbol{k}), b_\sigma(\boldsymbol{k}), g_\sigma(\boldsymbol{k}))$ are defined in Sec. 5.1.2.

λ	(n_1, n_2)	Eigenvalues E	$(r_\sigma(\boldsymbol{k}), b_\sigma(\boldsymbol{k}), g_\sigma(\boldsymbol{k}))$	Parity operator	$(-1)^\nu$
$\lambda < -2t$	$(1,0)$	$\left(\lambda - \sqrt{16t^2+\lambda^2}\right)/2$	$(-E/2, 0, t)$	$\mathrm{diag}(1,-1,1)$	
	$(0,1)$	$\left(\lambda - \sqrt{16t^2+\lambda^2}\right)/2$	$(-E/2, t, 0)$	$\mathrm{diag}(1,1,-1)$	$+1$
	$(1,1)$	λ	$(t, 0, 0)$	$\mathrm{diag}(1,-1,-1)$	
$\lambda > -2t$	$(1,0)$	$\left(\lambda - \sqrt{16t^2+\lambda^2}\right)/2$	$(-E/2, 0, t)$	$\mathrm{diag}(1,-1,1)$	
	$(0,1)$	$\left(\lambda - \sqrt{16t^2+\lambda^2}\right)/2$	$(-E/2, t, 0)$	$\mathrm{diag}(1,1,-1)$	-1
	$(1,1)$	$-2t$	$(0, -te^{is_z\phi}, 1)$	$\mathrm{diag}(1,-1,-1)$	

Table 5.2: Table summarizing the computation of the Z_2 topological invariant ν for an inversion and time-reversal symmetric system. In this example, we took the chemical potentials to be $\lambda_R = \lambda$ and $\lambda_B = \lambda_G = 0$. (n_1, n_2) define the time-reversal invariant momenta (see Chapter 3, Sec. 3.3.2), and the eigenvector's coefficients $(r_\sigma(\boldsymbol{k}), b_\sigma(\boldsymbol{k}), g_\sigma(\boldsymbol{k}))$ are defined in Sec. 5.1.2.

energy spectrum and the energy density of states (DoS) so that we can count the number of subbands arising from each parent band. We consider for instance $\mathcal{B}$ such that $1/f = 5$. Figure 5.4 show the density of states (DoS) at different values λ_α. At $\lambda_\alpha = 0$, $\alpha = R, B, G$, we see that we have $D_1 = 4$ subbands, $D_2 = 5$ subbands and $D_3 = 6$ subbands, which gives $\nu_1 = -\nu_3 = 1$, and $\nu_2 = 0$. We see that when $|\lambda_\alpha|$ starts increasing, counting the subbands becomes more and more difficult; when λ_α reaches a value of the order t or greater, the determination of the Chern number relying on this method becomes impracticable.

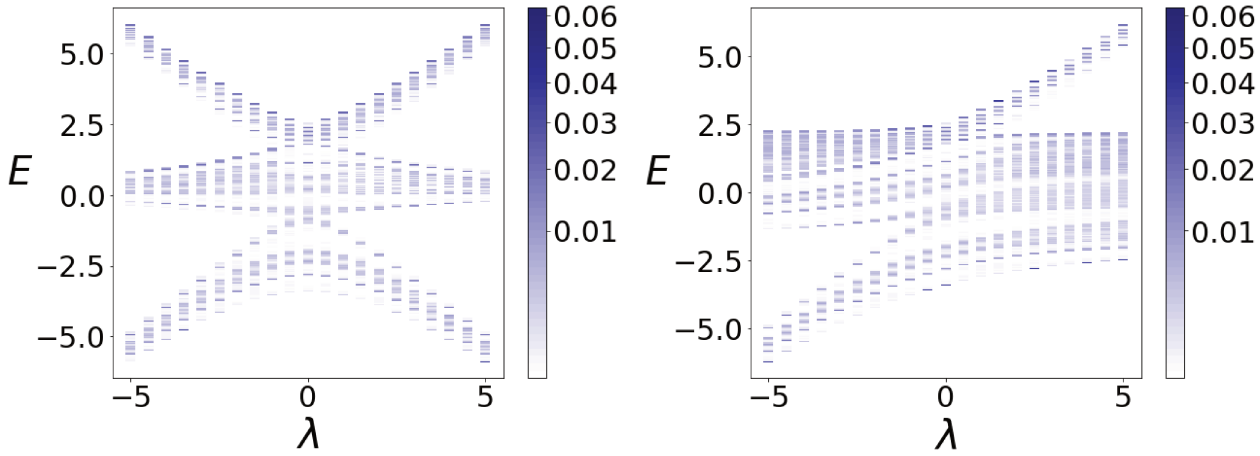

(a) (b)

Figure 5.4: (a) Density of states for the spin up part of the Hamiltonian with $\gamma = 0$, $1/f = 5$, and at $-\lambda_R = \lambda_B = \lambda$, $\lambda_G = 0$ and (b) $\lambda_R = \lambda$, $\lambda_B = \lambda_G = 0$.

5.2 Rashba spin-orbit coupling and Z_2 topological phase

In this section, we consider the effect of a Rashba spin orbit coupling term (see Chapter 1, Sec. 1.4.1) on the model we introduced in Sec. 5.1. This term breaks the inversion symmetry, varies the amplitude of the topological gap and whose physical origin is for instance a perpendicular electric field. First we write the Hamiltonian we considered here, for a cold atom system and we check explicitly the invariance under a time-reversal transformation. Then using the argument reviewed in Chapter 1, Sec. 1.3.3, we determine the topological phase

diagram using a numerical computation of the gap between the second lowest energy band and the third lowest energy band. We compare these results with the one obtained by our collaborators in Frankfurt [188] who used a numerical method based on twisted boundary conditions [313].

5.2.1 Hamiltonian and time-reversal symmetry

Similarly to the flux term, we write the Rashba spin-orbit coupling term along only one direction of the lattice (see Fig. 5.1(c)) and under a form potentially implementable through an artificial gauge field in cold atom gases

$$-t\sum_{\mathbf{r}} c^{\dagger}_{R,\mathbf{r}} e^{-i2\pi\gamma s_x} c_{G,\mathbf{r}} + c^{\dagger}_{G,\mathbf{r}} e^{-i2\pi\gamma s_x} c_{R,\mathbf{r}+\mathbf{e}_2} + H.c.\,. \tag{5.40}$$

We remind that s_x is the first Pauli matrix in spin space. We notice that the Rashba spin-orbit coupling terms act as a complex amplitude hopping term with spin flip and that it breaks inversion symmetry. The complete Hamiltonian is

$$\begin{aligned}\mathcal{H} &= -t\sum_{\mathbf{r}}\Big[c^{\dagger}_{R,\mathbf{r}}\mathbb{I}c_{B,\mathbf{r}} + c^{\dagger}_{R,\mathbf{r}+\mathbf{e}_1}\mathbb{I}c_{B,\mathbf{r}} + c^{\dagger}_{R,\mathbf{r}} e^{-i2\pi\gamma s_x} c_{G,\mathbf{r}} + c^{\dagger}_{G,\mathbf{r}} e^{-i2\pi\gamma s_x} c_{R,\mathbf{r}+\mathbf{e}_2} \\ &+ c^{\dagger}_{B,\mathbf{r}} e^{i\phi s_z} c_{G,\mathbf{r}} + c^{\dagger}_{B,\mathbf{r}+\mathbf{e}_3} e^{i\phi s_z} c_{G,\mathbf{r}} + H.c.\Big] + \sum_{\mathbf{r}}\sum_{\alpha=R,B,G}\lambda_\alpha n_{\alpha,\mathbf{r}},\end{aligned} \tag{5.41}$$

and in momentum space it reads

$$\mathcal{H} = \sum_{\mathbf{k}} \psi^{\dagger}_{\mathbf{k}} \begin{pmatrix} \mathcal{H}_{\uparrow}(\mathbf{k}) & \mathcal{H}_{SO}(\mathbf{k}) \\ \mathcal{H}^{\dagger}_{SO}(\mathbf{k}) & \mathcal{H}_{\downarrow}(\mathbf{k}) \end{pmatrix} \psi_{\mathbf{k}}\,, \tag{5.42}$$

with

$$\mathcal{H}_{\sigma}(\mathbf{k}) = \begin{pmatrix} \lambda_R & \varepsilon_1(\mathbf{k}) & \cos(2\pi\gamma)\varepsilon_2(\mathbf{k}) \\ \varepsilon_1(\mathbf{k}) & \lambda_B & e^{is_z\phi}\varepsilon_3(\mathbf{k}) \\ \cos(2\pi\gamma)\varepsilon_2(\mathbf{k}) & e^{-is_z\phi}\varepsilon_3(\mathbf{k}) & \lambda_G \end{pmatrix}, \tag{5.43}$$

$$\mathcal{H}_{SO}(\mathbf{k}) = \begin{pmatrix} 0 & 0 & \sin(2\pi\gamma)\xi(\mathbf{k}) \\ 0 & 0 & 0 \\ \sin(2\pi\gamma)\xi(\mathbf{k}) & 0 & 0 \end{pmatrix}. \tag{5.44}$$

$$\psi_{\mathbf{k}}^{\dagger} = \left(c_{R,\mathbf{k},\uparrow}^{\dagger}, c_{B,\mathbf{k},\uparrow}^{\dagger}, c_{G,\mathbf{k},\uparrow}^{\dagger}, c_{R,\mathbf{k},\downarrow}^{\dagger}, c_{B,\mathbf{k},\downarrow}^{\dagger}, c_{G,\mathbf{k},\downarrow}^{\dagger} \right) , \tag{5.45}$$

$\varepsilon_{\alpha} = -2t\cos(\mathbf{k}\cdot\mathbf{b}_{\alpha})$, $\xi(\mathbf{k}) = 2t\sin(\mathbf{k}\cdot\mathbf{b}_2)$ and $s_z = 1\,(-1)$ for $\sigma = \uparrow\ (\downarrow)$.

Let us check that the Hamiltonian in Eq. (5.41) is invariant under time-reversal symmetry: $\Theta\mathcal{H}\Theta^{-1} = \mathcal{H}$ (see App. B). Let us rewrite $e^{-i2\pi\gamma\sigma^x} = \mathbb{I}\cos 2\pi\gamma - i\sigma^x \sin 2\pi\gamma$ and $e^{i\phi\sigma^z} = \mathbb{I}\cos\phi + i\sigma^z\sin\phi$ and we remind that $\sigma^y\sigma^x\sigma^{y*} = \sigma^x$ and $\sigma^y\sigma^z\sigma^{y*} = \sigma^z$. Then we write $\mathcal{H} = \sum_{\mathbf{k}} \psi_{\mathbf{k}}^{\dagger}\mathcal{H}(\mathbf{k})\psi_{\mathbf{k}}$, with $\mathcal{H}(\mathbf{k})$ a generic notation for the momentum space Hamiltonian matrix which appears in Hamiltonian 5.42. We notice that we have $\mathcal{H}_{\sigma}(-\mathbf{k}) = \mathcal{H}_{\overline{\sigma}}(\mathbf{k})^*$ and $\mathcal{H}_{SO}(-\mathbf{k}) = -\left(\mathcal{H}_{SO}(\mathbf{k})^{\dagger}\right)^*$ and it leads to $\Theta\mathcal{H}(\mathbf{k})\Theta^{-1} = \mathcal{H}(-\mathbf{k})$ therefore $\mathcal{H}$ is invariant under a time-reversal transformation (see App. B).

5.2.2 Topological phase diagram

At $\gamma = 0$ the Hamiltonian in Eq. (5.41), the system is characterized by a quantum spin Hall phase $\nu = 1$ and hosts, at each edge, one spin σ chiral mode and its time-reversal conjugate anti-chiral mode, and the bulk is insulating; the system in the trivial phase is a trivial insulator. When $\gamma \neq 0$, the analytical computation of $\nu = 1$ relying on Eq. (1.111) is theoretically possible but much more complicated because we would have to compute and study the eigenstates of the 6×6 Hamiltonian in Eq. (5.41).

In fact, using the phase diagrams we found at $\gamma = 0$ and the energy gap phase diagrams for non-vanishing values of γ, it is possible to obtain the $\mathbb{Z}_2$ topological phase diagram for non-vanishing values of γ. In Sec. 1.3.3, we showed that, during an adiabatic evolution of the Hamiltonian, an integer bulk quantity computed from the bulk energy states can vary only if the bulk gap closes. This is applicable to the $\mathbb{Z}_2$ invariant which indeed is an integer (see Eq. (1.111)). The energy gap phase diagrams for the different configurations of the on-site energies we considered previously are shown in Fig. 5.5. From this and the phase diagrams at $\gamma = 0$ (see Figs. 5.3 and 5.2), we deduce the $\mathbb{Z}_2$ topological phase diagrams for non-vanishing values of γ which are shown in Fig. 5.5. This figure has in fact been obtained from

the numerical computation of the $\mathbb{Z}_2$ invariant performed by our collaborators in Frankfurt [188]. The numerical method they used takes advantage of twisted boundary conditions [191, 313, 314]. Let us remind, as we explained at the end of Sec. 1.4.1 in Chapter 1, that in the $\mathbb{Z}_2$ phase at $\gamma \neq 0$, the spin Hall conductivity is not quantized and the edge modes can not be labelled by a spin quantum number. Indeed the Rashba spin-orbit coupling term (s_x) does not commute with s_z, see Eq. (5.41).

Finally let us mention that we have checked the appearance of edge modes in a cylinder geometry (we used partial Fourier transformation on the Hamiltonian (5.41), see App. E). For instance, Fig. 5.6 show the energy spectrum at $\gamma = 0.05t$, for the on-site energy configuration $\lambda_B = -\lambda_R = \lambda$, $\lambda_G = 0$ and for two different values of λ. We have numerically evaluated the local density of states at a Fermi energy in the bulk gap between the second lowest energy band and the third lowest energy band (only the case in Fig. 5.6a is associated with states in the bulk gap). Both states of a time-reversed pair in the bulk gap show localization at the same edge of the cylinder.

5.3 Hubbard interactions

In this section, we investigate Hubbard interactions (with amplitude U) for the model we studied, at half filling, at $\gamma = 0$ and for the on-site energy configuration $\lambda_R = \lambda$, $\lambda_B = \lambda_G = 0$. The aim is to study the ground state of the system and to determine what range of interaction amplitudes enable the topology to survive.

We consider the Hamiltonian

$$\mathcal{H} = \mathcal{H}_t + \mathcal{H}_\lambda + \mathcal{H}_U, \tag{5.46}$$

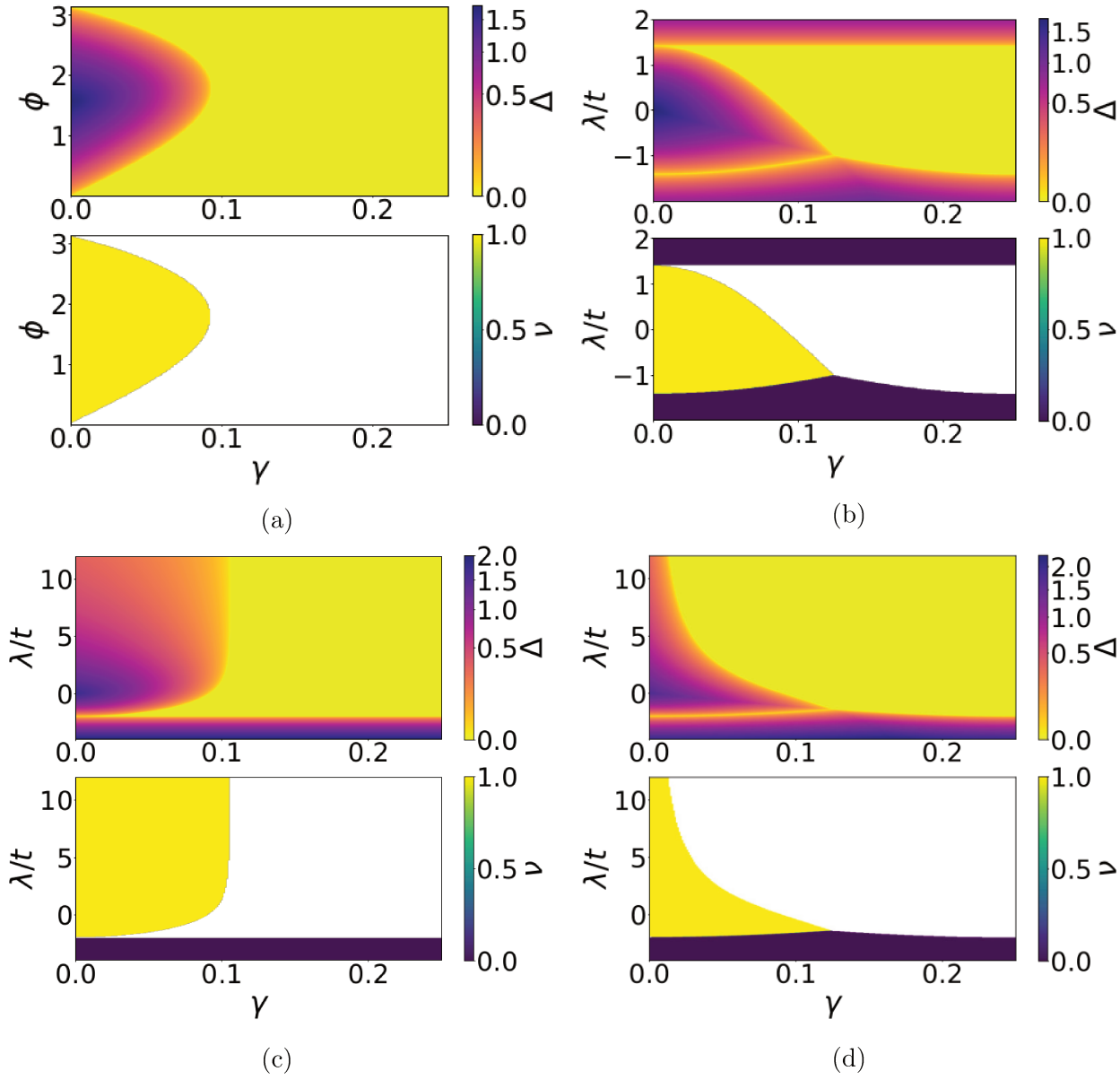

Figure 5.5: Value of the gap, Δ, between the second and the third energy bands and of the $\mathbb{Z}_2$ number ν associated to the Hamiltonian defined in Eq. (5.42). In the figures showing ν, the white regions correspond to the parameter space for which the gap closes, therefore ν is not defined in these regions. (a) $\lambda_R = \lambda_B = \lambda_G = 0$ and the quantities Δ and ν are shown as a function of the γ parameter and of the flux amplitude ϕ. (b) $\lambda_B = -\lambda_R = \lambda$, $\lambda_G = 0$, (c) $\lambda_R = \lambda$, $\lambda_G = \lambda_B = 0$ and (d) $\lambda_B = \lambda$, $\lambda_G = \lambda_R = 0$, the quantities Δ and ν are shown as a function of the γ parameter and of the on-site potential amplitude λ in units of t and here $\phi = \pi/2$. These figures are taken from Ref. [188] and were realized by I. Titvinidze.

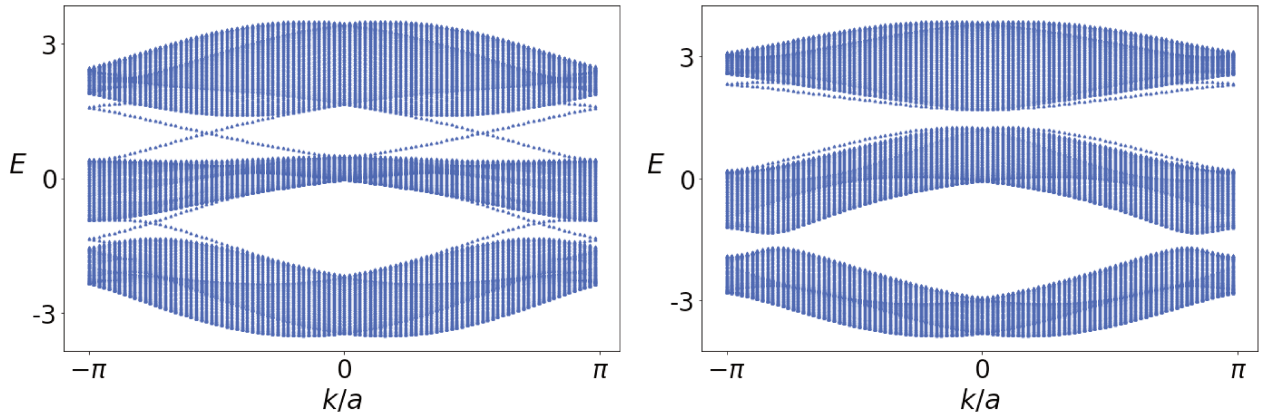

(a) (b)

Figure 5.6: Energy relation dispersion for a cylinder with the on-site energies such that $\lambda_B = -\lambda_R = \lambda$, $\lambda_G = 0$ and a flux $\phi = \pi/2$ at $\gamma = 0.05t$. In Fig. (a), $\lambda = 0.5t$ and in Fig. (b) $\lambda = 1.7t$.

with

$$\mathcal{H}_t = -t \sum_{\mathbf{r}} \Big[c^\dagger_{R,\mathbf{r}} \mathbb{I} c_{B,\mathbf{r}} + c^\dagger_{R,\mathbf{r}+\mathbf{e}_1} \mathbb{I} c_{B,\mathbf{r}} + c^\dagger_{R,\mathbf{r}} \mathbb{I} c_{G,\mathbf{r}} \tag{5.47a}$$

$$+ c^\dagger_{G,\mathbf{r}} \mathbb{I} c_{R,\mathbf{r}+\mathbf{e}_2} + c^\dagger_{B,\mathbf{r}} e^{i\phi s_z} c_{G,\mathbf{r}} + c^\dagger_{B,\mathbf{r}+\mathbf{e}_3} e^{i\phi s_z} c_{G,\mathbf{r}} + H.c. \Big],$$

$$\mathcal{H}_\lambda = \sum_{\mathbf{r},\sigma} \lambda \, n_{R,\mathbf{r},\sigma}, \tag{5.47b}$$

$$\tag{5.47c}$$

$$\mathcal{H}_U = U \sum_{\mathbf{r}} \sum_{\alpha=R,B,G} n_{\alpha,\mathbf{r},\uparrow} n_{\alpha,\mathbf{r},\downarrow}. \tag{5.47d}$$

In the following, we consider the limit $\lambda \gg t$. We study the case $U \gg t$ using perturbation theory (see App. F) and $\lambda \gg U$ using a mean field approach. We compare the results with the results obtained by our collaborators in Frankfurt who used real-space dynamical mean-field theory [246] to study the phase diagram for $-6 < \lambda/t < 10$ and $0 < U/t < 10$.

5.3.1 Perturbation theory at $\lambda \gg t$ and $U \gg t$

Let us first study the effective Hamiltonian in the limit $\lambda \gg t$ and $U \gg t$ and determine the associated classical ground state.

Effective Hamiltonian at second order

We use perturbation theory (see App. F) in the limit $\lambda \gg t$ and $U \gg t$ and considering $n = 2/3$ filling. The ground states of $\mathcal{H}_U + \mathcal{H}_\lambda$ are the states, that we denote $|\psi\rangle$, with no particles on the R-sublattice sites and one particle at each B and G sublattice sites. These states are linear combinations of the $\sim 2^{2N}$ states $|0, \sigma_{1,B}, \sigma_{1,G}, \ldots, 0, \sigma_{N,B}, \sigma_{N,G}\rangle$, with $\sigma_{i,\alpha} = \{\uparrow, \downarrow\}$, for $i \in [1, \ldots, N]$ and $\alpha = B, G$. The first order terms of the expansion in t/U and t/λ, $\langle\psi'| \mathcal{H}_t |\psi\rangle$ vanish. Here $|\psi\rangle$ and $|\psi'\rangle$ belong to the ground state subspace, that we denote S_0. Indeed, $\mathcal{H}_t |\psi\rangle$ is composed of states which are linear combination of states with 2 particles on a color B or G site or 1 particle on a color R site. Theses states are orthogonal to $|\psi'\rangle$. The second order terms give the effective Hamiltonian (at order 2), that we denote $\mathcal{H}_{\text{eff}}$

$$\langle\psi'| \mathcal{H}_{\text{eff}} |\psi\rangle = \sum_{|m\rangle \notin S_0} \frac{\langle\psi'| \mathcal{H}_t |m\rangle \langle m| \mathcal{H}_t |\psi\rangle}{-E_m}, \tag{5.48}$$

with $|m\rangle$ the eigenstates of $\mathcal{H}_U + \mathcal{H}_\lambda$ which do not belong to the ground state subspace S_0 and E_m is the corresponding eigenenergy. Here we note that the ground state energy is $E_0 = 0$. The numerator in the above equation is composed of terms like $\langle\psi'| c^\dagger_{i\sigma} c_{j\sigma} |m\rangle \langle m| c^\dagger_{k\sigma'} c_{l\sigma'} |\psi\rangle$ with $\langle i, j\rangle$, and $\langle k, l\rangle$ two pairs of nearest neighbors in the lattice. These are non vanishing only if $|m\rangle = c^\dagger_{k\sigma'} c_{l\sigma'} |\psi\rangle$ and $|m\rangle = c^\dagger_{j\sigma} c_{i\sigma} |\psi'\rangle$ which means $k = j$ and $l = i$, because $|\psi\rangle$ and $|\psi'\rangle$ are linear combinations of states which all are associated to no particle on the R sublattice sites and exactly one particle to each B and G sublattice site. The energy E_m associated with the intermediate states $|m\rangle$ is λ if j is the position of a R sublattice site and U if j is the position of a B or G sublattice site. We notice that if i is associated to a R sublattice site, then the term $\langle\psi'| c^\dagger_{i\sigma} c_{j\sigma} |m\rangle \langle m| c^\dagger_{k\sigma'} c_{l\sigma'} |\psi\rangle$ is vanishing.

Now we use the fermionic anti-commutation relations and the fact that $\langle \hat{n}_{i\uparrow} + \hat{n}_{i\downarrow} \rangle = 1$ for $i \in B, G$ and $\langle \hat{n}_{j\uparrow} \rangle = \langle \hat{n}_{j\downarrow} \rangle = 0$, for $j \in R$. Here $\langle \mathcal{O} \rangle$ is the eigenvalue of the operator $\mathcal{O}$ when acting on the ground state. In $\mathcal{H}_{\text{eff}}$, the terms proportional to t^2/λ are constant energy

terms; up to these terms, $\mathcal{H}_{\text{eff}}$ reads

$$\begin{aligned}\mathcal{H}_{\text{eff}} =& \frac{4t^2}{U}\sum_{\mathbf{r}}\Big[S^z_{B,\mathbf{r}}S^z_{G,\mathbf{r}} + S^z_{B,\mathbf{r}+\mathbf{e}_3}S^z_{G,\mathbf{r}} \\ &+ \cos 2\phi\Big(S^x_{B,\mathbf{r}}S^x_{G,\mathbf{r}} + S^y_{B,\mathbf{r}}S^y_{G,\mathbf{r}} + S^x_{B,\mathbf{r}+\mathbf{e}_3}S^x_{G,\mathbf{r}} + S^y_{B,\mathbf{r}+\mathbf{e}_3}S^y_{G,\mathbf{r}}\Big) \\ &+ \sin 2\phi\Big(S^x_{B,\mathbf{r}}S^y_{G,\mathbf{r}} - S^y_{B,\mathbf{r}}S^x_{G,\mathbf{r}} + S^x_{B,\mathbf{r}+\mathbf{e}_3}S^y_{G,\mathbf{r}} - S^y_{B,\mathbf{r}+\mathbf{e}_3}S^x_{G,\mathbf{r}}\Big)\Big],\end{aligned} \tag{5.49}$$

where $S^r_{\alpha,\mathbf{r}} = \frac{1}{2}c^\dagger_{\alpha,\mathbf{r},\beta}\sigma^r_{\beta,\gamma}c_{\alpha,\mathbf{r},\gamma}$ and $\sigma^r_{\beta,\gamma}$, $r = \{x, y, z\}$ are the Pauli matrices.

Correlations at $\phi = 0$ and $\phi = \pi/2$

First, when $\phi = 0$, the effective Hamiltonian is the one of decoupled antiferromagnetic 1D Heisenberg spin chains. This has been studied a lot, *e.g.* using the bosonization technique, and it is known to be characterized by an algebraic decay of the spin correlation function [315, 316].

When $\phi = \pi/2$, the transformation (that preserves the commutation relations)

$$S^x_{B,\mathbf{r}} \to -S^x_{B,\mathbf{r}},\ S^y_{B,\mathbf{r}} \to -S^y_{B,\mathbf{r}},\ \text{and } S^z_{B,\mathbf{r}} \to S^z_{B,\mathbf{r}}, \tag{5.50}$$

on the spin operators at the B-sublattice site in each G-B chain gives back the effective Hamiltonian at $\phi = 0$. We deduce that the z antiferromagnetic and xy ferrromagnetic effective Hamiltonian at $\phi = \pi/2$ is also characterized by an algebraic decay of the spin correlation function.

Ground state at $\phi \neq \{0, \pi/2\}$

At $\phi \neq \{0, \pi/2\}$ the effective Hamiltonian possesses XXZ anisotropy and also contains a so-called Dzyaloshinskii-Moriya interaction term, $S^x_i S^y_j - S^y_i S^x_j$, where i and j are the B and G nearest neighbors. Here we want to compute the ground state in the classical limit of large spin S. We write the value of the spin operators in the classical ground state $\langle S^x_{\alpha,\mathbf{r}}\rangle = \rho_{\alpha,\mathbf{r}}\sin\theta_{\alpha,\mathbf{r}}\cos\varphi_{\alpha,\mathbf{r}}$, $\langle S^y_{\alpha,\mathbf{r}}\rangle = \rho_{\alpha,\mathbf{r}}\sin\theta_{\alpha,\mathbf{r}}\sin\varphi_{\alpha,\mathbf{r}}$, and $\langle S^z_{\alpha,\mathbf{r}}\rangle = \rho_{\alpha,\mathbf{r}}\cos\theta_{\alpha,\mathbf{r}}$, with

$\theta_{\alpha,\mathbf{r}} \in [0,\pi]$, and $\varphi_{\alpha,\mathbf{r}} \in [0,2\pi]$ and $\rho_{\alpha,\mathbf{r}}$ is the norm of the spins in the classical ground state. In this limit, we obtain

$$\begin{aligned}\mathcal{H}_{\text{eff}} =& \frac{4t^2}{U}\sum_{\mathbf{r}} \rho_{B,\mathbf{r}}\rho_{G,\mathbf{r}}[\cos\theta_{B,\mathbf{r}}\cos\theta_{G,\mathbf{r}} + \sin\theta_{B,\mathbf{r}}\sin\theta_{G,\mathbf{r}}\cos\left[2\phi-(\varphi_{G,\mathbf{r}}-\varphi_{B,\mathbf{r}})\right]] \\ &+ \rho_{B,\mathbf{r}+\mathbf{e}_3}\rho_{G,\mathbf{r}}[\cos\theta_{B,\mathbf{r}+\mathbf{e}_3}\cos\theta_{G,\mathbf{r}} + \sin\theta_{B,\mathbf{r}+\mathbf{e}_3}\sin\theta_{G,\mathbf{r}}\cos\left[2\phi-(\varphi_{G,\mathbf{r}}-\varphi_{B,\mathbf{r}+\mathbf{e}_3})\right]],\end{aligned}$$

This is similar to the effective Hamiltonian for the Hofstadter-Hubbard model on a square lattice [317].

The classical ground state minimizing the energy associated to $\mathcal{H}_{\text{eff}}$ is associated to $\rho_{B,\mathbf{r}} = \rho_{B,\mathbf{r}+\mathbf{e}_3} = \rho_{G,\mathbf{r}}$, $\theta_{B,\mathbf{r}} = \theta_{B,\mathbf{r}+\mathbf{e}_3} = \pi - \theta_{G,\mathbf{r}}$ and $\varphi_{G,\mathbf{r}} - \varphi_{B,\mathbf{r}} = \varphi_{G,\mathbf{r}} - \varphi_{B,\mathbf{r}+\mathbf{e}_3} = 2\phi - \pi$. This is in agreement with the results mentioned above. Indeed, in the limit $\phi = 0$ and $\phi = \pi/2$, this is the classical ground state of respectively the antiferromagnetic Heisenberg spin chain and the z antiferromagnetic and xy ferromagnetic spin chain.

5.3.2 Mean field method

In this section we use a mean field approach (see for instance Ref. [44]) to obtain an approximation of the Hamiltonian which is quadratic in the creation and annihilation operators. This method is applied in the next section for the computation of the ground state of the system.

First we rewrite the Hubbard interaction term

$$\mathcal{H}_U = \frac{U}{2}\sum_{\mathbf{r}}\sum_{\alpha=R,B,G}\left(\mathbf{S}_{\alpha,\mathbf{r}}\cdot\mathbf{S}_{\alpha,\mathbf{r}} + S^0_{\alpha,\mathbf{r}}\right), \tag{5.51}$$

with $\mathbf{S}_{\alpha,\mathbf{r}}\cdot\mathbf{S}_{\alpha,\mathbf{r}} = \left(S^0_{\alpha,\mathbf{r}}\right)^2 - \left(S^x_{\alpha,\mathbf{r}}\right)^2 - \left(S^y_{\alpha,\mathbf{r}}\right)^2 - \left(S^z_{\alpha,\mathbf{r}}\right)^2$, $S^\upsilon_{\alpha,\mathbf{r}} = \frac{1}{2}c^\dagger_{\alpha,\mathbf{r},\beta}\sigma^\upsilon_{\beta,\gamma}c_{\alpha,\mathbf{r},\gamma}$ and $\sigma^0_{\beta,\gamma}$ is the identity and $\sigma^\upsilon_{\beta,\gamma}$, $\upsilon = \{x,y,z\}$ are the Pauli matrices. Using a mean field approximation, *i.e.* neglecting the terms of order $[\mathbf{S}_{\alpha,\mathbf{r}} - \langle\mathbf{S}_{\alpha,\mathbf{r}}\rangle]^2$, we find

$$\mathcal{H}_U \approx \frac{U}{2}\sum_{\mathbf{r},\alpha}\left[2\mathbf{S}_{\alpha,\mathbf{r}}\cdot\langle\mathbf{S}_{\alpha,\mathbf{r}}\rangle - \langle\mathbf{S}_{\alpha,\mathbf{r}}\rangle\cdot\langle\mathbf{S}_{\alpha,\mathbf{r}}\rangle + S^0_{\alpha,\mathbf{r}}\right]. \tag{5.52}$$

We define $\langle \mathbf{S}_{\alpha,\mathbf{r}} \rangle = -\boldsymbol{\phi}_{\alpha,\mathbf{r}}$. We have

$$\mathcal{H}_U \approx -U \sum_{\mathbf{r},\alpha} \left(\mathbf{S}_{\alpha,\mathbf{r}} \cdot \boldsymbol{\phi}_{\alpha,\mathbf{r}} + \frac{1}{2} \boldsymbol{\phi}_{\alpha,\mathbf{r}} \cdot \boldsymbol{\phi}_{\alpha,\mathbf{r}} \right) + \frac{U}{2} \sum_{\mathbf{r},\alpha} S^0_{\alpha,\mathbf{r}}. \tag{5.53}$$

We assume that the field $\boldsymbol{\phi}_{\alpha,\mathbf{r}}$ has the translation symmetry of the lattice, *i.e.* $\boldsymbol{\phi}_{\alpha,\mathbf{r}} = \boldsymbol{\phi}_{\alpha,\mathbf{r}+\mathbf{e}_\kappa}$, with $\kappa = 1, 2$, so we write $\boldsymbol{\phi}_{\alpha,\mathbf{r}} = \boldsymbol{\phi}_\alpha$. Using Fourier transformation, we get

$$\mathcal{H}_U \approx -U \sum_{\mathbf{k},\alpha} \left(\boldsymbol{\phi}_\alpha \cdot \mathbf{S}_{\alpha,\mathbf{k}} - \frac{S^0_{\alpha,\mathbf{k}}}{2} \right) - \frac{UN}{2} \sum_\alpha \boldsymbol{\phi}_\alpha \cdot \boldsymbol{\phi}_\alpha, \tag{5.54}$$

with $\mathbf{k}$ the momentum space variable and $N = N_1 N_2$ the total number of unit cells. We write

$$\mathcal{H}_U \approx \sum_{\mathbf{k}} \psi^\dagger_{\mathbf{k}} \mathcal{H}_{\text{int}} \psi_{\mathbf{k}} - \frac{UN}{2} \sum_\alpha \boldsymbol{\phi}_\alpha \cdot \boldsymbol{\phi}_\alpha, \tag{5.55}$$

with

$$\mathcal{H}_{\text{int}} = \frac{U}{4} \mathbb{I} + \begin{pmatrix} H^{\uparrow,\uparrow}_{\text{int}} & H^{\downarrow,\uparrow}_{\text{int}} \\ H^{\uparrow,\downarrow}_{\text{int}} & H^{\downarrow,\downarrow}_{\text{int}} \end{pmatrix}, \tag{5.56a}$$

$$H^{\sigma,\sigma}_{\text{int}} = -\frac{U}{2} \begin{pmatrix} \phi_{R,\sigma} & 0 & 0 \\ 0 & \phi_{B,\sigma} & 0 \\ 0 & 0 & \phi_{G,\sigma} \end{pmatrix}, \tag{5.56b}$$

$$H^{\downarrow,\uparrow}_{\text{int}} = \left[H^{\uparrow,\downarrow}_{\text{int}} \right]^\dagger = \frac{U}{2} \begin{pmatrix} \phi_{R,-} & 0 & 0 \\ 0 & \phi_{B,-} & 0 \\ 0 & 0 & \phi^-_G \end{pmatrix}. \tag{5.56c}$$

Here

$$\phi_{\alpha,\sigma} = \phi^0_\alpha - s_z \phi^z_\alpha, \tag{5.57a}$$

$$\phi_{\alpha,\pm} = \phi^x_\alpha \pm i \phi^y_\alpha, \tag{5.57b}$$

with $s_z = 1$ (-1) for $\sigma = \uparrow$ $(\downarrow)$ and

$$\psi^\dagger_{\boldsymbol{k}} = \left(c^\dagger_{R,\boldsymbol{k},\uparrow}, c^\dagger_{B,\boldsymbol{k},\uparrow}, c^\dagger_{G,\boldsymbol{k},\uparrow}, c^\dagger_{R,\boldsymbol{k},\downarrow}, c^\dagger_{B,\boldsymbol{k},\downarrow}, c^\dagger_{G,\boldsymbol{k},\downarrow} \right). \tag{5.58}$$

We also remind that $\mathcal{H}_t + \mathcal{H}_\lambda$ reads

$$\mathcal{H}_t + \mathcal{H}_\lambda = \sum_{\mathbf{k}} \psi^\dagger_{\mathbf{k}} \begin{pmatrix} \mathcal{H}_\uparrow(\mathbf{k}) & 0 \\ 0 & \mathcal{H}_\downarrow(\mathbf{k}) \end{pmatrix} \psi_{\mathbf{k}}, \tag{5.59a}$$

$$\mathcal{H}_\sigma(\mathbf{k}) = \begin{pmatrix} \lambda & \varepsilon_1(\mathbf{k}) & \varepsilon_2(\mathbf{k}) \\ \varepsilon_1(\mathbf{k}) & 0 & e^{is_z\phi}\varepsilon_3(\mathbf{k}) \\ \varepsilon_2(\mathbf{k}) & e^{-is_z\phi}\varepsilon_3(\mathbf{k}) & 0 \end{pmatrix}, \tag{5.59b}$$

with $\varepsilon_\gamma(\mathbf{k}) = -2t\cos(\mathbf{k}\cdot\mathbf{b}_\gamma)$, where $\gamma = 1, 2, 3$. Gathering $\mathcal{H}_U$ and $\mathcal{H}_t + \mathcal{H}_\lambda$, we obtain

$$\mathcal{H} \approx \sum_{\mathbf{k}} \psi^\dagger_{\mathbf{k}} h(\mathbf{k}) \psi_{\mathbf{k}} - \frac{UN}{2} \sum_{\alpha=R,B,G} \boldsymbol{\phi}_\alpha \cdot \boldsymbol{\phi}_\alpha, \tag{5.60}$$

with

$$h(\mathbf{k}) = \frac{U}{4}\mathbb{I} + \begin{pmatrix} h^{\uparrow,\uparrow} & h^{\downarrow,\uparrow} \\ h^{\uparrow,\downarrow} & h^{\downarrow,\downarrow} \end{pmatrix}, \tag{5.61a}$$

$$h^{\sigma,\sigma} = \begin{pmatrix} \lambda + \dfrac{U}{2}\phi_{R,\sigma} & \varepsilon_1(\mathbf{k}) & \varepsilon_2(\mathbf{k}) \\ \varepsilon_1(\mathbf{k}) & \dfrac{U}{2}\phi_{B,\sigma} & e^{i\phi}\varepsilon_3(\mathbf{k}) \\ \varepsilon_2(\mathbf{k}) & e^{-i\phi}\varepsilon_3(\mathbf{k}) & \dfrac{U}{2}\phi_{G,\sigma} \end{pmatrix}, \tag{5.61b}$$

$$h^{\downarrow,\uparrow} = \left[h^{\uparrow,\downarrow}\right]^\dagger = \begin{pmatrix} \dfrac{U}{2}\phi_{R,-} & 0 & 0 \\ 0 & \dfrac{U}{2}\phi_{B,-} & 0 \\ 0 & 0 & \dfrac{U}{2}\phi_{G,-} \end{pmatrix}.$$

Hamiltonian in Eq. (5.60) is quadratic in the creation and annihilation operators. A determination of the eigenstates associated to this Hamiltonian and a minimization of the ground state energy is feasible from the matrix $h(\mathbf{k})$.

5.3.3 Ordered parameter at $\lambda \gg t$ and $\lambda \gg U$

We can now determine the set of parameters ϕ^υ_α ($\upsilon = x, y, z$) which minimizes the ground state energy $E_{\mathbf{k}}$ associated to the Hamiltonian $\mathcal{H}$. We are interested in the limit $\lambda \gg t$ and

$\lambda \gg U$ for which the computation is tractable. Let us write the wave function $\psi_{\mathbf{k}}$ as follows

$$\tilde{\psi}^{\dagger}_{\boldsymbol{k}} = \left(c^{\dagger}_{R,\boldsymbol{k},\uparrow}, c^{\dagger}_{R,\boldsymbol{k},\downarrow}, c^{\dagger}_{B,\boldsymbol{k},\uparrow}, c^{\dagger}_{B,\boldsymbol{k},\downarrow}, c^{\dagger}_{G,\boldsymbol{k},\uparrow}, c^{\dagger}_{G,\boldsymbol{k},\downarrow}\right), \tag{5.62}$$

and correspondingly the Hamiltonian $h(\mathbf{k})$

$$\tilde{h}(\mathbf{k}) = \frac{U}{4}\mathbb{I} + \begin{pmatrix} \tilde{h}_R(\mathbf{k}) & \tilde{h}_{\Delta}(\mathbf{k}) \\ \tilde{h}^{\dagger}_{\Delta}(\mathbf{k}) & \tilde{h}_0(\mathbf{k}) \end{pmatrix}. \tag{5.63}$$

Here

$$\tilde{h}_R(\mathbf{k}) = \begin{pmatrix} \lambda - \dfrac{U}{2}\phi_{R,\uparrow} & \dfrac{U}{2}\phi_{R,-} \\ \dfrac{U}{2}\phi_{R,+} & \lambda - \dfrac{U}{2}\phi_{R,\downarrow} \end{pmatrix}, \tag{5.64a}$$

$$\tilde{h}_{\Delta}(\mathbf{k}) = \begin{pmatrix} \varepsilon_1(\mathbf{k}) & 0 & \varepsilon_2(\mathbf{k}) & 0 \\ 0 & \varepsilon_1(\mathbf{k}) & 0 & \varepsilon_2(\mathbf{k}) \end{pmatrix}, \tag{5.64b}$$

$$\tilde{h}_0(\mathbf{k}) = \begin{pmatrix} -\dfrac{U}{2}\phi_{B,\uparrow} & \dfrac{U}{2}\phi_{B,-} & e^{i\phi}\varepsilon_3(\mathbf{k}) & 0 \\ \dfrac{U}{2}\phi_{B,-} & -\dfrac{U}{2}\phi_{B,\downarrow} & 0 & e^{-i\phi}\varepsilon_3(\mathbf{k}) \\ e^{-i\phi}\varepsilon_3(\mathbf{k}) & 0 & -\dfrac{U}{2}\phi_{G,\uparrow} & \dfrac{U}{2}\phi_{G,-} \\ 0 & e^{i\phi}\varepsilon_3(\mathbf{k}) & \dfrac{U}{2}\phi_{G,+} & -\dfrac{U}{2}\phi_{G,\downarrow} \end{pmatrix}. \tag{5.64c}$$

We want to determine the four lowest eigenvalues X associated to $\tilde{h}(\mathbf{k})$. The two other eigenvalues are of order λ and do not interest us here. We have

$$\begin{aligned} &\det\left(\tilde{h}(\mathbf{k}) - \frac{U}{4}\mathbb{I} - X\mathbb{I}\right) = \det\left(\tilde{h}_R(\mathbf{k}) - X\mathbb{I}\right) \\ &\times \det\left(\tilde{h}_0(\mathbf{k}) - X\mathbb{I} - \tilde{h}^{\dagger}_{\Delta}(\mathbf{k})\left(\tilde{h}_R(\mathbf{k}) - X\mathbb{I}\right)^{-1}\tilde{h}_{\Delta}(\mathbf{k})\right). \end{aligned} \tag{5.65}$$

Here $\det\left(\tilde{h}_R(\mathbf{k}) - X\mathbb{I}\right) \neq 0$ and we write

$$\tilde{h}_{\text{eff}}(\mathbf{k}) = \tilde{h}_0(\mathbf{k}) - \tilde{h}^{\dagger}_{\Delta}(\mathbf{k})\left(\tilde{h}_R(\mathbf{k}) - X\mathbb{I}\right)^{-1}\tilde{h}_{\Delta}(\mathbf{k}). \tag{5.66}$$

It reads (with implicit $\mathbf{k}$ dependency)

$$\tilde{h}_{\text{eff}} = \tilde{h}_0 - \sum_{\substack{\sigma,\sigma' \\ L,L'}}\sum_{i=1}^{2} \frac{|L,\sigma\rangle\langle L,\sigma|\,\tilde{h}^{\dagger}_{\Delta}\,|R_i\rangle\langle R_i|\,\tilde{h}_{\Delta}\,|L',\sigma'\rangle\langle L',\sigma'|}{E_i - X}, \tag{5.67}$$

where the sum runs over the two color B and G for L and L' and σ and σ' run over both values of the spin degree of freedom. $|R_i\rangle$ and E_i are respectively the eigenvectors and the eigenvalues of $\tilde{h}_R(\mathbf{k})$. In both following subsections, we determine the set of parameters ϕ^{υ}_{α} ($\upsilon = x, y, z$) which minimizes the ground state energy associated to $\mathcal{H}$ at zeroth and first order in $1/\lambda$ for $\tilde{h}_{\text{eff}}$.

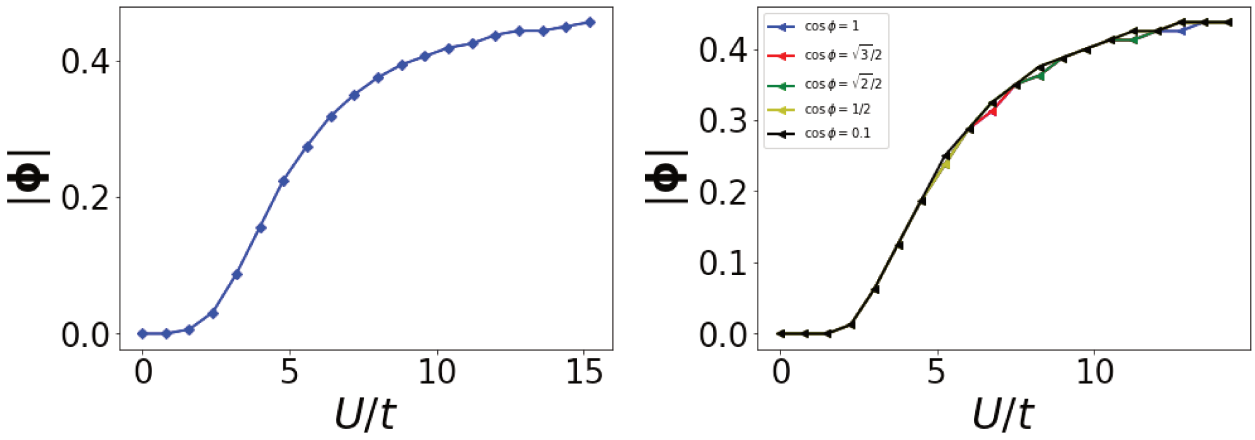

(a) (b)

Figure 5.7: (a) Order parameter $|\boldsymbol{\phi}|$ computed from the Eq. (5.77) as a function of U/t. (b) Solution $|\boldsymbol{\phi}|$ of Eq. (5.84), as a function of U/t, for different values of ϕ. Here, $\lambda = 30t$.

The lowest order in $1/\lambda$

The lowest order in $1/\lambda$ gives

$$\tilde{h}_{\text{eff}}(\mathbf{k}) = \tilde{h}_0(\mathbf{k}). \tag{5.68}$$

We assume that $\phi^0_B = \phi^0_G$ because there is no asymmetry in the system justifying that it should be different. We write $\phi^0 = \phi^0_B = \phi^0_G$. The equation $\det\left(\tilde{h}_0(\mathbf{k}) - X\mathbb{I}\right) = 0$ is equivalent to $\det\left(\tilde{h}_0(\mathbf{k}) + \frac{U}{2}\phi^0\mathbb{I} - \tilde{X}\mathbb{I}\right) = 0$ with $\tilde{X} = X + \frac{U}{2}\phi^0$. It gives $\tilde{X}^4 - h_1(\mathbf{k})\tilde{X}^2 + h_2(\mathbf{k}) = 0$ with

$$h_1(\mathbf{k}) = \left(\frac{U}{2}\right)^2 (\boldsymbol{\phi}_B \cdot \boldsymbol{\phi}_B + \boldsymbol{\phi}_G \cdot \boldsymbol{\phi}_G) + 2\varepsilon_3^2(\mathbf{k}), \tag{5.69}$$

and

$$h_2(\mathbf{k}) = \left(\frac{U}{2}\right)^4 |\boldsymbol{\phi}_B|^2|\boldsymbol{\phi}_G|^2 + \varepsilon_3^4(\mathbf{k}) - 2\varepsilon_3^2(\mathbf{k}) \left(\frac{U}{2}\right)^2 \phi_B^z \phi_G^z$$
$$- 2\varepsilon_3^2(\mathbf{k}) \left(\frac{U}{2}\right)^2 \left[\cos 2\phi \left(\phi_B^x \phi_G^x + \phi_B^y \phi_G^y\right) + \sin 2\phi \left(\phi_B^x \phi_G^y - \phi_B^y \phi_G^x\right)\right]. \tag{5.70}$$

The solution reads

$$X(\mathbf{k}) = -\frac{U}{2}\phi^0$$
$$\pm \frac{1}{\sqrt{2}} \left[2\varepsilon_3(\mathbf{k})^2 + \left(\frac{U}{2}\right)^2 \left(|\boldsymbol{\phi}_B|^2 + |\boldsymbol{\phi}_G|^2\right) \pm \frac{U}{2}\sqrt{\left(\frac{U}{2}\right)^2 \left(|\boldsymbol{\phi}_B|^2 - |\boldsymbol{\phi}_G|^2\right)^2 + 4\varepsilon_3(\mathbf{k})^2 g_{\boldsymbol{\phi}}}\right]^{1/2}, \tag{5.71}$$

with

$$g_{\boldsymbol{\phi}} = \left(\boldsymbol{\phi}_B + \boldsymbol{\phi}_G\right)^2 - 4\sin^2\phi \left(\phi_B^x \phi_G^x + \phi_B^y \phi_G^y\right) + 2\sin 2\phi \left(\phi_B^x \phi_G^y - \phi_B^y \phi_G^x\right). \tag{5.72}$$

The spectrum associated to $h(\mathbf{k})$ reads $E(\mathbf{k}) = \frac{U}{4} + X(\mathbf{k})$. To find the classical magnetic order associated to the system we minimize the total energy

$$E_{\text{tot}} = \sum_i \sum_{\mathbf{k}} E_i(\mathbf{k}) - \frac{UN}{2} \sum_{\alpha=R,B,G} \boldsymbol{\phi}_\alpha \cdot \boldsymbol{\phi}_\alpha, \tag{5.73}$$

where the sum over i runs over all the filled bands, which is fixed by the filling factor n. In our case $n = 2/3$. It means that the summation in Eq. (5.73) runs over $i = \{1, 2\}$. We look for the set of parameters $\{\phi_B^x, \phi_B^y, \phi_B^z, \phi_G^x, \phi_G^y, \phi_G^z\}$ which minimizes E_{tot}, by computing the solution of

$$\frac{\partial E_{\text{tot}}}{\partial \phi_L^\upsilon} = \sum_{\mathbf{k}} \left[\frac{\partial E_1}{\partial \phi_L^\upsilon} + \frac{\partial E_2}{\partial \phi_L^\upsilon}\right] + UN\phi_L^\upsilon = 0, \tag{5.74}$$

$L = \{B, G\}$ and $\upsilon = \{x, y, z\}$, associated to the lowest value of E_{tot}. This namely yields the following condition

$$\left(\frac{U}{2}\right)^2 \left(|\boldsymbol{\phi}_B|^2 - |\boldsymbol{\phi}_G|^2\right)^2 + 4\varepsilon_3(\mathbf{k})^2 g_{\boldsymbol{\phi}} = 0, \tag{5.75}$$

which does not depend on the value of U. Let us write the magnetic order parameters $\phi_\alpha^x = |\boldsymbol{\phi}_\alpha|\sin\theta_\alpha\cos\varphi_\alpha$, $\phi_\alpha^y = |\boldsymbol{\phi}_\alpha|\sin\theta_\alpha\sin\varphi_\alpha$, and $\phi_\alpha^z = |\boldsymbol{\phi}_\alpha|\cos\theta_\alpha$, with $|\boldsymbol{\phi}_\alpha| \in [0, 1/2]$, $\theta_\alpha \in [0, \pi]$, and $\varphi_\alpha \in [0, 2\pi]$. In these notations, we have

$$g_{\boldsymbol{\phi}} = |\boldsymbol{\phi}_B|^2 + |\boldsymbol{\phi}_G|^2 + 2|\boldsymbol{\phi}_B||\boldsymbol{\phi}_G|(\cos\theta_B\cos\theta_G + \sin\theta_B\sin\theta_G\cos[2\phi - (\varphi_G - \varphi_B)]). \quad (5.76)$$

Eq. 5.75 gives the condition $|\boldsymbol{\phi}_B| = |\boldsymbol{\phi}_G|$, $\theta_B = \pi - \theta_G$ and $\varphi_G - \varphi_B = 2\phi - \pi$, which is in agreement with the results we obtained from perturbation theory in the limit $U \gg t$. Besides, here, the minimization of E_{tot} also imposes the following condition on the value of $|\boldsymbol{\phi}| = |\boldsymbol{\phi}_B| = |\boldsymbol{\phi}_G|$ as a function of U

$$\frac{1}{U} = \frac{1}{2N}\sum_{\mathbf{k}} \frac{1}{\sqrt{4\varepsilon_3^2(\mathbf{k}) + U^2|\boldsymbol{\phi}|^2}}. \quad (5.77)$$

This condition can be satisfied for all values of U with the appropriate choice of $|\boldsymbol{\phi}|$ shown in figure 5.7a.

Our collaborators (see Ref. [246]) also performed R-DMFT computations in the case $\phi = \pi/2$ and for large enough on-site potential λ and Hubbard interaction U. Their results show the appearance of antiferromagnetic correlations in the z direction. This magnetic order is one of the solutions found from the analytical approach used in this section. It seems that the most general solution (at $\phi = \pi/2$) found from the analytical approach is antiferromagnetic correlations in the z direction and/or ferromagnetic correlations in the xy plane. Nevertheless, it seems that the behavior of the order parameter $|\boldsymbol{\phi}|$ found using both approaches is qualitatively the same, but there it shows a small quantitative difference. At the transition, the variation of the magnetization obtained from the R-DMFT method is bigger than the one obtained from the analytical mean field method.

First order in $1/\lambda$

Here we investigate the behavior of the order parameter, at order $1/\lambda$, assuming that the solution found at order 0 in $1/\lambda$ ($|\boldsymbol{\phi}_B| = |\boldsymbol{\phi}_G|$, $\theta_B = \pi - \theta_G$ and $\varphi_G - \varphi_B = 2\phi - \pi$) is still

valid. Up to the order $t^3/(\lambda \cdot \max(U,t))$ and neglecting the terms of order t^3/λ^2 and $(t^2U)/\lambda^2$ and higher order terms, we have

$$\det\left(\tilde{h}_{\text{eff}}(\mathbf{k}) + \frac{U}{2}\phi^0\mathbb{I} - X\mathbb{I}\right) = \frac{h_1/2 - X^2}{\lambda}\left(-\lambda X^2 - 2\left(\varepsilon_1^2 + \varepsilon_2^2\right)X + \lambda h_1/2 - 4\varepsilon_1\varepsilon_2\varepsilon_3\cos\phi\right). \tag{5.78}$$

The solutions to $\det\left(\tilde{h}_{\text{eff}}(\mathbf{k}) + \frac{U}{2}\phi^0\mathbb{I} - X\mathbb{I}\right) = 0$ are

$$X_1(\mathbf{k}) = -\sqrt{h_1/2} + \frac{2\varepsilon_1\varepsilon_2\varepsilon_3\cos\phi}{\lambda\sqrt{h_1/2}} - \frac{(\varepsilon_1^2+\varepsilon_2^2)}{\lambda}, \tag{5.79a}$$

$$X_2(\mathbf{k}) = -\sqrt{h_1/2}\,, \tag{5.79b}$$

$$X_3(\mathbf{k}) = \sqrt{h_1/2} - \frac{2\varepsilon_1\varepsilon_2\varepsilon_3\cos\phi}{\lambda\sqrt{h_1/2}} - \frac{(\varepsilon_1^2+\varepsilon_2^2)}{\lambda}, \tag{5.79c}$$

$$X_4(\mathbf{k}) = \sqrt{h_1/2}\,. \tag{5.79d}$$

We have

$$\varepsilon_1^2 + \varepsilon_2^2 \pm \frac{2\varepsilon_1\varepsilon_2\varepsilon_3\cos\phi}{\sqrt{h_1/2}} > 0,\ \forall U > 0\,\forall\mathbf{k}. \tag{5.80}$$

In the limit $\lambda \gg t$, this leads to

$$X_1(\mathbf{k}) < X_2(\mathbf{k}) < X_3(\mathbf{k}) < X_4(\mathbf{k}). \tag{5.81}$$

For each band, the spectrum is $E_i(\mathbf{k}) = \frac{U}{4} - \frac{U}{2}\phi^0 + X_i(\mathbf{k})$, $i = \{1,2,3,4\}$. The total energy reads

$$E_{\text{tot}} = \sum_i \sum_{\mathbf{k}} E_i(\mathbf{k}) - \frac{UN}{2}\sum_{\alpha=R,B,G}\boldsymbol{\phi}_\alpha\cdot\boldsymbol{\phi}_\alpha, \tag{5.82}$$

where the sum over i runs over all the filled bands, which is fixed by the filling factor n. In our case, as we already mentioned $n = 2/3$, which means that both lowest energy bands are filled, giving the following total energy

$$E_{\text{tot}} = -2\sqrt{h_1/2} + \frac{2\varepsilon_1\varepsilon_2\varepsilon_3\cos\phi}{\lambda\sqrt{h_1/2}} - \frac{(\varepsilon_1^2+\varepsilon_2^2)}{\lambda} - \frac{UN}{2}\sum_{\alpha=R,B,G}\boldsymbol{\phi}_\alpha\cdot\boldsymbol{\phi}_\alpha\,. \tag{5.83}$$

We look for the value of $|\boldsymbol{\phi}|$ which minimizes this energy. $\partial_{\phi^z}E_{\text{tot}} = 0$ gives

$$\frac{1}{U} = \frac{1}{2N}\sum_{\mathbf{k}}\frac{1}{\sqrt{4\varepsilon_3^2(\mathbf{k}) + U^2|\boldsymbol{\phi}|^2}}\left(1 + \frac{4\varepsilon_1\varepsilon_2\varepsilon_3\cos\phi}{\lambda\left(4\varepsilon_3^2(\mathbf{k}) + U^2|\boldsymbol{\phi}|^2\right)}\right). \tag{5.84}$$

The solution of the previous equation is given in Fig. 5.7b, from numerical evaluation at $\lambda = 30t$.

5.4 Conclusions

Motivated by the increasing experimental progress in cold atom setups [150, 156, 281, 287, 290, 293, 294, 300], we have studied the effect of flux and Rashba spin orbit coupling on the $\mathbb{Z}_2$ phase diagram of a new topological model on the kagome lattice. We have shown the appearance of $\mathbb{Z}_2$ topological phases for different types of on-site potentials, at filling $n = 2/3$.

First have investigated the $\mathbb{Z}_2$ topological phase diagram, at vanishing Rashba spin-orbit coupling. We have adapted the analytical computation developed in Chapter 3, Sec. 3.2.1 for several configurations of the on-site potentials, and arbitrary flux. From this, we have showed explicitly how the closure of the bulk gap results in a drastic change of the gauge we choose for the eigenstates. This yields a discontinuity in the value of the spin Chern numbers from one gapped phase to another gapped phase. The intrinsic spin-orbit interaction opens a topological gap and leads to a quantum spin Hall phase [11–14, 48, 144]. The topological gap can then be varied by on-site energy terms; this leads to a transition between a quantum spin Hall insulator and a trivial insulator. We have adapted another analytical method [190] to check the topological phase diagram, and, in agreement with the results obtained from the former method, we have observed that at the transition, a fundamental change in the parity eigenvalues at the high symmetry points yields a discontinuity in the $\mathbb{Z}_2$ number.

Then we have generalized the results in the case of non-vanishing Rashba spin-orbit coupling, relying on the energy gap diagram. The Rashba spin-orbit coupling term varies the topological gap; the quantum spin Hall effect is not conserved, however, as long as the Rashba term does not closes the gap, a $\mathbb{Z}_2$ topological phase is observed. This is analogue to Kane and Mele's results for a honeycomb system [144]. When the gap is closed, a metallic

phase is obtained. Several on-site energy configurations were considered; this led to different phase diagrams. For a (rather large) cylinder geometry, we have checked the appearance of a pair of counter-propagating edge modes in the $\mathbb{Z}_2$ topological phase.

In the last section, we have studied the effects of Hubbard interactions, at 2/3 filling and vanishing Rashba spin-orbit coupling for a particular configuration of the on-site potentials leading to a stripe-decoupled phase. In the case of large interaction, we have used perturbation theory to build an effective Hamiltonian. The latter shows anisotropic spin exchange coupling and depends on the flux term and its classical ground state shows antiferromagnetic or ferromagnetic correlations. For smaller amplitude of the interactions, we have used a mean field method [44] to investigate the ground state. We found, at zero temperature, in-plane magnetic correlations which depend on the flux and antiferromagnetic out-of-plane correlations. The magnetic order parameter undergoes a transition at $U/t \sim 2$, from vanishing values to finite values. The large U limit is consistent with the perturbation theory results and the transition observed is in agreement with the R-DMFT calculations performed by our collaborators [246].

As we discussed in the introduction, there has been many recent achievement in cold atom setups. The kagome lattice [281] and gauge fields [150, 156, 293, 294] have been experimentally realized. Hubbard interactions in cold atom fermionic systems have also been realized [268, 308–312]. It would be interesting to propose a protocol for the realization of a kagome lattice, with tunable on-site energy terms and gauge fields, altogether, with possibly the Hubbard interactions.

Conclusions and outlook

In this thesis we have studied topological phases on the honeycomb lattice and on the kagome lattice, in solid state systems and artificial systems.

First, in Chapter 2, we have studied a Haldane boson model. We have developed an explicit analytical computation of the Chern number in this model. To the best of our knowledge this explicit computation does not appear in the literature before our publication. From this computation we have noticed that the U(1) gauge of the wave functions has a special behavior at some points in parameter space. This led to the identification of functions which sign, at the Dirac points, determines the value of the topological invariant. Then we have considered a probe with local capacitive coupling to a Haldane cQED system. Using the knowledge gained from the computation of the Chern number and input-output formalism [318], we have shown how the local response of the system to a (microwave) light input can be used to probe the topological properties of the Haldane cQED system.

The explicit analytical computation of the topological invariant has been extended, in Chapters 3 and 5, to a tight-binding model on the kagome lattice with nearest neighbor spin-orbit coupling and different on-site energies configurations. We have explicitly shown how the closure of the bulk gap results in a drastic change of the gauge we may choose for the eigenstates and therefore in a discontinuity in the value of the spin Chern numbers.

In Chapter 4, we have study a magnetic and topological model on the kagome lattice, in relation with recently discovered quantum materials. We have considered a spin model, coupled, through a ferromagnetic Hund's coupling, to a topological non-interacting model

on this lattice. Depending on the parameters of the spin model, we have found either a ferromagnetic out-of-plane long range ordered phase or an in-plane ordered phase. Spin-wave excitations destabilize the ferromagnetic phase near the transition and always destabilize the in-plane (antiferromagnetic) phase. The in-plane phase is either a spin-liquid or a long-range ordered phase if further nearest neighbor spin-exchange is considered [220]. We have shown that each magnetic phase selects a specific topological phase of the system. Then we have argued that a variation of the external parameters, such as the temperature or the pressure, should result in a magnetic phase transition coupled to a topological phase transition. Depending on the amplitude of the Hund's coupling term, the topological phase transition is either in a QAH phase-QSH phase transition or a QAH phase-trivial phase transition.

In the last Chapter, we have studied a new time-reversal invariant kagome topological model with flux and Rashba spin-orbit coupling for a cold atom system. We have computed, with the analytical method aforementioned, the topological $\mathbb{Z}_2$ phase diagram when the amplitude of the Rashba spin-orbit coupling is vanishing and from the energy gap phase diagram we have obtained the $\mathbb{Z}_2$ topological invariant at finite Rashba spin-orbit coupling. We have also studied the effects of Hubbard interactions in this model at 2/3 filling and vanishing Rashba spin-orbit coupling for a particular configuration of the on-site potentials leading to a stripe-decoupled phase. By means of perturbation theory and mean field method [44], we have investigated the ground state. We found, at zero temperature, in-plane magnetic correlations which depend on the flux and antiferromagnetic out-of-plane correlations. The magnetic order parameter undergoes a transition at $U/t \sim 2$, from vanishing values to finite values.

We are left with a certain number of open questions concerning the work presented in this manuscript.

In Chapter 2, we have shown that the response to a local light input on a Haldane

cQED system is informative about the topological properties. The general form of the response function does not depend on the lattice system which is considered (see App. C). In Chapters 3 and 5 we have shown explicit analytical computations of the topological invariants for kagome systems. We observed that the closure of the bulk gap results in a drastic change of the gauge we may choose for the eigenstates. It seems possible to observe such a change thanks to the local response function. We have performed some numerical computations that seems to indicate that this response function is indeed informative about the topological invariant for kagome topological systems. It would be also very interesting to try to make a clear link between the Chern number and this local response function for an arbitrary lattice model.

Moreover, this protocol is not *a priori* restricted to cQED systems, it seems conceivable as long as

(i) the particles are bosons,

(ii) the topological system under study is not too small; numerical computations showed we could rebuild the topological phase diagram with a good very precision for a 50×50 unit cells system and with a rather good precision for smaller systems (it seems correct down to $\sim 30 \times 30$ unit cells), and

(iii) the coupling between the probe and the system is a capacitive coupling.

Therefore, it would be very interesting to propose specific protocols for other artificial systems, namely for cold atom gases for which the kagome lattice has already been implemented and which offer the possibility to realize artificial gauge potentials. Besides, it should be easier to realize a system having a sufficiently large size in cold atom gases compared to cQED systems. A further very interesting outlook would be to think about a generalization of this probe for a $\mathbb{Z}_2$ artificial system.

As mentioned at the end of Chapter 2, changing the statistics of the particles (considering a fermion Chern insulator) leads to a different form of the response function (particle-hole's

Green function). It seems more complicated than for boson systems to define a clear topological probe. This is an open question whether or not it is possible.

In Chapter 4, we have considered a magnetic and topological model on the kagome lattice; we have explained, qualitatively, the behavior of the system at non-zero temperature. It would be interesting to compute the entropy of the magnetic ground state and to study quantitatively the effect of the temperature on the magnetic and topological phases of the system, as it has been done for a similar spin model on the triangular lattice for instance in Ref. [241].

In Chapter 5, we have studied the effects of Hubbard interactions for a specific limit of the topological model we studied in this chapter. We computed the ground state of this model using a minimization of the free energy. It would be interesting to study the fluctuations in the charge and spin channels due to possibly non zero variation of the free energy in the ground state at second order in the variation of the Hubbard stratonovich fields [44]. Finally, in cold atom gases, the kagome lattice [281], gauge fields [150, 156, 293, 294] and Hubbard interactions [268, 308–312] have been experimentally realized. However, designing a protocol for the realization and the investigation of the model we studied is not a simple task, but it would be very interesting.

Appendix A: Résumé en français

Nous étudions théoriquement des modèles topologiques sur réseaux, pertinents pour des matériaux et des systèmes artificiels actuels. Nous développons un calcul analytique explicite du nombre de Chern pour les systèmes que l'on étudie et nous comparons ce calcul avec d'autres méthodes de calcul de cet invariant topologique. Nous proposons un protocole, à partir d'une mesure de la réponse locale à une excitation lumineuse (micro-onde), pour sonder les propriétés topologiques d'un modèle bosonique de Haldane, dans un système photonique. Sur le réseau de kagomé, nous étudions (i) une transition de phase magnétique et topologique pour un modèle à deux canaux en lien avec un matériau quantique récemment découvert, et (ii) un modèle topologique invariant par renversement du temps et contenant un terme de flux, un terme de couplage spin-orbite de type Rashba et un terme d'interactions de Hubbard, dont la réalisation est pertinente dans des gaz d'atomes froids.

A.1 Chapitre 1

Dans le chapitre 1, nous introduisons le formalisme, les concepts et les découvertes importantes en topologie de la matière condensée que l'on utilise dans ce manuscrit. Nous insistons en particulier sur deux systèmes à deux dimensions qui sont les principaux sujets d'étude de cette thèse : les isolants de Chern et les isolants topologiques.

Tout d'abord, dans la section 1.1, nous considérons une évolution adiabatique d'un système quantique et nous étudions la phase géométrique, appelée la phase de Berry [9], accumulée par les vecteurs propres du Hamiltonien lors d'une telle évolution. Cette étude est très importante pour la compréhension des systèmes topologiques en matière condensée. L'effet Hall quantique [6] est le point de départ de l'intense activité scientifique dans ce domaine de la topologie en matière condensée. L'invariant topologique qui caractérise l'effet Hall quantique entier peut être formulé comme une intégrale de la phase de Berry sur la zone de Brillouin [8]. Dans les sections 1.1.3 et 1.1.4, nous présentons la découverte expérimentale de l'effet Hall quantique entier et sa première interprétation théorique [6, 7, 45].

Ensuite, dans la section 1.2 nous introduisons le formalisme que l'on utilise pour décrire les systèmes invariants par translation, nous rappelons le théorème de Bloch [46] et la définition des fonctions de Wannier [47] que l'on utilise par la suite. Comme exemples de systèmes invariants par translation, nous présentons deux modèles dits "tight binding" sur les réseaux que nous considérons dans ce manuscrit, à savoir le réseau en nid d'abeille et le réseau de kagomé.

Dans la section 1.3, le lien entre le concept de phase de Berry et l'effet Hall quantique entier est expliqué grâce au calcul de la conductivité de Hall en utilisant la formule de Kubo [8]. Ceci permet d'introduire l'invariant topologique (le nombre de Chern) qui caractérise les systèmes Hall quantiques. Nous expliquons également que les modes de bords chiraux mentionnés dans la section 1.1.4 sont fondamentalement reliés à une valeur non-nulle du nombre de Chern. Finalement, dans la section 1.3, nous montrons le lien entre une valeur non-nulle du nombre

de Chern et la polarisation de charge, cette-dernière étant une observable caractérisant les isolants de Chern. Les concepts introduits dans cette section sont largement utilisés dans le reste du manuscrit.

Dans la section 1.4, nous présentons la théorie des bandes topologiques utilisée pour décrire les systèmes topologiques invariants par renversement du temps. En particulier, nous nous concentrons sur le modèle de Kane et Mele [11] et sur une formulation de l'invariant $\mathbb{Z}_2$ proposé par Fu et Kane [48]. Les concepts introduits dans cette section sont pertinents pour l'étude de systèmes avec couplage spin-orbite présentés dans les chapitres 4 et 5.

A.2 Chapitre 2

Dans le Chapitre 2, nous considérons un système de type circuit d'électrodynamique quantique (cQED) qui est décrit par un modèle de Haldane bosonique. Nous développons un calcul analytique explicite du nombre de Chern (section 2.2) pour ce modèle [5]. Nous montrons que le signe d'une fonction que l'on appelle h_2, aux points de Dirac, indique la valeur du nombre de Chern associé à chacune des bandes d'énergie. h_2 dépend de la masse de Semenoff M et de l'amplitude t_2 associée aux termes de saut seconds voisins dans le modèle de Haldane. Dans les systèmes unidimensionnels de type cQED, il a été montré que les propriétés topologiques sont mesurables via la réflexion de lumière micro-onde sur le système [30].

En utilisant la connaissance acquise par le calcul du nombre de Chern, nous proposons un protocole pour sonder les propriétés topologiques via la réponse à un signal lumineux local (section 2.3). Plus précisément, nous considérons une sonde locale avec un couplage capacitif au système (ce-dernier étant décrit par un Hamiltonien effectif de type modèle de Haldane bosonique), dans le régime de faibles amplitudes de couplage. Nous calculons explicitement le coefficient de réflexion qui fait le lien entre un signal entrant et un signal sortant dans la sonde, en fonction des paramètres du système. Nous montrons que le signe de la fonction h_2, à l'un des deux points de Dirac, mentionnée dans le paragraphe précédent, peut être rebâti par la mesure de ce coefficient de réflexion. Or, la transition de phase topologique associée au modèle de Haldane est déterminée par le signe de la fonction h_2 à l'un des deux points de Dirac (plus précisément, au niveau du point de Dirac pour lequel le gap d'énergie entre les deux bandes d'énergie est le plus faible). Par conséquent, la mesure du coefficient de réflexion (pour un signal entrant d'énergie égale à l'énergie de l'état propre du système évalué à l'un des deux points de Dirac) est suffisante pour rebâtir le diagramme de phase topologique. Dans les systèmes de type cQED faits de résonateurs de fréquence typique de l'ordre du GHz, le signal d'entrée dans la sonde est un signal micro-onde. Ce protocole est potentiellement applicable dans d'autres systèmes bosoniques pour lesquels un couplage capacitif à une sonde est réalisable.

A.3 Chapitre 3

Dans le chapitre 3, nous considérons deux modèles topologiques simples sur le réseau de kagomé, l'un mène à un isolant de Chern (associé à l'effet Hall anormal quantique), l'autre mène à un isolant topologique (associé à l'effet Hall quantique de spin). Ces modèles topologiques ont attiré beaucoup d'attention dans la communauté scientifique [31–42]. Tout d'abord (section 3.1), nous expliquons qu'un modèle simple sur le réseau de kagomé, avec des amplitudes de saut complexes entre proches voisins, brise la symétrie de renversement par rapport au temps et est associé à un flux total nul dans la cellule unitaire. Nous présentons le

spectre d'énergie d'un tel modèle et nous passons rapidement en revue un calcul analytique des modes de bord [34].

Le calcul du nombre de Chern (de spin) a été effectué via diverses méthodes, cependant, effectuer un calcul analytique explicite de cet invariant topologique (à partir de l'étude de la jauge choisie pour les fonctions d'onde du système) n'est pas aisé et n'apparait pas dans la littérature avant notre publication [188]. Motivés par ceci, nous développons un tel calcul dans la section 3.2.1. Nous définissons deux choix de jauge distincts pour les états propres du système et nous définissons deux surfaces complémentaires dans la zone de Brillouin. Nous appliquons un de ces deux choix de jauge pour une des deux surfaces définies dans la zone de Brillouin (cette surface contient un des points de haute symétrie de la zone de Brillouin) et l'autre choix de jauge pour l'autre surface (elle contient les autres points de haute symétrie de la zone de Brillouin). Nous montrons comment la différence de phase entre ces deux choix de jauge évolue à la frontière entre les deux surfaces et mène à un nombre de Chern entier et non nul pour la bande énergétique la plus basse, dans le cas où l'amplitude de saut entre proches voisins est complexe. Ce calcul se généralise aux autres bandes d'énergie du système.

Dans la section 3.2.2, nous étudions la robustesse des propriétés topologiques pour de petits systèmes avec bruit (Gaussien) sur les paramètres du modèle, via des estimations numériques d'observables locales. En particulier, nous évaluons la densité locale d'états et les courants chiraux dans le système et nous montrons que ces deux observables présentent des propriétés topologiques, même pour des valeurs assez élevées du bruit sur les paramètres. Nous comparons ceci avec une autre sonde des propriétés topologiques : sous un champ magnétique dont la direction est perpendiculaire au plan du réseau, chaque bande d'énergie "parent" est divisée en un certain nombre de sous-bandes qui dépend du nombre de Chern associée à la bande d'énergie "parent" [34, 194]. Grâce à une évaluation numérique de la densité d'états, nous retrouvons la valeur du nombre de Chern pour des systèmes dont la taille est supérieure à environ 30×30 cellules unitaires et avec un bruit Gaussien dont l'amplitude est inférieure à un pour cent.

Enfin, dans la section 3.3, nous considérons deux copies de spin du système précédemment mentionné (alors le système devient invariant par renversement du temps) et nous calculons l'invariant topologique $\mathbb{Z}_2$. Ce-dernier peut être obtenu à partir des nombres de Chern de spin car le Hamiltonien ne comprend pas de couplage entre spins [48, 189]. L'invariant topologique $\mathbb{Z}_2$ peut aussi être calculé en utilisant la symétrie d'inversion du système [190]; il est donné par le produit des valeurs propres de l'opérateur parité évalué aux quatre points de haute symétrie dans la zone de Brillouin. Nous adaptons un tel calcul pour le système que l'on considère, dans la section 3.3.2. Ces calculs sont étendus, dans le Chapitre 5, à un système plus complexe.

A.4 Chapitre 4

Dans le Chapitre 4, nous introduisons et étudions un modèle magnétique et topologique sur le réseau de kagomé [193], en lien avec de nouveaux matériaux quantiques [25–28, 38, 43]. Un modèle effectif de spin (associé à un canal de spins localisés) est couplé à un modèle topologique sans interactions sur ce réseau (associé à un canal d'électrons dits itinérants), via un terme de Hund ferromagnétique [216, 221, 222].

Le modèle magnétique est un modèle anisotropique de type Heisenberg avec un terme d'échange ferromagnétique dans la direction perpendiculaire au plan formé par le réseau de kagomé. L'origine microscopique de ce modèle vient d'une forte interaction répulsive sur-site de type Hubbard qui donne naissance à une physique de Mott et un mécanisme de double échange [221, 223–226] avec le canal d'électrons itinérants. Dans la section 4.2, nous étudions l'état fondamental du modèle de spin et les excitations associées de type

ondes de spin. En fonction des paramètres du modèle de spin, nous observons deux phases magnétiques distinctes: une phase ferromagnétique dans la direction perpendiculaire au plan formé par le réseau de kagomé ou une phase magnétique dans le plan. Cette dernière est soit une phase liquide de spin soit une phase antiferromagnétique avec ordre à longue portée si d'autres termes de couplage entre spins (au-delà des plus proches voisins) sont inclus dans le modèle [220].

La transition de phase magnétique est couplée à une transition de phase topologique (section 4.3). Les électrons itinérants sont décrits par un modèle sur le réseau de kagomé avec un terme de saut proches voisins et un terme de couplage de type spin-orbite [11, 36, 227, 228]. Dans la phase ferromagnétique, le couplage de Hund ferromagnétique agit comme un champ magnétique dans la direction perpendiculaire au réseau. Pour certaines valeurs du potentiel chimique (modulant le niveau de Fermi), le canal d'électrons itinérants est associé à une phase Hall anormale quantique. Quand le système est caractérisé par la phase magnétique dans le plan, le modèle associé aux électrons itinérants respecte la symétrie par renversement du temps. En fonction de la valeur de l'énergie de Fermi, ce-dernier est soit associé à une phase Hall quantique de spin ou à une phase métallique.

Nous discutons l'effet de paramètres extérieurs, tels que la température ou la pression, sur les propriétés magnétiques et topologiques du modèle. D'une part, à température finie, nous justifions que la phase ferromagnétique devrait être déstabilisée proche de la transition à cause de l'entropie finie associée aux excitations de type ondes de spin. Par conséquent, une augmentation de la température résulte en une transition magnétique et donc aussi (en vertu du paragraphe précédent) en une transition topologique. D'autre part, une augmentation de la pression génère une diminution du pas du réseau [229]. Dans notre modèle, nous justifions que ceci résulte en une augmentation des intégrales d'échange (c'est-à-dire des amplitudes associées aux termes de saut proches voisins). Ceci mène, par conséquent, à une variation du terme d'échange de spin dans le plan (pour le Hamiltonien effectif de spin) et induit donc une transition magnétique et topologique.

A.5 Chapitre 5

Dans le Chapitre 5, nous étudions un nouveau modèle topologique, invariant par renversement du temps, avec un terme de flux, un terme de couplage spin-orbite de type Rashba, différentes configurations de potentiels sur-site, et un terme d'interactions répulsives (modèle de Hubbard), sur le réseau de kagomé [188, 246]. Ce modèle est potentiellement réalisable pour des gaz d'atomes froids, qui sont des plateformes intéressantes pour l'implémentation de champs de jauge artificiels et pour l'étude des interactions de type Hubbard.

Dans un premier temps (section 5.1), nous calculons le diagramme de phase topologique (invariant topologique $\mathbb{Z}_2$) à remplissage 2/3, quand le terme de couplage spin-orbite Rashba et le terme d'interactions de Hubbard sont nuls, pour différentes configurations de potentiels sur-site, ce qui élargit la méthode analytique développée dans le Chapitre 3. Nous montrons de façon explicite comment la fermeture du gap d'énergie résulte en un changement très important du choix de jauge pour les vecteurs propres du Hamiltonien. Ceci mène à une discontinuité dans la valeur des nombres de Chern de spin quand les paramètres du Hamiltonien évoluent de telle façon que l'on passe d'une phase isolante à une autre (les deux étant séparées la fermeture du gap d'énergie). Le terme de flux est très important pour l'ouverture d'un gap d'énergie avec une phase Hall quantique de spin [11–14, 48, 144]; les termes de potentiels sur-site permettent de varier le gap d'énergie et d'observer des transitions entre des phases Hall quantiques de spin et des phases isolantes triviales. L'invariant topologique $\mathbb{Z}_2$ est aussi calculé en utilisant la symétrie d'inversion du système [190]. Nous prolongeons la méthode utilisée dans le chapitre 3 et nous obtenons des résultats cohérents

avec la méthode précédemment mentionnée. A la transition entre une phase Hall quantique de spin et une phase isolante triviale, nous observons un changement très important dans les valeurs propres de l'opérateur parité aux points de haute symétrie dans la zone de Brillouin; ceci génère une discontinuité dans la valeur de l'invariant $\mathbb{Z}_2$.

Ensuite, nous prolongeons le calcul de cet invariant topologique quand le terme de couplage spin-orbite de type Rashba est non nul (section 5.2). Ce-dernier varie l'amplitude du gap d'énergie et rend possible des processus de renversement de spin (« spin flip processes »). L'effet Hall quantique de spin n'est donc pas conservé, cependant, tant que le terme de spin-orbite Rashba ne ferme pas le gap d'énergie, une phase isolante topologique $\mathbb{Z}_2$ est observée. Ceci est analogue au résultat de Kane et Mele [144]. Nous considérons différentes configurations de potentiels sur-site, menant à différents diagrammes de phase. Pour une géométrie cylindrique (conditions périodiques aux bords dans une direction seulement), nous vérifions l'apparition d'une paire de modes de bord contre-propageants dans la phase topologique $\mathbb{Z}_2$.

Enfin, dans la dernière section (section 5.3), nous étudions l'effet des interactions de type Hubbard (toujours à remplissage 2/3), quand le terme de couplage spin-orbite Rashba est nul, pour une configuration particulière des potentiels sur-site. Pour des interactions de Hubbard de grande amplitude U, nous utilisons une théorie des perturbations afin d'obtenir un Hamiltonien effectif de spin. Ce-dernier présente des termes d'échange de spin anisotropiques, dépend du terme de flux et son état fondamental classique présente des corrélations ferromagnétiques et/ou antiferromagnétiques. Pour des interactions de Hubbard de plus petite amplitude U, nous utilisons une théorie de champ moyen [44] et nous étudions l'état fondamental du système. A température nulle, le système présente des corrélations magnétiques dans le plan du réseau qui dépendent du terme de flux et des corrélations antiferromagnétiques dans la direction perpendiculaire au plan du réseau. Le paramètre d'ordre magnétique montre une transition à $U/t \sim 2$ (t est l'amplitude de saut entre proches voisins). Au-delà de cette valeur, la phase est magnétique et isolante de Mott. La théorie de champ moyen est compatible avec la théorie des perturbations (pour de grandes valeurs de U). La transition observée est en accord avec les calculs R-DMFT effectués par nos collaborateurs [246].

Appendix B: Time-reversal symmetry

Time-reversal symmetry is one of the most important symmetries for the topological systems we studied in this manuscript. It is expected that this symmetry plays an important role in the quantum Hall effect, which, as we explained concerns systems where this symmetry is broken. If this symmetry is conserved, it may also play a very important role, as we saw in the quantum spin Hall effect. Here we underline some important properties of time-reversal symmetry for the topological systems studied in this manuscript. More details can be found in Ref. [66].

B.1 Time-reversal operators

A time-reversal transformation reverses the arrow of time. It means that this transformation reverses the momentum quantities. Spins are momentums, therefore the time-reversal operators is expressed differently in both cases of spinless and spinful systems. For a particle with no spin, the time-reversal operator θ is identical to the complex conjugation anti-unitary operator K, $\theta = K$. We have $\theta^2 = 1$.

For a spin system, things are different. The time-reversal operator θ, still anti-unitary, reads

$$\theta = UK, \tag{B.1}$$

with $U = \mathrm{e}^{-i\pi S_y}$ a unitary operator, S_y being the spin operator along the y axis. S_y is purely imaginary, therefore $\theta^2 = \mathrm{e}^{-i2\pi S_y}$. We immediately notice the following property: a 2π rotation of an integer spin is equivalent to the identity whereas under a 2π rotation a half-integer spin is multiplied by -1. We deduce that $\theta^2 = +1$ for a system made of integer spins or for a system made of an even number of half-integer spins and $\theta^2 = -1$ for a system made of an odd number of half-integer spins. This is very important because of Kramers' theorem which we now demonstrate.

B.2 Kramers' theorem

Consider system of particles described by the Hamiltonian H, with conserved time-reversal symmetry, *i.e.* $[\theta, H] = 0$, and with associated eigenstates $|\psi\rangle$ and eigenvalues E, $H|\psi\rangle = E|\psi\rangle$. From $[\theta, H] = 0$, we have $H\theta|\psi\rangle = E\theta|\psi\rangle$: $\theta|\psi\rangle$ is also an eigenstate of H and $\theta|\psi\rangle$ and $|\psi\rangle$ are associated to the same energy. $\theta^2 = -1$ constrains $\theta|\psi\rangle$ to be orthogonal to $|\psi\rangle$. Indeed, using $-1 = \theta^2 = UU^*$ and $UU^\dagger = 1$, we find $U^* = -U^\dagger$ and then

$$\langle\theta\psi|\psi\rangle = \sum_{m,n} \left(U_{n,m}\psi_m^*\right)^* \psi_n = -\sum_{m,n} \left(U_{m,n}\right)^* \psi_m\psi_n = -\langle\theta\psi|\psi\rangle\,, \tag{B.2}$$

which leads to $\langle\theta\psi|\psi\rangle = 0$. For half-integer spin systems, *i.e.* systems composed of an odd number of half-integer spin particles, and if the system is time-reversal invariant, each energy is degenerate at least twice.

B.3 Translation-invariant systems with time-reversal symmetry

The time reversal invariance links the Bloch Hamiltonian at momentum $\mathbf{k}$ and momentum $-\mathbf{k}$. Kramers' degeneracy theorem then tells us

Let us write

$$H = \sum_{\mathbf{k}} \Psi(\mathbf{k})^\dagger h(\mathbf{k}) \Psi(\mathbf{k}), \tag{B.3}$$

with $\Psi(\mathbf{k})$ the fermion field annihilation operator at momentum $(\mathbf{k})$, which contains the annihilation operators $c_{\mathbf{k},\alpha,\sigma}$ for a particle of momentum $\mathbf{k}$, with the different color α and both values of half-integer spin $\sigma = \{\uparrow, \downarrow\}$. We write $c_{i,\alpha,\sigma}$ the annihilation operator for a particle at unit cell position i, color α and half-integer spin σ. Under time-reversal, we have [66]

$$\theta c_{i,\alpha,\sigma} \theta^{-1} = i\sigma^y_{\sigma,\sigma'} c_{i,\alpha,\sigma'}, \tag{B.4a}$$

$$\theta c^\dagger_{i,\alpha,\sigma} \theta^{-1} = -i c^\dagger_{i,\alpha,\sigma'} \sigma^y_{\sigma',\sigma}, \tag{B.4b}$$

with σ^y the second Pauli matrix acting in spin space and implicit summation on the repeated indices is assumed. It gives, for the Fourier transforms of these operators

$$\theta c_{\mathbf{k},\alpha,\sigma} \theta^{-1} = i\sigma^y_{\sigma,\sigma'} c_{-\mathbf{k},\alpha,\sigma'}, \tag{B.5a}$$

$$\theta c^\dagger_{\mathbf{k},\alpha,\sigma} \theta^{-1} = -i c^\dagger_{-\mathbf{k},\alpha,\sigma'} \sigma^y_{\sigma',\sigma}. \tag{B.5b}$$

This leads to

$$\theta h(\mathbf{k}) \theta^{-1} = h(-\mathbf{k}). \tag{B.6}$$

Then, from Kramers' theorem, we know that if $|\psi(\mathbf{k})\rangle$ is an eigenstate of the Hamiltonian, then $\theta|\psi(\mathbf{k})\rangle$ is also an eigenstate with the same energy. In translation-invariant systems, we denoted $|\psi(\mathbf{k})\rangle$ the eigenstate of $h(\mathbf{k})$ with energy $E(\mathbf{k})$, $h(\mathbf{k})|\psi(\mathbf{k})\rangle = E(\mathbf{k})|\psi(\mathbf{k})\rangle$. $\theta|\psi(\mathbf{k})\rangle$ is in fact the eigenstate of $h(-\mathbf{k})$ with energy $E(-\mathbf{k}) = E(\mathbf{k})$, indeed

$$h(-\mathbf{k})\theta|\psi(\mathbf{k})\rangle = \theta h(\mathbf{k}) \theta^{-1} \theta|\psi(\mathbf{k})\rangle = \theta h(\mathbf{k})|\psi(\mathbf{k})\rangle = E(\mathbf{k})\theta|\psi(\mathbf{k})\rangle. \tag{B.7}$$

Let us here notice that at the time-reversal invariant points of the BZ $\mathbf{k} = -\mathbf{k}$, there are at least two degenerate states of energy $E(-\mathbf{k}) = E(\mathbf{k})$.

B.4 Scattering from a state $|\psi\rangle$ to its time-reversal partner

A quantum spin Hall system is characterized by at least one chiral edge mode and one anti-chiral edge mode, the later being the time-reversal conjugate of the former. Because of the

presence of counter-propagating modes in close proximity, we could expect that scattering process play an important role in this system, which would be described by non-negligible Hamiltonian coupling elements between the chiral and the anti-chiral modes. From the Kramers' theorem and the identity $\theta h(\mathbf{k})\theta^{-1} = h(-\mathbf{k})$, we know that the energy of the chiral and the anti-chiral modes is crossing at the time-reversal symmetric points $\mathbf{k} = -\mathbf{k}$ in the BZ. The study of a two-level system teaches us that off-diagonal coupling elements in the Hamiltonian operator opens a gap in the dispersion relation. Therefore, non-negligible scattering process would mean a non-negligible gap in the edge modes dispersion relation which could be important enough so that no modes cross the Fermi level, turning the spin-Hall insulating phase (characterized by a mobility gap) to a trivial insulating phase (characterized by a "true" gap).

In fact, for the single particle case, if the number of chiral modes (which is the same as the number of anti-chiral modes) is odd, the single-particle scattering process between the chiral and the anti-chiral modes is forbidden by time-reversal symmetry. This is what we show here, starting with the simple case with only one chiral mode $|\psi\rangle$ and one anti-chiral mode $\theta|\psi\rangle$. We consider a time-reversal invariant Hamiltonian H describing the possible scattering process (*a priori* $|\psi\rangle$ and $\theta|\psi\rangle$ are not H eigenstates since H is possibly composed of non-diagonal elements coupling these states). The coupling term between $|\psi\rangle$ and $\theta|\psi\rangle$ is

$$\langle\theta\psi|H|\psi\rangle = \sum_{m,n,p} (U_{m,p}K\psi_p)^* H_{m,n}\psi_n = \sum_{m,n,p} (U_{m,p})^* \psi_p H_{m,n}\psi_n = \sum_{m,n,p} \psi_p \left(U^\dagger\right)_{p,m} H_{m,n}\psi_n, \tag{B.8}$$

Using $H = \theta H\theta^{-1}$ and $\theta^{-1} = -\theta$, and U being self-adjoint, we find

$$\langle\theta\psi|H|\psi\rangle = -\sum_{m,n,p,q,r} \psi_p \left(U^\dagger\right)_{p,m} U_{m,q}H^*_{q,r}U^*_{r,n}\psi_n = -\sum_{n,p,r} \psi_p H^*_{p,r}U^*_{r,n}\psi_n, \tag{B.9}$$

and $H^\dagger = H$ gives

$$\langle\theta\psi|H|\psi\rangle = -\sum_{n,p,r} \psi_p H_{r,p}U^*_{r,n}\psi_n = -\sum_{n,p,r} (U_{r,n}\psi^*_n)^* H_{r,p}\psi_p. \tag{B.10}$$

Then we conclude that

$$\langle\theta\psi|H|\psi\rangle = -\langle\theta\psi|H|\psi\rangle = 0, \tag{B.11}$$

i.e. the single-particle scattering between the chiral edge mode and the anti-chiral edge mode is forbidden because the time-reversal symmetry is conserved in the system.

Now we ask whether or not a gap in a system with N chiral edge modes and N anti-chiral edge modes can be opened (*i.e.* turn the mobility gap into a true gap) by single-particle backscattering terms. To open a gap in such a system, where we have at least N twice-degenerate energy points, it is required to consider at least N excitations which scatter to their time-reversal conjugates; each excitation scattering term lifting the degeneracy of a time-reversal conjugate pair. However, because we have here $2N$ states, if we want to investigate single-particle scattering terms only, it is required to consider at most N excitations which scatter. Therefore, we consider exactly N excitations. We compute the probability that N particles which occupy N edges states (these are composed of a certain number of chiral modes plus a a certain number of anti-chiral modes) are scattered back to their N time-reversal conjugates.

Let us denote $|\psi_i\rangle$, $i \in [1, \ldots, N]$ these N occupied modes and their time-reversal conjugates are $\theta|\psi_i\rangle$. We denote $\mathcal{E}_i$ the vector space associated to the particle i, H_i the Hamiltonian

operator in $\mathcal{E}_i$ and θ_i the time-reversal operator in $\mathcal{E}_i$. The Hamiltonian operator describing the possible scattering processes and the time-reversal operator for the entire system are respectively $H = \sum_{i=1}^{N} H_i$ and $\theta = \bigotimes_{i=1}^{N} \theta_i$. The probability that the N occupied states are scattered to their N time-reversal conjugates is proportional to the Hamiltonian coupling element between the Slater determinant $|\psi_1, \ldots, \psi_N\rangle$ and the Slater determinant associated to the N time-reversal conjugates $\theta\,|\psi_1, \ldots, \psi_N\rangle$. We write

$$|\psi_1, \ldots, \psi_N\rangle = \sum_{\sigma \in S_N} \mathrm{sgn}(\sigma) \bigotimes_{i=1}^{N} |\psi_{\sigma_i}(i)\rangle\,, \tag{B.12}$$

with σ a permutation in S_N which is the set containing all permutations of $\{1, \ldots, N\}$ and $|\psi_{\sigma_i}(i)\rangle$ referring to the particle i in the state $|\psi_{\sigma_i}\rangle$. Let us define σ and $\sigma^{'}$ two permutations in S_N. First we extend both relations Eq. (B.2) and Eq. (B.10), using the assumptions $\theta^2 = -1$ and $H_i = \theta_i H_i \theta_i^{-1}$,

$$\langle \theta_i \psi_{\sigma_i}(i) | \psi_{\sigma_i'}(i)\rangle = -\langle \theta_i \psi_{\sigma_i'}(i) | \psi_{\sigma_i}(i)\rangle\,, \tag{B.13a}$$

$$\langle \theta_i \psi_{\sigma_i}(i)|\, H\, |\psi_{\sigma_i'}(i)\rangle = -\langle \theta_i \psi_{\sigma_i'}(i)|\, H\, |\psi_{\sigma_i}(i)\rangle\,, \tag{B.13b}$$

From these relations, we find

$$\left(\theta \bigotimes_{i=1}^{N} \langle \psi_{\sigma_i}(i)|\right) H \bigotimes_{i=1}^{N} |\psi_{\sigma_i'}(i)\rangle = (-1)^N \left(\theta \bigotimes_{i=1}^{N} \langle \psi_{\sigma_i'}(i)|\right) H \bigotimes_{i=1}^{N} |\psi_{\sigma_i}(i)\rangle\,, \tag{B.14}$$

and using Eq. (B.12), we get

$$\left(\theta\,\langle \psi_1, \ldots, \psi_N|\right) H\, |\psi_1, \ldots, \psi_N\rangle = (-1)^N \left(\theta\,|\psi_1, \ldots, \psi_N\rangle\right) H\, |\psi_1, \ldots, \psi_N\rangle\,, \tag{B.15}$$

We therefore conclude that, in an open time-reversal invariant system (with an insulating bulk) supporting an odd number of (half-integer spin) chiral edge modes and an odd number of (half-integer spin) anti-chiral edge modes, the single-particle scattering terms which could open a gap are in fact necessarily vanishing so these processes can not open a gap.

Appendix C: Local response to capacitively coupled probes in a two-dimensional lattice bosonic system

C.1 System under consideration

Total Hamiltonian We consider a 2-dimensional lattice system with periodic boundary conditions. Let us consider a set of resonant light probes which are coupled to the system. We write the Hamiltonian

$$H = H_{\text{lat}} + H_{\text{prb}} + H_{\text{cpl}}, \tag{C.1}$$

where H_{lat} is the (topological) lattice Hamiltonian, H_{prb} is the Hamiltonian associated to the probe(s) and H_{cpl} is the Hamiltonian associated to the coupling between the lattice and the probe(s).

Lattice Hamiltonian Let us call N_C the number of sites per unit cell in the lattice we consider and N the total number of unit cells. We label each sites within a unit cell with different colors, and two different sites belonging to the same Bravais lattice are labeled by the same color.
We define the Fourier transform of the annihilation operator of a (bosonic) particle at position $\mathbf{r}$ and the inverse relation

$$a_{j,\mathbf{k}} = \sum_{\mathbf{r}\in R_j} \mathrm{e}^{-i\mathbf{k}.\mathbf{r}} a_{\mathbf{r}} \quad \text{and} \quad a_{\mathbf{r}} = \frac{1}{N}\sum_{\mathbf{k}} \mathrm{e}^{i\mathbf{k}.\mathbf{r}} a_{j(\mathbf{r}),\mathbf{k}}, \tag{C.2}$$

with R_j the ensemble containing all the lattice positions of the color-j sites and the function $j(\mathbf{r})$ returns the color index at the $\mathbf{r}$ site. We formally write

$$H_{\text{lat}} = \sum_{\boldsymbol{k}} \Psi^\dagger_{\boldsymbol{k}} h_{\boldsymbol{k}} \Psi_{\boldsymbol{k}}, \tag{C.3}$$

with $\Psi^\dagger_{\mathbf{k}} = \left(a^\dagger_{1,\mathbf{k}}, \dots a^\dagger_{N,\mathbf{k}}\right)$. We write $h_{\mathbf{k}}$'s associated eigenvalues $E_{i,\mathbf{k}}$, where $i \in \{1,\dots,N_C\}$, and we write the associated eigenvectors

$$|\Phi_{i,\mathbf{k}}\rangle = \Phi^\dagger_{i,\mathbf{k}} |0\rangle = \sum_{j=1}^{N_C} \alpha^j_{i,\mathbf{k}} a^\dagger_{j,\mathbf{k}} |0\rangle , \tag{C.4}$$

with $\alpha^j_{i,\mathbf{k}} \in \mathbb{C}$. We have

$$H_{\text{lat}} = \sum_{\mathbf{k}} \sum_{i=1}^{N_C} E_{i,\mathbf{k}} \Phi^\dagger_{i,\mathbf{k}} \Phi_{i,\mathbf{k}}. \tag{C.5}$$

Probe(s) Each probes are resonators with a certain number of relevant modes, each mode q being characterized by the frequency ω_q. Therefore we write

$$H_{\text{prb}} = \sum_{\mathbf{r} \in R_p} \sum_{q} \omega_q b^\dagger_{\boldsymbol{r},q} b_{\mathbf{r},q}, \tag{C.6}$$

with $b_{\boldsymbol{r},q}$ the annihilation operators for the mode q of the probe at $\boldsymbol{r} \in R_p$, R_p being the ensemble of the positions of the nodes coupled to a probe.

Coupling We assume a capacitive coupling between each probe and a node of the lattice. The Hamiltonian reads

$$H_{\text{cpl}} = \sum_{\mathbf{r} \in R_p} \left(a_{\mathbf{r}} + a^\dagger_{\mathbf{r}}\right) \sum_{q} g_q \left(b_{\mathbf{r},q} + b^\dagger_{\mathbf{r},q}\right). \tag{C.7}$$

The coupling g_q amplitude is assumed not to depend on the position of the probe.

C.2 Input-output analysis for a set of resonant cavity probe coupled to the system

Here we use the input-output formalism as reviewed in Ref. [318]. Let us define the input voltage in the probe at $\mathbf{r}$

$$V^{\text{in}}_{\mathbf{r}}(t) = \sum_{q} g_q \left(\mathrm{e}^{-i\omega_q(t-t_i)} b_{\mathbf{r},q}(t_i) + h.c.\right), \tag{C.8}$$

and the output voltage in the probe at $\mathbf{r}$

$$V^{\text{out}}_{\mathbf{r}}(t) = \sum_{q} g_q \left(\mathrm{e}^{-i\omega_q(t-t_f)} b_{\mathbf{r},q}(t_f) + h.c.\right). \tag{C.9}$$

Let us call $x_{\mathbf{r}} = \dfrac{1}{\sqrt{2}}\left(a_{\mathbf{r}} + a^\dagger_{\mathbf{r}}\right)$. The Heisenberg equation of motion (EOM) for the b_{jq} operator reads

$$\dot{b}_{\mathbf{r},q} = i\left[H, b_{\mathbf{r},q}\right] = -i\omega_q b_{\mathbf{r},q} - i\sqrt{2} g_q x_{\mathbf{r}}. \tag{C.10}$$

Writing $t_i < t$ the initial time in the distant past, the solution of this equation of motion is

$$b_{\mathbf{r},q}(t) = \mathrm{e}^{-i\omega_q(t-t_i)} b_{\mathbf{r},q}(t_i) - i\sqrt{2} g_q \int_{t_i}^{t} d\tau \mathrm{e}^{-i\omega_q(t-\tau)} x_{\mathbf{r}}(\tau). \tag{C.11}$$

Considering $t_f > t$ a final time in the distant future gives an other solution

$$b_{\mathbf{r},q}(t) = \mathrm{e}^{-i\omega_q(t-t_f)} b_{\mathbf{r},q}(t_f) + i\sqrt{2} g_q \int_t^{t_f} d\tau \mathrm{e}^{-i\omega_q(t-\tau)} x_{\mathbf{r}}(\tau). \tag{C.12}$$

Combining the previous equations and their complex conjugate counterparts we get

$$V_{\mathbf{r}}^{\mathrm{in}}(t) - 2\sqrt{2} \sum_q g_q^2 \int_{t_i}^{t_f} d\tau \sin\left(\omega_q(t-\tau)\right) x_{\mathbf{r}}(\tau) = V_{\mathbf{r}}^{\mathrm{out}}(t). \tag{C.13}$$

We Fourier transform the previous equation with respect to the time variable t, we define $J(t) = 2\sqrt{2}i \sum_q g_q^2 \sin(\omega_q t)$ [319] and we get

$$V_{\mathbf{r}}^{\mathrm{out}}[\omega] = V_{\mathbf{r}}^{\mathrm{in}}[\omega] + iJ[\omega] x_{\mathbf{r}}[\omega]. \tag{C.14}$$

Notice that $J[\omega] \in \mathbb{R}$. Its explicit expression is

$$J[\omega] = 2\sqrt{2}\pi \sum_q g_q^2 \left(\delta(\omega - \omega_q) - \delta(\omega + \omega_q)\right), \tag{C.15}$$

where δ is the Dirac delta function. Let us notice that if the spectrum of the probe is symmetric with respect to 0, then $J[\omega]$ is vanishing (so as $J(t)$). In the following, we assume it is not the case.

C.3 Response function

Now we express $x_{\mathbf{r}}[\omega]$ as a function of $V_{\mathbf{r}}^{\mathrm{in}}[\omega]$. The Heisenberg EOM for the $\Phi_{i,\mathbf{k}}$ modes reads

$$\dot{\Phi}_{i,\mathbf{k}} = -iE_{i,\mathbf{k}}\Phi_{i,\mathbf{k}} - i \sum_{\mathbf{r}\in R_p} \left(\alpha_{i,\mathbf{k}}^{j(\mathbf{r})} \mathrm{e}^{i\mathbf{k}.\mathbf{r}}\right)^* \sum_q g_q \left(b_{\mathbf{r},q} + b_{\mathbf{r},q}^\dagger\right). \tag{C.16}$$

Using equation C.11 we have,

$$i\dot{\Phi}_{i,\mathbf{k}}(t) = E_{i,\mathbf{k}}\Phi_{i,\mathbf{k}}(t) + \sum_{\mathbf{r}\in R_p} \left(\alpha_{i,\mathbf{k}}^{j(\mathbf{r})} \mathrm{e}^{i\mathbf{k}.\mathbf{r}}\right)^* V_{\mathbf{r}}^{\mathrm{in}}(t) + \mathcal{O}(g^2), \tag{C.17}$$

with $g = \max_q(g_q)$ and in the limit of small g compared to the energies $(E_{i,\mathbf{k}})$ of the system. Now we use the Fourier transformation with respect to the time variable to write

$$\Phi_{i,\mathbf{k}}[\omega] = \frac{1}{-\omega - E_{i,\mathbf{k}} + i0^+} \sum_{\mathbf{r}\in R_p} \left(\alpha_{i,\mathbf{k}}^{j(\mathbf{r})} \mathrm{e}^{i\mathbf{k}.\mathbf{r}}\right)^* V_{\mathbf{r}}^{\mathrm{in}}[\omega] + \mathcal{O}(g_{q_0}^2), \tag{C.18}$$

and

$$\Phi_{i,\mathbf{k}}^\dagger[\omega] = -\frac{1}{-\omega + E_{i,\mathbf{k}} + i0^+} \sum_{\mathbf{r}\in R_p} \alpha_{i,\mathbf{k}}^{j(\mathbf{r})} \mathrm{e}^{i\mathbf{k}.\mathbf{r}} V_{\mathbf{r}}^{\mathrm{in}}[\omega] + \mathcal{O}(g^2), \tag{C.19}$$

Note that $\Phi_{i,\mathbf{k}}[\omega] = \text{T.F.}\left(\Phi_{i,\mathbf{k}}\right)[\omega]$, T.F. denoting the Fourier transform and $\Phi^\dagger_{i,\mathbf{k}}[\omega] = \text{T.F.}\left(\Phi^\dagger_{i,\mathbf{k}}\right)[\omega]$ so $\Phi_{i,\mathbf{k}}[\omega] \neq \left(\Phi^\dagger_{i,\mathbf{k}}[\omega]\right)^\dagger$.
We introduce the $\beta^j_{i,\mathbf{k}}$ coefficients such that

$$a^\dagger_{j,\mathbf{k}}\left|0\right\rangle = \sum_{i=1}^{N} \beta^i_{j,\mathbf{k}} \Phi^\dagger_{i,\mathbf{k}}\left|0\right\rangle. \tag{C.20}$$

Then we have

$$x_{\mathbf{r}} = \frac{1}{\sqrt{2}N} \sum_{\mathbf{k}} \sum_{i=1}^{N} \left(\mathrm{e}^{i\mathbf{k}\cdot\mathbf{r}} \left(\beta^i_{j(\mathbf{r}),\mathbf{k}}\right)^* \Phi_{i,\mathbf{k}} + h.c.\right), \tag{C.21}$$

and we obtain

$$x_{\mathbf{r}}[\omega] = \sum_{\mathbf{r}_0 \in R_p} \chi_{\mathbf{r},\mathbf{r}_0} V^{\text{in}}_{\mathbf{r}_0}[\omega] + \mathcal{O}(g^2), \tag{C.22}$$

with

$$\chi_{\mathbf{r},\mathbf{r}_0} = \frac{1}{\sqrt{2}N} \sum_{\substack{i=1 \\ \mathbf{k}}}^{N} \left(\frac{C^*_{i,\mathbf{k},\mathbf{r},\mathbf{r}_0}}{-\omega - E_{i,\mathbf{k}} + i0^+} - \frac{C_{i,\mathbf{k},\mathbf{r},\mathbf{r}_0}}{-\omega + E_{i,\mathbf{k}} + i0^+} \right), \tag{C.23}$$

and

$$C_{i,\mathbf{k},\mathbf{r},\mathbf{r}_0} = \beta^i_{j(\mathbf{r}),\mathbf{k}} \alpha^{j(\mathbf{r}_0)}_{i,\mathbf{k}} \mathrm{e}^{-i\mathbf{k}.(\mathbf{r}-\mathbf{r}_0)}. \tag{C.24}$$

Let us notice from the last equation that adding a probe with no input does not influence the response at the other probes (with or without input). This is because we restricted the response to first order in g_{q_0}.

Finally, Eq. (C.14) gives

$$V^{\text{out}}_{\mathbf{r}}[\omega] = V^{\text{in}}_{\mathbf{r}}[\omega] + iJ[\omega] \sum_{\mathbf{r}_0 \in R_p} \chi_{\mathbf{r},\mathbf{r}_0} V^{\text{in}}_{\mathbf{r}_0}[\omega] + \mathcal{O}(g^4), \tag{C.25}$$

which is the equation from which we start in Chapter 2 to investigate a Haldane cQED system.

Appendix D: Kubo formula

In this appendix we apply linear response formalism to a fermion insulating system subjected to a small electric, in the zero temperature limit. The general formalism presented here enables, for instance, to show the link between the Hall conductivity and the Chern number (see Sec. 1.3.1 of Chapter 1). For more details, we refer the reader to the Refs. [119, 320, 321].

Let us define $\Delta\langle O\rangle(t)$ the change, at time t, in the expectation value of an arbitrary observable O, from its equilibrium value $\langle O\rangle_{\rm eq} = {\rm Tr}\,\{\rho_c^{\rm eq}\, O\}$, under an adiabatic small perturbation described by a Hamiltonian which we write $H'(t) = \lambda(t)B$. B is an operator and $\lambda(t)$ is the time-dependent amplitude of the perturbation. Here, $\rho_c^{\rm eq} = {\rm e}^{-\beta H_0}/Z$ is the density matrix at time t_0, before the perturbation is applied, when the system is in global canonical equilibrium at temperature β^{-1} and described by the Hamiltonian H_0 and Z is the canonical partition function. The density matrix at time $t \geq t_0$ is given by the quantum Liouville equation.

We have [320]

$$\Delta\langle O\rangle(t) = \int_{-\infty}^{+\infty} dt' \xi_{OB}(t-t')\lambda(t') = -\frac{i}{\hbar}\int_{-\infty}^{+\infty} dt' {\rm Tr}\{\rho_c^{\rm eq}\,[O(t-t'), B]\}\lambda(t'), \tag{D.1}$$

with

$$\xi_{OB}(t-t') = -\frac{i}{\hbar}\theta(t-t'){\rm Tr}\{\rho_c^{\rm eq}\,[O(t-t'), B]\}. \tag{D.2}$$

We also have

$$[\rho_c^{\rm eq}, B(t)] = i\hbar\int_0^\beta d\tau \rho_c^{\rm eq}\frac{dB(t-i\hbar\tau)}{dt}, \tag{D.3}$$

with $O(t-t')$ and $B(t)$ the interaction representations of respectively the operators O and B

$$O(t-t') = {\rm e}^{iH_0(t-t')}B{\rm e}^{-iH_0(t-t')}, \tag{D.4a}$$

$$B(t) = {\rm e}^{iH_0 t}B{\rm e}^{-iH_0 t}. \tag{D.4b}$$

This gives

$$\xi_{OB}(t-t') = -\int_0^\beta d\tau {\rm Tr}\{\rho_c^{\rm eq}\frac{dB(t-i\hbar\tau)}{dt}O(t-t')\}. \tag{D.5}$$

Let us consider an adiabatic perturbation resulting from a small uniform and static electric field $\boldsymbol{\epsilon}$ perturbation, is switched on adiabatically from $t_0 = -\infty$ to t [322]. In this case we

write

$$H'(t) = \lambda(t) \cdot B, \tag{D.6a}$$

$$\lambda = -e\boldsymbol{\epsilon} \lim_{\zeta \to \infty} \mathrm{e}^{t/\zeta}, \tag{D.6b}$$

$$B = \int d\mathbf{r} n(\mathbf{r}) \mathbf{r}, \tag{D.6c}$$

with $n(\mathbf{r})$ the (number) density operator and $\mathbf{r}$ the positions of the particules in the system. Using the continuity equation, we obtain $dB/dt = \mathbf{j}(t)$ and $\mathbf{j}(t) = \int d\mathbf{r} \mathbf{j}(\mathbf{r}, t)$, with $\mathbf{j}(\mathbf{r}, t)$ the current operator in the interaction picture defined from the continuity equation for the number density operator. By definition, we have

$$\mathbf{j}(t) = \mathrm{e}^{iH_0 t} \mathbf{j} \mathrm{e}^{-iH_0 t}. \tag{D.7}$$

Moreover, we assume the electric field is along the direction $\mathbf{e}_\alpha$, and we write $\boldsymbol{\epsilon} = \epsilon_\alpha \mathbf{e}_\alpha$ and $\boldsymbol{j} = j_\alpha \mathbf{e}_\alpha$. We write $\Delta\langle O \rangle_\alpha$ the resulting change in O. We have

$$\Delta\langle O \rangle_\alpha = V \lim_{\zeta \to \infty} \int_0^{+\infty} dt \mathrm{e}^{-t/\zeta} \Bigg[\int_0^\beta d\tau \mathrm{Tr} \left\{ \rho_{\mathrm{eq}} \sum_{m,n} c_m^\dagger c_n \langle m | O | n \rangle \sum_{p,q} c_p^\dagger c_q \langle p | j_\alpha | q \rangle \mathrm{e}^{i(E_p - E_q)(t + i\hbar\tau)/\hbar} \right\} \epsilon_\alpha \Bigg], \tag{D.8}$$

where $|m\rangle$, $|n\rangle$, $|p\rangle$ and $|q\rangle$ are the eigenstates of H_0, E_m, E_n, E_p and E_q the associated eigenenergies and c_m, c_n, c_p and c_q the associated annihilation operators. Using $\mathrm{Tr}\rho_{\mathrm{eq}} c_m^\dagger c_n c_p^\dagger c_q = \delta_{mp}\delta_{nq} f(E_n)(1 - f(E_m)) + \delta_{mp}\delta_{mp} f(E_n) f(E_p)$, with f the Fermi-Dirac distribution and δ the Kronecker delta function,

$$\int_0^\beta d\tau \mathrm{e}^{-(E_p - E_q)\tau} = \frac{1 - \mathrm{e}^{-(E_p - E_q)\beta}}{E_p - E_q}, \tag{D.9}$$

and

$$\int_0^{+\infty} dt \mathrm{e}^{-t/\zeta} \mathrm{e}^{i(E_p - E_q)t/\hbar} = \frac{\hbar}{\hbar/\zeta - i(E_p - E_q)}, \tag{D.10}$$

we get

$$\Delta\langle O \rangle_\alpha = i\hbar e V \lim_{\zeta \to \infty} \sum_{m,n} \frac{f(E_m) f(E_n)}{E_n - E_m} \frac{\mathrm{e}^{\beta E_n} - \mathrm{e}^{\beta E_m}}{i\hbar/\zeta + (E_n - E_m)} \langle m | O | n \rangle \langle n | j_\alpha | m \rangle \epsilon_\alpha. \tag{D.11}$$

In the zero temperature limit, from the behavior of the Fermi-Dirac distribution, we obtain, for an insulating system (chemical potential μ in the energy gap)

$$\Delta\langle O \rangle_\alpha = i\hbar V e \lim_{\zeta \to \infty} \sum_{m,n} \frac{\mathbb{I}_{E_m < \mu < E_n} - \mathbb{I}_{E_n < \mu < E_m}}{(E_n - E_m)(E_n - E_m + i\hbar/\zeta)} \langle m | O | n \rangle \langle n | j_\alpha | m \rangle \epsilon_\alpha, \tag{D.12}$$

which leads to

$$\Delta\langle O \rangle_\alpha = i\hbar V e \sum_{E_m < \mu < E_n} \frac{\langle m | O | n \rangle \langle n | j_\alpha | m \rangle - \langle n | O | m \rangle \langle m | j_\alpha | n \rangle}{(E_n - E_m)^2} \epsilon_\alpha. \tag{D.13}$$

This is the equation we start from in Sec. 1.3.1 of Chapter 1.

Appendix E: Cylinder geometry and partial Fourier transformation

Here we give the detailed formulation of the Hamiltonian (5.41) (studied in Chapter 5) for a cylinder geometry which we used to compute the associated spectrum and eigenvalues. The Hamiltonian (5.41) reads

$$\begin{aligned}\mathcal{H} &= -t\sum_{\mathbf{r}}\Big[c^{\dagger}_{R,\mathbf{r}}\mathbb{I}c_{B,\mathbf{r}}+c^{\dagger}_{R,\mathbf{r}+\mathbf{e}_1}\mathbb{I}c_{B,\mathbf{r}}+c^{\dagger}_{R,\mathbf{r}}e^{-i2\pi\gamma s_x}c_{G,\mathbf{r}}+c^{\dagger}_{G,\mathbf{r}}e^{-i2\pi\gamma s_x}c_{R,\mathbf{r}+\mathbf{e}_2}\\ &+ c^{\dagger}_{B,\mathbf{r}}e^{i\phi s_z}c_{G,\mathbf{r}}+c^{\dagger}_{B,\mathbf{r}+\mathbf{e}_3}e^{i\phi s_z}c_{G,\mathbf{r}}+H.c.\Big]+\sum_{\mathbf{r}}\sum_{\alpha=R,B,G}\lambda_{\alpha}n_{\alpha,\mathbf{r}},\end{aligned} \tag{E.1}$$

and we consider open boundary conditions along the $\mathbf{e}_1$ direction and edges along the $\mathbf{e}_2$ direction.

Let us define

$$\Psi^{\dagger}_{\boldsymbol{r}}=\left(c^{\dagger}_{R,\boldsymbol{r},\uparrow},c^{\dagger}_{B,\boldsymbol{r}+\boldsymbol{b}_1,\uparrow},c^{\dagger}_{G,\boldsymbol{r}+\boldsymbol{b}_2,\uparrow},c^{\dagger}_{R,\boldsymbol{r},\downarrow},c^{\dagger}_{B,\boldsymbol{r}+\boldsymbol{b}_1,\downarrow},c^{\dagger}_{G,\boldsymbol{r}+\boldsymbol{b}_2,\downarrow}\right). \tag{E.2}$$

We also define r_α the coordinate along the $\mathbf{e}_\alpha$ direction and and $k_2=2\mathbf{k}\cdot\mathbf{b}_2$ and we write

$$\Psi^{\dagger}_{r_1,r_2}=\frac{1}{\sqrt{N}}\sum_{k_2}\mathrm{e}^{ik_2}\Psi^{\dagger}_{r_1,k_2}U^{\dagger}_{k_2}, \tag{E.3}$$

with

$$U_{k_2}=\mathrm{diag}\left(1,1,\mathrm{e}^{-ik_2/2},1,1,\mathrm{e}^{-ik_2/2}\right). \tag{E.4}$$

We perform a partial Fourier transformation and we obtain

$$H=\sum_{r_1,k_2}\left[\Psi^{\dagger}_{r_1,k_2}J_0(k_2)\Psi_{r_1,k_2}+\left(\Psi^{\dagger}_{r_1,k_2}J_1(k_2)\Psi_{r_1+1,k_2}+H.c.\right)\right], \tag{E.5}$$

with

$$J_0(k_2)=\begin{pmatrix}J_{0,(\uparrow,\uparrow)}(k_2) & J_{0,(\uparrow,\downarrow)}(k_2)\\ J_{0,(\downarrow,\uparrow)}(k_2) & J_{0,(\downarrow,\downarrow)}(k_2)\end{pmatrix},\qquad J_1(k_2)=\begin{pmatrix}J_{1,(\uparrow,\uparrow)}(k_2) & 0\\ 0 & J_{1,(\downarrow,\downarrow)}(k_2)\end{pmatrix}, \tag{E.6}$$

$$J_{0,(\sigma,\sigma)}(k_2) = \begin{pmatrix} \lambda_R & -t & \varepsilon_2 \cos(2\pi\gamma) \\ -t & \lambda_B & -t\mathrm{e}^{-i(k_2/2 - s_z\phi)} \\ \varepsilon_2 \cos(2\pi\gamma) & -t\mathrm{e}^{i(k_2/2 - s_z\phi)} & \lambda_G \end{pmatrix}, \tag{E.7}$$

$$J_{0,(\uparrow,\downarrow)}(k_2) = J_{0,(\downarrow,\uparrow)}(k_2) = \begin{pmatrix} 0 & 0 & \xi(\mathbf{k}) \sin(2\pi\gamma) \\ 0 & 0 & 0 \\ \xi(\mathbf{k}) \sin(2\pi\gamma) & 0 & 0 \end{pmatrix}, \tag{E.8}$$

$$J_{1,(\sigma,\sigma)}(k_2) = \begin{pmatrix} 0 & 0 & 0 \\ -t & 0 & -t\mathrm{e}^{i(k_2/2 + s_z\phi)} \\ 0 & 0 & 0 \end{pmatrix}, \tag{E.9}$$

and we remind that $\varepsilon_2 = -2t\cos(k_2/2)$, $\xi(k_2) = 2t\sin(k_2/2)$ and $s_z = 1\,(-1)$ for $\sigma = \uparrow\ (\downarrow)$. Now, we write the Hamiltonian

$$H = \sum_{k_2} \Psi^\dagger_{k_2} H(k_2) \Psi_{k_2}, \tag{E.10}$$

with

$$H(k_2) = \begin{pmatrix} \hat{J}_0(k_2) & \hat{J}_1(k_2) & 0 & . & . & . \\ \hat{J}_1(k_2)^\dagger & \hat{J}_0(k_2) & \hat{J}_1(k_2) & & & \\ 0 & \hat{J}_1(k_2)^\dagger & \hat{J}_0(k_2) & & & \\ . & & & . & & \\ . & & & & . & \\ . & & & & & . \end{pmatrix}, \tag{E.11}$$

and $\Psi_{k_2} = (\Psi_{0,k_2}, \Psi_{1,k_2}, \Psi_{2,k_2}, ..., \Psi_{N,k_2})$. The energies at each k_2 are found by performing numerical diagonalization of $H(k_2)$ (size $6N \times 6N$).

Appendix F: The resolvent method and perturbation theory

F.1 Effective Hamiltonian

Here we consider the Hamiltonian

$$\mathcal{H} = \mathcal{H}_0 + V, \tag{F.1}$$

where, in practice, $\mathcal{H}_0$ is a Hamiltonian for which the spectrum and the eigenvectors are computable and V is a perturbation (which amplitude may be small or not). We denote by P an orthogonal and hermitian projector which commutes with $\mathcal{H}_0$ and $Q = 1-P$ the associated complementary projector. In practice, P projects onto a subspace of eigenvectors of $\mathcal{H}_0$. We write $G(z) = (z - \mathcal{H})^{-1}$ the resolvent of the Hamiltonian $\mathcal{H}$. Considering $z = E + i\eta$ or $z = E - i\eta$ gives the Fourier transform (up to a factor $i\hbar$) of respectively the retarded or advanced Green function, which dictates the time evolution under $\mathcal{H}$. We have

$$PG(z)P = P\left(zP - \mathcal{H}_{\text{eff}}\right)^{-1}, \tag{F.2}$$

with

$$\mathcal{H}_{\text{eff}} = P\mathcal{H}P + PVQ\left(zQ - Q\mathcal{H}Q\right)^{-1} QVP, \tag{F.3}$$

being the effective Hamiltonian for the evolution of the system in the subspace in which P projects.

F.2 Perturbation theory up to second order in V

We write ϵ the energy amplitude associated to V and U the energy amplitude associated to $\mathcal{H}_0$. We consider $\epsilon \ll U$.

We denote by S_0 the subspace of eigenvectors of $\mathcal{H}_0$, corresponding to the ground state with energy E_0. To second order in ϵ/U, the effective Hamiltonian in S_0 is

$$\begin{aligned}\mathcal{H}_{\text{eff}} =& E_0 P + PVP \\ &+ PVQ\left(E_0 - Q\left(\mathcal{H}_U + \mathcal{H}_\lambda\right)Q\right)^{-1} QVP,\end{aligned} \tag{F.4}$$

where P here projects on S_0. The higher orders can be computed from Eq. (F.3). In practice, we consider two states $|\psi\rangle$, and $|\psi'\rangle$ in S_0, and from Eq. (F.4) we get (still at second order

in ϵ/U)

$$\begin{aligned}\langle\psi'|\,\mathcal{H}_{\text{eff}}\,|\psi\rangle =& E_0\,\langle\psi'|\psi\rangle + \langle\psi'|\,V\,|\psi\rangle \\ &+ \sum_{|m\rangle\notin S_0} \frac{\langle\psi'|\,V\,|m\rangle\,\langle m|\,V\,|\psi\rangle}{E_0 - E_m},\end{aligned} \tag{F.5}$$

with $|m\rangle$ the eigenstates of $\mathcal{H}_0$ which do not belong to the ground state subspace S_0 and E_m is the corresponding eigenenergy.

Bibliography

[1] S. Ryu, A. P. Schnyder, A. Furusaki, and A. W. W. Ludwig, "Topological insulators and superconductors: Tenfold way and dimensional hierarchy," *New Journal of Physics*, vol. 12, no. 6, p. 065 010, 2010. DOI: 10.1088/1367-2630/12/6/065010.

[2] M. Z. Hasan and C. L. Kane, "Colloquium: Topological insulators," *Rev. Mod. Phys.*, vol. 82, pp. 3045–3067, 4 2010. DOI: 10.1103/RevModPhys.82.3045.

[3] X.-L. Qi and S.-C. Zhang, "Topological insulators and superconductors," *Rev. Mod. Phys.*, vol. 83, pp. 1057–1110, 4 2011. DOI: 10.1103/RevModPhys.83.1057.

[4] N. Nagaosa, J. Sinova, S. Onoda, A. H. MacDonald, and N. P. Ong, "Anomalous hall effect," *Rev. Mod. Phys.*, vol. 82, pp. 1539–1592, 2 2010. DOI: 10.1103/RevModPhys.82.1539.

[5] F. D. M. Haldane, "Model for a quantum hall effect without landau levels: Condensed-matter realization of the "parity anomaly"," *Phys. Rev. Lett.*, vol. 61, pp. 2015–2018, 18 1988. DOI: 10.1103/PhysRevLett.61.2015.

[6] K. v. Klitzing, G. Dorda, and M. Pepper, "New method for high-accuracy determination of the fine-structure constant based on quantized hall resistance," *Phys. Rev. Lett.*, vol. 45, pp. 494–497, 6 1980. DOI: 10.1103/PhysRevLett.45.494.

[7] R. B. Laughlin, "Quantized hall conductivity in two dimensions," *Phys. Rev. B*, vol. 23, pp. 5632–5633, 10 1981. DOI: 10.1103/PhysRevB.23.5632.

[8] D. J. Thouless, M. Kohmoto, M. P. Nightingale, and M. den Nijs, "Quantized hall conductance in a two-dimensional periodic potential," *Phys. Rev. Lett.*, vol. 49, pp. 405–408, 6 1982. DOI: 10.1103/PhysRevLett.49.405.

[9] M. V. Berry, "Quantal phase factors accompanying adiabatic changes," *Proceedings of the Royal Society of London. Series A, Mathematical and Physical Sciences*, vol. 392, no. 1802, pp. 45–57, 1984, ISSN: 00804630.

[10] M. Kohmoto, "Topological invariant and the quantization of the hall conductance," *Annals of Physics*, vol. 160, no. 2, pp. 343–354, 1985, ISSN: 0003-4916. DOI: https://doi.org/10.1016/0003-4916(85)90148-4.

[11] C. L. Kane and E. J. Mele, "Quantum spin hall effect in graphene," *Phys. Rev. Lett.*, vol. 95, p. 226 801, 22 2005. DOI: 10.1103/PhysRevLett.95.226801.

[12] B. A. Bernevig and S.-C. Zhang, "Quantum spin hall effect," *Phys. Rev. Lett.*, vol. 96, p. 106 802, 10 2006. DOI: 10.1103/PhysRevLett.96.106802.

[13] B. A. Bernevig, T. L. Hughes, and S.-C. Zhang, "Quantum spin hall effect and topological phase transition in hgte quantum wells," *Science*, vol. 314, no. 5806, pp. 1757–1761, 2006. DOI: 10.1126/science.1133734.

[14] M. König, S. Wiedmann, C. Brüne, A. Roth, H. Buhmann, L. W. Molenkamp, X.-L. Qi, and S.-C. Zhang, "Quantum spin hall insulator state in hgte quantum wells," *Science*, vol. 318, no. 5851, pp. 766–770, 2007. DOI: 10.1126/science.1148047.

[15] N. Goldman, J. C. Budich, and P. Zoller, "Topological quantum matter with ultracold gases in optical lattices," *Nature Physics*, vol. 12, no. 7, pp. 639–645, 2016. DOI: 10.1038/nphys3803.

[16] N. R. Cooper, J. Dalibard, and I. B. Spielman, "Topological bands for ultracold atoms," *Rev. Mod. Phys.*, vol. 91, p. 015 005, 1 2019. DOI: 10.1103/RevModPhys.91.015005.

[17] L. Lu, J. D. Joannopoulos, and M. Soljačić, "Topological photonics," *Nature Photonics*, vol. 8, no. 11, pp. 821–829, 2014. DOI: 10.1038/nphoton.2014.248.

[18] T. Ozawa, H. M. Price, A. Amo, N. Goldman, M. Hafezi, L. Lu, M. C. Rechtsman, D. Schuster, J. Simon, O. Zilberberg, and I. Carusotto, "Topological photonics," *Rev. Mod. Phys.*, vol. 91, p. 015 006, 1 2019. DOI: 10.1103/RevModPhys.91.015006.

[19] A. Tomita and R. Y. Chiao, "Observation of berry's topological phase by use of an optical fiber," *Phys. Rev. Lett.*, vol. 57, pp. 937–940, 8 1986. DOI: 10.1103/PhysRevLett.57.937.

[20] S. Nakatsuji, N. Kiyohara, and T. Higo, "Large anomalous hall effect in a non-collinear antiferromagnet at room temperature," *Nature*, vol. 527, no. 7577, pp. 212–215, 2015. DOI: 10.1038/nature15723.

[21] K. Kuroda, T. Tomita, M. T. Suzuki, C. Bareille, A. A. Nugroho, P. Goswami, M. Ochi, M. Ikhlas, M. Nakayama, S. Akebi, R. Noguchi, R. Ishii, N. Inami, K. Ono, H. Kumigashira, A. Varykhalov, T. Muro, T. Koretsune, R. Arita, S. Shin, T. Kondo, and S. Nakatsuji, "Evidence for magnetic weyl fermions in a correlated metal," *Nature Materials*, vol. 16, no. 11, pp. 1090–1095, 2017. DOI: 10.1038/nmat4987.

[22] M. Ikhlas, T. Tomita, T. Koretsune, M.-T. Suzuki, D. Nishio-Hamane, R. Arita, Y. Otani, and S. Nakatsuji, "Large anomalous nernst effect at room temperature in a chiral antiferromagnet," *Nature Physics*, vol. 13, no. 11, pp. 1085–1090, 2017. DOI: 10.1038/nphys4181.

[23] Y. Chen, J. Gaudet, S. Dasgupta, G. G. Marcus, J. Lin, T. Chen, T. Tomita, M. Ikhlas, Y. Zhao, W. C. Chen, M. B. Stone, O. Tchernyshyov, S. Nakatsuji, and C. Broholm, "Antichiral spin order, its soft modes, and their hybridization with phonons in the topological semimetal Mn_3Ge," *Phys. Rev. B*, vol. 102, p. 054 403, 5 2020. DOI: 10.1103/PhysRevB.102.054403.

[24] Z. Lin, J.-H. Choi, Q. Zhang, W. Qin, S. Yi, P. Wang, L. Li, Y. Wang, H. Zhang, Z. Sun, L. Wei, S. Zhang, T. Guo, Q. Lu, J.-H. Cho, C. Zeng, and Z. Zhang, "Flatbands and emergent ferromagnetic ordering in Fe_3Sn_2 kagome lattices," *Phys. Rev. Lett.*, vol. 121, p. 096 401, 9 2018. DOI: 10.1103/PhysRevLett.121.096401.

[25] Q. Xu, E. Liu, W. Shi, L. Muechler, J. Gayles, C. Felser, and Y. Sun, "Topological surface fermi arcs in the magnetic weyl semimetal $Co_3Sn_2S_2$," *Phys. Rev. B*, vol. 97, p. 235 416, 23 2018. DOI: 10.1103/PhysRevB.97.235416.

[26] Q. Wang, Y. Xu, R. Lou, Z. Liu, M. Li, Y. Huang, D. Shen, H. Weng, S. Wang, and H. Lei, "Large intrinsic anomalous hall effect in half-metallic ferromagnet co3sn2s2 with magnetic weyl fermions," *Nature Communications*, vol. 9, no. 1, p. 3681, 2018, ISSN: 2041-1723. DOI: 10.1038/s41467-018-06088-2.

[27] Z. Guguchia, J. A. T. Verezhak, D. J. Gawryluk, S. S. Tsirkin, J.-X. Yin, I. Belopolski, H. Zhou, G. Simutis, S.-S. Zhang, T. A. Cochran, G. Chang, E. Pomjakushina, L. Keller, Z. Skrzeczkowska, Q. Wang, H. C. Lei, R. Khasanov, A. Amato, S. Jia, T. Neupert, H. Luetkens, and M. Z. Hasan, "Tunable anomalous hall conductivity through volume-wise magnetic competition in a topological kagome magnet," *Nature Communications*, vol. 11, no. 1, p. 559, 2020, ISSN: 2041-1723. DOI: 10.1038/s41467-020-14325-w.

[28] Y. Xu, J. Zhao, C. Yi, Q. Wang, Q. Yin, Y. Wang, X. Hu, L. Wang, E. Liu, G. Xu, L. Lu, A. A. Soluyanov, H. Lei, Y. Shi, J. Luo, and Z.-G. Chen, "Electronic correlations and flattened band in magnetic weyl semimetal candidate co3sn2s2," *Nature Communications*, vol. 11, no. 1, Aug. 2020. DOI: 10.1038/s41467-020-17234-0.

[29] M. Kang, L. Ye, S. Fang, J.-S. You, A. Levitan, M. Han, J. I. Facio, C. Jozwiak, A. Bostwick, E. Rotenberg, M. K. Chan, R. D. McDonald, D. Graf, K. Kaznatcheev, E. Vescovo, D. C. Bell, E. Kaxiras, J. van den Brink, M. Richter, M. Prasad Ghimire, J. G. Checkelsky, and R. Comin, "Dirac fermions and flat bands in the ideal kagome metal fesn," *Nature Materials*, vol. 19, no. 2, pp. 163–169, 2020. DOI: 10.1038/s41563-019-0531-0.

[30] T. Goren, K. Plekhanov, F. Appas, and K. Le Hur, "Topological zak phase in strongly coupled lc circuits," *Phys. Rev. B*, vol. 97, p. 041 106, 4 2018. DOI: 10.1103/PhysRevB.97.041106.

[31] K. Ohgushi, S. Murakami, and N. Nagaosa, "Spin anisotropy and quantum hall effect in the kagomé lattice: Chiral spin state based on a ferromagnet," *Phys. Rev. B*, vol. 62, R6065–R6068, 10 2000. DOI: 10.1103/PhysRevB.62.R6065.

[32] D. Green, L. Santos, and C. Chamon, "Isolated flat bands and spin-1 conical bands in two-dimensional lattices," *Phys. Rev. B*, vol. 82, p. 075 104, 7 2010. DOI: 10.1103/PhysRevB.82.075104.

[33] J. Koch, A. A. Houck, K. Le Hur, and S. M. Girvin, "Time-reversal-symmetry breaking in circuit-qed-based photon lattices," *Phys. Rev. A*, vol. 82, p. 043 811, 4 2010. DOI: 10.1103/PhysRevA.82.043811.

[34] A. Petrescu, A. A. Houck, and K. Le Hur, "Anomalous hall effects of light and chiral edge modes on the kagomé lattice," *Phys. Rev. A*, vol. 86, p. 053 804, 5 2012. DOI: 10.1103/PhysRevA.86.053804.

[35] R. Liu, W.-C. Chen, Y.-F. Wang, and C.-D. Gong, "Topological quantum phase transitions and topological flat bands on the kagomé lattice," *Journal of Physics: Condensed Matter*, vol. 24, no. 30, p. 305 602, 2012. DOI: 10.1088/0953-8984/24/30/305602.

[36] G. Xu, B. Lian, and S.-C. Zhang, "Intrinsic quantum anomalous hall effect in the kagome lattice $Cs_2LiMn_3F_{12}$," *Phys. Rev. Lett.*, vol. 115, p. 186 802, 18 2015. DOI: 10.1103/PhysRevLett.115.186802.

[37] L. Ye, M. Kang, J. Liu, F. von Cube, C. R. Wicker, T. Suzuki, C. Jozwiak, A. Bostwick, E. Rotenberg, D. C. Bell, L. Fu, R. Comin, and J. G. Checkelsky, "Massive dirac fermions in a ferromagnetic kagome metal," *Nature*, vol. 555, no. 7698, pp. 638–642, 2018, ISSN: 1476-4687. DOI: 10.1038/nature25987.

[38] E. Liu, Y. Sun, N. Kumar, L. Muechler, A. Sun, L. Jiao, S.-Y. Yang, D. Liu, A. Liang, Q. Xu, J. Kroder, V. Süß, H. Borrmann, C. Shekhar, Z. Wang, C. Xi, W. Wang, W. Schnelle, S. Wirth, Y. Chen, S. T. B. Goennenwein, and C. Felser, "Giant anomalous hall effect in a ferromagnetic kagome-lattice semimetal," *Nature Physics*, vol. 14, no. 11, pp. 1125–1131, 2018, ISSN: 1745-2481. DOI: 10.1038/s41567-018-0234-5.

[39] H.-M. Guo and M. Franz, "Topological insulator on the kagome lattice," *Phys. Rev. B*, vol. 80, p. 113 102, 11 2009. DOI: 10.1103/PhysRevB.80.113102.

[40] Z. Wang and P. Zhang, "Quantum spin hall effect and spin-charge separation in a kagomé lattice," *New Journal of Physics*, vol. 12, no. 4, p. 043 055, 2010. DOI: 10.1088/1367-2630/12/4/043055.

[41] G. Liu, S.-L. Zhu, S. Jiang, F. Sun, and W. M. Liu, "Simulating and detecting the quantum spin hall effect in the kagome optical lattice," *Phys. Rev. A*, vol. 82, p. 053 605, 5 2010. DOI: 10.1103/PhysRevA.82.053605.

[42] A. Bolens and N. Nagaosa, "Topological states on the breathing kagome lattice," *Phys. Rev. B*, vol. 99, p. 165 141, 16 2019. DOI: 10.1103/PhysRevB.99.165141.

[43] D. F. Liu, A. J. Liang, E. K. Liu, Q. N. Xu, Y. W. Li, C. Chen, D. Pei, W. J. Shi, S. K. Mo, P. Dudin, T. Kim, C. Cacho, G. Li, Y. Sun, L. X. Yang, Z. K. Liu, S. S. P. Parkin, C. Felser, and Y. L. Chen, "Magnetic weyl semimetal phase in a kagomé crystal," *Science*, vol. 365, no. 6459, pp. 1282–1285, 2019. DOI: 10.1126/science.aav2873.

[44] J. Hutchinson, P. W. Klein, and K. Le Hur, "Analytical approach for the mott transition in the kane-mele-hubbard model," *Phys. Rev. B*, vol. 104, p. 075 120, 7 2021. DOI: 10.1103/PhysRevB.104.075120.

[45] D. C. Tsui, H. L. Stormer, and A. C. Gossard, "Two-dimensional magnetotransport in the extreme quantum limit," *Phys. Rev. Lett.*, vol. 48, pp. 1559–1562, 22 1982. DOI: 10.1103/PhysRevLett.48.1559.

[46] F. Bloch, "Über die quantenmechanik der elektronen in kristallgittern," *Zeitschrift für Physik*, vol. 52, no. 7, pp. 555–600, 1929, ISSN: 0044-3328. DOI: 10.1007/BF01339455.

[47] G. H. Wannier, "The structure of electronic excitation levels in insulating crystals," *Phys. Rev.*, vol. 52, pp. 191–197, 3 1937. DOI: 10.1103/PhysRev.52.191.

[48] L. Fu and C. L. Kane, "Time reversal polarization and a Z_2 adiabatic spin pump," *Phys. Rev. B*, vol. 74, p. 195 312, 19 2006. DOI: 10.1103/PhysRevB.74.195312.

[49] Y. Aharonov and D. Bohm, "Significance of electromagnetic potentials in the quantum theory," *Phys. Rev.*, vol. 115, pp. 485–491, 3 1959. DOI: 10.1103/PhysRev.115.485.

[50] K. von Klitzing, T. Chakraborty, P. Kim, V. Madhavan, X. Dai, J. McIver, Y. Tokura, L. Savary, D. Smirnova, A. M. Rey, C. Felser, J. Gooth, and X. Qi, "40 years of the quantum hall effect," *Nature Reviews Physics*, vol. 2, no. 8, pp. 397–401, 2020, ISSN: 2522-5820. DOI: 10.1038/s42254-020-0209-1.

[51] R. P. Feynman, R. B. Leighton, and M. Sands, in *The Feynman Lectures on Physics*. Addison-Wesley, 1963, vol. II, ISBN: 9780465040834.

[52] A. Tonomura, N. Osakabe, T. Matsuda, T. Kawasaki, J. Endo, S. Yano, and H. Yamada, "Evidence for aharonov-bohm effect with magnetic field completely shielded from electron wave," *Phys. Rev. Lett.*, vol. 56, pp. 792–795, 8 1986. DOI: 10.1103/PhysRevLett.56.792.

[53] A. Messiah, in *Quantum Mechanics*. North-Holland / NY: John Wiley and Sons, 1966, vol. II, ISBN: 0486409244.

[54] B. Simon, "Holonomy, the quantum adiabatic theorem, and berry's phase," *Phys. Rev. Lett.*, vol. 51, pp. 2167–2170, 24 1983. DOI: 10.1103/PhysRevLett.51.2167.

[55] E. H. Hall, "On a new action of the magnet on electric currents," *American Journal of Mathematics*, vol. 2, no. 3, pp. 287–292, 1879, ISSN: 00029327, 10806377.

[56] F. Stern and W. E. Howard, "Properties of semiconductor surface inversion layers in the electric quantum limit," *Phys. Rev.*, vol. 163, pp. 816–835, 3 1967. DOI: 10.1103/PhysRev.163.816.

[57] G. Dorda, "Surface quantization in semiconductors," in *Festkörperprobleme 13: Plenary Lectures of the Divisions: Semiconductor Physics, Surface Physics, Low Temperature Physics, High Polymers, Thermodynamics and Statistical Mechanics of the German Physical Society Münster, March 19–24, 1973*, H. J. Queisser, Ed. Berlin, Heidelberg: Springer Berlin Heidelberg, 1973, pp. 215–239, ISBN: 978-3-540-75335-3. DOI: 10.1007/BFb0108573.

[58] T. Igarashi, J.-i. Wakabayashi, and S. Kawaji, "Hall effect in silicon inversion layers under strong magnetic fields," *Journal of the Physical Society of Japan*, vol. 38, no. 5, pp. 1549–1549, 1975. DOI: 10.1143/JPSJ.38.1549.

[59] S. Kawaji, T. Igarashi, and J.-i. Wakabayashi, "Quantum galvanomagnetic effect in n-channel silicon inversion layers under strong magnetic fields," *Progress of Theoretical Physics Supplement*, vol. 57, pp. 176–186, Mar. 1975, ISSN: 0375-9687. DOI: 10.1143/PTP.57.176.

[60] M. E. Cage, "Experimental aspects and metrological applications," in *The Quantum Hall Effect*, R. E. Prange and S. M. Girvin, Eds. New York, NY: Springer New York, 1990, pp. 37–68, ISBN: 978-1-4612-3350-3. DOI: 10.1007/978-1-4612-3350-3_2.

[61] L. Landau, "Diamagnetismus der metalle," *Zeitschrift für Physik*, vol. 64, no. 9, pp. 629–637, 1930, ISSN: 0044-3328. DOI: 10.1007/BF01397213.

[62] F. Schopfer and W. Poirier, "Testing universality of the quantum hall effect by means of the wheatstone bridge," *Journal of Applied Physics*, vol. 102, no. 5, p. 054 903, 2007. DOI: 10.1063/1.2776371.

[63] T. Ando, Y. Matsumoto, and Y. Uemura, "Theory of hall effect in a two-dimensional electron system," *Journal of the Physical Society of Japan*, vol. 39, no. 2, pp. 279–288, 1975. DOI: 10.1143/JPSJ.39.279.

[64] J.-i. Wakabayashi and S. Kawaji, "Hall effect in silicon mos inversion layers under strong magnetic fields," *Journal of the Physical Society of Japan*, vol. 44, no. 6, pp. 1839–1849, 1978. DOI: 10.1143/JPSJ.44.1839.

[65] K. von Klitzing, "The quantum hall effect," in *The Physics of the Two-Dimensional Electron Gas*, J. T. Devreese and F. M. Peeters, Eds. Boston, MA: Springer US, 1987, pp. 1–25, ISBN: 978-1-4613-1907-8. DOI: 10.1007/978-1-4613-1907-8_1.

[66] B. A. Bernevig and T. L. Hughes. Princeton University Press, 2013, ISBN: 9780691151755.

[67] B. I. Halperin, "Quantized hall conductance, current-carrying edge states, and the existence of extended states in a two-dimensional disordered potential," *Phys. Rev. B*, vol. 25, pp. 2185–2190, 4 1982. DOI: 10.1103/PhysRevB.25.2185.

[68] M. Marder, *Condensed Matter Physics*. Wiley, 2010, ISBN: 9780470949948.

[69] L. LANDAU and E. LIFSHITZ, "Chapter ii - energy and momentum," in *Quantum Mechanics (Third Edition)*, L. LANDAU and E. LIFSHITZ, Eds., Third Edition, Pergamon, 1977, pp. 25–49, ISBN: 978-0-08-020940-1. DOI: https://doi.org/10.1016/B978-0-08-020940-1.50009-8.

[70] W. Kohn, "Analytic properties of bloch waves and wannier functions," *Phys. Rev.*, vol. 115, pp. 809–821, 4 1959. DOI: 10.1103/PhysRev.115.809.

[71] N. Marzari and D. Vanderbilt, "Maximally localized generalized wannier functions for composite energy bands," *Phys. Rev. B*, vol. 56, pp. 12 847–12 865, 20 1997. DOI: 10.1103/PhysRevB.56.12847.

[72] K. S. Novoselov, A. K. Geim, S. V. Morozov, D. Jiang, Y. Zhang, S. V. Dubonos, I. V. Grigorieva, and A. A. Firsov, "Electric field effect in atomically thin carbon films," *Science*, vol. 306, no. 5696, pp. 666–669, 2004. DOI: 10.1126/science.1102896.

[73] H. W. Kroto, J. R. Heath, S. C. O'Brien, R. F. Curl, and R. E. Smalley, "C60: Buckminsterfullerene," *Nature*, vol. 318, no. 6042, pp. 162–163, 1985, ISSN: 1476-4687. DOI: 10.1038/318162a0.

[74] M. Dresselhaus, G. Dresselhaus, and P. Eklund, "Chapter 1 - historical introduction," in *Science of Fullerenes and Carbon Nanotubes*, M. Dresselhaus, G. Dresselhaus, and P. Eklund, Eds., San Diego: Academic Press, 1996, pp. 1–14, ISBN: 978-0-12-221820-0. DOI: https://doi.org/10.1016/B978-012221820-0/50001-0.

[75] W. Andreoni, in *The Physics of Fullerene-Based and Fullerene-Related Materials*. Springer Dordrecht, 2000.

[76] S. Iijima, "Helical microtubules of graphitic carbon," *Nature*, vol. 354, no. 6348, pp. 56–58, 1991, ISSN: 1476-4687. DOI: 10.1038/354056a0.

[77] M. Dresselhaus, G. Dresselhaus, and P. Eklund, "Chapter 20 - applications of carbon nanostructures," in *Science of Fullerenes and Carbon Nanotubes*, M. Dresselhaus, G. Dresselhaus, and P. Eklund, Eds., San Diego: Academic Press, 1996, pp. 870–917, ISBN: 978-0-12-221820-0. DOI: https://doi.org/10.1016/B978-012221820-0/50020-4.

[78] A. H. Castro Neto, F. Guinea, N. M. R. Peres, K. S. Novoselov, and A. K. Geim, "The electronic properties of graphene," *Rev. Mod. Phys.*, vol. 81, pp. 109–162, 1 2009. DOI: 10.1103/RevModPhys.81.109.

[79] T. Ando, T. Nakanishi, and R. Saito, "Berry's phase and absence of back scattering in carbon nanotubes," *Journal of the Physical Society of Japan*, vol. 67, no. 8, pp. 2857–2862, 1998. DOI: 10.1143/JPSJ.67.2857.

[80] A. M. Dudarev, R. B. Diener, I. Carusotto, and Q. Niu, "Spin-orbit coupling and berry phase with ultracold atoms in 2d optical lattices," *Phys. Rev. Lett.*, vol. 92, p. 153 005, 15 2004. DOI: 10.1103/PhysRevLett.92.153005.

[81] Y. Zhang, Y.-W. Tan, H. L. Stormer, and P. Kim, "Experimental observation of the quantum hall effect and berry's phase in graphene," *Nature*, vol. 438, no. 7065, pp. 201–204, 2005, ISSN: 1476-4687. DOI: 10.1038/nature04235.

[82] K. S. Novoselov, E. McCann, S. V. Morozov, V. I. Fal'ko, M. I. Katsnelson, U. Zeitler, D. Jiang, F. Schedin, and A. K. Geim, "Unconventional quantum hall effect and berry's phase of 2π in bilayer graphene," *Nature Physics*, vol. 2, no. 3, pp. 177–180, 2006, ISSN: 1745-2481. DOI: 10.1038/nphys245.

[83] Z. Qiao, S. A. Yang, W. Feng, W.-K. Tse, J. Ding, Y. Yao, J. Wang, and Q. Niu, "Quantum anomalous hall effect in graphene from rashba and exchange effects," *Phys. Rev. B*, vol. 82, p. 161 414, 16 2010. DOI: 10.1103/PhysRevB.82.161414.

[84] L. Zhang, Y. Zhang, J. Camacho, M. Khodas, and I. Zaliznyak, "The experimental observation of quantum hall effect of l=3 chiral quasiparticles in trilayer graphene," *Nature Physics*, vol. 7, no. 12, pp. 953–957, 2011, ISSN: 1745-2481. DOI: 10.1038/nphys2104.

[85] H. M. Price and N. R. Cooper, "Mapping the berry curvature from semiclassical dynamics in optical lattices," *Phys. Rev. A*, vol. 85, p. 033 620, 3 2012. DOI: 10.1103/PhysRevA.85.033620.

[86] A. F. Young, Y. Zhang, and P. Kim, "Experimental manifestation of berry phase in graphene," in *Physics of Graphene*, H. Aoki and M. S. Dresselhaus, Eds. Cham: Springer International Publishing, 2014, pp. 3–27, ISBN: 978-3-319-02633-6. DOI: 10.1007/978-3-319-02633-6_1.

[87] Z. Qiao, W. Ren, H. Chen, L. Bellaiche, Z. Zhang, A. H. MacDonald, and Q. Niu, "Quantum anomalous hall effect in graphene proximity coupled to an antiferromagnetic insulator," *Phys. Rev. Lett.*, vol. 112, p. 116 404, 11 2014. DOI: 10.1103/PhysRevLett.112.116404.

[88] A. Raoux, M. Morigi, J.-N. Fuchs, F. Piéchon, and G. Montambaux, "From dia- to paramagnetic orbital susceptibility of massless fermions," *Phys. Rev. Lett.*, vol. 112, p. 026 402, 2 2014. DOI: 10.1103/PhysRevLett.112.026402.

[89] D. Di Sante, A. Stroppa, P. Barone, M.-H. Whangbo, and S. Picozzi, "Emergence of ferroelectricity and spin-valley properties in two-dimensional honeycomb binary compounds," *Phys. Rev. B*, vol. 91, p. 161 401, 16 2015. DOI: 10.1103/PhysRevB.91.161401.

[90] L. Cai, M. Liu, S. Chen, Y. Liu, W. Shu, H. Luo, and S. Wen, "Quantized photonic spin hall effect in graphene," *Phys. Rev. A*, vol. 95, p. 013 809, 1 2017. DOI: 10.1103/PhysRevA.95.013809.

[91] C. Dutreix, H. González-Herrero, I. Brihuega, M. I. Katsnelson, C. Chapelier, and V. T. Renard, "Measuring the berry phase of graphene from wavefront dislocations in friedel oscillations," *Nature*, vol. 574, no. 7777, pp. 219–222, 2019, ISSN: 1476-4687. DOI: 10.1038/s41586-019-1613-5.

[92] S. Slizovskiy, E. McCann, M. Koshino, and V. I. Fal'ko, "Films of rhombohedral graphite as two-dimensional topological semimetals," *Communications Physics*, vol. 2, no. 1, p. 164, 2019, ISSN: 2399-3650. DOI: 10.1038/s42005-019-0268-8.

[93] Y. Zheng and T. Ando, "Hall conductivity of a two-dimensional graphite system," *Phys. Rev. B*, vol. 65, p. 245 420, 24 2002. DOI: 10.1103/PhysRevB.65.245420.

[94] K. S. Novoselov, A. K. Geim, S. V. Morozov, D. Jiang, M. I. Katsnelson, I. V. Grigorieva, S. V. Dubonos, and A. A. Firsov, "Two-dimensional gas of massless dirac fermions in graphene," *Nature*, vol. 438, no. 7065, pp. 197–200, 2005, ISSN: 1476-4687. DOI: 10.1038/nature04233.

[95] J.-C. Charlier, X. Blase, and S. Roche, "Electronic and transport properties of nanotubes," *Rev. Mod. Phys.*, vol. 79, pp. 677–732, 2 2007. DOI: 10.1103/RevModPhys.79.677.

[96] A. K. Geim and K. S. Novoselov, "The rise of graphene," *Nature Materials*, vol. 6, no. 3, pp. 183–191, 2007, ISSN: 1476-4660. DOI: 10.1038/nmat1849.

[97] M. Gmitra, S. Konschuh, C. Ertler, C. Ambrosch-Draxl, and J. Fabian, "Band-structure topologies of graphene: Spin-orbit coupling effects from first principles," *Phys. Rev. B*, vol. 80, p. 235 431, 23 2009. DOI: 10.1103/PhysRevB.80.235431.

[98] M. Mucha-Kruczynski, I. L. Aleiner, and V. I. Fal'ko, "Strained bilayer graphene: Band structure topology and landau level spectrum," *Phys. Rev. B*, vol. 84, p. 041 404, 4 2011. DOI: 10.1103/PhysRevB.84.041404.

[99] B. Rasche, A. Isaeva, M. Ruck, S. Borisenko, V. Zabolotnyy, B. Büchner, K. Koepernik, C. Ortix, M. Richter, and J. van den Brink, "Stacked topological insulator built from bismuth-based graphene sheet analogues," *Nature Materials*, vol. 12, no. 5, pp. 422–425, 2013, ISSN: 1476-4660. DOI: 10.1038/nmat3570.

[100] K. S. Kim, A. L. Walter, L. Moreschini, T. Seyller, K. Horn, E. Rotenberg, and A. Bostwick, "Coexisting massive and massless dirac fermions in symmetry-broken bilayer graphene," *Nature Materials*, vol. 12, no. 10, pp. 887–892, 2013, ISSN: 1476-4660. DOI: 10.1038/nmat3717.

[101] P. Ruffieux, S. Wang, B. Yang, C. Sánchez-Sánchez, J. Liu, T. Dienel, L. Talirz, P. Shinde, C. A. Pignedoli, D. Passerone, T. Dumslaff, X. Feng, K. Müllen, and R. Fasel, "On-surface synthesis of graphene nanoribbons with zigzag edge topology," *Nature*, vol. 531, no. 7595, pp. 489–492, 2016, ISSN: 1476-4687. DOI: 10.1038/nature17151.

[102] H. C. Po, L. Zou, T. Senthil, and A. Vishwanath, "Faithful tight-binding models and fragile topology of magic-angle bilayer graphene," *Phys. Rev. B*, vol. 99, p. 195 455, 19 2019. DOI: 10.1103/PhysRevB.99.195455.

[103] J. Liu, J. Liu, and X. Dai, "Pseudo landau level representation of twisted bilayer graphene: Band topology and implications on the correlated insulating phase," *Phys. Rev. B*, vol. 99, p. 155 415, 15 2019. DOI: 10.1103/PhysRevB.99.155415.

[104] F. Xie, Z. Song, B. Lian, and B. A. Bernevig, "Topology-bounded superfluid weight in twisted bilayer graphene," *Phys. Rev. Lett.*, vol. 124, p. 167 002, 16 2020. DOI: 10.1103/PhysRevLett.124.167002.

[105] B.-B. Chen, Y. D. Liao, Z. Chen, O. Vafek, J. Kang, W. Li, and Z. Y. Meng, "Realization of topological mott insulator in a twisted bilayer graphene lattice model," *Nature Communications*, vol. 12, no. 1, p. 5480, 2021, ISSN: 2041-1723. DOI: 10.1038/s41467-021-25438-1.

[106] P. R. Wallace, "The band theory of graphite," *Phys. Rev.*, vol. 71, pp. 622–634, 9 1947. DOI: 10.1103/PhysRev.71.622.

[107] D. P. DiVincenzo and E. J. Mele, "Self-consistent effective-mass theory for intralayer screening in graphite intercalation compounds," *Phys. Rev. B*, vol. 29, pp. 1685–1694, 4 1984. DOI: 10.1103/PhysRevB.29.1685.

[108] E. H. Ph.D., "Xviii. on the "rotational coefficient" in nickel and cobalt," *The London, Edinburgh, and Dublin Philosophical Magazine and Journal of Science*, vol. 12, no. 74, pp. 157–172, 1881. DOI: 10.1080/14786448108627086.

[109] R. Karplus and J. M. Luttinger, "Hall effect in ferromagnetics," *Phys. Rev.*, vol. 95, pp. 1154–1160, 5 1954. DOI: 10.1103/PhysRev.95.1154.

[110] M. Onoda and N. Nagaosa, "Quantized anomalous hall effect in two-dimensional ferromagnets: Quantum hall effect in metals," *Phys. Rev. Lett.*, vol. 90, p. 206 601, 20 2003. DOI: 10.1103/PhysRevLett.90.206601.

[111] C.-X. Liu, X.-L. Qi, X. Dai, Z. Fang, and S.-C. Zhang, "Quantum anomalous hall effect in $Hg_{1-y}Mn_yTe$ quantum wells," *Phys. Rev. Lett.*, vol. 101, p. 146 802, 14 2008. DOI: 10.1103/PhysRevLett.101.146802.

[112] C.-Z. Chang, J. Zhang, X. Feng, J. Shen, Z. Zhang, M. Guo, K. Li, Y. Ou, P. Wei, L.-L. Wang, Z.-Q. Ji, Y. Feng, S. Ji, X. Chen, J. Jia, X. Dai, Z. Fang, S.-C. Zhang, K. He, Y. Wang, L. Lu, X.-C. Ma, and Q.-K. Xue, "Experimental observation of the quantum anomalous hall effect in a magnetic topological insulator," *Science*, vol. 340, no. 6129, pp. 167–170, 2013. DOI: 10.1126/science.1234414.

[113] U. Englich, C. Frommen, and W. Massa, "Jahn-teller ordering in kagome-type layers of compounds $A_2A'Mn_3^{III}F_{12}$ (A = Rb, Cs; A = Li, Na, K)," *Journal of Alloys and Compounds*, vol. 246, no. 1, pp. 155–165, 1997, ISSN: 0925-8388. DOI: https://doi.org/10.1016/S0925-8388(96)02478-4.

[114] M. P. Shores, E. A. Nytko, B. M. Bartlett, and D. G. Nocera, "A structurally perfect s = 1/2 kagomé antiferromagnet," *Journal of the American Chemical Society*, vol. 127, no. 39, pp. 13 462–13 463, 2005, PMID: 16190686. DOI: 10.1021/ja053891p.

[115] Y.-p. Wang, W.-x. Ji, C.-w. Zhang, P. Li, P.-j. Wang, B. Kong, S.-s. Li, S.-s. Yan, and K. Liang, "Discovery of intrinsic quantum anomalous hall effect in organic mn-dca lattice," *Applied Physics Letters*, vol. 110, no. 23, p. 233 107, 2017. DOI: 10.1063/1.4985144.

[116] J.-X. Yin, S. S. Zhang, H. Li, K. Jiang, G. Chang, B. Zhang, B. Lian, C. Xiang, I. Belopolski, H. Zheng, T. A. Cochran, S.-Y. Xu, G. Bian, K. Liu, T.-R. Chang, H. Lin, Z.-Y. Lu, Z. Wang, S. Jia, W. Wang, and M. Z. Hasan, "Giant and anisotropic many-body spin–orbit tunability in a strongly correlated kagome magnet," *Nature*, vol. 562, no. 7725, pp. 91–95, 2018, ISSN: 1476-4687. DOI: 10.1038/s41586-018-0502-7.

[117] A Mielke, "Ferromagnetic ground states for the hubbard model on line graphs," *Journal of Physics A: Mathematical and General*, vol. 24, no. 2, pp. L73–L77, 1991. DOI: 10.1088/0305-4470/24/2/005.

[118] A Mielke, "Exact ground states for the hubbard model on the kagome lattice," *Journal of Physics A: Mathematical and General*, vol. 25, no. 16, pp. 4335–4345, 1992. DOI: 10.1088/0305-4470/25/16/011.

[119] M. Di Ventra, *Electrical Transport in Nanoscale Systems*. Cambridge University Press, 2008. DOI: 10.1017/CBO9780511755606.

[120] Y. Hatsugai, "Chern number and edge states in the integer quantum hall effect," *Phys. Rev. Lett.*, vol. 71, pp. 3697–3700, 22 1993. DOI: 10.1103/PhysRevLett.71.3697.

[121] X.-L. Qi, Y.-S. Wu, and S.-C. Zhang, "General theorem relating the bulk topological number to edge states in two-dimensional insulators," *Phys. Rev. B*, vol. 74, p. 045 125, 4 2006. DOI: 10.1103/PhysRevB.74.045125.

[122] R. Resta and D. Vanderbilt, "Theory of polarization: A modern approach," in *Physics of Ferroelectrics: A Modern Perspective*. Berlin, Heidelberg: Springer Berlin Heidelberg, 2007, pp. 31–68, ISBN: 978-3-540-34591-6. DOI: 10.1007/978-3-540-34591-6_2.

[123] R. D. King-Smith and D. Vanderbilt, "Theory of polarization of crystalline solids," *Phys. Rev. B*, vol. 47, pp. 1651–1654, 3 1993. DOI: 10.1103/PhysRevB.47.1651.

[124] E. Blount, "Formalisms of band theory," in ser. Solid State Physics, F. Seitz and D. Turnbull, Eds., vol. 13, Academic Press, 1962, pp. 305–373. DOI: https://doi.org/10.1016/S0081-1947(08)60459-2.

[125] R. Resta, M. Posternak, and A. Baldereschi, "Towards a quantum theory of polarization in ferroelectrics: The case of $KNbO_3$," *Phys. Rev. Lett.*, vol. 70, pp. 1010–1013, 7 1993. DOI: 10.1103/PhysRevLett.70.1010.

[126] G. Sághi-Szabó, R. E. Cohen, and H. Krakauer, "First-principles study of piezoelectricity in tetragonal $PbTiO_3$ and $PbZr_{1/2}Ti_{1/2}O_3$," *Phys. Rev. B*, vol. 59, pp. 12 771–12 776, 20 1999. DOI: 10.1103/PhysRevB.59.12771.

[127] D. Berlincourt and H. H. A. Krueger, "Domain processes in lead titanate zirconate and barium titanate ceramics," *Journal of Applied Physics*, vol. 30, no. 11, pp. 1804–1810, 1959. DOI: 10.1063/1.1735059.

[128] R. Wahl, D. Vogtenhuber, and G. Kresse, "$SrTiO_3$ And $BaTiO_3$ revisited using the projector augmented wave method: Performance of hybrid and semilocal functionals," *Phys. Rev. B*, vol. 78, p. 104 116, 10 2008. DOI: 10.1103/PhysRevB.78.104116.

[129] J. E. Hirsch, "Spin hall effect," *Phys. Rev. Lett.*, vol. 83, pp. 1834–1837, 9 1999. DOI: 10.1103/PhysRevLett.83.1834.

[130] J. Sinova, D. Culcer, Q. Niu, N. A. Sinitsyn, T. Jungwirth, and A. H. MacDonald, "Universal intrinsic spin hall effect," *Phys. Rev. Lett.*, vol. 92, p. 126 603, 12 2004. DOI: 10.1103/PhysRevLett.92.126603.

[131] C.-X. Liu, S.-C. Zhang, and X.-L. Qi, "The quantum anomalous hall effect: Theory and experiment," *Annual Review of Condensed Matter Physics*, vol. 7, no. 1, pp. 301–321, 2016. DOI: 10.1146/annurev-conmatphys-031115-011417.

[132] M. Onoda and N. Nagaosa, "Topological nature of anomalous hall effect in ferromagnets," *Journal of the Physical Society of Japan*, vol. 71, no. 1, pp. 19–22, 2002. DOI: 10.1143/JPSJ.71.19.

[133] D. Bohm, "Quantum theory," in Prentice Hall, 1951.

[134] H. Min, J. E. Hill, N. A. Sinitsyn, B. R. Sahu, L. Kleinman, and A. H. MacDonald, "Intrinsic and rashba spin-orbit interactions in graphene sheets," *Phys. Rev. B*, vol. 74, p. 165 310, 16 2006. DOI: 10.1103/PhysRevB.74.165310.

[135] Y. Yao, F. Ye, X.-L. Qi, S.-C. Zhang, and Z. Fang, "Spin-orbit gap of graphene: First-principles calculations," *Phys. Rev. B*, vol. 75, p. 041 401, 4 2007. DOI: 10.1103/PhysRevB.75.041401.

[136] S. H. Groves, R. N. Brown, and C. R. Pidgeon, "Interband magnetoreflection and band structure of hgte," *Phys. Rev.*, vol. 161, pp. 779–793, 3 1967. DOI: 10.1103/PhysRev.161.779.

[137] A. Moritani, K. Taniguchi, C. Hamaguchi, and J. Nakai, "Electroreflectance study of cdxhg1-xte," *Journal of the Physical Society of Japan*, vol. 34, no. 1, pp. 79–88, 1973. DOI: 10.1143/JPSJ.34.79.

[138] B. S. Ralf Dornhaus Günter Nimtz, "Narrow-gap semiconductors," in Springer Berlin, Heidelberg, 1983.

[139] M. König, H. Buhmann, L. W. Molenkamp, T. Hughes, C.-X. Liu, X.-L. Qi, and S.-C. Zhang, "The quantum spin hall effect: Theory and experiment," *Journal of the Physical Society of Japan*, vol. 77, no. 3, p. 031 007, 2008. DOI: 10.1143/JPSJ.77.031007.

[140] B. Büttner, C. X. Liu, G. Tkachov, E. G. Novik, C. Brüne, H. Buhmann, E. M. Hankiewicz, P. Recher, B. Trauzettel, S. C. Zhang, and L. W. Molenkamp, "Single valley dirac fermions in zero-gap hgte quantum wells," *Nature Physics*, vol. 7, no. 5, pp. 418–422, 2011. DOI: 10.1038/nphys1914.

[141] C. Brüne, A. Roth, H. Buhmann, E. M. Hankiewicz, L. W. Molenkamp, J. Maciejko, X.-L. Qi, and S.-C. Zhang, "Spin polarization of the quantum spin hall edge states," *Nature Physics*, vol. 8, no. 6, pp. 485–490, 2012. DOI: 10.1038/nphys2322.

[142] S. Murakami, N. Nagaosa, and S.-C. Zhang, "Dissipationless quantum spin current at room temperature," *Science*, vol. 301, no. 5638, pp. 1348–1351, 2003. DOI: 10.1126/science.1087128.

[143] S. Murakami, N. Nagaosa, and S.-C. Zhang, "Spin-hall insulator," *Phys. Rev. Lett.*, vol. 93, p. 156 804, 15 2004. DOI: 10.1103/PhysRevLett.93.156804.

[144] C. L. Kane and E. J. Mele, "Z_2 Topological order and the quantum spin hall effect," *Phys. Rev. Lett.*, vol. 95, p. 146 802, 14 2005. DOI: 10.1103/PhysRevLett.95.146802.

[145] J. E. Moore and L. Balents, "Topological invariants of time-reversal-invariant band structures," *Phys. Rev. B*, vol. 75, p. 121 306, 12 2007. DOI: 10.1103/PhysRevB.75.121306.

[146] X.-L. Qi, T. L. Hughes, and S.-C. Zhang, "Topological field theory of time-reversal invariant insulators," *Phys. Rev. B*, vol. 78, p. 195 424, 19 2008. DOI: 10.1103/PhysRevB.78.195424.

[147] R. Roy, "Z_2 Classification of quantum spin hall systems: An approach using time-reversal invariance," *Phys. Rev. B*, vol. 79, p. 195 321, 19 2009. DOI: 10.1103/PhysRevB.79.195321.

[148] Z. Wang, X.-L. Qi, and S.-C. Zhang, "Equivalent topological invariants of topological insulators," *New Journal of Physics*, vol. 12, no. 6, p. 065 007, 2010. DOI: 10.1088/1367-2630/12/6/065007.

[149] M. C. Rechtsman, J. M. Zeuner, Y. Plotnik, Y. Lumer, D. Podolsky, F. Dreisow, S. Nolte, M. Segev, and A. Szameit, "Photonic floquet topological insulators," *Nature*, vol. 496, no. 7444, pp. 196–200, 2013. DOI: 10.1038/nature12066.

[150] G. Jotzu, M. Messer, R. Desbuquois, M. Lebrat, T. Uehlinger, D. Greif, and T. Esslinger, "Experimental realization of the topological haldane model with ultracold fermions," *Nature*, vol. 515, no. 7526, pp. 237–240, 2014, ISSN: 1476-4687. DOI: 10.1038/nature13915.

[151] T. Oka and H. Aoki, "Photovoltaic hall effect in graphene," *Phys. Rev. B*, vol. 79, p. 081 406, 8 2009. DOI: 10.1103/PhysRevB.79.081406.

[152] W. Zheng and H. Zhai, "Floquet topological states in shaking optical lattices," *Phys. Rev. A*, vol. 89, p. 061 603, 6 2014. DOI: 10.1103/PhysRevA.89.061603.

[153] A. Eckardt and E. Anisimovas, "High-frequency approximation for periodically driven quantum systems from a floquet-space perspective," *New Journal of Physics*, vol. 17, no. 9, p. 093 039, 2015. DOI: 10.1088/1367-2630/17/9/093039.

[154] K. Plekhanov, G. Roux, and K. Le Hur, "Floquet engineering of haldane chern insulators and chiral bosonic phase transitions," *Phys. Rev. B*, vol. 95, p. 045 102, 4 2017. DOI: 10.1103/PhysRevB.95.045102.

[155] C.-Z. Chang, C.-X. Liu, and A. H. MacDonald, "Colloquium: Quantum anomalous hall effect," in arXiv, 2022.

[156] M. Aidelsburger, M. Lohse, C. Schweizer, M. Atala, J. T. Barreiro, S. Nascimbène, N. R. Cooper, I. Bloch, and N. Goldman, "Measuring the chern number of hofstadter bands with ultracold bosonic atoms," *Nature Physics*, vol. 11, no. 2, pp. 162–166, 2015, ISSN: 1745-2481. DOI: 10.1038/nphys3171.

[157] M. Atala, M. Aidelsburger, J. T. Barreiro, D. Abanin, T. Kitagawa, E. Demler, and I. Bloch, "Direct measurement of the zak phase in topological bloch bands," *Nature Physics*, vol. 9, no. 12, pp. 795–800, 2013. DOI: 10.1038/nphys2790.

[158] L. Duca, T. Li, M. Reitter, I. Bloch, M. Schleier-Smith, and U. Schneider, "An aharonov-bohm interferometer for determining bloch band topology," *Science*, vol. 347, no. 6219, pp. 288–292, 2015. DOI: 10.1126/science.1259052.

[159] T. Li, L. Duca, M. Reitter, F. Grusdt, E. Demler, M. Endres, M. Schleier-Smith, I. Bloch, and U. Schneider, "Bloch state tomography using wilson lines," *Science*, vol. 352, no. 6289, pp. 1094–1097, 2016. DOI: 10.1126/science.aad5812.

[160] B. K. Stuhl, H.-I. Lu, L. M. Aycock, D. Genkina, and I. B. Spielman, "Visualizing edge states with an atomic bose gas in the quantum hall regime," *Science*, vol. 349, no. 6255, pp. 1514–1518, 2015. DOI: 10.1126/science.aaa8515.

[161] M. Mancini, G. Pagano, G. Cappellini, L. Livi, M. Rider, J. Catani, C. Sias, P. Zoller, M. Inguscio, M. Dalmonte, and L. Fallani, "Observation of chiral edge states with neutral fermions in synthetic hall ribbons," *Science*, vol. 349, no. 6255, pp. 1510–1513, 2015. DOI: 10.1126/science.aaa8736.

[162] N. Fläschner, B. S. Rem, M. Tarnowski, D. Vogel, D.-S. Lühmann, K. Sengstock, and C. Weitenberg, "Experimental reconstruction of the berry curvature in a floquet bloch band," *Science*, vol. 352, no. 6289, pp. 1091–1094, 2016. DOI: 10.1126/science.aad4568.

[163] J. W. McIver, D. Hsieh, H. Steinberg, P. Jarillo-Herrero, and N. Gedik, "Control over topological insulator photocurrents with light polarization," *Nature Nanotechnology*, vol. 7, no. 2, pp. 96–100, 2012. DOI: 10.1038/nnano.2011.214.

[164] F. de Juan, A. G. Grushin, T. Morimoto, and J. E. Moore, "Quantized circular photogalvanic effect in weyl semimetals," *Nature Communications*, vol. 8, no. 1, p. 15 995, 2017. DOI: 10.1038/ncomms15995.

[165] D. T. Tran, A. Dauphin, A. G. Grushin, P. Zoller, and N. Goldman, "Probing topology by "heating": Quantized circular dichroism in ultracold atoms," *Science Advances*, vol. 3, no. 8, e1701207, 2017. DOI: 10.1126/sciadv.1701207.

[166] L. Asteria, D. T. Tran, T. Ozawa, M. Tarnowski, B. S. Rem, N. Fläschner, K. Sengstock, N. Goldman, and C. Weitenberg, "Measuring quantized circular dichroism in ultracold topological matter," *Nature Physics*, vol. 15, no. 5, pp. 449–454, 2019. DOI: 10.1038/s41567-019-0417-8.

[167] D. Rees, K. Manna, B. Lu, T. Morimoto, H. Borrmann, C. Felser, J. E. Moore, D. H. Torchinsky, and J. Orenstein, "Helicity-dependent photocurrents in the chiral weyl semimetal rhsi," *Science Advances*, vol. 6, no. 29, eaba0509, 2020. DOI: 10.1126/sciadv.aba0509.

[168] P. W. Klein, A. G. Grushin, and K. Le Hur, "Interacting stochastic topology and mott transition from light response," *Phys. Rev. B*, vol. 103, p. 035 114, 3 2021. DOI: 10.1103/PhysRevB.103.035114.

[169] K. Le Hur, "Global and local topological quantized responses from geometry, light, and time," *Phys. Rev. B*, vol. 105, p. 125 106, 12 2022. DOI: 10.1103/PhysRevB.105.125106.

[170] F. D. M. Haldane and S. Raghu, "Possible realization of directional optical waveguides in photonic crystals with broken time-reversal symmetry," *Phys. Rev. Lett.*, vol. 100, p. 013 904, 1 2008. DOI: 10.1103/PhysRevLett.100.013904.

[171] S. Raghu and F. D. M. Haldane, "Analogs of quantum-hall-effect edge states in photonic crystals," *Phys. Rev. A*, vol. 78, p. 033 834, 3 2008. DOI: 10.1103/PhysRevA.78.033834.

[172] Z. Wang, Y. D. Chong, J. D. Joannopoulos, and M. Soljačić, "Reflection-free one-way edge modes in a gyromagnetic photonic crystal," *Phys. Rev. Lett.*, vol. 100, p. 013 905, 1 2008. DOI: 10.1103/PhysRevLett.100.013905.

[173] Z. Wang, Y. Chong, J. D. Joannopoulos, and M. Soljačić, "Observation of unidirectional backscattering-immune topological electromagnetic states," *Nature*, vol. 461, no. 7265, pp. 772–775, 2009. DOI: 10.1038/nature08293.

[174] S. Mukherjee, A. Spracklen, M. Valiente, E. Andersson, P. Öhberg, N. Goldman, and R. R. Thomson, "Experimental observation of anomalous topological edge modes in a slowly driven photonic lattice," *Nature Communications*, vol. 8, no. 1, p. 13 918, 2017. DOI: 10.1038/ncomms13918.

[175] L. J. Maczewsky, J. M. Zeuner, S. Nolte, and A. Szameit, "Observation of photonic anomalous floquet topological insulators," *Nature Communications*, vol. 8, no. 1, p. 13 756, 2017. DOI: 10.1038/ncomms13756.

[176] R. Fleury, D. L. Sounas, C. F. Sieck, M. R. Haberman, and A. Alù, "Sound isolation and giant linear nonreciprocity in a compact acoustic circulator," *Science*, vol. 343, no. 6170, pp. 516–519, 2014. DOI: 10.1126/science.1246957.

[177] S. Kim, X. Xu, J. M. Taylor, and G. Bahl, "Dynamically induced robust phonon transport and chiral cooling in an optomechanical system," *Nature Communications*, vol. 8, no. 1, p. 205, 2017. DOI: 10.1038/s41467-017-00247-7.

[178] B. M. Anderson, R. Ma, C. Owens, D. I. Schuster, and J. Simon, "Engineering topological many-body materials in microwave cavity arrays," *Phys. Rev. X*, vol. 6, p. 041 043, 4 2016. DOI: 10.1103/PhysRevX.6.041043.

[179] C. Owens, A. LaChapelle, B. Saxberg, B. M. Anderson, R. Ma, J. Simon, and D. I. Schuster, "Quarter-flux hofstadter lattice in a qubit-compatible microwave cavity array," *Phys. Rev. A*, vol. 97, p. 013 818, 1 2018. DOI: 10.1103/PhysRevA.97.013818.

[180] K. Le Hur, L. Henriet, A. Petrescu, K. Plekhanov, G. Roux, and M. Schiró, "Many-body quantum electrodynamics networks: Non-equilibrium condensed matter physics with light," *Comptes Rendus Physique*, vol. 17, no. 8, pp. 808–835, 2016, Polariton physics / Physique des polaritons, ISSN: 1631-0705. DOI: https://doi.org/10.1016/j.crhy.2016.05.003.

[181] X. Gu, A. F. Kockum, A. Miranowicz, Y. xi Liu, and F. Nori, "Microwave photonics with superconducting quantum circuits," *Physics Reports*, vol. 718-719, pp. 1–102, 2017, Microwave photonics with superconducting quantum circuits, ISSN: 0370-1573. DOI: https://doi.org/10.1016/j.physrep.2017.10.002.

[182] P. Roushan *et al.*, "Chiral ground-state currents of interacting photons in a synthetic magnetic field," *Nature Physics*, vol. 13, pp. 146–151, 2 2017. DOI: 10.1038/nphys3930.

[183] S. Mittal, J. Fan, S. Faez, A. Migdall, J. M. Taylor, and M. Hafezi, "Topologically robust transport of photons in a synthetic gauge field," *Phys. Rev. Lett.*, vol. 113, p. 087 403, 8 2014. DOI: 10.1103/PhysRevLett.113.087403.

[184] D. L. Underwood, W. E. Shanks, J. Koch, and A. A. Houck, "Low-disorder microwave cavity lattices for quantum simulation with photons," *Phys. Rev. A*, vol. 86, p. 023 837, 2 2012. DOI: 10.1103/PhysRevA.86.023837.

[185] M. J. Hartmann, "Quantum simulation with interacting photons," *Journal of Optics*, vol. 18, no. 10, p. 104 005, 2016. DOI: 10.1088/2040-8978/18/10/104005.

[186] G. W. Semenoff, "Condensed-matter simulation of a three-dimensional anomaly," *Phys. Rev. Lett.*, vol. 53, pp. 2449–2452, 26 1984. DOI: 10.1103/PhysRevLett.53.2449.

[187] M. Hafezi, E. A. Demler, M. D. Lukin, and J. M. Taylor, "Robust optical delay lines with topological protection," *Nature Physics*, vol. 7, no. 11, pp. 907–912, 2011. DOI: 10.1038/nphys2063.

[188] I. Titvinidze, J. Legendre, M. Grothus, B. Irsigler, K. Le Hur, and W. Hofstetter, "Spin-orbit coupling in the kagome lattice with flux and time-reversal symmetry," *Phys. Rev. B*, vol. 103, p. 195 105, 19 2021. DOI: 10.1103/PhysRevB.103.195105.

[189] D. N. Sheng, Z. Y. Weng, L. Sheng, and F. D. M. Haldane, "Quantum spin-hall effect and topologically invariant chern numbers," *Phys. Rev. Lett.*, vol. 97, p. 036 808, 3 2006. DOI: 10.1103/PhysRevLett.97.036808.

[190] L. Fu and C. L. Kane, "Topological insulators with inversion symmetry," *Phys. Rev. B*, vol. 76, p. 045 302, 4 2007. DOI: 10.1103/PhysRevB.76.045302.

[191] T. Fukui, Y. Hatsugai, and H. Suzuki, "Chern numbers in discretized brillouin zone: Efficient method of computing (spin) hall conductances," *Journal of the Physical Society of Japan*, vol. 74, no. 6, pp. 1674–1677, 2005. DOI: 10.1143/JPSJ.74.1674.

[192] J.-X. Yin, W. Ma, T. A. Cochran, X. Xu, S. S. Zhang, H.-J. Tien, N. Shumiya, G. Cheng, K. Jiang, B. Lian, Z. Song, G. Chang, I. Belopolski, D. Multer, M. Litskevich, Z.-J. Cheng, X. P. Yang, B. Swidler, H. Zhou, H. Lin, T. Neupert, Z. Wang, N. Yao, T.-R. Chang, S. Jia, and M. Zahid Hasan, "Quantum-limit chern topological magnetism in tbmn6sn6," *Nature*, vol. 583, no. 7817, pp. 533–536, 2020. DOI: 10.1038/s41586-020-2482-7.

[193] J. Legendre and K. Le Hur, "Magnetic topological kagome systems," *Phys. Rev. Research*, vol. 2, p. 022 043, 2 2020. DOI: 10.1103/PhysRevResearch.2.022043.

[194] M. Chang and Q. Niu, "Berry phase, hyperorbits, and the hofstadter spectrum," *Phys. Rev. Lett.*, vol. 75, pp. 1348–1351, 7 1995. DOI: 10.1103/PhysRevLett.75.1348.

[195] K. Ohgushi, S. Murakami, and N. Nagaosa, "Spin anisotropy and quantum hall effect in the kagomé lattice: Chiral spin state based on a ferromagnet," *Phys. Rev. B*, vol. 62, R6065–R6068, 10 2000. DOI: 10.1103/PhysRevB.62.R6065.

[196] J. Zou, Z. He, and G. Xu, "The study of magnetic topological semimetals by first principles calculations," *npj Computational Materials*, vol. 5, no. 1, p. 96, 2019, ISSN: 2057-3960. DOI: 10.1038/s41524-019-0237-5.

[197] V. Y. Irkhin and Y. N. Skryabin, "Topological phase transitions in strongly correlated systems: Application to co3sn2s2," *JETP Letters*, vol. 114, no. 9, pp. 551–555, 2021, ISSN: 1090-6487. DOI: 10.1134/S0021364021210013.

[198] A. Rossi, V. Ivanov, S. Sreedhar, A. L. Gross, Z. Shen, E. Rotenberg, A. Bostwick, C. Jozwiak, V. Taufour, S. Y. Savrasov, and I. M. Vishik, "Electronic structure and topology across T_c in the magnetic weyl semimetal $Co_3Sn_2S_2$," *Phys. Rev. B*, vol. 104, p. 155 115, 15 2021. DOI: 10.1103/PhysRevB.104.155115.

[199] D. F. Liu, E. K. Liu, Q. N. Xu, J. L. Shen, Y. W. Li, D. Pei, A. J. Liang, P. Dudin, T. K. Kim, C. Cacho, Y. F. Xu, Y. Sun, L. X. Yang, Z. K. Liu, C. Felser, S. S. P. Parkin, and Y. L. Chen, "Direct observation of the spin–orbit coupling effect in magnetic weyl semimetal co3sn2s2," *npj Quantum Materials*, vol. 7, no. 1, p. 11, 2022. DOI: 10.1038/s41535-021-00392-9.

[200] A. B. Harris, C. Kallin, and A. J. Berlinsky, "Possible néel orderings of the kagomé antiferromagnet," *Phys. Rev. B*, vol. 45, pp. 2899–2919, 6 1992. DOI: 10.1103/PhysRevB.45.2899.

[201] A. Chubukov, "Order from disorder in a kagomé antiferromagnet," *Phys. Rev. Lett.*, vol. 69, pp. 832–835, 5 1992. DOI: 10.1103/PhysRevLett.69.832.

[202] J. N. Reimers and A. J. Berlinsky, "Order by disorder in the classical heisenberg kagomé antiferromagnet," *Phys. Rev. B*, vol. 48, pp. 9539–9554, 13 1993. DOI: 10.1103/PhysRevB.48.9539.

[203] J. T. Chalker, P. C. W. Holdsworth, and E. F. Shender, "Hidden order in a frustrated system: Properties of the heisenberg kagomé antiferromagnet," *Phys. Rev. Lett.*, vol. 68, pp. 855–858, 6 1992. DOI: 10.1103/PhysRevLett.68.855.

[204] S. Sachdev, "Kagome´- and triangular-lattice heisenberg antiferromagnets: Ordering from quantum fluctuations and quantum-disordered ground states with unconfined bosonic spinons," *Phys. Rev. B*, vol. 45, pp. 12 377–12 396, 21 1992. DOI: 10.1103/PhysRevB.45.12377.

[205] D. A. Huse and A. D. Rutenberg, "Classical antiferromagnets on the kagomé lattice," *Phys. Rev. B*, vol. 45, pp. 7536–7539, 13 1992. DOI: 10.1103/PhysRevB.45.7536.

[206] P. Lecheminant, B. Bernu, C. Lhuillier, L. Pierre, and P. Sindzingre, "Order versus disorder in the quantum heisenberg antiferromagnet on the kagomé lattice using exact spectra analysis," *Phys. Rev. B*, vol. 56, pp. 2521–2529, 5 1997. DOI: 10.1103/PhysRevB.56.2521.

[207] C. Waldtmann, H. U. Everts, B. Bernu, C. Lhuillier, P. Sindzingre, P. Lecheminant, and L. Pierre, "First excitations of the spin 1/2 heisenberg antiferromagnet on the kagomé lattice," *The European Physical Journal B - Condensed Matter and Complex Systems*, vol. 2, no. 4, pp. 501–507, 1998. DOI: 10.1007/s100510050274.

[208] J. Schulenburg, A. Honecker, J. Schnack, J. Richter, and H.-J. Schmidt, "Macroscopic magnetization jumps due to independent magnons in frustrated quantum spin lattices," *Phys. Rev. Lett.*, vol. 88, p. 167 207, 16 2002. DOI: 10.1103/PhysRevLett.88.167207.

[209] G. Misguich, D. Serban, and V. Pasquier, "Quantum dimer model with extensive ground-state entropy on the kagome lattice," *Phys. Rev. B*, vol. 67, p. 214 413, 21 2003. DOI: 10.1103/PhysRevB.67.214413.

[210] D. C. Cabra, M. D. Grynberg, P. C. W. Holdsworth, A. Honecker, P. Pujol, J. Richter, D. Schmalfuß, and J. Schulenburg, "Quantum kagomé antiferromagnet in a magnetic field: Low-lying nonmagnetic excitations versus valence-bond crystal order," *Phys. Rev. B*, vol. 71, p. 144 420, 14 2005. DOI: 10.1103/PhysRevB.71.144420.

[211] K. Essafi, O. Benton, and L. D. C. Jaubert, "A kagome map of spin liquids from xxz to dzyaloshinskii–moriya ferromagnet," *Nature Communications*, vol. 7, no. 1, p. 10 297, 2016. DOI: 10.1038/ncomms10297.

[212] S. Depenbrock, I. P. McCulloch, and U. Schollwöck, "Nature of the spin-liquid ground state of the $S = 1/2$ heisenberg model on the kagome lattice," *Phys. Rev. Lett.*, vol. 109, p. 067 201, 6 2012. DOI: 10.1103/PhysRevLett.109.067201.

[213] Y. Iqbal, F. Becca, and D. Poilblanc, "Projected wave function study of $\mathbb{Z}_2$ spin liquids on the kagome lattice for the spin-$\frac{1}{2}$ quantum heisenberg antiferromagnet," *Phys. Rev. B*, vol. 84, p. 020 407, 2 2011. DOI: 10.1103/PhysRevB.84.020407.

[214] M. Hermele, Y. Ran, P. A. Lee, and X.-G. Wen, "Properties of an algebraic spin liquid on the kagome lattice," *Phys. Rev. B*, vol. 77, p. 224 413, 22 2008. DOI: 10.1103/PhysRevB.77.224413.

[215] S. Yan, D. A. Huse, and S. R. White, "Spin-liquid ground state of the $S = 1/2$ kagome heisenberg antiferromagnet," *Science*, vol. 332, no. 6034, pp. 1173–1176, 2011. DOI: 10.1126/science.1201080.

[216] H. D. Rosales, F. A. G. Albarracín, and P. Pujol, "From frustrated magnetism to spontaneous chern insulators," *Phys. Rev. B*, vol. 99, p. 035 163, 3 2019. DOI: 10.1103/PhysRevB.99.035163.

[217] S. Capponi, O. Derzhko, A. Honecker, A. M. Läuchli, and J. Richter, "Numerical study of magnetization plateaus in the spin-$\frac{1}{2}$ kagome heisenberg antiferromagnet," *Phys. Rev. B*, vol. 88, p. 144 416, 14 2013. DOI: 10.1103/PhysRevB.88.144416.

[218] K. Kumar, H. J. Changlani, B. K. Clark, and E. Fradkin, "Numerical evidence for a chiral spin liquid in the xxz antiferromagnetic heisenberg model on the kagome lattice at $m = \frac{2}{3}$ magnetization," *Phys. Rev. B*, vol. 94, p. 134 410, 13 2016. DOI: 10.1103/PhysRevB.94.134410.

[219] S. Nishimoto, N. Shibata, and C. Hotta, "Controlling frustrated liquids and solids with an applied field in a kagome heisenberg antiferromagnet," *Nature Communications*, vol. 4, no. 1, p. 2287, 2013. DOI: 10.1038/ncomms3287.

[220] H. J. Changlani, D. Kochkov, K. Kumar, B. K. Clark, and E. Fradkin, "Macroscopically degenerate exactly solvable point in the spin-1/2 kagome quantum antiferromagnet," *Phys. Rev. Lett.*, vol. 120, p. 117 202, 11 2018. DOI: 10.1103/PhysRevLett.120.117202.

[221] C. Zener, "Interaction between the d-shells in the transition metals. ii. ferromagnetic compounds of manganese with perovskite structure," *Phys. Rev.*, vol. 82, pp. 403–405, 3 1951. DOI: 10.1103/PhysRev.82.403.

[222] V. I. Anisimov, M. A. Korotin, M. Zölfl, T. Pruschke, K. Le Hur, and T. M. Rice, "Electronic structure of the heavy fermion metal LiV_2O_4," *Phys. Rev. Lett.*, vol. 83, pp. 364–367, 2 1999. DOI: 10.1103/PhysRevLett.83.364.

[223] P. W. Anderson and H. Hasegawa, "Considerations on double exchange," *Phys. Rev.*, vol. 100, pp. 675–681, 2 1955. DOI: 10.1103/PhysRev.100.675.

[224] P. G. de Gennes, "Effects of double exchange in magnetic crystals," *Phys. Rev.*, vol. 118, pp. 141–154, 1 1960. DOI: 10.1103/PhysRev.118.141.

[225] E. Kogan and M. Auslender, "Paramagnetic-ferromagnetic transition in a double-exchange model," *Phys. Rev. B*, vol. 67, p. 132 410, 13 2003. DOI: 10.1103/PhysRevB.67.132410.

[226] V.-N. Phan and M.-T. Tran, "Doping change and distortion effect on double-exchange ferromagnetism," *Phys. Rev. B*, vol. 72, p. 214 418, 21 2005. DOI: 10.1103/PhysRevB.72.214418.

[227] Nozières, P. and Lewiner, C., "A simple theory of the anomalous hall effect in semiconductors," *J. Phys. France*, vol. 34, no. 10, pp. 901–915, 1973. DOI: 10.1051/jphys:019730034010090100.

[228] E. Tang, J.-W. Mei, and X.-G. Wen, "High-temperature fractional quantum hall states," *Phys. Rev. Lett.*, vol. 106, p. 236 802, 23 2011. DOI: 10.1103/PhysRevLett.106.236802.

[229] W. Schnelle, A. Leithe-Jasper, H. Rosner, F. M. Schappacher, R. Pöttgen, F. Pielnhofer, and R. Weihrich, "Ferromagnetic ordering and half-metallic state of $sn_2co_3s_2$ with the shandite-type structure," *Phys. Rev. B*, vol. 88, p. 144 404, 14 2013. DOI: 10.1103/PhysRevB.88.144404.

[230] N. D. Mermin and H. Wagner, "Absence of ferromagnetism or antiferromagnetism in one- or two-dimensional isotropic heisenberg models," *Phys. Rev. Lett.*, vol. 17, pp. 1133–1136, 22 1966. DOI: 10.1103/PhysRevLett.17.1133.

[231] Y. S. Dedkov, M Holder, S. L. Molodtsov, and H Rosner, "Electronic structure of shandite $Co_3Sn_2S_2$," *Journal of Physics: Conference Series*, vol. 100, no. 7, p. 072 011, 2008. DOI: 10.1088/1742-6596/100/7/072011.

[232] M. Holder, Y. S. Dedkov, A. Kade, H. Rosner, W. Schnelle, A. Leithe-Jasper, R. Weihrich, and S. L. Molodtsov, "Photoemission study of electronic structure of the half-metallic ferromagnet $Co_3Sn_2S_2$," *Phys. Rev. B*, vol. 79, p. 205 116, 20 2009. DOI: 10.1103/PhysRevB.79.205116.

[233] C. Zeng and V. Elser, "Numerical studies of antiferromagnetism on a kagomé net," *Phys. Rev. B*, vol. 42, pp. 8436–8444, 13 1990. DOI: 10.1103/PhysRevB.42.8436.

[234] J. N. Reimers, A. J. Berlinsky, and A.-C. Shi, "Mean-field approach to magnetic ordering in highly frustrated pyrochlores," *Phys. Rev. B*, vol. 43, pp. 865–878, 1 1991. DOI: 10.1103/PhysRevB.43.865.

[235] I. Ritchey, P. Chandra, and P. Coleman, "Spin folding in the two-dimensional heisenberg kagomé antiferromagnet," *Phys. Rev. B*, vol. 47, pp. 15 342–15 345, 22 1993. DOI: 10.1103/PhysRevB.47.15342.

[236] P. W. Leung and V. Elser, "Numerical studies of a 36-site kagome´ antiferromagnet," *Phys. Rev. B*, vol. 47, pp. 5459–5462, 9 1993. DOI: 10.1103/PhysRevB.47.5459.

[237] A. M. Läuchli, J. Sudan, and E. S. Sørensen, "Ground-state energy and spin gap of spin-$\frac{1}{2}$ kagomé-heisenberg antiferromagnetic clusters: Large-scale exact diagonalization results," *Phys. Rev. B*, vol. 83, p. 212 401, 21 2011. DOI: 10.1103/PhysRevB.83.212401.

[238] H. J. Changlani, S. Pujari, C.-M. Chung, and B. K. Clark, "Resonating quantum three-coloring wave functions for the kagome quantum antiferromagnet," *Phys. Rev. B*, vol. 99, p. 104 433, 10 2019. DOI: 10.1103/PhysRevB.99.104433.

[239] Q. Zhang, S. Okamoto, G. D. Samolyuk, M. B. Stone, A. I. Kolesnikov, R. Xue, J. Yan, M. A. McGuire, D. Mandrus, and D. A. Tennant, "Unusual exchange couplings and intermediate temperature weyl state in $Co_3Sn_2S_2$," *Phys. Rev. Lett.*, vol. 127, p. 117 201, 11 2021. DOI: 10.1103/PhysRevLett.127.117201.

[240] C. Liu, J. Shen, J. Gao, C. Yi, D. Liu, T. Xie, L. Yang, S. Danilkin, G. Deng, W. Wang, S. Li, Y. Shi, H. Weng, E. Liu, and H. Luo, "Spin excitations and spin wave gap in the ferromagnetic weyl semimetal co3sn2s2," *Science China Physics, Mechanics & Astronomy*, vol. 64, no. 1, p. 217 062, 2020. DOI: 10.1007/s11433-020-1597-6.

[241] T. Momoi and M. Suzuki, "Ground-state properties and phase diagram of the quantum xxz antiferromagnet on a triangular lattice," *Journal of the Physical Society of Japan*, vol. 61, no. 10, pp. 3732–3744, 1992. DOI: 10.1143/JPSJ.61.3732.

[242] A. A. Burkov and L. Balents, "Weyl semimetal in a topological insulator multilayer," *Phys. Rev. Lett.*, vol. 107, p. 127 205, 12 2011. DOI: 10.1103/PhysRevLett.107.127205.

[243] A. A. Zyuzin, S. Wu, and A. A. Burkov, "Weyl semimetal with broken time reversal and inversion symmetries," *Phys. Rev. B*, vol. 85, p. 165 110, 16 2012. DOI: 10.1103/PhysRevB.85.165110.

[244] C. Lei, S. Chen, and A. H. MacDonald, "Magnetized topological insulator multilayers," *Proceedings of the National Academy of Sciences*, vol. 117, no. 44, pp. 27 224–27 230, 2020. DOI: 10.1073/pnas.2014004117.

[245] L. Muechler, E. Liu, J. Gayles, Q. Xu, C. Felser, and Y. Sun, "Emerging chiral edge states from the confinement of a magnetic weyl semimetal in $Co_3Sn_2S_2$," *Phys. Rev. B*, vol. 101, p. 115 106, 11 2020. DOI: 10.1103/PhysRevB.101.115106.

[246] I. Titvinidze, J. Legendre, K. Le Hur, and W. Hofstetter, "Hubbard model on the kagome lattice with time-reversal invariant flux and spin-orbit coupling," *Phys. Rev. B*, vol. 105, p. 235 102, 23 2022. DOI: 10.1103/PhysRevB.105.235102.

[247] G. Liu, P. Zhang, Z. Wang, and S.-S. Li, "Spin hall effect on the kagome lattice with rashba spin-orbit interaction," *Phys. Rev. B*, vol. 79, p. 035 323, 3 2009. DOI: 10.1103/PhysRevB.79.035323.

[248] J. Hubbard and B. H. Flowers, "Electron correlations in narrow energy bands," *Proceedings of the Royal Society of London. Series A. Mathematical and Physical Sciences*, vol. 276, no. 1365, pp. 238–257, 1963. DOI: 10.1098/rspa.1963.0204.

[249] J. Schnack, J. Schulenburg, A. Honecker, and J. Richter, "Magnon crystallization in the kagome lattice antiferromagnet," *Phys. Rev. Lett.*, vol. 125, p. 117 207, 11 2020. DOI: 10.1103/PhysRevLett.125.117207.

[250] T. Ohashi, N. Kawakami, and H. Tsunetsugu, "Mott transition in kagomé lattice hubbard model," *Phys. Rev. Lett.*, vol. 97, p. 066 401, 6 2006. DOI: 10.1103/PhysRevLett.97.066401.

[251] W. Koshibae and S. Maekawa, "Electronic state of a CoO_2 layer with hexagonal structure: A kagomé lattice structure in a triangular lattice," *Phys. Rev. Lett.*, vol. 91, p. 257 003, 25 2003. DOI: 10.1103/PhysRevLett.91.257003.

[252] Y. Imai, N. Kawakami, and H. Tsunetsugu, "Low-energy excitations of the hubbard model on the kagomé lattice," *Phys. Rev. B*, vol. 68, p. 195 103, 19 2003. DOI: 10.1103/PhysRevB.68.195103.

[253] N. Bulut, W. Koshibae, and S. Maekawa, "Magnetic correlations in the hubbard model on triangular and kagomé lattices," *Phys. Rev. Lett.*, vol. 95, p. 037 001, 3 2005. DOI: 10.1103/PhysRevLett.95.037001.

[254] S. Kuratani, A. Koga, and N. Kawakami, "Mott transition of correlated electrons on the kagomé lattice," *Journal of Physics: Condensed Matter*, vol. 19, no. 14, p. 145 252, 2007. DOI: 10.1088/0953-8984/19/14/145252.

[255] Y. Furukawa, T. Ohashi, Y. Koyama, and N. Kawakami, "Mott transition in the hubbard model on the anisotropic kagome lattice," *Phys. Rev. B*, vol. 82, p. 161 101, 16 2010. DOI: 10.1103/PhysRevB.82.161101.

[256] M. L. Kiesel, C. Platt, and R. Thomale, "Unconventional fermi surface instabilities in the kagome hubbard model," *Phys. Rev. Lett.*, vol. 110, p. 126 405, 12 2013. DOI: 10.1103/PhysRevLett.110.126405.

[257] T. Kita, T. Ohashi, and N. Kawakami, "Field-induced mott transition in kagome lattice hubbard model," *Phys. Rev. B*, vol. 87, p. 155 119, 15 2013. DOI: 10.1103/PhysRevB.87.155119.

[258] S. K. Kim and J. Zang, "U(1) symmetry of the spin-orbit coupled hubbard model on the kagome lattice," *Phys. Rev. B*, vol. 92, p. 205 106, 20 2015. DOI: 10.1103/PhysRevB.92.205106.

[259] W.-S. Wang, Y.-C. Liu, Y.-Y. Xiang, and Q.-H. Wang, "Antiferromagnetism, f-wave, and chiral p-wave superconductivity in a kagome lattice with possible application to sd^2 graphenes," *Phys. Rev. B*, vol. 94, p. 014 508, 1 2016. DOI: 10.1103/PhysRevB.94.014508.

[260] R.-Y. Sun and Z. Zhu, "Metal-insulator transition and intermediate phases in the kagome lattice hubbard model," *Phys. Rev. B*, vol. 104, p. L121118, 12 2021. DOI: 10.1103/PhysRevB.104.L121118.

[261] K. A. Chao, J Spalek, and A. M. Oles, "Kinetic exchange interaction in a narrow s-band," *Journal of Physics C: Solid State Physics*, vol. 10, no. 10, pp. L271–L276, 1977. DOI: 10.1088/0022-3719/10/10/002.

[262] J. E. Hirsch, "Attractive interaction and pairing in fermion systems with strong on-site repulsion," *Phys. Rev. Lett.*, vol. 54, pp. 1317–1320, 12 1985. DOI: 10.1103/PhysRevLett.54.1317.

[263] P. Mendels and F. Bert, "Quantum kagome antiferromagnet zncu3(oh)6cl2," *Journal of the Physical Society of Japan*, vol. 79, no. 1, p. 011 001, 2010. DOI: 10.1143/JPSJ.79.011001.

[264] P. Mendels and F. Bert, "Quantum kagome frustrated antiferromagnets: One route to quantum spin liquids," *Comptes Rendus Physique*, vol. 17, no. 3, pp. 455–470, 2016, Physique de la matière condensée au XXIe siècle: l'héritage de Jacques Friedel, ISSN: 1631-0705. DOI: https://doi.org/10.1016/j.crhy.2015.12.001.

[265] A. Andreanov and M. V. Fistul, "Frustration-induced highly anisotropic magnetic patterns in the classical xy model on the kagome lattice," *Phys. Rev. B*, vol. 102, p. 140 405, 14 2020. DOI: 10.1103/PhysRevB.102.140405.

[266] K. Kumar, K. Sun, and E. Fradkin, "Chern-simons theory of magnetization plateaus of the spin-$\frac{1}{2}$ quantum xxz heisenberg model on the kagome lattice," *Phys. Rev. B*, vol. 90, p. 174 409, 17 2014. DOI: 10.1103/PhysRevB.90.174409.

[267] J. Colbois, B. Vanhecke, L. Vanderstraeten, A. Smerald, F. Verstraete, and F. Mila, "Partial lifting of degeneracy in the $J_1 - J_2 - J_3$ ising antiferromagnet on the kagome lattice," in arXiv, 2022.

[268] U. Schneider, L. Hackermüller, S. Will, T. Best, I. Bloch, T. A. Costi, R. W. Helmes, D. Rasch, and A. Rosch, "Metallic and insulating phases of repulsively interacting fermions in a 3d optical lattice," *Science*, vol. 322, no. 5907, pp. 1520–1525, 2008. DOI: 10.1126/science.1165449.

[269] I. Bloch, J. Dalibard, and W. Zwerger, "Many-body physics with ultracold gases," *Rev. Mod. Phys.*, vol. 80, pp. 885–964, 3 2008. DOI: 10.1103/RevModPhys.80.885.

[270] W Hofstetter and T Qin, "Quantum simulation of strongly correlated condensed matter systems," *Journal of Physics B: Atomic, Molecular and Optical Physics*, vol. 51, no. 8, p. 082 001, 2018. DOI: 10.1088/1361-6455/aaa31b.

[271] C. C. Bradley, C. A. Sackett, J. J. Tollett, and R. G. Hulet, "Evidence of bose-einstein condensation in an atomic gas with attractive interactions," *Phys. Rev. Lett.*, vol. 75, pp. 1687–1690, 9 1995. DOI: 10.1103/PhysRevLett.75.1687.

[272] M. H. Anderson, J. R. Ensher, M. R. Matthews, C. E. Wieman, and E. A. Cornell, "Observation of bose-einstein condensation in a dilute atomic vapor," *Science*, vol. 269, no. 5221, pp. 198–201, 1995. DOI: 10.1126/science.269.5221.198.

[273] K. B. Davis, M. O. Mewes, M. R. Andrews, N. J. van Druten, D. S. Durfee, D. M. Kurn, and W. Ketterle, "Bose-einstein condensation in a gas of sodium atoms," *Phys. Rev. Lett.*, vol. 75, pp. 3969–3973, 22 1995. DOI: 10.1103/PhysRevLett.75.3969.

[274] B. DeMarco and D. S. Jin, "Onset of fermi degeneracy in a trapped atomic gas," *Science*, vol. 285, no. 5434, pp. 1703–1706, 1999. DOI: 10.1126/science.285.5434.1703.

[275] A. G. Truscott, K. E. Strecker, W. I. McAlexander, G. B. Partridge, and R. G. Hulet, "Observation of fermi pressure in a gas of trapped atoms," *Science*, vol. 291, no. 5513, pp. 2570–2572, 2001. DOI: 10.1126/science.1059318.

[276] F. Schreck, L. Khaykovich, K. L. Corwin, G. Ferrari, T. Bourdel, J. Cubizolles, and C. Salomon, "Quasipure bose-einstein condensate immersed in a fermi sea," *Phys. Rev. Lett.*, vol. 87, p. 080 403, 8 2001. DOI: 10.1103/PhysRevLett.87.080403.

[277] D. Jaksch, C. Bruder, J. I. Cirac, C. W. Gardiner, and P. Zoller, "Cold bosonic atoms in optical lattices," *Phys. Rev. Lett.*, vol. 81, pp. 3108–3111, 15 1998. DOI: 10.1103/PhysRevLett.81.3108.

[278] T. Müller-Seydlitz, M. Hartl, B. Brezger, H. Hänsel, C. Keller, A. Schnetz, R. J. C. Spreeuw, T. Pfau, and J. Mlynek, "Atoms in the lowest motional band of a three-dimensional optical lattice," *Phys. Rev. Lett.*, vol. 78, pp. 1038–1041, 6 1997. DOI: 10.1103/PhysRevLett.78.1038.

[279] S. E. Hamann, D. L. Haycock, G. Klose, P. H. Pax, I. H. Deutsch, and P. S. Jessen, "Resolved-sideband raman cooling to the ground state of an optical lattice," *Phys. Rev. Lett.*, vol. 80, pp. 4149–4152, 19 1998. DOI: 10.1103/PhysRevLett.80.4149.

[280] C. Orzel, A. K. Tuchman, M. L. Fenselau, M. Yasuda, and M. A. Kasevich, "Squeezed states in a bose-einstein condensate," *Science*, vol. 291, no. 5512, pp. 2386–2389, 2001. DOI: 10.1126/science.1058149.

[281] G.-B. Jo, J. Guzman, C. K. Thomas, P. Hosur, A. Vishwanath, and D. M. Stamper-Kurn, "Ultracold atoms in a tunable optical kagome lattice," *Phys. Rev. Lett.*, vol. 108, p. 045 305, 4 2012. DOI: 10.1103/PhysRevLett.108.045305.

[282] L. Santos, M. A. Baranov, J. I. Cirac, H.-U. Everts, H. Fehrmann, and M. Lewenstein, "Atomic quantum gases in kagomé lattices," *Phys. Rev. Lett.*, vol. 93, p. 030 601, 3 2004. DOI: 10.1103/PhysRevLett.93.030601.

[283] H. Zhang, X. Chen, Z. Ma, and Y. Zhou, "Kagome lattices for ultracold atoms induced by additional lightfields," *Journal of Physics B: Atomic, Molecular and Optical Physics*, vol. 49, no. 11, p. 115 301, 2016. DOI: 10.1088/0953-4075/49/11/115301.

[284] M. Lewenstein, A. Sanpera, V. Ahufinger, B. Damski, A. Sen(De), and U. Sen, "Ultracold atomic gases in optical lattices: Mimicking condensed matter physics and beyond," *Advances in Physics*, vol. 56, no. 2, pp. 243–379, 2007. DOI: 10.1080/00018730701223200.

[285] A. Klein and D. Jaksch, "Phonon-induced artificial magnetic fields in optical lattices," *EPL (Europhysics Letters)*, vol. 85, no. 1, p. 13 001, 2009. DOI: 10.1209/0295-5075/85/13001.

[286] N. Goldman, I. Satija, P. Nikolic, A. Bermudez, M. A. Martin-Delgado, M. Lewenstein, and I. B. Spielman, "Realistic time-reversal invariant topological insulators with neutral atoms," *Phys. Rev. Lett.*, vol. 105, p. 255 302, 25 2010. DOI: 10.1103/PhysRevLett.105.255302.

[287] F. Gerbier and J. Dalibard, "Gauge fields for ultracold atoms in optical superlattices," *New Journal of Physics*, vol. 12, no. 3, p. 033 007, 2010. DOI: 10.1088/1367-2630/12/3/033007.

[288] J. Dalibard, F. Gerbier, G. Juzeliūnas, and P. Öhberg, "Colloquium: Artificial gauge potentials for neutral atoms," *Rev. Mod. Phys.*, vol. 83, pp. 1523–1543, 4 2011. DOI: 10.1103/RevModPhys.83.1523.

[289] V. Galitski and I. B. Spielman, "Spin–orbit coupling in quantum gases," *Nature*, vol. 494, no. 7435, pp. 49–54, 2013, ISSN: 1476-4687. DOI: 10.1038/nature11841.

[290] N Goldman, G Juzeliūnas, P Öhberg, and I. B. Spielman, "Light-induced gauge fields for ultracold atoms," *Reports on Progress in Physics*, vol. 77, no. 12, p. 126 401, 2014. DOI: 10.1088/0034-4885/77/12/126401.

[291] X.-J. Liu, K. T. Law, and T. K. Ng, "Realization of 2d spin-orbit interaction and exotic topological orders in cold atoms," *Phys. Rev. Lett.*, vol. 112, p. 086 401, 8 2014. DOI: 10.1103/PhysRevLett.112.086401.

[292] F. Grusdt, T. Li, I. Bloch, and E. Demler, "Tunable spin-orbit coupling for ultracold atoms in two-dimensional optical lattices," *Phys. Rev. A*, vol. 95, p. 063 617, 6 2017. DOI: 10.1103/PhysRevA.95.063617.

[293] M. Aidelsburger, M. Atala, M. Lohse, J. T. Barreiro, B. Paredes, and I. Bloch, "Realization of the hofstadter hamiltonian with ultracold atoms in optical lattices," *Phys. Rev. Lett.*, vol. 111, p. 185 301, 18 2013. DOI: 10.1103/PhysRevLett.111.185301.

[294] H. Miyake, G. A. Siviloglou, C. J. Kennedy, W. C. Burton, and W. Ketterle, "Realizing the harper hamiltonian with laser-assisted tunneling in optical lattices," *Phys. Rev. Lett.*, vol. 111, p. 185 302, 18 2013. DOI: 10.1103/PhysRevLett.111.185302.

[295] T. D. Stanescu, V. Galitski, and S. Das Sarma, "Topological states in two-dimensional optical lattices," *Phys. Rev. A*, vol. 82, p. 013 608, 1 2010. DOI: 10.1103/PhysRevA.82.013608.

[296] Y.-J. Lin, K. Jiménez-García, and I. B. Spielman, "Spin–orbit-coupled bose–einstein condensates," *Nature*, vol. 471, no. 7336, pp. 83–86, 2011, ISSN: 1476-4687. DOI: 10.1038/nature09887.

[297] P. Wang, Z.-Q. Yu, Z. Fu, J. Miao, L. Huang, S. Chai, H. Zhai, and J. Zhang, "Spin-orbit coupled degenerate fermi gases," *Phys. Rev. Lett.*, vol. 109, p. 095 301, 9 2012. DOI: 10.1103/PhysRevLett.109.095301.

[298] L. W. Cheuk, A. T. Sommer, Z. Hadzibabic, T. Yefsah, W. S. Bakr, and M. W. Zwierlein, "Spin-injection spectroscopy of a spin-orbit coupled fermi gas," *Phys. Rev. Lett.*, vol. 109, p. 095 302, 9 2012. DOI: 10.1103/PhysRevLett.109.095302.

[299] J.-Y. Zhang, S.-C. Ji, Z. Chen, L. Zhang, Z.-D. Du, B. Yan, G.-S. Pan, B. Zhao, Y.-J. Deng, H. Zhai, S. Chen, and J.-W. Pan, "Collective dipole oscillations of a spin-orbit coupled bose-einstein condensate," *Phys. Rev. Lett.*, vol. 109, p. 115 301, 11 2012. DOI: 10.1103/PhysRevLett.109.115301.

[300] A. Manchon, H. C. Koo, J. Nitta, S. M. Frolov, and R. A. Duine, "New perspectives for rashba spin–orbit coupling," *Nature Materials*, vol. 14, pp. 871–882, 2015. DOI: 10.1038/nmat4360.

[301] S.-L. Zhu, H. Fu, C.-J. Wu, S.-C. Zhang, and L.-M. Duan, "Spin hall effects for cold atoms in a light-induced gauge potential," *Phys. Rev. Lett.*, vol. 97, p. 240 401, 24 2006. DOI: 10.1103/PhysRevLett.97.240401.

[302] X.-J. Liu, X. Liu, L. C. Kwek, and C. H. Oh, "Optically induced spin-hall effect in atoms," *Phys. Rev. Lett.*, vol. 98, p. 026 602, 2 2007. DOI: 10.1103/PhysRevLett.98.026602.

[303] M. C. Beeler, R. A. Williams, K. Jiménez-García, L. J. LeBlanc, A. R. Perry, and I. B. Spielman, "The spin hall effect in a quantum gas," *Nature*, vol. 498, no. 7453, pp. 201–204, 2013, ISSN: 1476-4687. DOI: 10.1038/nature12185.

[304] P. Courteille, R. S. Freeland, D. J. Heinzen, F. A. van Abeelen, and B. J. Verhaar, "Observation of a feshbach resonance in cold atom scattering," *Phys. Rev. Lett.*, vol. 81, pp. 69–72, 1 1998. DOI: 10.1103/PhysRevLett.81.69.

[305] S. Inouye, M. R. Andrews, J. Stenger, H. J. Miesner, D. M. Stamper-Kurn, and W. Ketterle, "Observation of feshbach resonances in a bose–einstein condensate," *Nature*, vol. 392, no. 6672, pp. 151–154, 1998. DOI: 10.1038/32354.

[306] M. Greiner, O. Mandel, T. Esslinger, T. W. Hänsch, and I. Bloch, "Quantum phase transition from a superfluid to a mott insulator in a gas of ultracold atoms," *Nature*, vol. 415, no. 6867, pp. 39–44, 2002, ISSN: 1476-4687. DOI: 10.1038/415039a.

[307] T. Stöferle, H. Moritz, C. Schori, M. Köhl, and T. Esslinger, "Transition from a strongly interacting 1d superfluid to a mott insulator," *Phys. Rev. Lett.*, vol. 92, p. 130 403, 13 2004. DOI: 10.1103/PhysRevLett.92.130403.

[308] R. Jördens, N. Strohmaier, K. Günter, H. Moritz, and T. Esslinger, "A mott insulator of fermionic atoms in an optical lattice," *Nature*, vol. 455, no. 7210, pp. 204–207, 2008, ISSN: 1476-4687. DOI: 10.1038/nature07244.

[309] M. Köhl, H. Moritz, T. Stöferle, K. Günter, and T. Esslinger, "Fermionic atoms in a three dimensional optical lattice: Observing fermi surfaces, dynamics, and interactions," *Phys. Rev. Lett.*, vol. 94, p. 080 403, 8 2005. DOI: 10.1103/PhysRevLett.94.080403.

[310] N. Strohmaier, Y. Takasu, K. Günter, R. Jördens, M. Köhl, H. Moritz, and T. Esslinger, "Interaction-controlled transport of an ultracold fermi gas," *Phys. Rev. Lett.*, vol. 99, p. 220 601, 22 2007. DOI: 10.1103/PhysRevLett.99.220601.

[311] U. Schneider, L. Hackermüller, J. P. Ronzheimer, S. Will, S. Braun, T. Best, I. Bloch, E. Demler, S. Mandt, D. Rasch, and A. Rosch, "Fermionic transport and out-of-equilibrium dynamics in a homogeneous hubbard model with ultracold atoms," *Nature Physics*, vol. 8, no. 3, pp. 213–218, 2012. DOI: 10.1038/nphys2205.

[312] S. S. Kondov, W. R. McGehee, W. Xu, and B. DeMarco, "Disorder-induced localization in a strongly correlated atomic hubbard gas," *Phys. Rev. Lett.*, vol. 114, p. 083 002, 8 2015. DOI: 10.1103/PhysRevLett.114.083002.

[313] T. Fukui and Y. Hatsugai, "Topological aspects of the quantum spin-hall effect in graphene: Z_2 Topological order and spin chern number," *Phys. Rev. B*, vol. 75, p. 121 403, 12 2007. DOI: 10.1103/PhysRevB.75.121403.

[314] P. Kumar, T. Mertz, and W. Hofstetter, "Interaction-induced topological and magnetic phases in the hofstadter-hubbard model," *Phys. Rev. B*, vol. 94, p. 115 161, 11 2016. DOI: 10.1103/PhysRevB.94.115161.

[315] T. Giamarchi, "Quantum physics in one dimension," in Clarendon Press, Oxford, 2003.

[316] A. O. Gogolin, A. A. Nersesyan, and A. M. Tsvelik, "Bosonization and strongly correlated systems," in Cambridge University Press, Cambridge, UK, 2004.

[317] P. P. Orth, D. Cocks, S. Rachel, M. Buchhold, K. L. Hur, and W. Hofstetter, "Correlated topological phases and exotic magnetism with ultracold fermions," *Journal of Physics B: Atomic, Molecular and Optical Physics*, vol. 46, no. 13, p. 134 004, 2013. DOI: 10.1088/0953-4075/46/13/134004.

[318] A. A. Clerk, M. H. Devoret, S. M. Girvin, F. Marquardt, and R. J. Schoelkopf, "Introduction to quantum noise, measurement, and amplification," *Rev. Mod. Phys.*, vol. 82, pp. 1155–1208, 2 2010. DOI: 10.1103/RevModPhys.82.1155.

[319] M. Schiró and K. Le Hur, "Tunable hybrid quantum electrodynamics from nonlinear electron transport," *Phys. Rev. B*, vol. 89, p. 195 127, 19 2014. DOI: 10.1103/PhysRevB.89.195127.

[320] R. Kubo, "Statistical-mechanical theory of irreversible processes. i. general theory and simple applications to magnetic and conduction problems," *Journal of the Physical Society of Japan*, vol. 12, no. 6, pp. 570–586, 1957. DOI: 10.1143/JPSJ.12.570.

[321] P. B. Allen, "Chapter 6 electron transport," 2006.

[322] Z. Fan, J. H. Garcia, A. W. Cummings, J. E. Barrios-Vargas, M. Panhans, A. Harju, F. Ortmann, and S. Roche, "Linear scaling quantum transport methodologies," *Physics Reports*, vol. 903, pp. 1–69, 2021, Linear scaling quantum transport methodologies, ISSN: 0370-1573. DOI: https://doi.org/10.1016/j.physrep.2020.12.001.

ECOLE DOCTORALE

Titre : Phases topologiques, réponse à la lumière et réseau de kagomé

Mots clés : Matière condensée, Phases topologiques, Réseau de kagomé

Résumé : Nous étudions théoriquement des modèles topologiques sur réseaux, pertinents pour des matériaux et des systèmes artificiels actuels. Nous développons un calcul analytique explicite du nombre de Chern pour les systèmes que l'on étudie et nous comparons ce calcul avec d'autres méthodes de calcul de cet invariant topologique. Nous proposons un protocole, à partir d'une mesure de la réponse locale à une excitation lumineuse (micro-onde), pour sonder les propriétés topologiques d'un modèle bosonique de Haldane, dans un système photonique. Sur le réseau de kagomé, nous étudions (i) une transition de phase magnétique et topologique pour un modèle à deux canaux en lien avec un matériau quantique récemment découvert, et (ii) un modèle topologique invariant par renversement du temps et contenant un terme de flux, un terme de couplage spin-orbit de type Rashba et un terme d'interactions de Hubbard, dont la réalisation est pertinente dans des gaz d'atomes froids.

Title : Topological phases, light response and kagome lattice

Keywords : Condensed Matter, Topological phases, Kagome lattice

Abstract : We theoretically study topological lattice models relevant to current experimental solid-state and artificial systems. We develop an explicit analytical computation of the Chern number in the systems we study and we compare it with other computation methods of this topological invariant. We propose a protocol, based on the local response to a light input, to probe the topological properties of a Haldane boson model in a photonic system. On the kagome lattice, we investigate (i) a magnetic and topological phase transition for a two-channel model, in relation with recently discovered quantum materials, and (ii) a time-reversal topological model with flux, Rashba spin-orbit coupling and Hubbard interactions, relevant for realization in cold-atom gases.

Institut Polytechnique de Paris
91120 Palaiseau, France